The complex morphology of radio-quiet active galactic nuclei : multi-wavelength radiative transfer and polarization

Frédéric Marin

UNIVERSITÉ DE STRASBOURG

École et Observatoire des Sciences de la Terre

Observatoire Astronomique de Strasbourg

THÈSE

présentée par :

Frédéric MARIN

soutenue le : **20 Septembre 2013**

pour obtenir le grade de : **Docteur de l'université de Strasbourg**

Discipline/ Spécialité : Astrophysique

Étude de la morphologie complexe des Noyaux Actifs de Galaxie

Transfert radiatif multi-longueurs d'ondes et polarisation

THÈSE dirigée par :

Mr GOOSMANN René	Maitre de conférence HDR, université de Strasbourg
Mme PORQUET Delphine	Chargée de recherche HDR, université de Strasbourg

RAPPORTEURS :

Mr HAMEURY Jean-Marie	Directeur de recherche, université de Strasbourg
Mme LIRA Paulina	Maitre de conférence HDR, Universidad de Chile
Mr COSTA Enrico	Directeur de recherche, Istituto di Astrofisica

---

AUTRES MEMBRES DU JURY :

Mr DOVCIAK Michal	Chargé de recherche, Astronomicky Ustav, Praha

À qui donc parles-tu [Nébuleuse], flocon lointain qui passes ?
À peine entendons-nous ta voix dans les espaces.
Nous ne te distinguons que comme un nimbe obscur,
Au coin le plus perdu du plus nocturne azur.

Victor Hugo
La légende des siècles

Mon fils, tu comprendras comment fonctionne le soleil
avant de comprendre comment fonctionnent les femmes ...

Mon père

UNIVERSITÉ DE STRASBOURG

UNIVERSITÉ DE STRASBOURG

Ecole et Observatoire des Sciences de la Terre

Résumé

Lorsque l'on veut sonder les structures internes de sources astronomiques non résolues par nos instruments modernes, la technique de la spectropolarimétrie a démontré etre une méthode à la fois indépendante et complémentaire des analyses spectrales et temporelles. Dans cette thèse, j'explore de façon théorique le signal de polarisation résultant des Noyaux Actifs de Galaxies (NAG en français, AGN en anglais), dans lesquels on suppose que l'énergie radiative principale est crée par accrétion autour d'un trou noir super-massif et qu'une partie importante des échappements de matère se fait sous la forme de vents d'éjection. Selon le Schéma Unifié des NAG, l'émission radiative résultante est fortement anisotrope, due au confinement des photons par un corps de poussère obscurcissant situé au niveau du plan équatorial. Les radiations sont donc forcées de s'échapper dans les directions polaires, photo-ionisant au passage les vents d'éjection coniques. Cette configuration asymétrique permet de justifier la dichotomie observationnelle des NAG en fonction de leur inclinaison spatiale; cependant, leurs propriétés difèrent aussi en fonction de la bande énergétique d'observation. Donc, afin de vérifier la stabilité du moèle unifié, il est nécessaire de le tester sur de multiples échelles de longueur d'onde afin d'en déduire de fortes contraintes morphologiques.

Mots-clefs : transfert du rayonnement – polarisation – Noyaux Actifs de Galaxie – optique / ultraviolet / rayons X

Résumé en anglais

When probing the inner structures of unresolved astrophysical sources, spectropolarimetry has proven to be a solid tool, both independent and complementary to spectral and timing anal- yses. In this thesis, I theoretically explore the polarization of Active Galactic Nuclei (AGN), which are powered by accretion onto supermassive black holes and often reveal significant mass outflows. Their emission is strongly anisotropic and the standard model of AGN postulates that the anisotropy is caused by a confinement of the radiation in the funnel of an obscuring body of circumnuclear dust; the radiation is thus forced to escape along the funnel where it photo-ionizes conically shaped outflows. The asymmetrical configuration explains an observational dichotomy where AGN properties are characterized according to the observer's line-of-sight. However, AGN observations differ significantly from one waveband to another and the broadband validity of the unified model has to be tested by a method that gives strong constraints on the AGN morphology. In this thesis, I subsequently investigate how morphological and composition constraints on the different sub-structures in thermal, radio-quiet Active Galactic Nuclei can be deduced from optical, UV and X-ray polarization properties.

Keywords : radiative transfer – polarization – Active Galactic Nuclei – optical / ultraviolet / X-rays

Acknowledgements

A thesis does not solely consist of bibliographic work, research, and conferences; it can also involve random encounters, cultural exchanges, and newly acquainted friendships.

I never would have managed to immerse myself so deeply in the subject of active galactic nuclei without the debonair endorsement of my supervisor Rene W. Goosmann, whom I consider my father of science. Because of his deep kindness, unwavering patience, and persistent dedication, I am able to progress in the field of astrophysics. His scholarly explanations and continuous support has made me the researcher I am today, and I hope some day I can return the same favor to my future students. As another member of my scientific family, I also would like to thank Delphine Porquet, co-director of my thesis, who has placed in such a high outlook of which I hope I have not disappointed. She is one of the few people who's level of knowledge is as high as her kindness. Generator of ideas, she is the seed of half of my publications.

The Astronomical Observatory of Strasbourg is a fertile breeding ground for scientific spirits and fraternal colleagues. I would like to thank the director, Hervé Wozniak, for hosting me in his observatory and for always guiding me and keeping an eye on me. Our dual conference was a rewarding and a pleasant experience. I would also like to thank Nicolas Grosso for his informed points and scientific rigor on the writing of our joint publications. I also want to thank the High Energy team, who has continously supported me, as well as the rest of the researchers for their discussions and assistance throughout my thesis. I also wish to extend my thanks to our secretaries, Sandrine Langenbacher and Véronique Trimbour. They have made my life easier, and I do not know how I will do without them in the years to come.

Among the other European institutes and observatories I visited, I would like to share my gratitude to the Astronomický Ústav in Prague, where my colleagues Michal Dovčiak, Michal Bursa, Tomáš Pecháček, and Vladimír Karas generously hosted me for several months of highly fructifying collaboration. My thanks also goes to the Università degli Studi in Rome, where Giorgio Matt and Fabio Muleri helped me perform valuable work. A big thank you also to Agata Różańska from the Centrum Astronomiczne im. Mikolaja Kopernika in Warsaw for their hospitality. I must also thank my friends and colleagues from the Jardin des Sciences and the Planetarium of Strasbourg, Milène Wendling and Saïd Hasnaoui, as well as all the other ones, with whom I have spent many nights volunteering to allow children and adults to participate in night observations, public conferences, and scientific outreaches. Although this stems back to my master's career, my deepest gratitude goes to a particular person at the University of Montpellier, Eric Josselin, who I met in my second year of my Master's. He was one of the most important contributor in my entry to the Astronomical Observatory of Strasbourg, and I owe him my scientific career. I will never forget his gesture and his invaluable support.

Beyond the leading roles of this scientific establishment, I want to emphasize the importance of some friends and dear colleagues who have equally contributed to the development of this manuscript and to its most Machiavellian delay. My first thought goes to Jonathan Chardin, colleague, partner, and longtime friend who accompanied me from our first year of our Master's degree to our doctoral epilogue. He provided unwavering support, even in our crazy culinary concoctions of vinous exaltations of red-wine soaked omelets. I must also thank the new PhD students, Anaïs Gonneau, Carole Faure, Jean-Baptiste Salomon, François Nehlig, and Benjamin Laevens, who were able to fill our offices with sudden aperitifs and mimed concerts. Francesco Tamborra, a newly recruited postdoctoral employee who I have known as a friend, also added a wonderful Italian color to our merry band. Even if they do not belong to the circle of the observatory, I could have never developed myself in Alsace without my companions: Adam Alloul and Miruna Parchirie, followers of walks in winemaker's cellars; Paul Bantzhaff and Nuria Moratal, musicians, handymen, and adorable cooks; Ana-Maria Natu for her vitality and inexhaustible joy; my adorable toilsome neighbor Pauline Kirsch and our shared passion for stupid TV series and penguins; my great philosopher Audrey Ginting and our long evenings of transcendent debates; Camille Beluffi for her obsession to visit the cathedral *in naturalibus*; and finally to my dear New Yorker Susan Seeman for her unwavering support and advice in my English translations. I can not name everyone here, but I am most grateful to all the friends of my early youth who always welcome me as a brother every time I set foot in our so beautiful Duchy of Savoy.

I want to conclude by thanking those who contributed the most to make me who I am, who raised me in love, wisdom, and curiosity about the world around us, supporting me in all my choices, sometimes even pushing me in the right direction, and always believing in me, despite the distance that separates us: my family. To my parents Odile and Gérard, and my little sister Charlène, I send my love and eternal gratitude.

Remerciements

Une thèse, ce n'est pas que de la bibliographie, de la recherche et des conférences, c'est aussi des rencontres, des échanges, des amitiés.

Il est plus qu'évident que je n'aurais jamais réussi à me pencher si profondément sur le sujet des noyaux actifs de galaxies sans l'appui débonnaire de celui que je considère comme un père scientifique, mon directeur de thèse René W. Goosmann. D'une profonde gentillesse, d'une patience inébranlable et d'une conscience professionnelle peu commune, c'est grâce à lui que j'ai pu autant progresser dans le domaine de l'astrophysique. Par ses savantes explications et son aide continue, il a fait de moi le chercheur que je suis aujourd'hui; et j'espère pouvoir un jour rendre la pareille à mes futurs étudiants. Et comme une famille ne se fonde pas unilatéralement, je veux remercier Delphine Porquet, ma co-directrice de thèse, qui aura placé en moi de grands espoirs que j'espère ne pas avoir déçus. Il y a peu de personnes qui savent aussi bien qu'elle allier un niveau de connaissance aussi extrême avec une amabilité aussi rayonnante. Génératrice d'idées, je lui dois bien la moitié de mes publications jusque là.

L'Observatoire Astronomique de Strasbourg est un vivier d'esprits fertiles et de fraternels collègues. Il m'est alors important d'en remercier son directeur, Hervé Wozniak, pour m'avoir accueilli dans son établissement et avoir toujours discrètement gardé un œil sur moi depuis son impérial bureau. Notre conférence duale aura été une expérience tout aussi enrichissante que plaisante. Nicolas Grosso a aussi largement contribué à mon travail grâce à ses remarques judicieuses et sa rigueur scientifique lors de la relecture de nos publications communes. Je veux aussi remercier l'ensemble de l'équipe Hautes Énergies qui m'a soutenue continuellement, ainsi que le reste des chercheurs pour leurs discussions et leurs aides ponctuelles tout au long de ma thèse. Je tiens aussi à adresser mes remerciements à nos secrétaires, Sandrine Langenbacher et Véronique Trimbour, qui m'auront tellement simplifié la vie que je ne sais pas comment je vais faire dans les années à venir sans elles.

Au nombre des autres instituts et observatoires européens visités, j'ai une chaleureuse pensée pour l'Astronomický Ústav de Prague où mes collègues Michal Dovčiak, Michal Bursa, Tomáš Pecháček et Vladimír Karas m'ont accueilli généreusement pour plusieurs mois de travail et de collaboration hautement fructifiant. Mes amitiés vont aussi à l'Università degli Studi à Rome, où Giorgio Matt et Fabio Muleri m'ont aidé à accomplir de précieux travaux. Un grand merci aussi à Agata Różańska du Centrum Astronomiczne im. Mikolaja Kopernika de Varsovie pour son accueil. Plus proche géographiquement, je me dois aussi de remercier mes amis et collaborateurs du Jardin des Sciences et du Planétarium de Strasbourg, Milène Wendling, Saïd Hasnaoui et tous les autres, avec qui j'ai passé de nombreuses nuits à faire rêver les petits et grands grâce aux observations nocturnes, aux conférences pour le grand public et aux ateliers de divulgation scientifique que j'ai eu le plaisir d'animer bénévolement. Quoique cela remontasse à plus loin dans le temps et l'espace, mes plus sincères gratitudes vont à une personne particulière de l'Université de Montpellier où j'ai réalisé ma seconde année de Master, Éric Josselin. Il a été l'acteur le plus important de mon entrée à l'Observatoire Astronomique de Strasbourg et je lui dois ma carrière scientifique. Jamais je n'oublierai son geste et son soutien inestimable.

Au delà des premiers rôles de ce théâtre scientifique, je veux souligner l'importance d'amis et de collaborateurs chers qui auront tout autant contribué au développement de ce manuscrit qu'à son

frein le plus machiavélique. Ma première pensée va à Jonathan Chardin, confrère, binôme et ami de longue date qui m'a accompagné de la première année de Master jusqu'à l'épilogue doctoral. A raison d'omelettes au vin rouge, d'émission culinaires déjantées et d'exaltations viniques, il a été un support inébranlable de ma vie Strasbourgeoise. A lui doivent s'additionner les thésards des nouvelles années, Anaïs Gonneau, Carole Faure, Jean-Baptiste Salomon, François Nehlig et Benjamin Laevens qui ont su animer nos bureaux par de francs moments de rigolade, d'apéros soudains et de concerts mimés avec la plus grande maestria. Francesco Tamborra, nouvellement recruté au titre de post-doctorant mais ami depuis plus longtemps, aura permis d'apporter une touche ausonienne non négligeable à notre joyeuse troupe. N'appartenant pas au cercle de l'observatoire mais à celui civil, jamais je n'aurais pu m'épanouir aussi bien en Alsace sans mes compagnons Adam Alloul et Miruna Parchirie, adeptes de promenades dans les caves vigneronnes, Paul Bantzhaff et Nuria Moratal, musiciens, bricoleurs, et cuisiniers adorables, Ana-Maria Natu pour sa vitalité et son peps inépuisables, mon adorablement horripilante voisine Pauline Kirsch et notre passion commune pour les séries stupides et les pingouins, ma philosophe d'Audrey Ginting pour nos longues soirées de débats transcendants, Camille Beluffi pour son obsession de visiter la cathédrale *in naturalibus* et enfin ma chère New-Yorkaise de Susan Seeman pour son indéfectible soutien et son aide linguistique en anglais. Je ne puis citer tout le monde ici, mais mes pensées les plus reconnaissantes vont à tous les amis de ma prime jeunesse qui m'accueillent comme un frère à chaque fois que je peux remettre les pieds dans notre si beau duché de Savoie.

Je veux conclure en remerciant ceux qui ont le plus contribué à faire de moi ce que je suis, en m'ayant élevé dans l'amour, la sagesse et la curiosité du monde qui nous entoure, en m'ayant soutenu dans chacun de mes choix, en m'ayant parfois intelligemment poussé dans certaines directions et en ayant toujours cru en moi malgré la distance qui nous sépare: ma famille. A mes parents Odile et Gérard, à ma petite sœur Charlène, j'adresse mon amour et ma gratitude éternels.

Contents

Chapter

Tables

Table

Figures

Figure

Chapter 1

Introduction

All the stars seen at night belong to the Milky Way galaxy. The attractive gravity forces, preventing them to scatter in space, originate from the potential produced by the stars, the action of the so-called *dark matter* and, in the very center of the galaxy, by a compact and massive object, a supermassive black hole. Around the potential well created by a black hole, matter can spiral down to the compact object in the form of an accretion disk. The Milky Way's accretion rate being fairly low, accretion happens through a hot flow, but when the accretion rate approaches a large enough fraction of the so-called Eddington limit, a disk can form. If it does, the viscous matter bound by gravity starts to radiate colossal amounts of energy ranging from the infrared to the X-ray bands, and the galaxy is said to be *active*. As most of the subsequent bolometric luminosity is emitted in the few inner parsecs of such a galaxy, studies usually focus on the bright core of what is called *Active Galactic Nucleus* (AGN).

Discovered in the beginning of the twentieth century, AGN are still intriguing. Over a broad spectral range, they exhibit numerous spectroscopic signatures from neutral to highly ionized atomic features, broad and/or narrow emission/absorption lines, outflowing and/or inflowing gases, general relativistic broadening, strong variability and even superluminal jet motions. Describing AGN using a unique picture is a rather challenging task, but unification theories slowly emerged. A so far very successful theory predicts that most of the differences can be explained by an orientation effect: AGN properties differ if the system is seen from a polar, an intermediate or an equatorial inclination, the difference being attributed to circumnuclear obscuration. If it is true, AGN are strongly *anisotropic*.

Based on this unified model, broadband observations started to disentangle the complex morphology of AGN. The most widely accepted picture of the inner core of an AGN assumes that the supermassive black hole and its accretion disk power the system by emitting ultraviolet to infrared radiation. Some of the radiation is up-scattered in an assumed hot corona situated above the disk and released in the form of X-ray radiation. The accretion disk irradiates an equatorial distribution of rapidly moving ionized clouds, responsible for the broad emission lines seen at pole-on (type-1) AGN. At larger distances from the radiation source, an optically thick, obscuring dusty medium surrounds the equatorial plane and blocks the optical/UV flux towards an observer at an edge-on position of the object (type-2). According to the Unified Scheme, this circumnuclear gas, also called the "dusty torus", is responsible for the spectroscopic dichotomy between type-1 and type-2 AGN and was confirmed by recent mid-IR observations. While the opaque torus prevents radiation to escape along the equator, it supposedly also collimates massive winds towards polar directions. The outflowing gas decelerates while progressing in the interstellar medium surrounding

the AGN, mixing with the dusty environment and producing narrow absorption lines. A few tens of percent of all AGN may exhibit strongly collimated jets detected in the radio band and made off matter that is boosted to relativistic speeds. Such AGN are called "radio loud" in comparison with jet-free, "radio quiet" objects. The jets extend out to the scale of the galaxy bulge or the intergalactic medium.

While such a global picture emerges from the numerous observational AGN properties, much remains to be explored: what is the morphology of the AGN constituents? Are the general relativistic effects really responsible for the distorted iron lines seen in peculiar type-1 objects? Is the torus a final extension of a fragmented distribution of inner gas clouds? Where do the outflows and the jets originate? Does the unified model solve everything? To answer this non-exhaustive list of (mainly morphological) questions, spectroscopic, imaging and timing observations are undertaken since the middle of the twentieth century. Unfortunately, due to their distance, AGN are hardly resolved.

Another independent technic may be considered to disentangle the inner AGN geometry. This method focuses on the most important aspect of the unified theory: AGN are anisotropic objects. When radiation propagates through the multiple reprocessing regions surrounding the central black hole, its electromagnetic properties are modified by scattering, affecting its *polarization* state. Polarization is highly sensitive to the geometry of the scattering material and is enhanced by the asymmetry of the system. When considering the complex geometry of AGN, polarimetry has proven to be a solid tool that lead among other things to the discovery of hidden type-1 nuclei in type-2 objects, a pioneering discovery laying the foundations of the unified theory.

In order to support observational spectropolarimetric campaigns, the need for numerical predictions grew proportionally. Monte Carlo simulations are the most suitable technique to simulate the propagation of randomly emitted photons and to compute the polarization vector resulting from Thomson, Mie or Compton scattering. As polarization is sensitive to both the morphology and the composition of the reprocessing materials, numerical tests are able to (in)validate spectropolarimetric predictions about the true nature of AGN inner regions and can help to investigate the physical processes occurring behind the eventually obscured equatorial plane.

Using the Monte Carlo code STOKES, that simulates the radiative transfer equations between radiatively coupled emitting and reprocessing media, computes the polarization vector and operates from the near-infrared to the hard X-ray band, we undertook the examination of the complex morphology of thermal AGN. We focused on radio quiet objects as 1) they are more numerous than radio loud AGN and 2) synchrotron emission produced by the ballistic jet can reach the wavelengths of interest and "pollute" the polarization signal.

In the first chapters of this thesis, we give a broad overview on AGN, from their historical discovery to the actual models describing step by step their inner regions (Chap. 2). In Chap. 3, details on the polarization mechanisms that one can encounter from the optical to the X-ray band are reviewed. We leave aside polarization induced by magnetic interactions, as well as bremsstrahlung emission, as magnetic fields and the motion of free electrons are not included in STOKES. We present our results about the polarization signatures induced by multiple scattering in complex AGN models in Chap. 4 and derive numerical constraints on the morphology and opacity of the dusty torus, the polar outflows and the hot inner flow. We move from the general to the particular case by targeting the archetypal NGC 1068 galaxy. Taking into account the peculiar (tilted) geometry of the ionized outflows in NGC 1068, we successfully reproduce the observational levels of linear polarization and discriminate between several dust grain models (Chap. 5). As a few measurements

of circular polarization in NGC 1068 were obtained in past observations, we also investigate the circular polarization induced by Mie scattering in a dusty torus in Chap. 6. It happens that we are able to reproduce similar circular polarization levels only when considering the input spectrum to be already linearly polarized with a $\pm$ 45° orientation of the Stokes vector. Dichroic extinction is thus thought to be a more adequate mechanism to reach those levels of circular polarization. Motivated by observational and theoretical hints stating that persistent AGN scattering regions should have a fragmented structure, we enhance the complexity of our models by using clumpy reprocessing media in Chap. 7. Disruption of the equatorial regions is found to profoundly alter the polarization results while polar cloud distributions only have a small impact on our previous results. A complex, clumpy model of AGN is presented and is found to be closer to the observations than models based upon continuous media. In Chap. 8, we explore an empirical model of AGN where most of the spectroscopic signatures are explained by a disk-born wind. We test this model using spectropolarimetric data and find it its default parameterization not to be apt to reproduce the observed polarization signatures. We investigate different realizations of this model and find a new set of morphological and composition parameters to meet observational constraints in the optical and UV band. Pushing STOKES to the X-ray band in Chap. 9, we highlight the complementarity in multi-waveband investigations and present the current state in the technology of X-ray polarimetry. We explore the debated question of the apparent broadening of the iron K_α line in NGC 1365 and MCG-6-30-15 and show that even a small pathfinder X-ray mission equipped with the latest version of the Gas Pixel Detector would be able to shed new light on the topic. Encouraging the development of a future X-ray observatory dedicated to polarimetry, we draw our conclusions and final remarks in Chap. 10.

Chapter 2

A broad overview of Active Galactic Nuclei

The topic of AGN is wide, complex and pluritechnical. While it started a hundred years ago with the discovery of quasi-stellar objects (Fath 1909a,b), it took more than fifty years for the community to realize that AGN can be fantastic laboratories for matter under extreme conditions. From their inner core where general and special relativity are ruling the accretion and emission mechanisms, to their external boundaries where classical physics and dusty mixtures prevail, AGN can be used as a test ground for astrophysical mechanisms. As their intrinsic composition remains a major challenge to explain due to the variety of their spectroscopic, timing and polarimetric signatures, numerical simulations commonly isolate and examine each component separately. From there, reconstructing the quasar morphology may be a little bit more straightforward.

This is the path the first chapter of this manuscript follows. Departing from the supermassive black hole lying in the center of a quasi-stellar object, each individual AGN component are presented according to their theoretical and observational properties. We sum up the different components to finally present the most widely accepted unified picture of AGN (Antonucci 1993; Urry & Padovani 1995). For completeness, the history of quasar discovery is presented at the very beginning of this chapter, in order to honor the main actors that lead the community to unveil part of the mysteries hidden behind the extreme luminosity of active galactic nuclei.

2.1 Historical discovery

In the beginning of the twentieth century, many different *nebulae* were well known to astronomers but their nature was not yet entirely understood. One specific type of object in the first Messier and NGC catalogs, called *spiral nebula*, was generating a lot of debate. In particular, the scientific community was wondering whether *spiral nebulae* were relatively close, galactic gaseous objects similar to the Orion nebula, implying that the Milky Way was identical with large part of the entire universe (Shapley 1921), or very distant, extra-galactic collections of unresolved stars, extending the known boundaries of the Universe much farther than previously estimated (Curtis 1921).

In order to clarify the true nature of the spiral nebulae, Fath (1909a,b) undertook a series of photographic spectroscopic observations at the Lick Observatory. Pointing at six faint objects (NGC 224, NGC 1023, NGC 1068, NGC 3031, NGC 4736 and NGC 7331), he found that NGC 224 had a continuous spectrum with stellar absorption lines, indicating an unresolved system of solar type stars. On the other hand, the composite spectrum of NGC 1068 showed, in addition to the usual absorption lines, five *bright*[1] lines that were similar to the ones already observed in the spectra

[1] To be understood: bright *emission* lines, but the notion of emission lines was not established yet in astronomy.

of *gaseous nebulae*. The other four objects having spectra lying between those two extremes. The bright lines of NGC 1068 were later implicitly confirmed by the spectral velocity measurements of Slipher (1917), who discussed a possible disk origin for the line broadening. Systematic observations of additional sources started with the discovery of galaxies showing nuclear emission lines by Seyfert (1943). From the spectrograms he obtained, Seyfert showed that spiral nebulae were similar to galaxies with nearly stellar nuclei showing emission lines superimposed on a normal, solar-type spectrum. Despite this discovery, and due to observational limitations, the subject of the spiral nebulae remained of a low interest.

In the mean time, the development of radio astronomy took a big step with the work of Jansky (1932, 1933, 1935) in the radio communication domain. Conducting a $\lambda \sim 14.6$ m study of the sources of static affecting trans-Atlantic communications, he recorded a steady hiss type static of unknown origin. While he first associated this static noise with the Sun, a deeper study of the data finally proved that the radiation was coming from the entire disk of the Milky Way, with a maximum located in the direction of the galactic center (Jansky 1933, 1935). There were multiple attempts to explain the origin of the galactic radio background detected by Jansky (1932): thermal emission by interstellar dust (Whipple & Greenstein 1937), bremsstrahlung emission by ionized gas in the interstellar medium (Reber 1940) ... But it was Alfvén & Herlofson (1950)'s theory involving cosmic rays trapped in a magnetic field, emitting by synchrotron processes, that led Kiepenheuer (1950) and Ginzburg (1951) to explain the radio background. The first identification of a radio galaxy with an optically known object goes back to Bolton et al. (1949) who associated Virgo A with M 87, the central galaxy in the Virgo cluster, and Centaurus A with NGC 5128, a bright nearby elliptical galaxy encircled by an optically thick dust lane. Further observers tried to calculate the amount of energy stocked in double-lobed radio galaxies and the results fascinated the community: 10^{60} ergs (Burbidge 1959).

Such a discovery enhanced the number of radio surveys in the 1950s and 1960s in order to determine the true nature of those objects. Coupled to optical identifications of sources in order to determine their position, the two famous catalogs of Cambridge 3C (159 MHz, Edge et al. 1959) and 3C revised (178 MHz, Bennett 1962) were the base material to a major breakthrough in 1963. Looking at the optical broad emission line spectrum of 3C 273, in comparison with 3C 48 (Fig 2.1), Schmidt (1963) pointed out that the lines were emitted at unusual wavelengths and were clearly not related to any stellar type spectrum. In particular, he noticed the presence of four emission lines of decreasing amplitude in the blue part of the spectrum, similar to the Balmer series of Hydrogen spectral lines shifted in energies. The presence of the Hα and Mg II lines in both 3C 273 and 3C 48 spectra but at different wavelengths was the second hint for a present red-shift leading to the evaluation of the cosmological distances of the two sources, z = 0.16 and z = 0.37 for 3C 273 (Schmidt 1963; Hazard et al. 1963; Oke 1963) and 3C 48 respectively (Greenstein 1963). Those objects were first considered as galactic stars with a very high density, giving a large gravitational redshift. But this theory was not coherent with the widths of the permitted emission lines and the presence of forbidden lines. A much more convincing explanation was that the objects were extragalactic, with redshifts reflecting the Hubble expansion (Schmidt 1963; Hazard et al. 1963; Oke 1963; Greenstein 1963).

Considering cosmological redshifts, Greenstein & Schmidt (1964) calculated the electron densities in 3C 48 and 3C 273 using the forbidden λ 2973 [Ne V] emission line. They estimated the emitting volumes from the electron densities and the observed luminosities in Hβ and Mg II, establishing from spherical emission models that the sizes of the radiating region were confined to

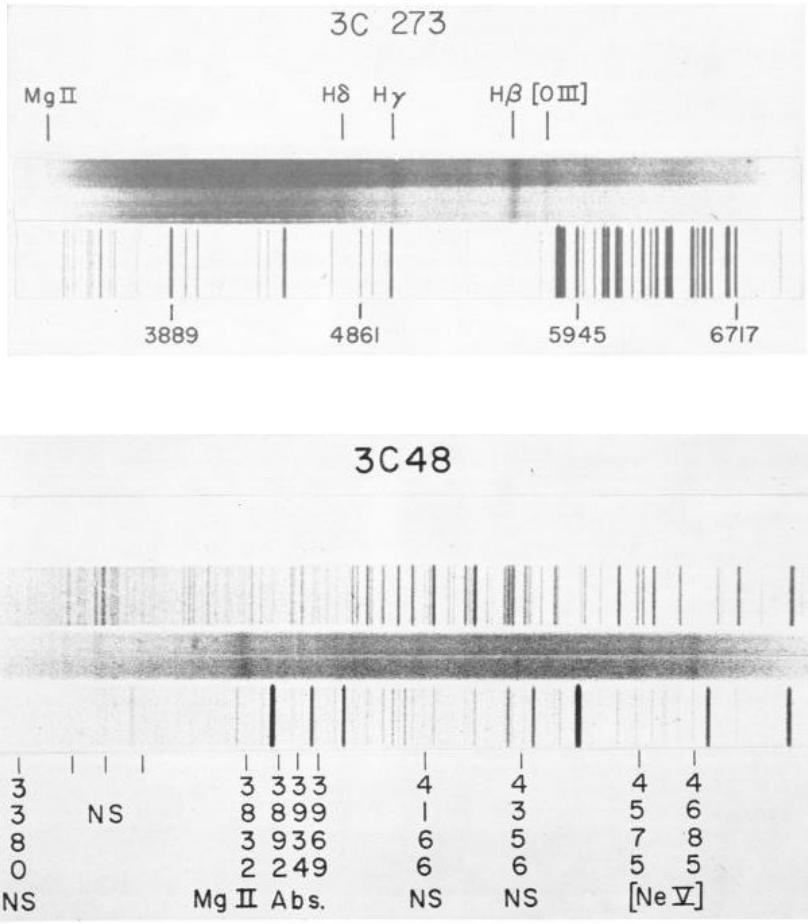

Figure 2.1: Two prime-focus spectra of the quasi-stellar objects 3C 273 (*top*, 400 Å/mm) and 3C 48 (*bottom*, 190 Å/mm) (Greenstein & Schmidt 1964). *NS* indicates night-sky emission; *Abs* is absorption. The Balmer series of hydrogen is reported for 3C 273 as well as the Magnesium II and Neon V emission lines for 3C 48.

1.2 and 11 pc, for 3C 273 and 3C 48 respectively. In order to be gravitationally bounded, such compact regions should be of a mass higher than 10^9 $M_\odot$ to provide the system with energies up to 10^{60} ergs (Burbidge 1959). Using the relation between the time for an electron to lose, by synchrotron process, half of its original energy in correlation with the observed optical variability (Oort & Walraven 1956; Matthews & Sandage 1963; Smith & Hoffleit 1963), Greenstein & Schmidt (1964) proposed a model in which the central source of optical continuum was surrounded by the emission-line region, and a still larger radio emitting region. They suggested that the central mass of 10^9 $M_\odot$ previously supposed might provide adequate energy generation for a lifetime superior to 10^6 years, implied by the size of the jet of 3C 273 and by the nebulosity of 3C 48. Noting that such a mass would correspond to a Schwarzschild radius of $\sim 10^{-4}$ pc, they started to explore the possibility of energy generation and mass input from such a collapsed region (Lynden-Bell 1969a).

From this point, one last question remained: are quasars isolated in space or do they belong to a larger structure? The hypothesis of quasars lying in galaxy clusters was soon excluded by photographic measurements (Sandage & Miller 1966) and Greenstein & Schmidt (1964) pointed out that no galactic signatures have been found around quasars, possibly excluding the presence of a host galaxy. However, several studies started to observe similarities between the spectra, colors and variability of quasars, Seyfert and N galaxies[2] (Burbidge et al. 1963; Pacholczyk & Weymann 1968; O'Connell 1971; Evans et al. 1972). The first evidence for quasars being hosted by faint galaxies came from the pioneering work of Kristian (1973), who successfully observed the diffuse galaxy surrounding several AGN on photographic plates. Direct detection of AGN host galaxies became more regular with the advances of technology, leading to the discovery that jet-dominated quasars are preferentially found in elliptical-like galaxies while jet-free AGN are mostly found in spiral-like objects (Malkan 1984).

Beyond this discovery, the initial mysteries about quasars were unveiled: they were found to be extremely bright extra-galactic objects situated in the inner regions of a much fainter host galaxy. Their variable, intrinsic luminosity must be provided by a sub-parsec, compact region that produces both absorption and emission lines. Finally, they were a direct proof of the Universe expansion. But now that their global properties were identified, they needed to be explained: the AGN field as a major topic of astrophysics research began[3] .

2.2 The complex composition of AGN

With further advances in observational techniques, a wide variety of quasi stellar objects appeared. They soon became subdivided in classes according to their apparent morphology, their luminosity, the eventual presence of a relativistic jet and the spectral shape of their emission and absorption (in any) lines. Nowadays, the approximated structure and composition of AGN are known but much of the detailed physics remains literally obscured.

In order to move towards a more comprehensive, broadband AGN scheme, the following subsections review the theoretical emission and absorption regions that are supposed to lie in the heart of active galaxies from the X-ray band down to radio frequencies,

2.2.1 The supermassive black hole (SMBH)

Quasars and AGN are the most powerful and long-term stable astronomical sources known. Not uncommonly, L $\sim 10^{46}$ erg.s^{-1}, which is 10 times the luminosity of the brightest galaxies. However, while being stable for long periods, their intrinsic luminosity may vary in a timescale of hours or less, depending on the energy domain considered. Considering the propagation of radiation level change at the speed of light, the overall emission region is necessarily compact and of a phenomenal energy. A stellar-origin fueling of the AGN was soon studied by Lynden-Bell (1969a), who showed that any attempt to power quasars by nuclear reactions alone was largely insufficient.

Demonstration:

Let's consider that most of the 10^{61} erg energy released by an AGN is stocked inside its

[2] N galaxy: a class of galaxy showing a compact, bright, blue nucleus superimposed to a fainter red background.

[3] For a more extensive review of the history of AGN discovery, please refer to Trimble (1992), Shields (1999) and references therein.

radio halo. By measuring the size of the emission region, one can find that 10^{61} ergs corresponds to a mass of $\sim 10^7$ $M_\odot$. Knowing that nuclear reactions give less than 1 % conversion matter $\leftrightarrow$ energy, of which 0.75 % comes from hydrogen to helium conversion, the initial mass of the AGN inner region must be about 10^9 $M_\odot$.
If all the mass in concentrated within the radius R of the central, nuclear object, then its binding energy would be greater than $3GM^2$ / 5R. If R = 1.50×10^{13} cm (equals to 1 astronomical unit), then $E_{bind} \sim 10^{64}$ erg.

It is not unusual that a quasar luminosity varies by one magnitude within 10 hours. From speed of light crossing distance considerations, R would be lower than 10^{15} cm, implying the gravitational binding energy of the nuclear core to be superior to 10^{62} erg. So, while trying to fuel our model with nuclear energy, we ended with a model producing enough energy by gravitational contraction.

The work of Salpeter (1964) and Zel'dovich & Novikov (1964) braced Lynden-Bell (1969a)'s hypothesis on the gravitational fueling theory while, in the meantime, exotic black hole alternatives such as single supermassive stars (Hoyle & Fowler 1963) and spinars (Ginzburg & Ozernoi 1977) were shown to be dynamically unstable and hence short-lived (Lynden-Bell 1978).

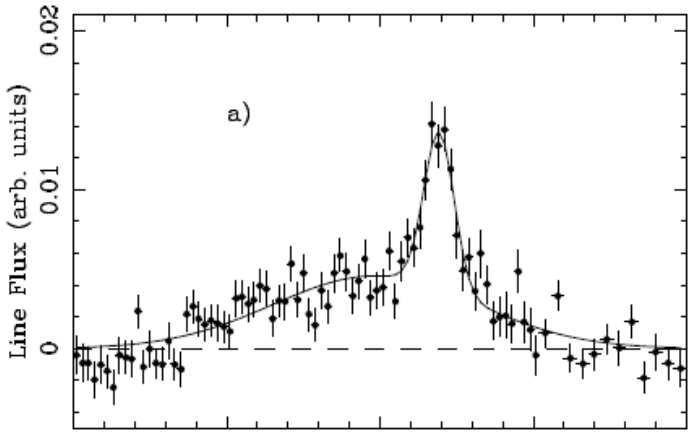

Figure 2.2: Mean Fe Kα line profile of the Seyfert 1 galaxy *ASCA* survey by Nandra et al. (1997). The narrower component of the fit peaks at 6.4 keV and the broader component (carrying most of the flux) is strongly distorted in the red part of the spectrum, giving an integrated centroid energy of 6.1 keV. The enormous Doppler / general relativistic broadening and the asymmetric line profiles are consistent with relativistic boosting and dimming in the approaching and receding parts, respectively, of SMBH accretion disks as small as a few Schwarzschild radii, R_S.

By definition, a gravitationally-powered system would attract everything close to its gravity field, including photons. Thus, the detection of AGN black holes with M $\geq 10^6$ $M_\odot$, also known as supermassive black holes (SMBH), must be indirect. Two main methods are actually used in this purpose: one lies in the X-range and is based on the detection of distorted Fe K_α emission

lines. The broadening of the iron red-wing is due to general relativistic effects that tend to shift the line centroid according the the SMBH spin and disk inclination. Fitting the soft X-ray spectra by general relativistic reflection models allow an estimation of the black hole key parameters (see Fig 2.2 and Chap 9 for further details). The second, most accepted technique implies the detection of optical and ultraviolet broadened emission lines, with Doppler-induced line widths of 2000 to 10000 km·s^{-1} (Ho & Kormendy 2000). One of the most direct methods for measurement of the SMBH mass is the reverberation mapping of those emission lines which allows direct measurements of the size of the broad-line region (BLR, see Sect. 2.2.4) in these objects (Blandford & McKee 1982; Netzer & Peterson 1997). The distance from the radiation source at which the broad emission line response is the most significant can be evaluated from the monitoring of the UV and optical continuum variability and the delayed response of the emission lines. The difference, due to the light travel time, then gives information about the size of the BLR. If the velocity widths of the emission lines is resolved in wavelength, they may trace the Doppler motion of the line-emitting gas. Assuming a gravitational relation with the velocity field of the BLR, one can compute the gravitational potential in which the gas moves and then deduce the mass of the central object (i.e. the SMBH) using the virial theorem $M \approx r\sigma^2/G$, where σ is the velocity and r the size estimated for the line-emitting gas (Peterson & Wandel 2000).

To the day of this manuscript, most of the SMBH have a mass range between 10^6 and a few 10^8 $M_\odot$, the most massive one weighing 1.7×10^{10} $M_\odot$ (NGC 1277, van den Bosch et al. 2012).

2.2.2 Accretion onto SMBH

The previous section showed that a gravitational-origin fueling of AGN is the most probable mechanism to produce extreme amounts of radiation. To do so, matter around the SMBH must somehow loose its energy; but placing an isolated particle (with angular momentum) around a potential well only results in a circular motion. By removing energy and angular moment from the particle, the trajectory of the particle is altered and starts to spiral inwards the gravitational potential until it ultimately crosses the Schwarzschild radius[4] . The amount of energy available through such a process is equal to the binding energy of the innermost stable circular orbit (ISCO, with $r_{ISCO} < r_S$). Below the ISCO radius, no stable circular motions are possible. It follows that the more compact the object is, the more energy can be extracted. According to Pringle (1981), of the order of 10 % of the rest mass of the particle can be released from orbits around a neutron star and up to around 40 % for orbits around a rotating Kerr black hole.

In theory, accretion processes are efficient enough to produce high amounts of energies by converting rest mass into radiation. But, in order to ignite accretion, energy and angular momentum must be removed from the particles. According to the theory developed by Pringle & Rees (1972) and Shakura & Sunyaev (1973), black holes are surrounded by large amount of hot gases, rotating around the potential well (see Fig 2.3). A particle colliding with other gas elements transfers its kinetic and potential energy to the medium, while being heated by shocks and then radiatively cooled. Since the orbit of least energy for a given angular momentum is a circular one, the gas settles into moving on circular orbits in the form of a thin, optically thick disk around the black hole. The accretion itself is due to viscosity processes (Shakura & Sunyaev 1973), also know as

[4] The Schwarzschild radius, R_S or R_G, of a collapsing celestial object is the mass-dependent radius at which gravitational forces require an escape velocity that exceeds the velocity of light. For an object of mass M, with G the universal gravitational constant and c the speed of light, $R_S = 2GM/c^2$. In strong gravity regimes, all length are scaled according to the black hole mass.

the alpha viscosity prescription that describes the resistance of a fluid to the deformation induced by either shear or tensile stresses. Viscosity is damping out shearing motions while the energy is dissipated in the fluid as heat, and thence radiated away with a temperature profile similar to a quasi-black body[5] with $T(R) \propto R^{-3/4}$. Thus, viscosity extracts the only energy source present in the gas (that comes from the gravitational potential) and makes the accretion disk particles to fall into the potential well. In theory, such a viscous prescription is the most efficient manner to convert gravitational potential energy into an AGN-required amount of radiation. However, it is interesting to note that several authors proved that ordinary molecular viscosity is too weak in real astrophysical accretion disks and should be replaced by a model of turbulences driven by magneto-rotational instability (MRI, Balbus & Hawley 1991; Hawley & Balbus 1991; Balbus & Hawley 1998; Abramowicz & Fragile 2011).

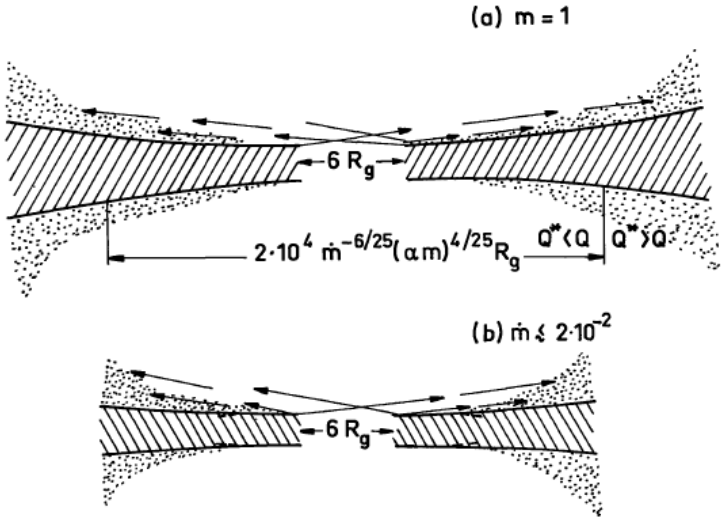

Figure 2.3: Shakura & Sunyaev (1973)'s first scheme of an accretion disk. The thickness of the disk is a function of the distance to the black hole. It is interesting to note the presence of an evaporated medium in the outer edges of the disk, represented as dots, that is discussed in Sect. 2.2.3. The arrows are the trajectories of X-rays and UV quanta which are heating the medium.

From an observational point of view, Shields (1978) was the first to suggest that the UV bump observed in AGN and quasars' electromagnetic spectra was due to thermal emission originating from the accretion disk. Strengthened by the model of thin accretion disks by Shakura & Sunyaev (1973), where most of the radiation is emitted in the UV and optical ranges, the continuum radiation is expected to come from synchrotron radiation. As accretion disks are highly conducting, the orbiting material thus generates magnetic field that varies through viscosity. A variation of magnetic fields leads to the creation of electric fields that accelerate charged particles away from disk as the radiation pressure exceeds the gas pressure. Predominantly below 1000 R_S, the accretion disk

[5] More precisely, $T(R) = \left[\frac{3GM\dot{M}}{8\pi\sigma R^3}\left(1-\sqrt{\frac{6R_S}{R}}\right)\right]^{1/4}$, with σ the Stefan-Boltzmanns constant, M the black hole mass and $\dot{M}$ the accretion rate.

thus becomes thicker, hotter and is ultimately responsible for the UV and optical thermal emission. From 10^{4-5} R_S, the gas pressure dominates and a thin disk is supported by gas pressure, producing the IR radiation. Beyond 10^5 R_S the accretion disk ultimately breaks up. However, accretion disks in AGN are unable to produce radiation at very long or very short wavelengths, so far-infrared and X-ray emissions are thought to be of different origins (Bertout et al. 1991). In particular, the X-ray emission is theoretically seeded by UV photons from the accretion disk reprocessed in a hot disk corona.

2.2.3 The hot corona

Within the theories described by Pringle & Rees (1972) and Shakura & Sunyaev (1973), the UV and optical continuum radiation is expected to be produced by accretion onto a supermassive black hole. However, the presence of high X-ray fluxes observed in AGN (Walter & Courvoisier 1992) is a serious challenge for the accretion disk theory as it is unable to explain their origin and spectral shape.

If we consider that accretion disks are the only radiation sources in AGN, then one of the easiest way to produce X-ray photons is to consider (multiple) inverse Compton upscattering events in a hot plasma. By Comptonization processes (Sunyaev & Titarchuk 1980), ultraviolet seed photons emerging from the accretion disk are reprocessed in a hypothetical, optically thin plasma situated in both sides of the disk surface (the accretion disk corona, Haardt & Maraschi 1991, 1993). The resulting X-ray spectrum then only depends on two parameters of the corona: its electron temperature and optical depth. The relative strength of the hard X-ray component of the spectrum, in comparison with the UV/soft X-ray tail, defines the hardness of the spectra and reveals the predominance of energy dissipation in the accretion disk (soft excess, Pringle & Rees 1972; Frank et al. 2002) or of energy dissipation in the corona by thermal comptonization (hard excess, Rees et al. 1982; Narayan & Yi 1994; Abramowicz et al. 1995).

Empirically, a power law of the form $N_E \propto E^{-\Gamma}$, with a photon index $\Gamma \sim 2$ best describes the 1-100 keV X-ray emission coming from the accretion disk corona, below 30 R_S, for radio-quiet AGN and quasar with $0.5 < z < 6$ (Reeves & Turner 2000; Page et al. 2005). The variation of Γ is considered as an accretion rate indicator in AGN seen from the pole (Boroson & Green 1992), as high accretion rate would increase the accretion disk temperature, hence producing more soft X-ray radiation and, at the same time, increase the Compton cooling of the corona and steepen the hard X-ray power law; low accretion rate hardens the power law via the inverse mechanism (Shemmer et al. 2006).

The interaction between the matter driven away from the accretion disk by radiation pressure and the hot corona is rather complicated as it couples the processes producing X-rays and UV photons (Proga 2005). Galeev et al. (1979) and Field & Rogers (1993) explored magnetic connections between energy dissipation from the accretion disk and the heating mechanism of the corona but a detailed investigation of the radiative coupling between an accretion disk and a hot corona presented in Liu et al. (2002, 2003) shows that the energy deposit in the corona is not enough to keep itself hot above the disk against strong Compton cooling in AGN systems. Other heating mechanisms besides the disk-born outflow are required to maintain such a hot temperature in the corona lying above the disk and to produce the observed X-ray luminosity. A promising mechanism arises from coupling MRI in the disk and the upward force exerted by the magnetic field, resulting in magnetic reconnection events in the corona that can heat the plasma up to 10^9 Kelvin (Di Matteo 1998; Di

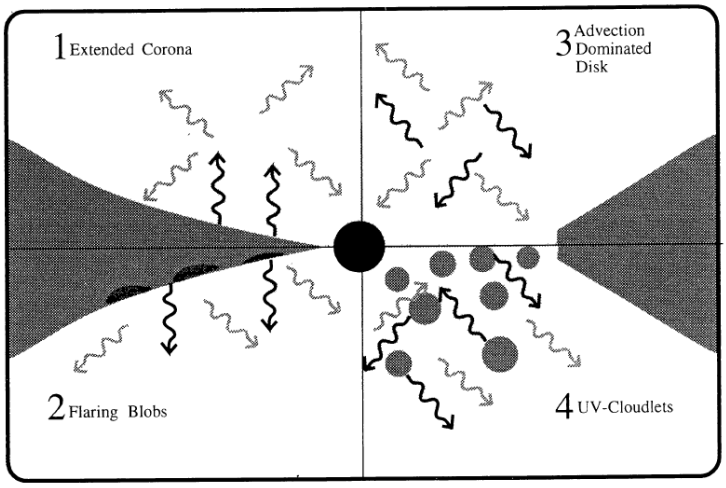

Figure 2.4: The different corona models proposed by Haardt (1997) to illustrate the production of X-ray photons in radio-quiet AGN. The dark arrows represent seed photons for comptonization (from the infrared to the extreme UV, depending on the accretion disk model). The white arrows are the X-rays photon created by inverse Compton scattering. *Models are not scaled.*

Matteo et al. 1999; Miller & Stone 2000). Moreover, magnetic reconnection might explain the time variability observed in AGN and help to create an inhomogeneous medium (Kawaguchi et al. 2000). Unfortunately, due to the proximity between the corona and the SMBH, direct measurements of the plasma morphology, opacity and radiation mechanisms remain impossible (Reynolds & Nowak 2003 and Fig 2.4).

2.2.4 The Broad Line Regions (BLRs)

Since the first optical spectroscopic observation of AGN by Seyfert (1943), it is unambiguous that all quasars have relatively strong emission lines. Since then, the shapes and intensities of the emission lines are used as tracers of the physical and kinematic properties in the central part of AGN. While the emission mechanism of narrow lines is identified with a quite well-characterized AGN component (the Narrow Line Region, see Sect. 2.2.6), much questions remain about the original region responsible for the broad lines. In particular, it is quite puzzling to reconcile the presence of broad emission (in type-1 AGN) and absorption line (in BALQSO) under a unified picture.

When looking at spectroscopic observations of AGN, one can deduce from the broad emission lines that the actual amount of emission-line gas required is rather small as line emission is very efficient in high-density gases (taking into account that the emissivity per unit volume is proportional to n_e^2). The broad line region (BLR) must be then dense. From the variation of the emission-line fluxes in comparison with the continuum flux, the BLR signal varies with a very short time delay (e.g. Akn 564: $\Delta t_{cont/line} \sim 3$ days at $\lambda = 1216$ Å, for a SMBH of 8×10^6 $M_\odot$, Collier et al. 2001). Hence, using light-travel time arguments, the BLR is necessary quite small and thus close to the central engine (Akn 564: $R_{BLR} \sim 1$ light day, Collier et al. 2001). As the BLR is located on a

relatively small distances from the AGN central energy source, the matter in the BLR is likely to be irradiated by the strong continuum flux originating from the accretion disk and the hot corona. Kwan & Krolik (1981) were the first to suggest that the UV and optical irradiation of the BLR was leading to photo-ionization of the matter, heating the gas up and being responsible for the observed spectra of AGN. Plus, if the gas is photo-ionized, the BLR must be optically thick to ionizing continuum radiation. This led to the idea that the BLR comprises discrete gas clouds associated with the accreting supermassive black hole at the heart of AGN (Davidson & Netzer 1979; Mathews & Capriotti 1985). Non-radiatively heating processes such as recombination and collisional excitation were also considered by Dumont et al. (1998) and were found to be relevant processes in the physics of the BLR. In particular, at larger ionization parameters recombination cannot be neglected; at low ionization parameters, the collisional excitation also becomes important (Osterbrock 1989; Popović et al. 2008).

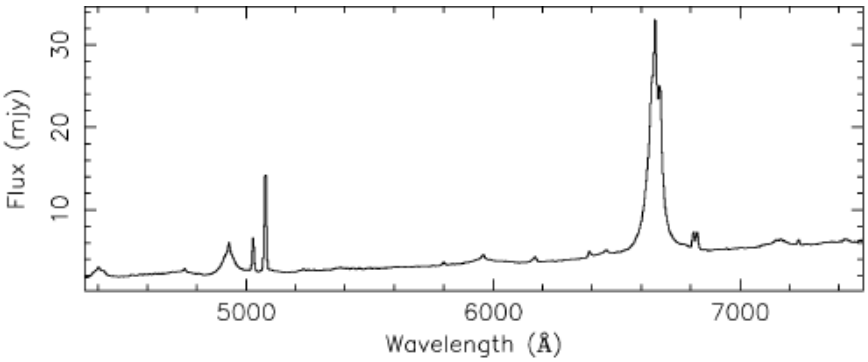

Figure 2.5: Total flux intensity of the Seyfert 1 galaxy Fairall 51 obtained in October 1998 by Smith et al. (2002b) at the 3.9 m Anglo-Australian Telescope (AAT). Broad emission lines originating from the BLR are detected (Hα λ6563 and Hβ λ4861) as well as narrow emission lines from the NLR ([O III] λ4959 and λ5007); *redshift to be considered.*

A typical AGN spectrum (see Fig 2.5) showing broadened lines emitted by the BLR may include resonance metal lines (C IV λ1549, N V λ1240, O VI λ1035, ...), inter-combination lines (C III] λ1909, N III] λ1750, O III] λ1663, N IV] λ1486, ...), broad forbidden lines ([O III] λ4363, [O III] λ5007, ...), the hydrogen spectrum (Hα, Hβ and Lyα) and/or the helium spectrum (He I λ5876, He I λ10830, ...). Most of the observed lines are moderate or high ionization lines, but the presence of low excitation lines such as Fe II, Mg II, Ca II indicates that some lines are produced in a partly neutral region of the BLR clouds (Netzer 1990).

Besides the strong emission lines emitted by the BLR, broad, blueshifted absorption features in the UV part of spectra are present in $\sim$ 10 % of quasars (Popović 2006) and show both high and low broad ionization lines (Reichard et al. 2003). To take into account both the emission and absorption lines in quasar, the usual interpretation supposes that AGN spectra are a superposition of the continuum emission from the central engine, with broad emission lines from the BLR emitted near the hot center of the AGN, and the broad absorption lines originating from the colder, outer edge of the BLR (Gaskell & Sparke 1986; Gaskell et al. 2007). Based on this reasoning, Goad et al. (1993) argued that the geometry and possible stratification in the BLR may affect the continuum and line spectra of AGN.

The question of the exact BLR geometry is thus of a prime importance. The concept of discrete clouds (Davidson & Netzer 1979; Mathews & Capriotti 1985) is still not largely accepted as it seems to suffer from a number of drawbacks. In particular, such clouds would expend adiabatically and blend together if no external medium is present to confine them. But, due to the necessary requisite pressure confining, the medium would ultimately heat and become a source of X-rays (Krolik et al. 1981), which is eluded by the absence of detection. One of the possible re-interpretation of the BLR morphology comes from Shields (1977), who suggested that the broad lines can originate from condensations or filaments within an outflow from the accretion disk, accelerated by radiation and/or magnetic pressure. Such a wind would be responsible for the broad absorption lines and can also be the source of the broad emission lines in all quasars and AGN (Elvis 2000). Indeed, a continuous flow of matter would explain the observed smoothness of the line profiles, which cannot be explained by a distribution of discrete cloudlets (Arav et al. 1997, 1998; Eracleous 2006) if we consider that the bulk of the line emission originates from the inner parts of the outflow, where the density is maximum. The flattened configuration of the structures proposed by Shields (1977) and Elvis (2000) is largely supported by reverberation mapping of Seyfert galaxies, where there was found no evidence for predominantly radial motion of the gas (Peterson 1998).

While detected, the motion of the BLR (whether in infall, outflow, or orbital motion) remains unknown. There are no strong constraints from the emission line profiles as a wide variety of kinematic models are able to reproduce the non-Gaussian profiles detected in AGN (Bon et al. 2009). Plus, the wide variety of structures observed in the BLR line profiles, such as "double-peaked" lines or "asymmetrical" wings, are found to be variable in time (Peterson 2006). While the combined technique of reverberation mapping (Blandford & McKee 1982) and multi-waveband continuum variability (O'Brien et al. 1998) has proven to be an invaluable tool to investigate the AGN innermost regions (Peterson 1993), it fails to elucidate the BLR kinematic problem. The technique of velocity-resolved reverberation mapping (Gaskell 1988) is a step forward and tends to rule out any significant outflow from the AGN, while detecting a slight inflow (Gaskell et al. 2007). In addition to that, it implies that the dominant motion is Keplerian, or worst, random.

In summary, the BLR, which is still highly enigmatic, seem to be a flattened region of high-density ($n_e \sim 10^{10}$ cm^3), with a fast Keplerian motion ($v_K \sim 0.05 - 0.001$c), a medium infall ($v_i \sim$ 1000 km·s^{-1}) and no significant outflow. The overall region is optically thick in the continuum for $h\nu > 13.6$ eV (Gaskell 2009). The gas in its inner radius is highly ionized while the temperature decreases as the distance from the central source increases, due to a shielding effect; at the outer edge of the BLR, the gas is lowly ionized. At the far end of the BLR, Netzer & Laor (1993), lately supported by reverberation mapping observations of Suganuma et al. (2006) and Gaskell et al. (2007), suggested that the low ionization gas region of the BLR coincides with the dust sublimation radius of an extended, optically and geometrically thick, circumnuclear region: the so called "dusty torus".

2.2.5 Circumnuclear obscuration

Early observations of AGN stated that a fraction (to be still properly determined) of the active galactic spectra present both broad and narrow emission lines, while only narrow features are detected for the remainder. The intriguing absence of broadened lines originating from the BLR raised the question of the unity of AGN classes until the suggestion of Rowan-Robinson (1977). Rowan-Robinson (1977) discussed the possibility that the BLR emission of Seyfert galaxies seen

along the equatorial plane was obscured by dust, rather than being truly absent. A toroidal geometry for the circumnuclear obscuring region was proposed by Osterbrock (1978), lately improved by Krolik & Begelman (1988) and Rowan-Robinson & Crawford (1989), and supported by the discovery of ionized winds outflowing along the AGN poles (Pogge 1988a,b). The presence of an opaque, equatorial media is now confirmed in many objects, such as NGC 1068 where Jaffe et al. (2004) and Wittkowski et al. (2004) spatially resolved the direct emission coming from the outer parts of a torus-like structure. Using the MID infrared Interferometric instrument (MIDI) at the *Very Large Telescope* (VLT), Raban et al. (2009) constrained the size of the NGC 1068 torus to a compact (0.45×1.35 pc) component; which is in agreement with Elitzur (2005) high-resolution IR observations indicating that torus sizes might be no more than a few parsecs.

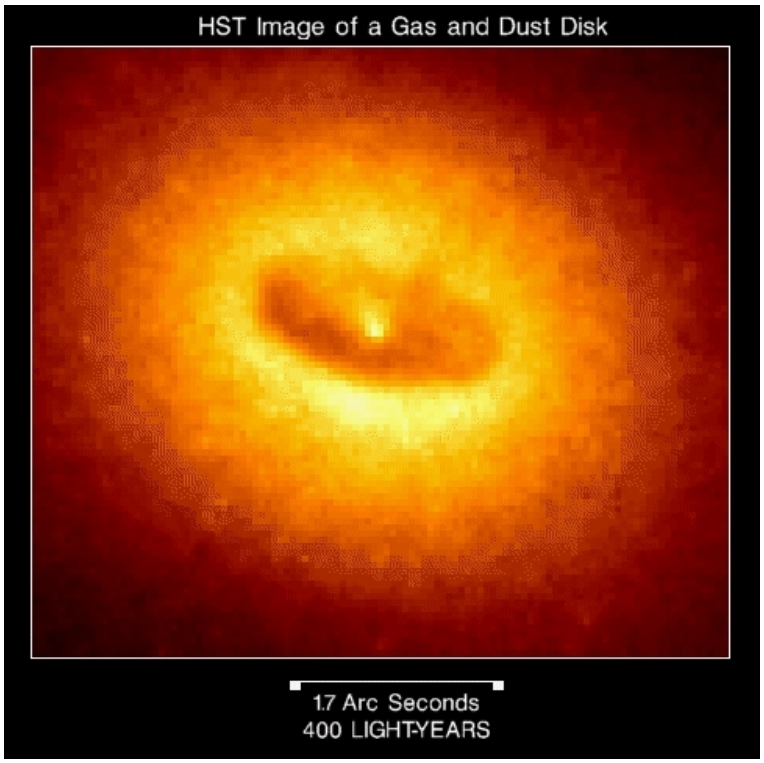

Figure 2.6: A false-color image from the Hubble Space Telescope (HST), showing a dark, doughnut-shaped structure surrounding the central AGN engine. Credit: W. Jaffe, Leiden Observatory; Holland Ford, STScI, NASA.

The commonly admitted features of the optically thick circumnuclear region hiding the AGN central core are, to the present day (Elitzur & Shlosman 2006):

(1) Anisotropic obscuration of the central AGN core. The torus thus distinguishes between objects with both broad and narrow lines and objects with only narrow lines, respectively divided in nomenclature by the terms *type 1* and *type 2* AGN. Type 1 objects are seen by the pole, where the BLR region is not obscured, and type 2 AGN are seen edge-on, where the central irradiation is totally absorbed.

(2) From the statistics of Seyfert 1 and 2 galaxies, the torus height[6] H and radius R obey the relation H/R $\sim$ 1 (Schmitt et al. 2001). R (so is H) strongly depends on the AGN UV/soft X-ray luminosity, as the inner radius of the torus is set where dust starts to survive evaporation (Lawrence 1991). The torus of low-luminosity AGN is thus expected to be larger than for high-luminosity AGN.

(3) Soft X-ray/UV/optical photons generated by the accretion disk and/or the corona are absorbed by the circumnuclear matter, which thermally re-emits in the infrared band, leading to the idea that the circumnuclear matter is composed of dust. Using this emission mechanism and ultraviolet/infrared light variability, it is possible to constrain the torus radial extension.

If the presence of an obscuring media is now accepted, the exact morphology of the torus is still unconstrained (the *HST* image of NGC 4261, Fig 2.6, shows the outer regions of the torus-like structure; its funnel being unresolved). While the first suggestions by Osterbrock (1978) considered a toroidal structure for the circumnuclear matter, there are more and more indications from observations and modeling in the IR that the obscuring torus should also have a clumpy structure (Nenkova et al. 2008b,a, 2010; Schartmann et al. 2008; Hönig & Kishimoto 2010; Heymann & Siebenmorgen 2012). In such a hydrodynamic scenario, the circumnuclear torus has a doughnut-like structure populated by molecular clouds accreted from the galaxy (Krolik & Begelman 1988). The clumpy nature of the dusty torus might then resolve the known problem that a geometrically thick torus lacks stability against self-gravity and therefore cannot be in hydrostatic equilibrium. But the origin of vertical motions capable of sustaining the clouds in a hydrodynamic structure (with the H/R $\sim$ 1 constraint) is still problematic and has no solution so far (Davies et al. 2006).

Other authors (Emmering et al. 1992; Konigl & Kartje 1994; Kartje & Königl 1996; Bottorff et al. 1997, 2000; Kartje et al. 1999; Elvis 2000; Everett 2005; Elitzur & Shlosman 2006), based on the work done by Blandford & Payne (1982), consider that the torus could rather be interpreted as a dynamical region of flowing, optically thick clouds embedded in a hydromagnetic disk wind. In this approach the torus is merely a region in the wind that happens to provide the required toroidal obscuration; i.e., it is that region wherein the clouds are dusty and optically thick.

One must notice that both of those theories share a similar feature: the central funnel of the obscuring region is matter-free along the vertical symmetry axis of the model, allowing radiation to escape at poloidal directions.

2.2.6 Outflowing polar winds (UFO, NLR, WA)

In more than 50 % of the Seyfert 1 galaxies (Crenshaw et al. 2003; Kriss 2004; Steenbrugge et al. 2005) and quasars (Piconcelli et al. 2005; Misawa et al. 2007), X-ray and UV outflows have been detected in absorption with velocities comprised between 500 and 5000 km·s^{-1}. Similarly, outflows have also been observed in [O III] emission lines, using the HST/STIS instrument, showing slowly increasing velocities out to $\sim$ 100 pc and then decreasing in motion at larger distances (Crenshaw & Kraemer 2000; Das et al. 2005, 2007). More recently, evidences have been emerging for much higher velocity (up to 0.4 c) outflows (also known as ultra fast winds, "UFO") seen in absorbed X-ray lines (Chartas et al. 2002, 2007; Pounds et al. 2003; O'Brien et al. 2005; Tombesi et al. 2010, 2011, 2012a). Depending on the distance from the inner AGN core, the outflow density, ionization

[6] The highest point where the optical depth τ is close to unity along the line of sight is considered as the torus height.

stage, velocity and most of the other characteristics are found to be different in X-ray energies and UV/optical wave bands. Interpreting the different observations in order to draw a "unified" model of AGN winds (Gallagher & Everett 2007; Tombesi et al. 2012b) is an actual debate (Kaspi & Behar 2006; Pounds & Page 2006).

The most fundamental question is: where do quasar winds originate? The AGN outflows extend up to hundreds of parsec from the central source in a conic or double conic geometry, as revealed by narrow-band images around some luminous AGN, particularly radio-loud quasars) as well as radio galaxies (Stockton et al. 2006). Similar ionization cones irradiated by the intense radiation from the AGN core often appear in lower luminosity Seyfert galaxies (Unger et al. 1987; Tadhunter & Tsvetanov 1989; Wilson 1996). Such a geometry may be explained if we consider that the outflows, originating close to the SMBH, are collimated by the inner funnel of the circumnuclear torus. When expelled from the inner AGN core, the outflows are blocked by the torus inner walls and escape along the polar directions in a characteristic hourglass shape. It is interesting to note that the problem can be solved starting from the other end: the energetic, polar outflows may blast away a primeval spherical dust layer surrounding the AGN core, leaving only obscuring matter along the equatorial plane (Lawrence 1991).

Independently of the shaping mechanism, measuring the AGN ionized outflow location requires the independent determination of a quantity which is not directly observable: the electron density n_e of the outflowing material. Such a parameter might be derived from the emission lines of helium-like ions in the X-ray outflows (Porquet & Dubau 2000; Porquet et al. 2010) or inferred from the evolution in time of the ionization degree of the gas coupled to time-evolving photo-ionization models (Nicastro et al. 2008). A major step forward was recently taken by Tombesi et al. (2012b) who found significant correlations indicating that there is a proportional relation between the distance from the SMBH and the outflows ionization stage, column density and outflowing velocity. The outflowing medium is thought to be continuous, with UFO detected close to the central engine and warm absorbers (WA) at the end of the cloud distribution. It indicates a possible, similar origin for all the X-ray winds detected so far.

The ionized medium seen in optical and UV wavelengths is already thought to be associated with the WA (Komossa 1999). The distant narrow line region (NLR), responsible for the narrow absorption and emission lines seen in type 1 and 2 AGN, might be the final extension of the AGN outflow were an optically thin dust medium can survive beyond the sublimation radius. All hints tend to point to a global picture of AGN outflows, summarized in Fig 2.7.

The second important question to date is: what is the AGN mechanism providing the necessary kinetic power to propel the outflows? Addressing this question is extremely important for cosmological feedback and galaxy-enrichment implications, as well as understanding the inner physics of AGN. Ruiz et al. (2005)'s HST observation of 10 Seyfert galaxies NLR showed bright emission-line knots, implying a lack of any symmetry and maybe an outflow process from the AGN center. Complex flow geometry (Crenshaw & Kraemer 2005), transverse motion (Crenshaw et al. 2003) and inhomogeneity (Arav et al. 2005) of the polar winds are in favor of very complex flows, and neither spherical nor axial symmetry are applicable. To overcome those problems, several multidimensional models of outflows are actually debated in order to reproduce the complex wind geometry and dynamics and ultimately fit observations[7] :

• **Jet interaction**. Even in radio-quiet objects, a small-scale radio jet might be detected,

[7] Further models for outflowing mechanisms are detailed in Proga (2007) and Everett (2007).

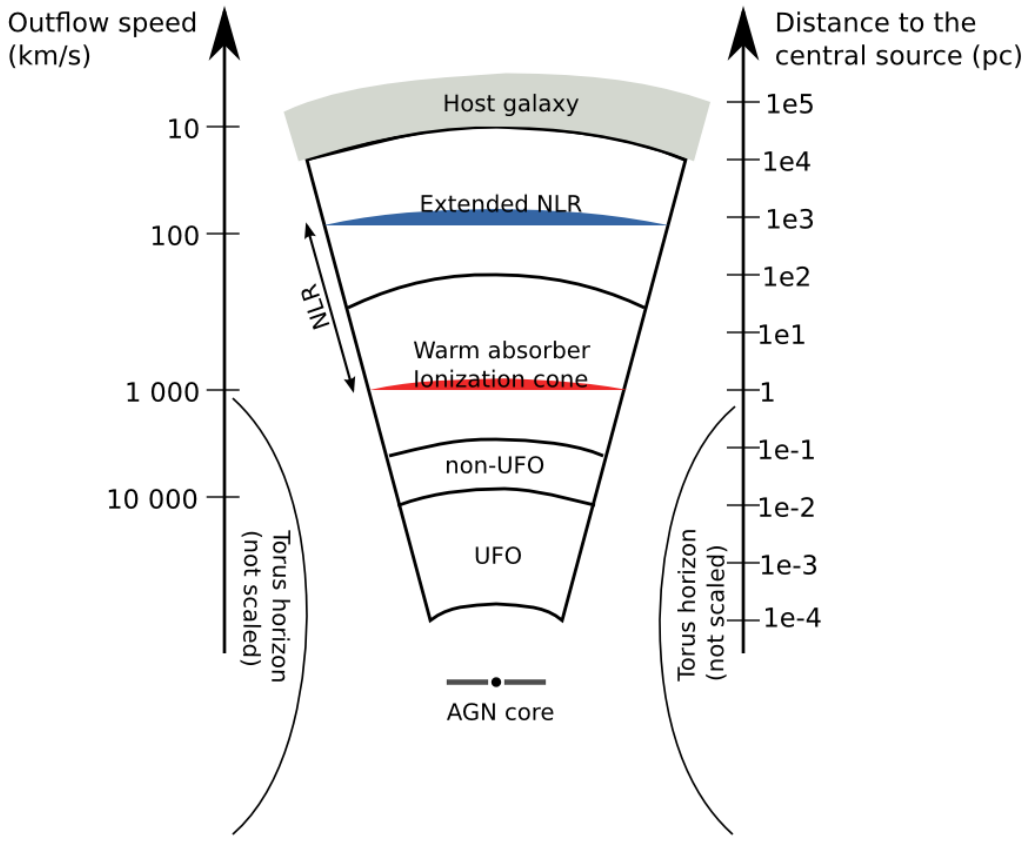

Figure 2.7: Schematic overview of the different AGN outflowing regions according to Tombesi et al. (2010, 2011, 2012a,b) for the UFO, non-UFO and WA zones, and Barvainis (1987); Unger et al. (1987); Hamann (2000); Whittle (2000); Tielens (2005); Cracco et al. (2011); Marin et al. (2012c); Marin & Goosmann (2012) for the ionization cones, NLR and extended NLR (ENLR). The red stripe indicates where hot dust starts to survive; the blue stripe designates the cold, icy dust from the interstellar medium (ISM), see Sitko et al. (1993); Oknyanskij & Horne (2001); Tielens (2005)

lying within the UV ionization cones. However, in many cases, the gas must be ionized by irradiation from the central source rather than direct interaction with the jet, as seen from narrow line widths and relatively low electron temperatures. According to Keel et al. (2012), jet/wind shocks become even less likely when considering extended NLR, probing that jet interaction is no more a viable accelerating mechanism.

• **Radiative acceleration**. Considering the AGN and QSO high luminosities, one can imagine from the momentum in both the radiation field and the outflow that there should be enough energy to drive a wind by radiative acceleration (Scargle et al. 1970; Shields 1977). The large absorption seen in Broad Absorption Line (BAL) QSO is a second hint in favor of a momentum extraction from the radiation field, thus contributing to the flow acceleration. One of the important features of the radiative acceleration model is the continuity and uniformity of the outflow (Arav

et al. 1998), which is in contradiction with observations (Capetti et al. 1995, 1997; Packham et al. 1997; Ruiz et al. 2005). In addition, the high X-ray fields produced by the model tend to destroy the UV transitions that radiative driving depends on (Gallagher & Everett 2007). Arranging solutions (Murray & Chiang 1995; Murray et al. 1995; Proga & Kallman 2004) have been found but the models do not convince the entire scientific community.

• **Magneto-centrifugal winds**. Originally developed to explain the launching and collimation of radio jet (Blandford & Payne 1982), magneto-centrifugal forces can be a potential mechanism to generate highly ionized winds. Considering magnetic fields anchored to a rotating accretion disk, the resulting centrifugal forces accelerate the gas using magnetic tension as the dominant contribution to the Lorentz force. The gas rises from the disk atmosphere and is driven away by helical magnetic fields created by the magnetic forces. The disk-wind magnetic interaction also helps to remove angular momentum from the accreted matter but fails to reproduce the mass loss rate (Proga 2007). Additionally, the magneto-centrifugal winds require *ad hoc* assistance to flow freely and steadily from the surface of the disk.

• **Thermally driven winds**. As seen from Fig 2.3, an accretion disk in hydrostatic equilibrium might loose its mass by radiative ejection, when the radiations from the inner, hot disk irradiate the outer, cooler parts of the system. When the outer disk section is heated up to 10^7 Kelvin, a thermal wind is expected to be launched (Begelman & McKee 1983; Ostriker et al. 1991). However, when thermal wind models are trying to drive the wind at large scales, they fail to maintain the temperature of the flow against adiabatic cooling (Everett & Murray 2007), even with the turbulent heating processes lately added to the outflow by Chelouche & Netzer (2005).

While the question of the origin of the outflows, both in location and launching mechanism, is still unresolved, it is possible to extrapolate from the broadband observations that AGN outflows can be a key aspect of the QSO understanding. Moreover, the impact of the ENLR elongated structure may play a significant role in AGN-host-galaxy and AGN-IGM feedback processes (Blustin et al. 2005).

2.2.7 Jet emission

The presence of a single or double, kilo-parsec, relativistic jet, previously mentioned in Sect. 2.1 and Sect. 2.2.6, is a particular feature that 15 to 30 % of AGN share.[8] It logically led to a classification of quasars according to the presence/absence of an elongated jet structure: when jets are detected, the AGN are designated as radio-loud objects; when there is an absence of detection, the AGN is labeled as radio-quiet. A more specific sub-class of radio-loud objects with relativistic jets oriented close to the observer's line of sight is know as "blazar".

While most of their internal physics remains unknown, plasma jets are considered to be generated and propelled outwards from the central regions of AGN by magnetic forces surrounding the SMBH (Blandford & Payne 1982). An accretion disk origin seems to be the most probable theory since Shibata & Uchida (1985) showed, on the basis of a magnetized accretion tori, that jets are launched whenever the accretion flow is in differential rotation and threaded by a global magnetic field with a strong axial component; however, this model assumes a peculiar magnetic

[8] The ratio of radio-loud to radio-quiet AGN strongly depends on the observational waveband. About 15 to 20 % of radio-bright AGN are considered as radio-loud if their ratio of radio (5 GHz) to optical (B-band) flux is superior to 10 (Kellermann et al. 1989). This fraction increases up to 30 % with optically-bright (Padovani 1993; La Franca et al. 1994) and X-ray bright (della Ceca et al. 1994) AGN.

field configuration. To overcome this problem, Hirose et al. (2004) and McKinney (2006) added a weak magnetic field to the initial hot, geometrically thick torus (a prescription close to the advection-dominated accretion flow, ADAF, models). Coupling the differential torus rotation and the weak magnetic fields excites MRI and generates magneto-hydrodynamic (MHD) turbulences. Such a turbulent medium naturally restructures the magnetic fields in the poloidal regions of the torus, a perfect configuration for jet launching. Meier (2005) ameliorated the previous model, that was predicting too powerful jets, using a magnetically-dominated accretion flow (MDAF). A less hot central region ($< 10^{10}$ K) results from the MDAF model, the ratio of gas to magnetic pressure drops, and magnetic forces dominate over plasma forces. A jet would then be launched out along the open field lines. But all those models suffer from instabilities and short collimation radii. Further models are still investigated.

Fig 2.8 shows the presence of a relativistic jet in 3C 175. This quasar is representative of the complex morphology of radio-loud AGN: first, one can distinguish the presence of a narrow jet pointing toward the observer. The fact that it is beamed up to a distance of several thousand of parsecs is still not understood. If we consider that the MDAF model holds to launch a jet along helicoidal fields, the magnetic structure is maintained only up to a dozen of R_S. Afterwards, the natural pinching action of the magnetic field tightens the field lines, leading to a collimation shock[9] and disrupting the beam (O'Sullivan & Gabuzda 2008). In the particular case of 3C 175, Königl (2007) successfully reproduced a continuous, beamed flow of relativistic matter up to distances of several parsecs using MHD simulations but the clue for kpc, ballistic jets is still missing. Back to Fig 2.8 (bottom), one can also see that the structure of the jet is neither continuous nor regular: the jet is slightly curved to the south, patchy and clumpy; plus, a counter-jet is missing. Even velocity mapping of the structures bring more complications than solutions to the problems: the flux knots appear stationary, sub- or even superluminal (with $v \geq 20c$, Jorstad et al. 2001; Kellermann et al. 2004; Jorstad et al. 2005). Finally, gigantic radio lobes are detected at the end of the jet, when the beam finally slows down and starts to dilute with the intergalactic medium (IGM). Varying from objects to objects, the morphology of radio jets is thus rather complicated and far from being explained.

As jets are born with bulk relativistic speeds, wrapped in helicoidal magnetic fields, synchrotron radiation imposes itself as the dominant emission mechanism. If we consider a steady emitting source immersed in a constant magnetic field B, with an initial power-law distribution of electron energies E, the power-law continuum spectrum can be expressed as $N(E)\,dE = N_0\,E^{-s}\,dE$, with a spectral index $\alpha = (s-1)/2$. For extended components such as the jets, observations give an average value of $\alpha = 0.7$ ($s \approx 2.4$; Peterson 1997). Subsequently, radio-loud AGN jets emit in nearly all the wavebands, but not with the same strength: at sub-parsec scales, the non-thermal flat spectrum of radio-loud quasars is dominated by two peculiar broad components associated with the radio jet (Rees 1967; Konigl 1981). Firstly in the infrared, where IR and optical synchrotron photons are boosted due to Doppler effects (Blandford & Rees 1978; Blandford & Königl 1979), and secondly in the MeV domain, where lower energy photons are boosted by inverse Compton scattering (von Montigny et al. 1995). However, at parsec and larger scales, where the jet is unstable as dominated by instabilities of the jet flow (preponderantly Kelvin-Helmholtz instabilities Lobanov & Zensus 2001; Lobanov et al. 2003) the jet decelerates and starts to dilute in space. It starts to become optically thin even at very low radio frequencies and the final lobes mostly emit

[9] Such a shock is inferred to be seen in the millimetric waveband (Marscher 2005; Marscher et al. 2008).

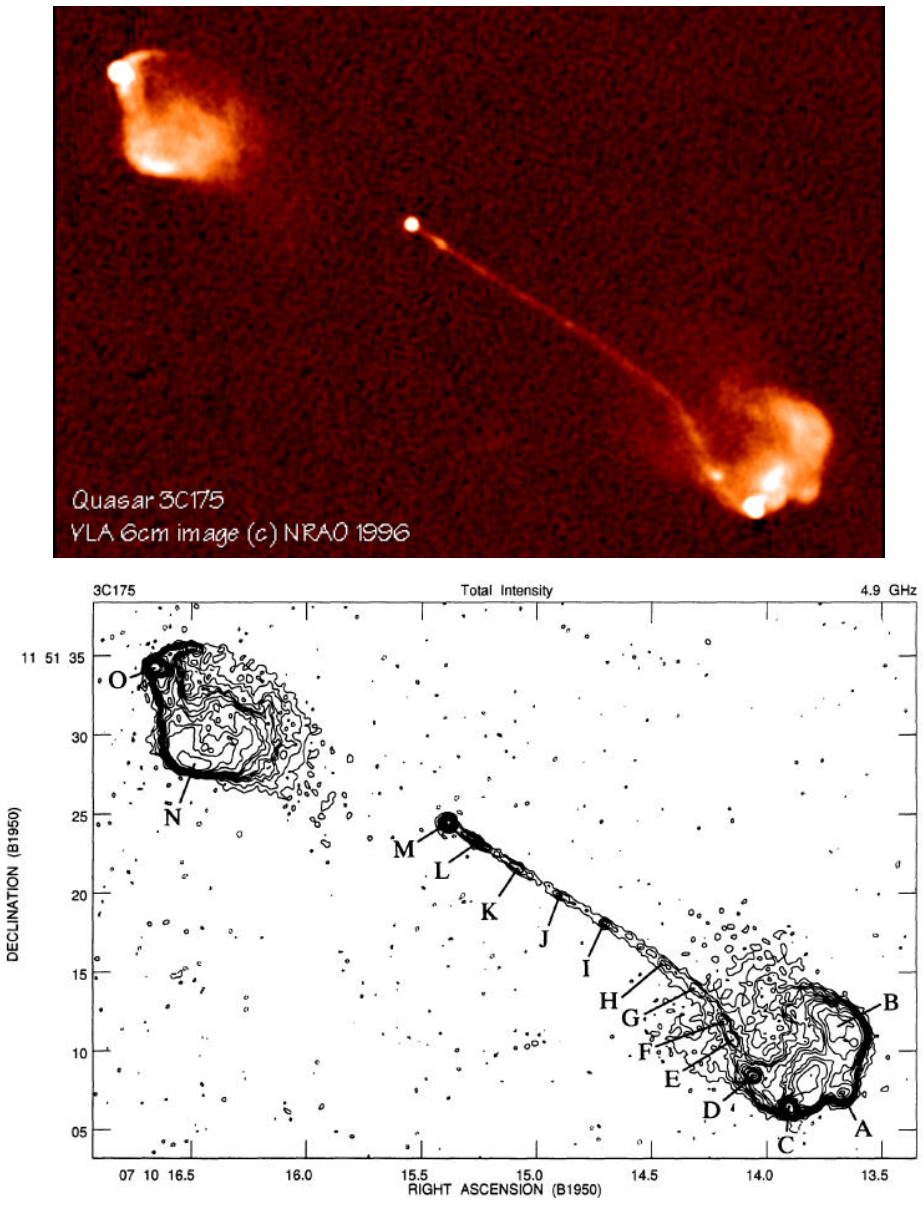

Figure 2.8: Very Large Array (VLA) images of the FR II 3C 175 radio jet with 0".38 full width at half maximum (FWHM) resolution. The complex structure of the jet is highlighted by the total intensity contours drawn in the bottom figure. M is the central flux source, N, L, K, J, I H, G, F, E, D, A and B are bright flux knots, C is the jetted flux spot and O is the counter-jetted hot spot. No counter-jet candidates are detected (Bridle et al. 1994).

in the radio domain where the relativistic particle densities are low. At this point, the idea of an environmental enrichment of the IGM by extended, relativistic jet follows naturally.

2.2.8 AGN feedback

Sect. 2.2.6 and Sect. 2.2.7 described how both AGN ENLR and jets can reach extreme distances from the SMBH, from kilo- to even mega-parsec scales, carrying energy and matter all along their extension. But what could be the impact of such processes on their host galaxy, the IGM and the galactic environment?

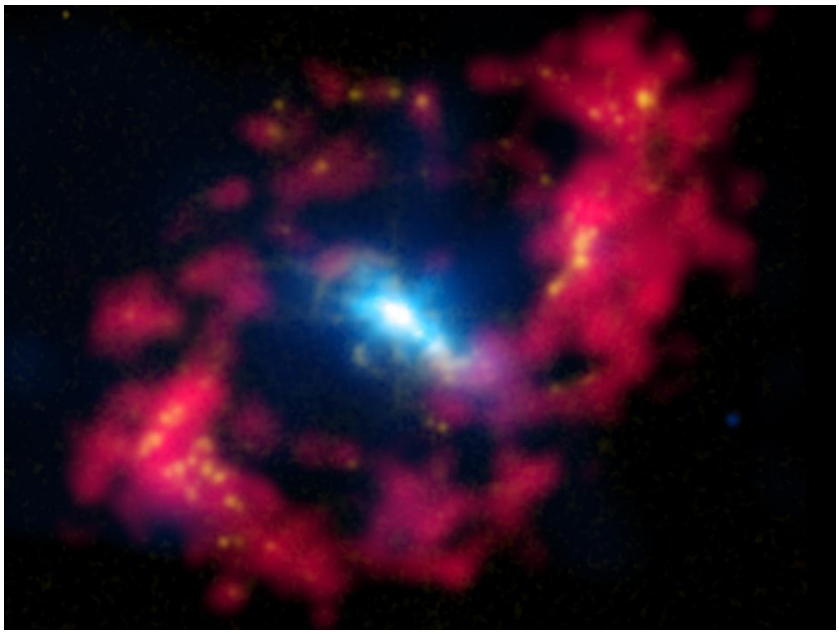

Figure 2.9: Composite image (X-rays - *blue* - from the Chandra X-ray Observatory, optical H II - *yellow* - from the 1-meter Jacobus Kapteyn Telescope, radio H I - *red*- from the VLA) of the Seyfert galaxy NGC 4151. Due to the AGN proximity, the interaction between NGC 4151 central SMBH and the surrounding gas of the host galaxy can be investigated in details. Credit: NASA/CXC/CfA/Wang et al. (2010); Isaac Newton Group of Telescopes, La Palma/Jacobus Kapteyn Telescope; NSF/NRAO/VLA.

The simplest semi-analytic models of galaxy formation predict a much larger number of both very faint and very bright galaxies than observed (Benson et al. 2003). This provides evidence for an unknown phenomenon preventing the "over-cooling" of baryonic matter in the halo of both low and high-mass galaxies, inhibiting gas infall onto the galaxy, and thus truncating the star formation (Fernandes et al. 2009). Cole et al. (2000) and Benson et al. (2003), taking into account the effect of supernovae (SN) and winds in their numerical simulations, succeeded to match the predictions to the observations of the faint-end of the luminosity function but failed to justify the observed lack of the brightest and most massive galaxies. Part of the answer came from quasar jet observations, where the role of the relativistic plasma was found to play crucial roles in the evolution of the host galaxies (McCarthy et al. 1987; Chambers et al. 1987; Eales et al. 1997; Best et al. 2006; Croft et al. 2006) and of other nearby galaxies where it can suppress the star formation (Rawlings & Jarvis 2004; Shabala et al. 2011). But the role of the central black hole on the star formation of the bulge was only considered a decade ago, when theories showed that accretion onto SMBH provides

feedback mechanisms capable of expelling significant amounts of gas out of the galaxy (Silk & Rees 1998 and Fig. 2.9), heating the gas in the halos and efficiently shutting down the star formation (it is noteworthy to mention that accretion energy does not significantly affect the stars already existing in the host galaxy). Demonstrating that the growth of the central black hole by accretion can have a profound effect on its host galaxy was demonstrated by Fabian (2012):

Demonstration:

Lets consider a host galaxy with mass M_g, velocity dispersion σ and a binding energy E_g such as $E_g = M_g\sigma^2$. We also parametrize its central supermassive black hole using a mass M_{BH} and an accretion efficiency α. The energy released by accretion processes, E_{BH}, thus equals $E_{BH} = \alpha M_{BH}c^2$.

Taking into account the empirically-derived relation between the galactic bulge and the SMBH masses $M_{BH} \approx 1.4 \times 10^{-3} M_g$ (Häring & Rix 2004; Merritt & Ferrarese 2001; Kormendy & Gebhardt 2001), one can derive that the relation between the energy released by a black hole and the galactic binding energy: $E_{BH}/E_g \approx 1.4 \times 10^{-3}\alpha(c/\sigma)^2$.

Considering an accretion efficiency of 10 % and $\sigma < 400$ km·s^{-1}, we find $E_{BH}/E_g >> 1$. It indicates that the energy generated by accretion onto a SMBH is much more powerful than the galaxy's binding energy. Even if only a small fraction of this energy supply is transfered to the surrounding gas, the SMBH activity can deeply affect the evolution of its host galaxy.

From a scaling point of view, the size of a galaxy hosting an active black hole is about 10^8 - 10^9 times bigger than the SMBH itself. So, in order to impact its distant environment, the feedback process must operate over a thousand million-fold range of scale (Fabian 2012). Such a condition is hard to achieve, both in observations and theories. Two different scenarios are actually discussed in order to explain how SMBH-generated outflows can have such a deep impact on the host galaxies:

• **The quasar mode**[10] . Also known as radiative or wind mode, the quasar mode operates when SMBH are accreting close to the Eddington limit[11] . A disk-born wind is created and expels the cold gas from the bulge, thereby quenching star formation in the forming galaxy (Croton et al. 2006; Hopkins et al. 2006).

• **The radio mode**. Also known as kinetic or maintenance mode, the radio mode initiates when the host galaxy is still in its hot halo and the accreting SMBH has powerful jets. The star formation is slowed down due to the mechanical energy of the synchrotron radiation that inhibits cooling of the ambient gas. (Croton et al. 2006; Best 2007).

Although observational evidence supporting AGN feedback is growing exponentially (Best et al. 2006; Bundy et al. 2008), its impact on galaxy formation and evolution is still poorly understood. The common belief is that the triggering of radio AGN activity is a strong function of host galaxy properties, linked to different stages of massive galaxy formation (Smolčić 2009). The next

[10] The reader is cautioned not to confuse the terms "quasar" and "radio" modes with any actual quasars. A quasar/AGN might have a radio mode feedback or a quasar mode feedback. A deeper explanation will be presented in Sect. 2.3.

[11] The Eddington luminosity (also referred to as the Eddington limit) of a source is defined as the maximum luminosity where the continuum radiation force outwards balances the gravitational force inwards in hydrostatic equilibrium. In order for matter to be gravitationally bound, the Eddington luminosity L_{Edd} must not exceed a peculiar value: $L_{Edd} \leq 1.26 \times 10^{38}$ M/M$_\odot$ erg·s^{-1}.

radio-telescope generation (SKA, LOFAR) is expected to shed new light on the real mode affecting the stellar formation and unveil some of the AGN mysteries surrounding the SMBH by looking at the other, far edge of the system.

The relatively young, broadband topic of AGN feedback lies at the frontiers between AGN physics and galaxy formation/evolution, and even enters the field of cosmology. Currently focusing on the third star population and SN feedback (Chardin et al. 2012), cosmic reionization scenarios of neutral hydrogen slowly start to take into account AGN (Haiman & Loeb 1998) and Lyman Break Galaxies (LBG, Pentericci et al. 2011) feedback as potential key elements[12] . Moreover, QSO at cosmological distances might also help us to probe the distant, far Universe and solve the mystery of SMBH origin. Thus, the study of AGN feedback will remain a vigorous part of astronomy for the foreseeable future.

2.3 The unified scheme

The previous sections, from Sect. 2.2.1 to Sect. 2.2.8, presented (all) the theoretical emitting, absorbing and reprocessing regions that are supposed to compose an AGN. A natural idea is to build a unified model that could explain all the AGN and QSO observations. However, the reality is much more complicated as AGN are divided observationally into a number of (sub-)classes based on their optical spectrum and radio properties. If the BLR are directly visible in the optical wave band, the AGN is of type-1, while if the BLR are not visible, it is of type-2. The AGN can also be divided into "radio-loud" and "radio-quiet" AGN, depending on the relative strength of the kpc-scale radio jets and lobes. Table. 2.3 (Whittle 2000) summarizes the actual classification of AGN and QSO according to the unified scheme (Antonucci 1993; Urry & Padovani 1995).

Radio Luminosity	Emission lines	$L_{nucl} \geq L_{gal}$	$L_{nucl} \leq L_{gal}$	$L_{nucl} << L_{gal}$
Radio-quiet	Broad + Narrow	QSO	Seyfert 1	LINER
$L_{radio} \leq 10^{-4} L_{opt}$	Narrow only	NL QSO	Seyfert 2	Seyfert 2
	None	–	–	
Radio-loud	Broad + Narrow	RL QSO	BLRG	FR I
$L_{radio} \geq 10^{-2} L_{opt}$	Narrow only	–	NLRG	FR II
	None	OVV, BL Lac	–	Weak lines LINER

Table 2.1: Classes of AGN and QSO. Note that radio-quiet AGN host galaxies are mostly early type, disturbed spiral galaxies, and radio-loud AGN host galaxies are mostly lenticular or elliptical galaxies with possible nuclear dust lanes. The table is taken from Whittle (2000).

Blandford & Rees (1978) were the first to suggested that BL Lacertae (BL Lac) objects were radio-loud AGN, whose jets are aimed close to our line of sight. Keel (1980) discovered that nearby type-1 AGN are preferentially oriented face-on while nearby type-2 AGN are randomly oriented. These discoveries showed that the viewing angle of the observer is a key element in AGN classification (Antonucci 1993). The apparent absence of a BLR in type-2 AGN is explained by a dusty medium that hides the BLR at certain viewing angles from the observer. The ionizing

[12] Fontanot et al. (2012) showed that a relatively steep faint-end of the AGN luminosity function provides a relevant contribution to recover the required ionizing photon rates with an escape fraction of $f_{esc} \sim 5$ % up to $z \sim 7$.

continuum source and its surrounding BLR sit inside the funnel of the torus. In this scenario the half-opening angle of the torus can be estimated from the ratio of type-1 to type-2 AGN in an isotropically selected sample and from the "infra-red calorimeter" – the relative strength of the mid-IR continuum that arises from dust reprocessing of the higher-energy continuum (see Antonucci 2012). There are evidences that the opening angle is a function of luminosity (Lawrence 1991) or accretion history (Wang & Zhang 2007).

The distinction between radio-loud and radio-quiet objects is not orientation-dependent and therefore cannot be explained as a geometry effect. Furthermore, it has been argued by Antonucci (2012) that there is a fundamental difference in the dominant energy generation between high-accretion-rate sources, which are believed to release the bulk of their radiated energy via thermal disk emission in the far-ultraviolet (see Gaskell 2008) and low-accretion-rate AGN, which are dominated by non-thermal emission. The latter class of AGN includes the so-called "naked" AGN (Panessa & Bassani 2002; Georgantopoulos & Zezas 2003; Gliozzi et al. 2007; Bianchi et al. 2008; Panessa et al. 2009)[13] , where low accretions rates inhibit the formation of BLR (Nicastro et al. 2003; Elitzur & Ho 2009; Cao 2010). The transition between the two modes of dominant energy generation take place at an Eddington ratio of $\sim 10^{-3}$ (Antonucci 2012). Following Antonucci (2012), these two types of AGN will be refereed as "thermal AGN" and "non-thermal AGN", respectively[14] . The thermal/non-thermal dichotomy is the causal consequence of the accretion mode (related to the accretion rate) that has an impact on the accretion disk and thus on the eventual observation of its thermal emission. By definition, thermal AGN always have a big blue bump. As far as is known (see Antonucci 2012), they also always have a BLR, although the BLR might be hidden, as in type-2 AGN [15] . Non-thermal AGN are FR I radio galaxies and LINERs. It is important to note that the thermal/non-thermal distinction is **not** the same as the radio-quiet/radio-loud distinction. A radio-loud AGN can be either a thermal AGN (for example, 3C 273) or a non-thermal AGN (such as M87). For completeness it is noteworthy to point out that optically violently variable (OVV) behaviour in blazars can arise from both thermal and non-thermal AGN.

Fig. 2.10 [unscaled] and Fig. 2.11 [scaled in gravitational radii] synthesize the unified model of AGN. The upper part of the figure depicts a radio-quiet AGN while the bottom part shows the presence of a characteristic, powerful, kilo-parsec jet. Quasars appear highly anisotropic as the equatorial plane defined by the torus and accretion disk is populated by geometrically flat regions while extended outflows fill the space along the vertical AGN axis (i.e. the revolution symmetry axis of the torus). The type 1 / type 2 dichotomy naturally appears when the observer's line of sight is crossing the obscuring dust horizon. For radio-loud objects and observer's viewing angles along the jet propagation axis, the AGN is classified as a blazar. While most of the features are reported into the figure, the exact morphology of the overall system is still a major challenge to fulfill. In particular, the radiative and energetic coupling between the jet and the outflows is still neither observed or explained; the only shred of knowledge recognized is that the jet emission dominates the outflow signatures.

[13] "Naked" AGN are a subclass of radio-quiet Seyfert 2 galaxies (so-called "non-hidden BLR" Seyfert 2s = NHBLR Seyfert 2s) but show a less extended accretion regime than their parents. See Zhang & Wang (2006) for a parallel between NHBLR Seyfert 2s and Narrow Line Seyfert 1 AGN (NLS1), which both show high accretion rates.

[14] In the literature on the possible role of AGN feedback on galaxy growth the two modes are sometimes referred to as "quasar mode" and "radio mode" but the labels "thermal" and "non-thermal" will be preferred since historically the word "quasar" refers to a high-luminosity, radio-loud AGN. While all "quasars" are thermal AGN, the converse is not true because the majority of thermal AGN have a low luminosity.

[15] There is an ongoing debate where there are NHBLR Seyfert 2s. Antonucci (2012) argued that we cannot conclude that NHBLR Seyfert 2s exist from existing evidence.

Thus, in order to clarify the picture and explore the central engine response without any jet signatures pollution, the remainder of this thesis focuses on thermal, radio-quiet AGN.

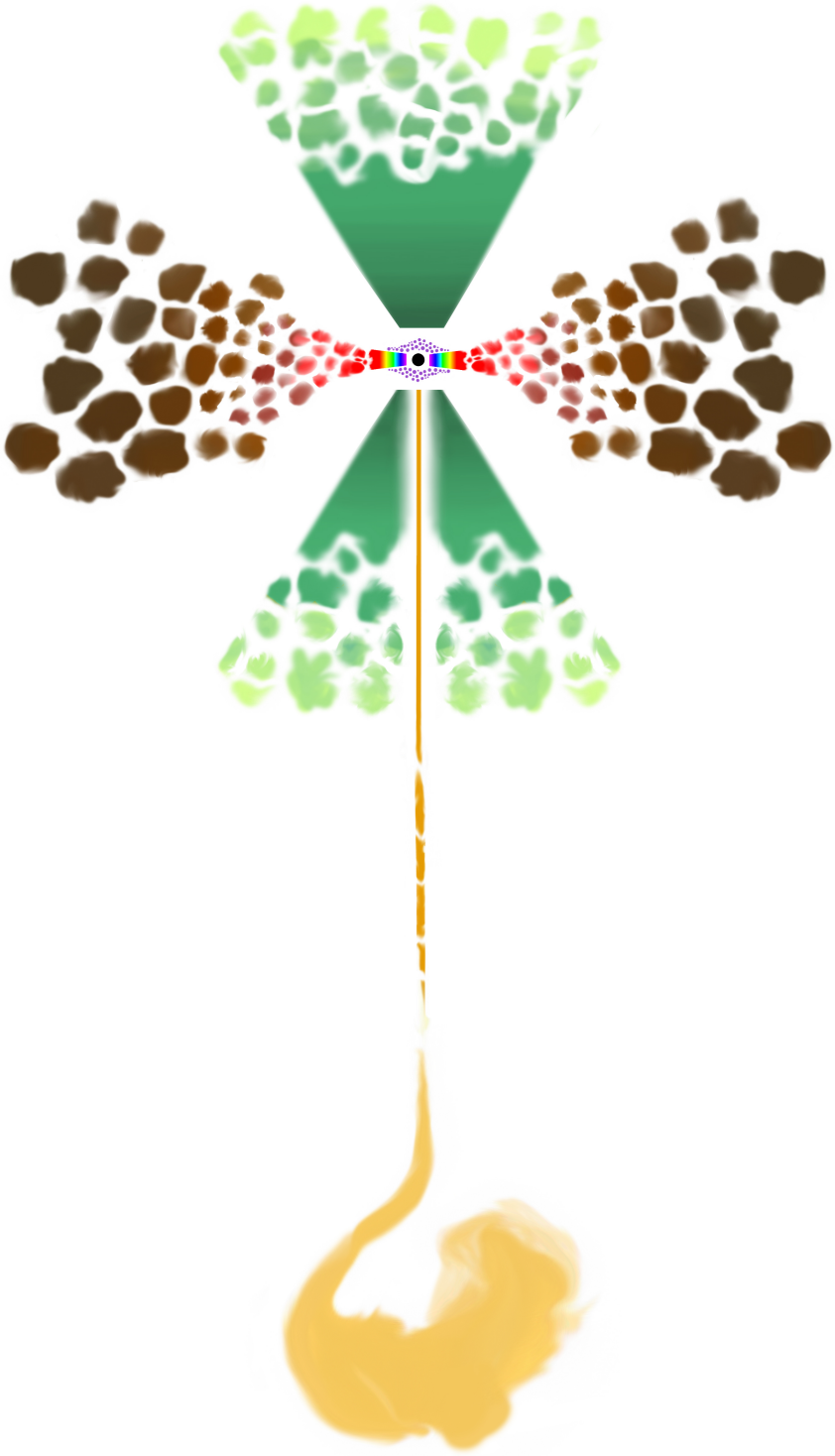

Figure 2.10: Unscaled sketch of the AGN unification theory. *Credits: Jûles Garreau.*

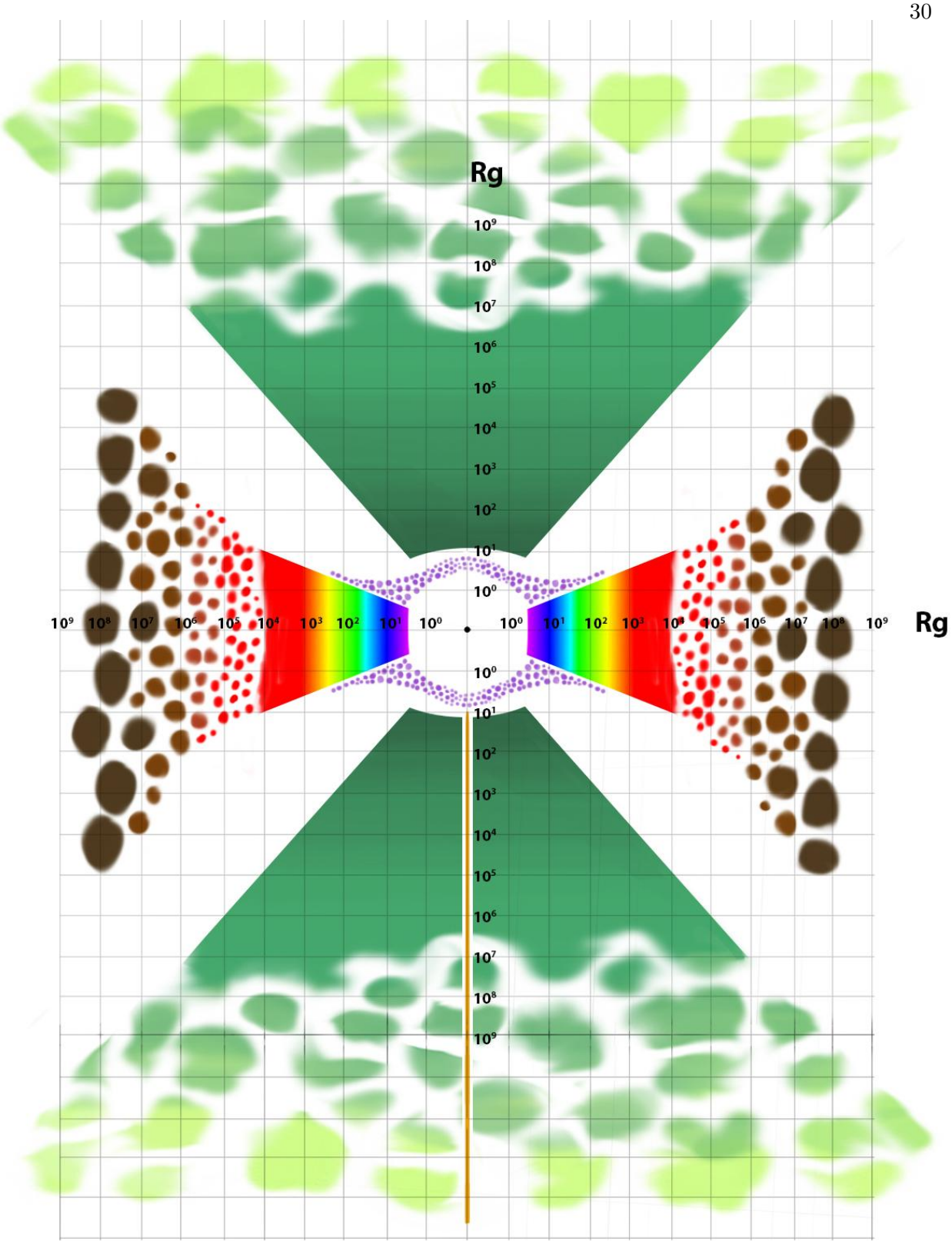

Figure 2.11: Sketch of the AGN unification theory scaled in gravitational radii, taking into account a $\sim 10^7$ $M_\odot$ SMBH. The radio-loud part of the scheme is not shown. *Credits: Jûles Garreau.*

Chapter 3

Exploring AGN using polarimetry

According to the theoretical unified scheme (Antonucci 1993; Urry & Padovani 1995), AGN are anisotropic objects where most of the radiation comes from below 10^4 Schwarzschild radii. In order to escape, photons must then undergo multiple scattering events on/in the SMBH surrounding regions. And when scattering on asymmetrical structures is involved, polarization is usually hiding under the carpet.

Polarization yields two more independent observables (P and ψ) than a pure intensity-spectrum, and can be produced in any astronomical object where the asymmetry is intrinsic (within the source itself) and/or along the observer line of sight (usually produced by an inhomogeneous ISM). Geometric asymmetries or the presence of magnetic fields are the most common sources of asymmetries in the distribution of scattered radiation. As most of the celestial radiation sources are either magnetized or asymmetrical, polarimetry can be used as a diagnostic tool from (proto-)stars to (extra-)solar planets, ISM/IGM to astrobiology. AGN, being highly luminous, are then prime candidates for polarization measurements. For instance, early radio and optically selected surveys of the most luminous known AGN and quasars showed that they could be divided into two classes by their optical polarization properties (Moore & Stockman 1984): most of the objects show low optical polarization ($P < 3$ %, Stockman et al. 1984) while ~ 1 % of the sample, lately known as OVV, exhibited higher and variable polarization (Moore & Stockman 1981).

Polarimetry has played a crucial role in the advancement of the unified scheme of AGN. Miller & Antonucci (1983) spectropolarimetric measurements of the nucleus of NGC 1068 helped to identify electron and dust scattering as the main mechanisms producing a continuum polarization in radio-quiet AGN. Going further, Antonucci & Miller (1985) extensive high-resolution, high signal-to-noise ratio (S/N) spectropolarimetric observation of the same AGN revealed the presence of highly polarized, broad, symmetric Balmer and permitted Fe II lines. The polarization spectrum was found to be closely similar to typical Seyfert 1 galaxies, supporting the idea that Seyfert 2 AGN are hiding a Seyfert 1 core behind an equatorial, circumnuclear obscuring medium. This discovery was a key argument in favor of an unified model of AGN were the orientation of the system is determining the AGN observed properties (see Sect. 2).

High spatial resolution polarimetry provides a unique insight into the near-nuclear AGN environments and multi-wavelength studies may be used to observe the asymmetry in different parts of the object, remodeling the interior regions and leading toward a single coherent model. Polarimetry, as well as spectropolarimetry and velocity-resolved spectropolarimetry, can play a decisive role in answering questions about the nuclear activity in AGN. Coupled to radiative transfer modeling including a treatment of polarization, polarimetry is a unique tool for determining the geometry and velocity of reprocessing regions such as the polar outflows, the BLR or even the

accretion disk.

3.1 Theory of polarization

Any electromagnetic wave can be characterized by four main parameters: its intensity, frequency, polarization and phase. While being very effective, the human vision is only sensitive to the colour associated with the modulation frequency as well as its intensity. We do not distinguish the vectorial nature of light and therefore it was long been seen as a scalar quantity. It is only in the early nineteenth century that the transverse vibration of light was demonstrated by Young (1801) and Fresnel (1821). With the development of the theory of electromagnetism, the notion of polarization was introduced. Polarization describes the temporal evolution of tip of the electric vector. If this trend is stationary during the measurement time, the wave is said to be polarized, otherwise it is said to be partially or totally depolarized. When a light-wave propagates through a medium, undergoing several scattering events, its polarization is affected; the variation of the polarization state is then used to characterize the scattering system.

The study of light passing through a succession of polarizing elements can be facilitated by the use of various formalisms. Stokes (1852) developed the foundations of the polarization of light as a pure mathematical theory. The major advantage of Stokes's work is to have shown that four parameters associated with measurable quantities were sufficient to fully characterize the polarization state of a wave that is partially polarized. These four parameters are now well known as the Stokes parameters and are presented in the following sections.

3.1.1 Principles

The electric field vector ($\vec{E}$-vector) of a (quasi-)monochromatic, electromagnetic plane wave may be decomposed into three orthogonal components in a Cartesian coordinate system. In the general case, the $\vec{E}$-vector may be written in the form:

$$\vec{E}(x,y,z,t) = E_x(x,y,z,t)\vec{x} + E_y(x,y,z,t)\vec{y} + E_z(x,y,z,t)\vec{z} \tag{3.1}$$

where $\vec{x}$, $\vec{y}$ and $\vec{z}$ are the unitary vectors of the reference system axis.
In the case of a quasi-monochromatic plane wave:

$$\vec{E_i}(x,y,z,t) = \vec{E}_{0i}\cos(\omega t - \vec{k}.\vec{r} + \varphi_i) \tag{3.2}$$

where $\vec{k}.\vec{r} = \mathrm{k}_x\mathrm{x} + \mathrm{k}_y\mathrm{y} + \mathrm{k}_z\mathrm{z}$, and $i = x$, y or z. φ is a phase term and E_{0i} is a positive amplitude term.

If we opt for a wave propagation along the z-axis, knowing that the wave vector $\vec{k}$ and $\vec{E}$ are orthogonal in an isotropic medium (i.e. $\mathrm{k}_x = \mathrm{k}_y = 0$), thus the electric field is transverse (i.e. $\mathrm{E}_z = 0$). We obtain the following simplified system:

$$\vec{E_x}(z,t) = \vec{E}_{0x}\cos(\omega t - kz + \varphi_x) \tag{3.3}$$

$$\vec{E_y}(z,t) = \vec{E}_{0y}\cos(\omega t - kz + \varphi_y) \tag{3.4}$$

$$\vec{E_z}(t) = 0 \tag{3.5}$$

where k = $2\pi n/\lambda$, with λ the wavelength (in vacuum), and n the refractive index seen by the wave along the propagation direction.

For the sake of relief writing, the time dependence will be implied, thus $E_i(t)$ becomes E_i. If we combine the equations (3.3) and (3.4), the end of the electric field vector describes an ellipse described by the following equation:

$$\frac{E_x^2}{E_{0x}^2} + \frac{E_y^2}{E_{0y}^2} - 2\frac{E_x E_y}{E_{0x} E_{0y}} \cos(\varphi) = \sin^2(\varphi) \tag{3.6}$$

with $\varphi = \varphi_x$ - φ_y.

The polarization state is fully defined if we know all the parameters of the ellipse (see Fig. 3.1): its ellipticity ϵ, azimuth θ, phase difference φ and rotational direction (linked with the sign of $\sin(\varphi)$).

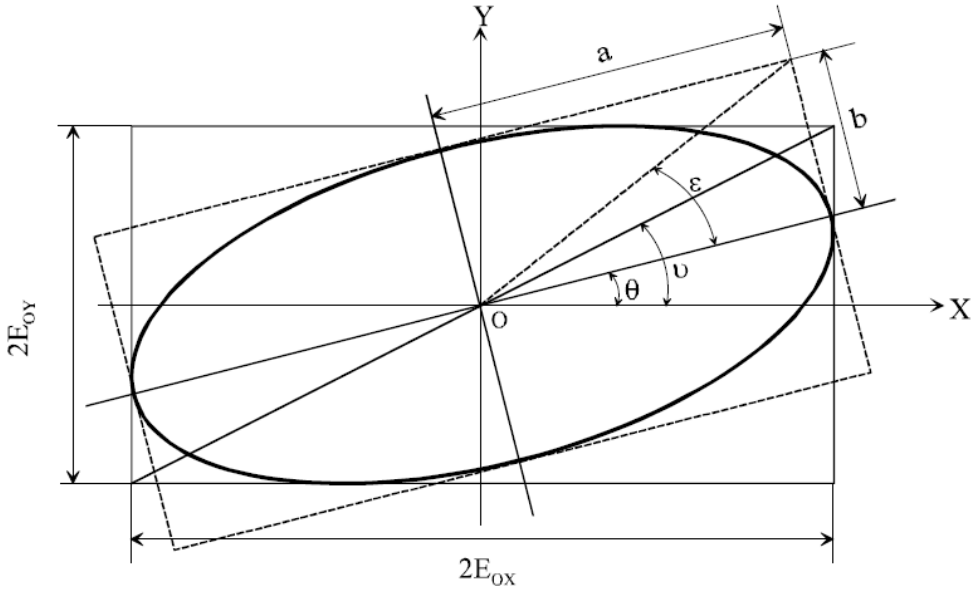

Figure 3.1: Polarization ellipse induced by the motion of the electric field vector inside the polarization plane. O is the center of the (X,Y) coordinate system

Thus, when $\varphi = 0$ or $\varphi = \pi$(modulo 2π), the electromagnetic wave is linearly polarized. When $\varphi = \pi/2$ or $\varphi = 3\pi/2$ and $E_{0x} = E_{0y}$, the ellipse becomes a circle and the polarization is described as circular. The possible polarization states are unpolarized, horizontally polarized, vertically polarized, circularly polarized or elliptically polarized.

The ellipse parameters are related to the wave parameters through the following equations:

$$a^2 + b^2 = E_{0x}^2 + E_{0y}^2 \tag{3.7}$$

$$\pm ab = E_{0x} E_{0y} \sin(\varphi) \tag{3.8}$$

$$(E_{0x}^2 - E_{0y}^2)\tan(2\theta) = 2E_{0x}E_{0y}\cos(\varphi) \tag{3.9}$$

$$\frac{E_{0y}}{E_{0x}} = \tan(\nu) \tag{3.10}$$

$$\frac{b}{a} = \tan(\epsilon) \tag{3.11}$$

The ellipse is right-handed or left-handed depending on the direction of rotation of the field vector. By convention, it is right-handed when an observer looking in the opposite direction to the propagation direction sees a clockwise rotation. Thus, in equation (3.8), the positive sign denotes a left-handed rotation and the minus sign denotes a right-handed one.

3.1.2 Stokes formalism

The polarization of light being intrinsically and naturally vectorial, Stokes (1852) decided to use a vectorial mathematical representation in order to easily manipulate partially polarized waves. His polarization vector is based on quantities that are directly measurable: the intensities. This formalism is particularly adapted to astronomical measurements of polarized light as the only observable quantities have energetic dimensions.

In the Stokes formalism, the polarization of light is described by a 4-dimension vector called the "Stokes vector".

$$\vec{S} = \begin{bmatrix} S_0 \\ S_1 \\ S_2 \\ S_3 \end{bmatrix} = \begin{bmatrix} \langle E_{0x}^2 \rangle + \langle E_{0y}^2 \rangle \\ \langle E_{0x}^2 \rangle - \langle E_{0y}^2 \rangle \\ 2\langle E_{0x}E_{0y}\cos(\varphi) \rangle \\ 2\langle E_{0x}E_{0y}\sin(\varphi) \rangle \end{bmatrix} = \begin{bmatrix} I \\ Q \\ U \\ V \end{bmatrix} \tag{3.12}$$

The actual detectors used in astrophysics have integration times largely superior to the optical wave oscillation periods ($\sim 10^{-15}$ s). The measured quantities are then integrated over time: the symbols $\langle$ and $\rangle$ represent a temporal average of the signal so that $\langle \mathrm{E}_x\ \mathrm{E}_y \rangle = \lim_{T\to\infty} \frac{1}{T} \int_0^T E_x E_y \, \mathrm{d}t$, where T is the integration time of the detector.

Looking at the four Stokes vector components in detail, I represents the total intensity of the photon flux. The three other quantities (Q,U,V) are linked with intensities of complementary polarization modes: Q is the difference between the vertical and horizontal polarization state, U is the difference between the linear polarization oriented at +45° and -45° from the vertical polarization state. V is the the difference between the clockwise and anti-clockwise rotational directions. Figure 3.2 shows different polarization states according to their Stokes parameters.

Three different polarization states can be encountered:

• **Unpolarized light**. For a completely unpolarized monochromatic plane wave, the terms of amplitude E_{0x} and E_{0y}, as well as the difference between the phase terms φ_x and φ_y are time-independent. In this case the four Stokes parameters become:

$$I = E_{0x}^2 + E_{0y}^2 \tag{3.13}$$

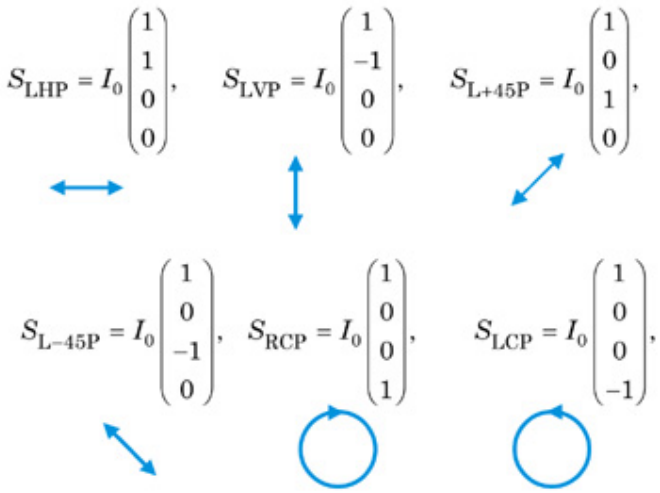

Figure 3.2: Stokes vectors for a variety of elementary polarization states. LHP stands for linear horizontal polarization, LVP linear vertical polarization, $L + 45°$ linear polarization oriented at $+45°$, $L - 45°$ linear polarization oriented at -45°, RCP right-handed (clockwise) circular polarization and LCP left-handed (anti-clockwise) circular polarization

$$Q = E_{0x}^2 - E_{0y}^2 \tag{3.14}$$

$$U = 2E_{0x}E_{0y}\cos(\varphi) \tag{3.15}$$

$$V = 2E_{0x}E_{0y}\sin(\varphi) \tag{3.16}$$

Thus, for an unpolarized wave $Q = U = V = 0$.

• **Fully polarized light**. In the case of fully polarized light, the situation is very similar to the previous one, expect that $I^2 = Q^2 + U^2 + V^2$

• **Partially polarized light**. Using the Schwartz inequality[1] , it is possible to demonstrate that, for any polarization state, the Stokes parameters always fulfill the following relation: $I^2 \geq Q^2 + U^2 + V^2$.

Therefore, the degree of polarization P of the wave can be defined by:

$$P = \frac{I_{pol}}{I_{tot}} = \frac{\sqrt{Q^2 + U^2 + V^2}}{I^2} \tag{3.18}$$

If $P = 0$, the wave is unpolarized, if $P = 1$ the wave is fully polarized and for intermediate values, the wave is partially polarized.

[1] Schwartz inequality:

$$|\langle E_x(t)E_y^*(t)\rangle|^2 \leq \langle|E_x(t)|^2\rangle\langle|E_y(t)|^2\rangle \tag{3.17}$$

It follows that any wave characterized by a Stokes vector can be decomposed into a completely polarized part and a completely depolarized counterpart:

$$\begin{bmatrix} S_0 \\ S_1 \\ S_2 \\ S_3 \end{bmatrix} = \begin{bmatrix} S_0 - \sqrt{S_1^2 + S_2^2 + S_3^2} \\ 0 \\ 0 \\ 0 \end{bmatrix} + \begin{bmatrix} \sqrt{S_1^2 + S_2^2 + S_3^2} \\ S_1 \\ S_2 \\ S_3 \end{bmatrix} \tag{3.19}$$

In addition to the degree of polarization, the Stokes parameters can be shown to be related to the orientation and ellipticity angles, ψ and χ respectively:

$$\psi = \frac{1}{2}\tan^{-1}(\frac{U}{Q}) \tag{3.20}$$

$$\chi = \frac{1}{2}\sin^{-1}(\frac{V}{I}) \tag{3.21}$$

P, ψ and χ are the values associated with the Stokes vector that completely describe the state of polarization of an incoming electromagnetic wave. However, during a scattering event, they are meant to change according to the reprocessing process.

3.1.3 Mueller matrices

The Stokes parameters are used to fully characterize the state of polarization of a light wave. Mueller (1948), meanwhile, showed that there was a linear relationship between the in-coming ($\vec{S_i}$) and out-going ($\vec{S_o}$) Stokes vector during a scattering event[2] :

$$\vec{S_o} = [M]\vec{S_i} \tag{3.22}$$

Where [M] is the Mueller matrix whose elements m_{ij} (i, j = 0, 1, 2, 3) are real and directly connected to the measurement. It may be regarded as the polarization transfer matrix of a given environment. Knowing [M], the polarization state of the system output can be predicted when the incident conditions are known.

The matrix properties determine the Mueller matrix of an optical system formed by a succession of elements. It is the product of the matrices of the elements constituting the system. Considering n optical elements traversed by a light ray in the order 1, 2, ... n, then the resulting Mueller matrix is:

$$[M] = [M_n][M_{n-1}][M_{n-2}]...[M_2][M_1] \tag{3.23}$$

Going further, Fry & Kattawar (1981) and Gil & Bernabeu (1985) used the following equality to characterize a non-depolarizing optical system:

$$tr([M]^T[M]) = \sum_{i=0}^{3}\sum_{j=0}^{3} m_{ij}^2 = 4m_{00}^2 \tag{3.24}$$

[2] Curiously, Soleillet (1929) and Perrin (1942) were the first to find similar results but History mostly remembers Mueller (1948).

Another parameter that can be extracted from the Mueller matrix is the depolarization index P_d, which is similar to the degree of polarization introduced for Stokes vectors (Eq. 3.18), since it reflects the depolarizing tendency of the medium described by the Mueller matrix. This parameter was introduced by Gil & Bernabeu (1985, 1986) and provides an average measure of the polarizing power of an optical system:

$$P_d = \sqrt{\frac{\sum_{i,j=0}^{3} m_{ij}^2 - m_{00}^2}{3m_{00}^2}} \tag{3.25}$$

with $0 \leq P_d \leq 1$. If $P_d = 1$, the resulting matrix describes a non-depolarizing medium. If $P_d = 0$, the medium is meant to fully depolarize the incoming radiation. For a dense (optically thick) system, where multiple scattering events may occur, such a depolarization effect is expected to appear as the medium depolarization index is lower than 1.

3.2 Polarization mechanisms from the optical to the X-ray band

Celestial bodies have numerous faces strongly correlated with the wavelength range at which they are observed. A well known example is the Milky Way galaxy broadband observation showing characteristic features at different wavebands. The continuum radio emission at 2.5 GHz is the signature of warm, ionized gases that surround the stellar formation regions. The thermal infrared waveband reveals the interstellar hot gases emission as well as the presence of complex molecules. In the optical, around 6000 Å, the stellar luminosity is highly absorbed by interstellar clouds, limiting the observations to the solar environment. In fact, the most obscured regions correspond to the most luminous ones in the IR. Looking at higher energies, the galactic center starts to be visible in the X-ray regime and beyond 100 MeV, cosmic rays coming from galactic pulsars and some extragalactic objects are detected.

A multi-wavelength study of any astrophysical source may reveal hidden properties, and lead to a better comprehension of their inner physics. This thesis focuses on radio-quiet AGN, and a deeper exploration of their central engine is achieved by looking at the polarization properties in the optical, UV and X-ray wavebands were a large amount of observational data are already available[3] .

To do so, it is important to know what are the scattering mechanisms that might affect the photons trajectory and how they influence the resulting state of polarization. Using the Stokes formalism and Mueller matrices, the next subsections describe in detail the main polarization mechanisms occurring in the optical to X-ray domains[4] .

3.2.1 Thomson scattering

The simplest model describing the interaction between a radiation and a particle is the harmonic oscillator where the electron is considered as a dipole oscillating under the effect of a

[3] An extension of our study to the IR domain is actually under consideration.

[4] Magnetic fields are not yet included in STOKES; thus, polarization mechanisms associated with any magnetic origin such as synchrotron radiation, Faraday rotation, Zeeman effect and Hanle effect are not considered. They are briefly treated in Appendix B. Some high energy phenomenon occurring between photons and electrons, leading to a polarized outgoing radiation, such as pair production, electron-ejection by the Photoelectric effect and the Positron Annihilation-in-flight are not described at all.

radiation field.

If we consider an atom with a bound electron e, under the effect of a radiation field E_ν, e oscillates, maintained by an attractive force $m_e k x$. The equation of motion of the oscillating dipole is:

$$m_e \ddot{x} = \underbrace{-m_e \gamma \dot{x}}_{Frictionnal\ force} - \underbrace{m_e \omega_0^2 x}_{Restoring\ force} + \underbrace{E_\omega^0 e^{i\omega t}}_{External\ force} \tag{3.26}$$

with the dipole resonance frequency defined such as $\omega_0 = 2\pi\nu_0$.

According to the conservation laws, an incident radiation undergoing a collision event with an electron is scattered off the charged particle. The total kinetic energy of the electron-photon system is preserved since there is no net conversion of kinetic energy into other forms. The scattering event is considered as elastic. Thus, in the frame of non-relativistic, elastic collisions, the scattering cross section σ_ω of an incoming radiation with $\omega = 2\pi\nu$ onto a particle can be defined as:

$$\sigma_\omega = \frac{8\pi}{3}\, r_0^2\, \frac{\omega^4}{(\omega_0^2 - \omega^2)^2 + \Gamma_{cl}^2 \frac{\omega^6}{\omega_0^4}} \tag{3.27}$$

with

$$\Gamma_{cl} = \frac{2r_0}{3c}\, \omega_0^2 \;=\; \frac{4\pi}{3}\frac{r_0}{\lambda_0}\, \omega_0 \tag{3.28}$$

using r_0 as the classical electron radius such as $r_0 \sim 2.8 \times 10^{-15}$ m.

Now, lets consider a non-relativistic plasma such as the ionization cones in AGN where the medium is electron-dominated with free electrons at rest energy. In this case electrons are not bound to the atom and $\nu_0 \to 0$. It implies that $\omega >> \omega_0$ and the scattering cross section can be approximated such as:

$$\sigma \;\simeq\; \frac{8\pi}{3}\, r_0^2 \;\simeq\; 0.665 \times 10^{-24}\ \mathrm{cm}^2 \tag{3.29}$$

The scattering cross section σ becomes wavelength-independent, such as the intensity of the scattered radiation. No wavelength shift can be expected. Such a scattering mechanism is called *Thomson scattering*.

However, the scattering phase function does not include enough scattering characteristics. An important unknown is the scattering angle between the incident and outgoing photon direction. To solve this problem, the scattering phase function is defined according to two scattering angles θ and ϕ, giving the density of probability that a given, scattered photon flies away along a certain direction. θ is the scattering angle between the incoming and outgoing radiation in the scattering plane and ϕ is the azimuthal angle. The scattering phase function is given in steradian^{-1} (sr^{-1}) and is equal to:

$$\int_0^{4\pi} P(\theta,\phi)\mathrm{d}\Omega = \int_0^{2\pi} \mathrm{d}\phi \int_0^{\pi} \mathrm{d}\theta \sin(\theta,\phi) = 4\pi \tag{3.30}$$

$P(\theta,\phi)/4\pi$ represents the density of probability of a scattering event, normalized to 1. In the case of spherical particles, or of isotropically, randomly aligned non-spherical particles, the scattering phase function becomes ϕ-independent. This is the case of Thomson scattering as the

electron is considered as a spherical particle. Peculiarly, the scattering phase function of electron scattering in the Thomson regime is not isotropic (especially for polarized light) and wavelength-independent; a behavior that helped to determine the scattering mechanisms operating in many astrophysical sources (Antonucci 1993; Code et al. 1993; Antonucci et al. 1994).

The Thomson scattering matrix describing the polarization transformations induced by a scattering event is not described in this subsection as it is very similar to the Rayleigh scattering matrix described in the following paragraph.

3.2.2 Rayleigh scattering

While the previous section described the elastic interaction of an incoming radiation with a poorly bound or even free electron, a second scattering mechanism can originate from the collision event between radiation and an atom. It is the *Rayleigh scattering* mechanism, proposed to explain the radiation scattering process occurring in stellar atmospheres (Bond & Siewert 1967; Schnatz & Siewert 1971).

The theory is similar to Sect. 3.2.1 but in the case of Rayleigh scattering, the electron is bound to the atom ($\omega << \omega_0$), so the scattering cross section becomes:

$$\sigma_\omega \simeq \frac{8\pi}{3} r_0^2 \left(\frac{\omega}{\omega_0}\right)^4 \tag{3.31}$$

The scattering cross section is now wavelength-dependent. It increases with the frequency of the incident radiation (approximatively increasing with λ^{-4}). A particularly well known example is the optical scattering of the sunlight by the optically thick Earth atmosphere where the UV band of the sunlight spectrum is the most widely scattered by high altitude molecules, giving the sky its blue color[5] .

The scattering matrix describing the transformation of the incoming Stokes vector is given by the following equation. The same matrix is used to model electron scattering events in the case of Thomson scattering:

$$\widehat{R}(\mu) = \frac{3}{4} \begin{pmatrix} 1+\mu^2 & \mu^2-1 & 0 & 0 \\ \mu^2-1 & 1+\mu^2 & 0 & 0 \\ 0 & 0 & 2\mu & 0 \\ 0 & 0 & 0 & 2\mu \end{pmatrix} \tag{3.32}$$

Here the constant 3/4 is such that the scattering is normalized for unpolarized radiation integrated over all angles. That is, the scattered intensity integrated over all directions equals the intensity of the incoming beam. μ is defined as the common notation $\mu = \cos(\theta)$.

The Thomson/Rayleigh scattering matrix holds for non-relativistic electrons and atoms with sizes inferior to 0.2 λ. If the incoming radiation is highly energetic, the scattering is not anymore elastic and the associated mechanism is Compton scattering. In the case of relativistic particles, it is more likely that the particles give energy to the photon, leading to the Inverse Compton effect.

[5] However, the sky appears blue and not purple to the human vision because the eye is more sensitive to blue. Plus, the UV part of the sunlight spectrum decreases more strongly than the blue part, resulting in a smaller contribution to the total flux.

Finally, if the size of the scattering target is similar or superior to the radiation wavelength, Mie scattering is involved.

3.2.3 Compton scattering

The *Compton scattering* mechanism is the inelastic scattering of an energetic photon by an electron. In the rest frame of the electron, $h\nu_0'$ is the incident photon energy and $h\nu_1'$ the outgoing photon energy. The angle between the two radiation directions is noted as θ'. The electron acquires a momentum p' related to the scattering event such as $p' = \gamma m_e v'$, with an angle α' between the photon incident direction and the electron new momentum (see Fig. 3.3).

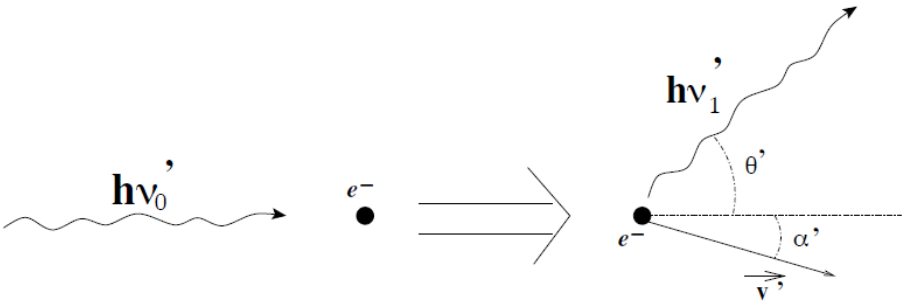

Figure 3.3: Scattering scheme of a Compton event, where an electron scatters off an incident photon. The outgoing photon energy is diminished according to the energy transfered to the electron.

Following the total energy and momentum conservation laws, the relation between the outgoing photon frequency with the incident photon frequency and the photon emission angle can be expressed as:

$$\nu_1' = \frac{\nu_0'}{1 + \frac{h\nu_0'}{m_e c^2}(1 - \cos(\theta'))} \tag{3.33}$$

indicating that, independently of the angle θ, the outgoing photon frequency has a lower frequency than the incident radiation (the rest of the energy being transfered to the electron as recoil energy). Thus, a wavelength shift is expected from Compton scattering events.

The Compton scattering phase function (Klein & Nishina 1929) is given by:

$$\frac{\mathrm{d}\sigma}{\mathrm{d}\Omega} = \frac{\xi^2}{2}\left(\frac{\hbar}{m_e c}\right)^2 \epsilon^2 \left(\epsilon + \frac{1}{\epsilon} - 1 + \cos^2(\theta')\right) \tag{3.34}$$

where $\epsilon = \nu_1'/\nu_0'$ and ξ is the fine structure constant $\xi = e^2/\hbar c = 1/137$. The scattering cross section for Compton scattering is obtained when integrating the previous equation over a sphere with $\mathrm{d}\Omega = 2\pi\sin(\theta')\mathrm{d}\theta'$:

$$\sigma = 2\pi r_0^2 \left\{\frac{1+\delta}{\delta^3}\left(\frac{2\delta(1+\delta)}{1+2\delta} - \ln(1+2\delta)\right) + \frac{\ln(1+2\delta)}{\delta} - \frac{1+3\delta}{(1+2\delta)^2}\right\} \tag{3.35}$$

with $\delta = h\nu'_0/m_e c^2$.

Looking at the different possible values of δ, two main regimes appear:

• **The Thomson regime**. In the case $\delta << 1$, the photon energy is small in comparison with electron mass energy and the Compton scattering cross section tends toward the Thomson scattering cross section. It follows that, regardless to the wavelength shift, the Rayleigh scattering matrix is a good approximation to model the scattering events occurring in the UV/optical range as well as in the X-ray domain if the electrons are not embedded in a hot plasma.

• **The Klein-Nishina regime**. In the case $\delta >> 1$, the photon energy is large in comparison with the electron mass energy. The scattering cross section becomes much smaller than the Thomson cross section:

$$\lim_{\delta \to +\infty} \sigma = \frac{3\sigma_{Thomson}}{4\delta} << \sigma_{Thomson} \tag{3.36}$$

thus high energy photons may pass through non-relativistic electron plasma without interaction.

It is noteworthy to mention that, for high electron temperatures, the Rayleigh matrix was found to predict much larger polarization values than the Compton matrix (Poutanen & Vilhu 1993; Nagirner & Poutanen 1993a,b), and thus cannot be used as an approximation. Another scattering matrix must be taken into account: the Inverse Compton matrix.

3.2.4 Inverse Compton scattering

The previous section defined the Compton scattering as the inelastic reprocessing event of a high energy photon on an electron at rest mass energy. The $Inverse\ Compton\ effect$, also known as $Comptonization$ or $up-scattering$, considers the same scattering case but taking into account the motion of the electron at relativistic speed. If the motion of the electron is much lower than the speed of light, the wavelength shift between the electron and the observer reference frames is small; a Compton treatment of the scattering effect holds. However, if the electron energies are assumed to be distributed in accordance with the relativistic Maxwellian distribution, then relativistic effects are expected to play a crucial role.

The Maxwellian distribution is given by:

$$f(\chi) = \frac{y}{4\pi K_2(y)} e^{-y\chi} \tag{3.37}$$

with

$$y = \frac{m_e c^2}{kT_e} \tag{3.38}$$

where T_e is the temperature of the electron gas, k the Boltzmann constant, χ is the electron energy in units of the rest energy $m_e c^2$ and K_2 is the modified Bessel function of the second kind (Macdonald function).

Using the same sketch as in Fig. 3.3, with R the observer frame and R' the electron frame, using $\beta = v/c$, $\gamma = 1/\sqrt{1-\beta}$ and Lorentz transformations between the two reference frames, one can obtain the photon wavelength shift due to Comptonization:

$$\frac{\nu_1}{\nu_0} = \gamma^2 \frac{(1-\beta\cos(\alpha))(1+\beta\cos(\theta'))}{1+\delta(1-\cos(\theta'))} \tag{3.39}$$

with $\delta = h\nu_0'/m_e c^2$. The maximal amplification of the photon's wavelength is expected for frontal collisions between the radiation and the electron ($\alpha = \pi$) where the photon is re-emitted along the direction of the electron motion. Thus, if $\alpha = \pi$, $\nu_1/\nu_0 = 4\gamma$ and the photon is scattered backward.

The scattering phase function is given by the Klein-Nishina formula in terms of the Thomson scattering cross section:

$$\lim_{\epsilon \to 1} \frac{\mathrm{d}\sigma}{\mathrm{d}\Omega}(\theta') = \frac{3\sigma_{Thomson}}{16\pi}(1+\cos^2(\theta')) \tag{3.40}$$

And the high precision Comptonization scattering cross section derived by Pozdnyakov et al. (1983) becomes:

$$\sigma(x) = \begin{cases} \frac{1}{3} + 0.141x - 0.12x^2 + (1+0.5x)(1+x)^{-2} & \text{if} \quad x \leq 0.5 \\ (\ln(1+x) + 0.06)x^{-1} & \text{if} \quad x \leq 0.5 \leq 3.5 \\ (\ln(1+x) + 0.5 - (2+0.076x)^{-1})x^{-1}) & \text{if} \quad 0.5 \leq x \end{cases} \tag{3.41}$$

with

$$x = \frac{2h\nu}{m_e c^2}\gamma\left(1-\beta\cos(\theta')\right) \tag{3.42}$$

Now, let x be the initial photon beam energy with $x = h\nu/m_e c^2$ and x' the scattered photon beam, then the Compton scattering matrix of polarized radiation on an isotropic electron gas with a fixed energy χ is:

$$\widehat{R}(x, x_1, \mu, \chi) = \begin{pmatrix} R & R_I & 0 & 0 \\ R_I & R_Q & 0 & 0 \\ 0 & 0 & R_U & 0 \\ 0 & 0 & 0 & R_V \end{pmatrix} \tag{3.43}$$

with

$$\begin{array}{lcl} R & = & R_a + R_b \\ R_I & = & R_a + R_c \\ R_Q & = & \frac{2}{Q} + 2\frac{u-Q}{rq}[\frac{u-Q}{rq}(2Q+u) - 4] + \frac{2u}{vq} + 2R_c \\ R_U & = & R_U + R_a \\ R_V & = & R_b - qR_a \end{array} \tag{3.44}$$

where

$$\begin{array}{lcl} R_a & = & u\frac{(u^2-Q^2)(u^2+5v)}{2q^2v^3} + u\frac{Q^2}{q^2v^2} \\ R_b & = & \frac{2}{Q} + \frac{u}{v}(1-2\frac{2}{q}) \\ R_c & = & \frac{u}{vq}(\frac{u^2-Q^2}{rq} - 2) \end{array} \tag{3.45}$$

and

$$\begin{aligned} q &= x x_1 (1-\mu) \\ Q^2 &= x^2 + x_1^2 - 2 x x_1 \mu \\ u &= a_1 - a \\ v &= a a_1 \\ r &= \frac{1+\mu}{1-\mu} \\ a^2 &= (\chi - x)^2 + r \\ a_1^2 &= (\chi + x_1)^2 + r \end{aligned} \tag{3.46}$$

The resulting scattering matrix for Comptonization is thus valid for non-relativistic and relativistic electron speeds, taking into account a high accuracy scattering cross section and an overall agreement with experiences superior to 99 % (Pozdnyakov et al. 1983). However, the Macdonald function $K2$ is extremely heavy to compute, especially if it has to be done for each scattering event. Thus, depending on the waveband, the Compton scattering matrix, based on the Rayleigh mechanism, is the most used by the community as it is a correct approximation.

3.2.5 Mie scattering

We saw that scattering events by small particles with dimensions smaller than the incident photon wavelength are called Rayleigh scattering. In the case of spherical particles of the same or larger size than the wavelength, Rayleigh scattering does not hold anymore and one must take into account another scattering mechanism. Based on Maxwell's equations, Mie (1908) was the first to elaborate a scattering mechanism for scattering off spheres immersed in an isotropic medium, having a homogeneous refractive index and dimensions in the range of the incoming wavelength, a mechanism lately known as *Mie scattering*. Mie scattering, sometimes also refereed as the Lorentz-Mie solution, received numerous and valuable contributions by Debye (1909) and is used in connection with polarization (Perrin 1942; Perrin & Abragam 1951) to characterize a media filled with heavy grains. Mie scattering is particularly relevant in astrophysics as it helps to probe the composition of the ISM and IGM (Gupta et al. 2005), as well as the dusty regions around celestial objects, from protostellar clouds (Daniel 1980) to AGN (Nenkova et al. 2008b,a).

Mie theory studies the problem of scattering of dust particles using spherical series (i.e. infinite sums of spherical harmonics[6]). Knowing that Mie scattering is independent of the light intensity and of the exact nature of the particle, its scattering cross section can be expressed such as:

$$\sigma = \frac{10\pi}{3} a^2 (ak)^4 \tag{3.47}$$

with a the radius of the spherical particle and k the wavenumber of the incident, plane electromagnetic wave ($k = 2\pi/\lambda = \omega^2$). When $\lambda << \mathrm{a}$, $\sigma \sim \lambda^{-4}$, which is the signature of Rayleigh scattering. If $\lambda \geq \mathrm{a}$, then the dominant factor is the grain size a. The grain size is also used to defined the grain size parameter x:

$$x = \frac{2\pi N a}{\lambda} \tag{3.48}$$

[6] Spherical harmonics are particular harmonic functions, characterized by a null Laplacian and used to solve rotational-invariant problems.

with N is the refractive index of the medium surrounding the particles. The grain size parameter is predominantly used to characterize the dust grain models (Stratton & Chu 1941a,b).

Defining θ as the usual angle between the incident and scattered photon, knowing that the scattering mechanism is cylindrically symmetric along the axis given by $\theta = 0$, the scattering phase function becomes:

$$\frac{\mathrm{d}\sigma}{\mathrm{d}\Omega}(\theta) = a^2(ka)^4 \left[\frac{5}{8}(1+\cos^2(\theta)) + \cos(\theta)\right] \tag{3.49}$$

One can see that the favored scattering angle is given by $\theta = 0$, where the scattering phase function is maximal, implying that forward scattering is the preferred reprocessing direction.

The polarization properties of a scattered radiation on a dust grain were studied by numerous authors using different formalisms (Perrin 1942; Perrin & Abragam 1951; Bohren & Huffman 1983; Wolf 2003). From a general point of view and in accordance with the Stokes formalism, there are linear relations between the incident (i) and scattered (o) parameters of the Stokes vector:

$$\begin{bmatrix} I_o \\ Q_o \\ U_o \\ V_o \end{bmatrix} = \begin{bmatrix} a_1 & b_1 & -b_3 & b_3 \\ b_1 & a_2 & -b_4 & b_6 \\ b_3 & b_4 & a_3 & b_2 \\ b_5 & b_6 & -b_2 & a_4 \end{bmatrix} \begin{bmatrix} I_i \\ Q_i \\ U_i \\ V_i \end{bmatrix} \tag{3.50}$$

In the case of an ideal, homogeneous, isotropic medium filled with dust grains, if there system is symmetric with respect to any central point, the grains have no rotational capabilities and the coefficients b_3, b_4, b_5 and b_6 are equal to 0. For a dust prescription with identical particles $a_1 = a_2$, $a_3 = a_4$ and a_1^2 - (a_3^2+b_1^2+b_2^2) = 0. However, if the dust model includes dust grains with different sizes and composition (such as graphite and silicate), the scattering and extinction properties must be integrated. The parameter d is used to characterize the inhomogeneity of the medium:

$$d^2 = \frac{a_1^2 - (a_3^2 + b_1^2 + b_2^2)}{a_1^2} \tag{3.51}$$

In a Mueller formalism, the scattering matrix can be expressed as:

$$\widehat{R}(\theta) = \begin{pmatrix} S_{11} & S_{12} & 0 & 0 \\ S_{21} & S_{22} & 0 & 0 \\ 0 & 0 & S_{33} & S_{34} \\ 0 & 0 & S_{43} & S_{44} \end{pmatrix} \tag{3.52}$$

with $S_{11} = S_{22}$, $S_{12} = S_{21}$, S_{34} = -S_{43} and $S_{33} = S_{44}$ for scattering off isotropic, homogeneous, dielectric spheres.

Denoting the abundances of the various dust components by a row of constants g_l with l = 1, 2, 3 ...n and $\sum_{l=0}^{n} g_l = 0$, σ_{ext} as the extinction cross section and σ_{sca} as the scattering cross section, the integrated absorption and scattering properties of the dust prescription are:

$$\langle \sigma_{ext} \rangle = \frac{1}{K} \sum_{l=0}^{l_{max}} \int_{a_{min}}^{a_{max}} g_l \; \sigma_{ext} \; a^s \; \mathrm{d}a \tag{3.53}$$

$$\langle albedo \rangle = \frac{1}{K} \sum_{l=0}^{l_{max}} \int_{a_{min}}^{a_{max}} albedo\ \sigma_{ext}\ a^s\ \mathrm{d}a \tag{3.54}$$

$$\langle S_{11} \rangle = \langle S_{22} \rangle = \frac{1}{K} \sum_{l=0}^{l_{max}} \int_{a_{min}}^{a_{max}} S_{11}\ \sigma_{ext}\ a^s\ \mathrm{d}a \tag{3.55}$$

$$\langle S_{12} \rangle = \frac{1}{K} \sum_{l=0}^{l_{max}} \int_{a_{min}}^{a_{max}} S_{12}\ \sigma_{ext}\ a^s\ \mathrm{d}a \tag{3.56}$$

$$\langle S_{33} \rangle = \frac{1}{K} \sum_{l=0}^{l_{max}} \int_{a_{min}}^{a_{max}} S_{33}\ \sigma_{ext}\ a^s\ \mathrm{d}a \tag{3.57}$$

$$\langle S_{44} \rangle = \frac{1}{K} \sum_{l=0}^{l_{max}} \int_{a_{min}}^{a_{max}} S_{44}\ \sigma_{ext}\ a^s\ \mathrm{d}a \tag{3.58}$$

with s the grain size index, the albedo defined as the ratio between σ_{sca} and σ_{ext} and K a normalization constant such as:

$$K = \int_{a_{min}}^{a_{max}} a^s\ \mathrm{d}a \tag{3.59}$$

Mie scattering on dust particles absorbs a large fraction of the incoming radiation, depending on the albedo. The dust grains are then heated and will relax their energy in a longer wavelength domain, usually the infrared in form of a thermal, unpolarized emission. Such emission is important to study obscuring regions such as the circumnuclear matter around the inner core of AGN as the radiation properties hold the signature of the dust prescription.

3.2.6 Dichroic extinction

Mie scattering describes the interaction of light with an ideal model of spherical dust grains, but reality is much more unsymmetrical. In fact, an ovoidal grain can be characterized by its parallel and perpendicular symmetry axis to which two distinct absorption cross sections can be attributed along the particle vertical and horizontal planes. And if the dust grains are immersed in a magnetic environment, they statistically align along the magnetic fields[7] . Aligned non-spherical grains produce scattered polarization signatures in optical wavelengths and polarized emission in far-IR wavelengths by a mechanism called *dichroic extinction*.

Dichroic extinction is the selective attenuation of different components of the electric vector when radiation passes through a medium filled with dust-aligned grains. When a magnetic field is present, the grains align with their short axes parallel to the field (Roberge 1996). As light traverses these aligned grains, the component of the electric vector parallel to the long axis of the grains is preferentially absorbed, which gives a net polarization parallel to the magnetic field direction; then the Q parameter of the Stokes vector changes in the frame of the magnetic field. If the photon is already carrying a non-null U parameter, the V component is also altered, a phenomenon called

[7] Alignment by magnetic fields is the most common process but radiation or stellar winds can also align the dust grain without invoking any magnetic force (Wood 1997).

birefringence. Dichroic extinction is thought to be responsible for the large[8] circular polarization levels measured in some proto-stars (from 1 % to 17 %, Lonsdale et al. 1980; Chrysostomou et al. 1996, 1997, 2000) as well as for the interstellar polarization observed toward many stars in our Galaxy (Mathewson & Ford 1970a). It has been used also to map out the magnetic field of the Milky Way and other galaxies (Mathewson & Ford 1970b; Wood 1997).

The scattering properties of aligned grains have been less well studied than spherical mixtures because of the complexity of the problem. The scattering phase functions are complicated to calculate and are not amenable to simple analytic radiative transfer solutions (Whitney & Wolff 2002). Recent theoretical and computational advances in the calculation of the scattering phase functions from non-spherical grains start to allow numerical simulation of dichroic extinction by radiative transfer. In particular, Mishchenko et al. (2000) have considerably improved the T-Matrix[9] computational method (Waterman 1965).

The analytical solutions to the simplest case of radiative transfer in the forward-scattering direction, in the presence of a constant particle density, with no light scattered into the beam, is given by:

$$\frac{\mathrm{d}}{\mathrm{d}s}\begin{bmatrix} I \\ Q \\ U \\ V \end{bmatrix} = n(s)\begin{pmatrix} \sigma_{11}(s) & \sigma_{12}(s) & \sigma_{13}(s) & \sigma_{14}(s) \\ \sigma_{21}(s) & \sigma_{22}(s) & \sigma_{23}(s) & \sigma_{24}(s) \\ \sigma_{31}(s) & \sigma_{32}(s) & \sigma_{33}(s) & \sigma_{34}(s) \\ \sigma_{41}(s) & \sigma_{42}(s) & \sigma_{43}(s) & \sigma_{44}(s) \end{pmatrix}\begin{bmatrix} I \\ Q \\ U \\ V \end{bmatrix} \tag{3.60}$$

where s is the spatial dimension along the photon path, $n(s)$ is the particle density, and $\sigma_{ij}(s)$ are the forward-scattering cross section components for the relevant Stokes vector elements.

According to Martin (1974) and Mishchenko (1991), the extinction matrix can be simplified such as

$$\frac{\mathrm{d}}{\mathrm{d}s}\begin{bmatrix} I \\ Q \\ U \\ V \end{bmatrix} = n(s)\begin{pmatrix} C_{ext} & C_{lpol} & 0 & 0 \\ C_{lpol} & C_{ext} & 0 & 0 \\ 0 & 0 & C_{ext} & C_{cpol} \\ 0 & 0 & -C_{cpol} & C_{ext} \end{pmatrix}\begin{bmatrix} I \\ Q \\ U \\ V \end{bmatrix} \tag{3.61}$$

only if the particles are axisymmetrical (which is the case if ovoidal grains are considered). C_{ext}, C_{lpol}, and C_{cpol} are the extinction, linear polarization, and circular polarization cross sections, respectively. Assuming constant particle properties and densities along the spatial dimension s, the previous equation can be decomposed in two sets of independent equations:

$$\frac{\mathrm{d}}{\mathrm{d}s}\begin{bmatrix} I \\ Q \end{bmatrix} = n(s)\begin{pmatrix} C_{ext} & C_{lpol} \\ C_{lpol} & C_{ext} \end{pmatrix}\begin{bmatrix} I \\ Q \end{bmatrix} \tag{3.62}$$

$$\frac{\mathrm{d}}{\mathrm{d}s}\begin{bmatrix} U \\ V \end{bmatrix} = n(s)\begin{pmatrix} C_{ext} & C_{cpol} \\ -C_{cpol} & C_{ext} \end{pmatrix}\begin{bmatrix} U \\ V \end{bmatrix} \tag{3.63}$$

[8] Randomly oriented or spherical grains produce only very small amounts of circular polarization (usually much less than 1 %), even in the most favorable scattering geometries (Shafter & Jura 1980; Fischer et al. 1994, 1996; and Marin et al. in prep.).

[9] Also known as the "extended boundary technique method" or the "null field technique", the T-Matrix method computes the scattering matrix elements evaluated by matching boundary conditions for solutions of Maxwell equations.

that can be solved using a simple substitution scheme with A = I + Q, B = I - Q for Eq. (3.62):

$$\begin{pmatrix} I+Q \\ I-Q \end{pmatrix} = \begin{Bmatrix} (I'+Q')e^{-ns(C_{ext}-C_{cpol})} \\ (I'-Q')e^{-ns(C_{ext}-C_{cpol})} \end{Bmatrix} \tag{3.64}$$

and a routine eigen problem for Eq. (3.63) (Whitney & Wolff 2002):

$$\begin{pmatrix} U \\ V \end{pmatrix} = e^{-nsC_{ext}} \begin{Bmatrix} U'\cos(nsC_{cpol}) - V'\sin(nsC_{cpol}) \\ U'\sin(nsC_{cpol}) + V'\cos(nsC_{cpol}) \end{Bmatrix} \tag{3.65}$$

This solution for radiative transfer calculation of the dichroic extinction in the forward-scattering direction is applicable to the case of a distribution of grain sizes and multiple grain populations, where $\sigma_{ij}(s)$ are obtain by integration/summation of the concerned parameter (size, albedo, dust component ...). The above equations also work for an orientation-averaging of the dust mixture alignment.

3.2.7 Resonant scattering

The Thomson scattering mechanism comes into play if a free electron scatters the incoming radiation ($\omega >> \omega_0$); if it is a bound electron, the Rayleigh mechanism is favored ($\omega << \omega_0$). A special case appears when the incoming radiation has the same frequency ω as the classical oscillator ω_0: the system resonates. Its is the *resonant scattering* mechanism ($\omega \sim \omega_0$).

From the general scattering cross section defined for elastic scattering in the Thomson regime, focusing on low ω - ω_0 order terms, and remembering that Γ_{cl} is small in comparison with ω_0, the scattering cross section for resonant scattering becomes:

$$\sigma_\omega \simeq \frac{8\pi}{3} r_0^2 \frac{\omega_0^2}{4(\omega_0-\omega)^2+\Gamma_{cl}} \tag{3.66}$$

Knowing that

$$\Gamma_{cl} = \frac{2r_0}{3c}\omega_0^2 = \frac{4\pi}{3}\frac{r_0}{\lambda_0}\omega_0 \tag{3.67}$$

The resonant scattering cross section can be interpreted as:

$$\sigma_\omega \simeq \frac{3\lambda_0^2}{2\pi} \frac{\Gamma_{cl}^2/4}{(\omega_0-\omega)^2+\Gamma_{cl}^2/4} \tag{3.68}$$

which shows a Lorentzian shape.

Fig. 3.4 shows the expected Lorentzian variation of the scattering cross section around σ_ω. If the incoming photon has a frequency equals to $3\lambda_0^2/2\pi$, the resonance is particularly high, more than 18 times the Rayleigh scattering cross section. Quantum mechanical calculations give approximatively the same results for the scattering cross section if the line width of the peculiar transition is considered instead of Γ_{cl}.

In the quantum mechanics approach, the radiation absorption is quasi-immediately followed by the de-excitation of the new, superior energy level and a photon is emitted in a random direction,

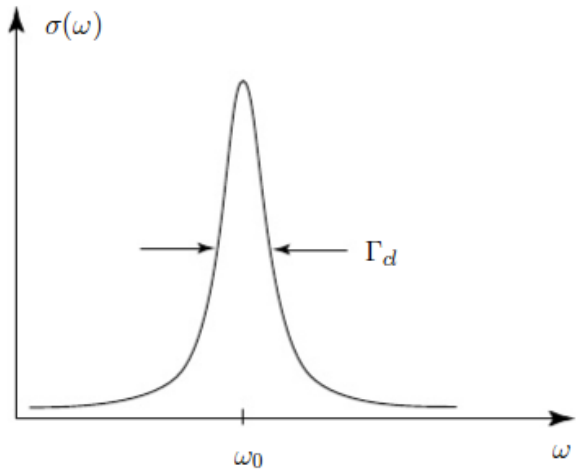

Figure 3.4: Schematic view of the scattering cross section of resonant scattering. In the optical waveband, the ratio ω_0/Γ_{cl} (the quality factor of the resonant scattering) is of the order 10^8. Those classical results hold well in a quantum description.

with the same frequency as the incoming radiation. If the excitation of the atom is due to external mechanisms (such as collisions), the situation is quite different from resonant scattering. Collisions may excite an atom to different energy levels, leading sometimes to a frequency shift, and they don't have the directivity specific to polarization processes. The scattering phase function as well as the polarization state and the emission probability of the re-emitted photon can be computed from quantum mechanics (Lee et al. 1994; Lee 1994). They strongly depend on the transition state between the ground and excited levels of the atom and can be estimated from the Clebsch-Gordon coefficients (Merzbacher 1961). Examples of Monte Carlo modeling of the polarization in quasars induced by resonant scattering can be found in Lee & Blandford (1997) and Wang et al. (2005, 2007)

3.2.8 Raman effect

Raman (1928), followed by Raman & Krishnan (1928b,a), discovered that the wavelength of a small fraction (approximately 1 in 10 millions) of the radiation scattered by certain molecules differs from that of the incident beam, and furthermore that the shifts in wavelength depend upon the chemical structure of the molecules responsible for the scattering. In fact, there is an energetic exchange between the molecule and the radiation that can produce either an emission line at the same frequency or emission lines at shifted frequencies. This is the *Raman effect* also known as the *Raman scattering* mechanism.

In order to understand the Raman effect, lets remind ourselves that for each bound between the atoms of a molecule vibrating at a frequency ν, a peculiar amount of molecular energy is associated: E_0, E_1, E_2 ... The difference between those energy levels is denoted ΔE. As the molecular vibration frequencies are very high (10^{12} – 10^{13} Hz), it is more common to use a quantity

called the wavenumber defined as $\nu = 1/\lambda$, where λ is the wavelength of the incoming radiation. ν is expressed in cm^{-1} and ν_{ex} coincides with the incoming radiation wavelength λ_{ex} that excites the system.

For a system in an equilibrium state, the Boltzmann distribution function allows to calculate the number of molecules characterized by their energy E_0, E_1, E_2, ... noted NE_0, NE_1, NE_2, ... They correspond to the population of the different energy levels. Using a Boltzmann factor, the ratio between two successive energy level may be expressed as:

$$\frac{NE_1}{NE_0} = e^{-\Delta E/k_B T} \tag{3.69}$$

It implies that the lowest energy level is the most populated and that its population decreases exponentially according to the energy level considered.

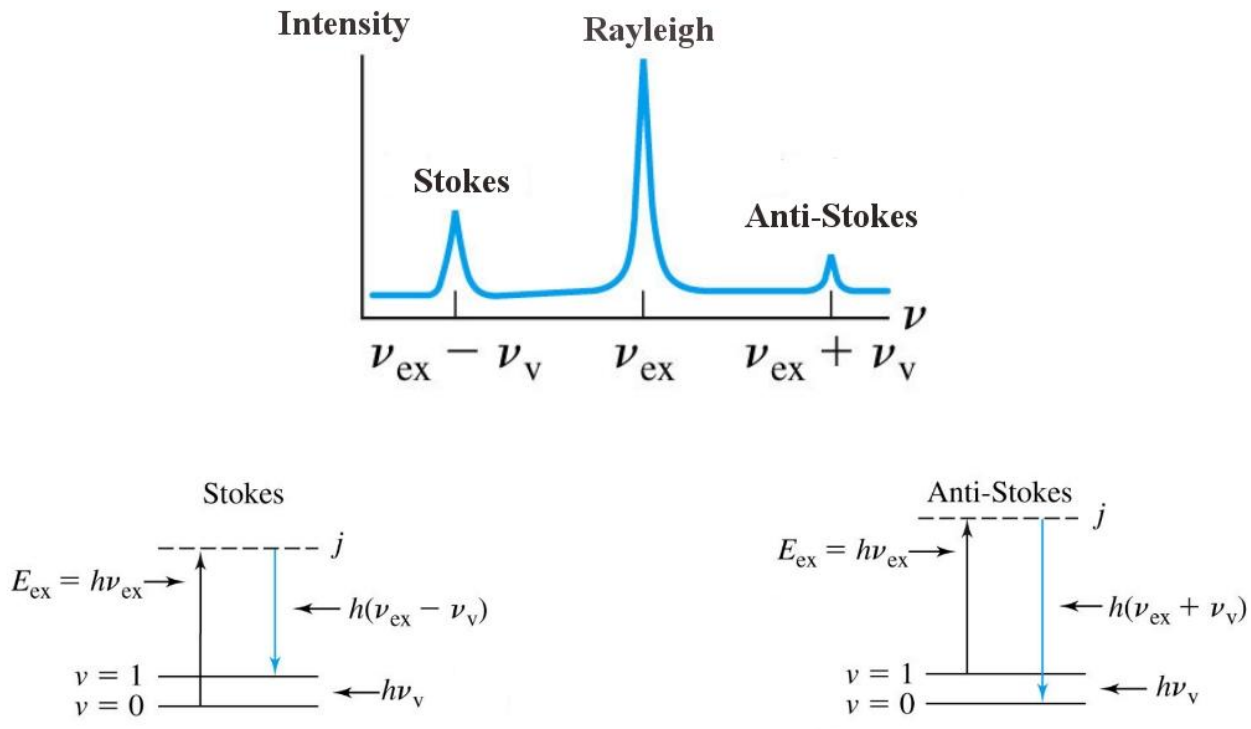

Figure 3.5: The complex behavior of a Raman scattering event. The central emitted line is due to the elastic Rayleigh mechanism while the left- and right-handed emission lines (also called Stokes and anti-Stokes lines respectively) are due to the inelastic resonance mechanism happening in the microscopic scales.

Now, lets consider an incoming radiation with a frequency ν_{ex} scattering on the atoms and molecules of the medium. According to Sect. 3.2.2, an elastic Rayleigh mechanism should occur and the scattered photon will be re-emitted with the same frequency ν_{ex}. From a quantum point of view, the incoming radiation may vary the vibrational quanta of energy of the reprocessing

molecule, and excites an electron. If the excited electron comes back to the initial energy level, a photon with the same frequency ν_{ex} is re-emitted: it is the expected Rayleigh process. However, if the electron goes to an energy level superior to the initial one, it emits a radiation with a shorter wavelength than of the incoming photon ($E_1 < E_0$ and $\Delta E < 0$); it is a rare phenomenon called (*Raman*) *Stokes scattering*. Even more rarely, if the electron goes to an energy level inferior to the initial one, it emits a radiation with a longer wavelength than of the incoming photon ($E_0 < E_1$ and $\Delta E > 0$); it is called a (*Raman*) $Anti - Stokes\ scattering$. The relative populations of the two upper energy states are such that Stokes emission is much favored over Anti-Stokes. Rayleigh scattering has a considerably higher probability of occurring than Raman because the most probable event is the energy transfer to molecules in the ground state and reemission by the return of these molecules to the ground state. The ratio of anti-Stokes to Stokes intensities increases with temperature because a larger fraction of the molecules will be in the first vibrationally excited state under these circumstances. At the very most, the intensities of Raman lines are 0.001 % of the intensity of the source. Figure 3.5 summarizes the Raman effect; the abscissa of Raman spectrum is the wavenumber shift $\Delta\nu$, which is defined as the difference in wavenumbers between the observed radiation and that of the source.

The Raman cross section and wavelength shift depend on the atoms or molecules filling the scatter medium. Empirical tables can be found on the literature and examples are given in Table 3.2.8 for common species in the astrophysical domain. A Rayleigh treatment of the reprocessing events can be a good first approximation for the outgoing photons polarization state. However, a small depolarization ratio (intensity ratio between the perpendicular and the parallel component of the scattered light) exists and must be measured from laboratory experiment too.

Molecule	Raman shift (cm^{-1})	Scattering phase function (10^{-30} cm/sr)
N_2	2331	1
O_2	1556	1.41
C_2	1832	-
CN	2045	-
CO	2145	1.04
CH	2633	-
NH	3048	-
HCN	3311	-
H_2O	3652	1.96
OH	3665	-
H_2	4160	1.85

Table 3.1: Raman shifts and scattering phase functions for different molecules at λ_{5320} Å (Carlson & Fenner 1972 and reference therein).

3.2.9 Bremsstrahlung

The classical theory of electromagnetism predicts that if a particle of mass m and charge z passes in the vicinity of the electric field of a nucleus of charge Z, it is deflected from its original path

and slowed down. The energy given away by the particle results in the emission of electromagnetic radiation with a continuous spectrum, called a *bremsstrahlung* spectrum.

The energy carried by the escaping radiation is defined by the energy loss ΔE_{br} such as:

$$\Delta E_{br} = \frac{z^2\ Z^2\ e^4}{m^2\ r^4} \tag{3.70}$$

with r the distance between the electron and the charged particle and e the elemental electron charge (see Fig 3.6).

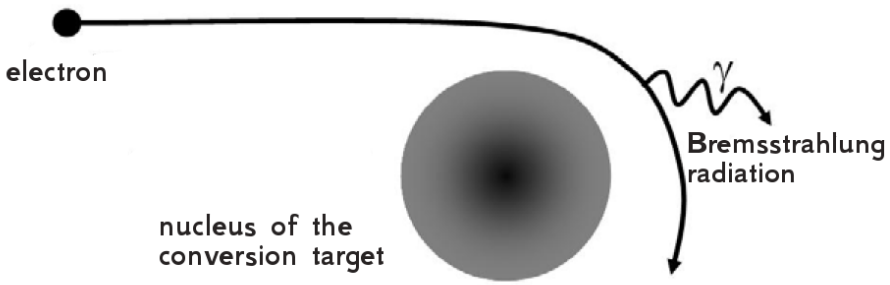

Figure 3.6: Schematic view of a bremsstrahlung process.

The bremsstrahlung cross section and the angular distribution of the emitted photons with respect to the incident electron can be expressed according to Koch & Motz (1959):

$$\mathrm{d}\sigma_{k,\theta} = \frac{4Z^2 r_0^2}{137}\frac{\mathrm{d}k}{k} y \mathrm{d}y \left(\frac{16y^2E}{(y^2+1)^4E_0} - \frac{(E_0+E)^2}{(y^2+1)^2E_0^2} + \left[\frac{E_0^2+E^2}{(y^2+1)^2E_0^2} - \frac{4y^2E}{(y^2+1)^4E_0} \right] \ln(M(y)) \right) \tag{3.71}$$

with k the photon energy, θ the emission angle with respect to the electron's direction of motion, E_0 and E the initial and final electron energy in units of $m_e c^2$, r_0 the classical electron radius and Z the atomic number of the material. y and $M(y)$ are defined as:

$$y = E_0\theta \tag{3.72}$$

and

$$\frac{1}{M(y)} = \left(\frac{k}{2E_0E}\right)^2 + \left(\frac{Z^{1/3}}{111(y^2+1)}\right)^2 \tag{3.73}$$

It is noteworthy to mention that bremsstrahlung radiation is generally polarized regardless of the polarization state of the incident electron. The interaction matrix (McMaster 1961) is given by:

$$\widehat{R}(\epsilon,k)=\frac{2Z^2}{137}r_0^2\frac{\mathrm{d}\xi}{\epsilon_1}\frac{\mathrm{d}k}{k}\begin{pmatrix} I & 0 & 0 & 0\\ D & 0 & 0 & 0\\ 0 & 0 & 0 & 0\\ 0 & -L & -T & 0\end{pmatrix} \tag{3.74}$$

where

$$\begin{aligned}
\xi &= \tfrac{1}{1+u^2}\\
u &= \text{component of the electron initial momentum perpendicular to the direction axis k}\\
\epsilon &= \text{total electron energy in units of } mc^2\\
k &= \text{total photon energy in units of } mc^2\\
I &= (\epsilon_1^2+\epsilon_2^2)(3+2\Gamma)-2\epsilon_1\epsilon_2(1+4u^2\xi^2\Gamma)\\
D &= 8\epsilon_1\epsilon_2u^2\xi^2\Gamma\\
L &= k[(\epsilon_1+\epsilon_2)(3+2\Gamma)-2\epsilon_2(1+4u^2\xi^2\Gamma)]\\
T &= 4k\epsilon_2(1-2\xi)\xi\Gamma\\
\epsilon_2 &= \epsilon_1-k
\end{aligned} \tag{3.75}$$

introducing Γ, containing the Coulomb and screening effects of surrounding, other electrons, such as:

$$\Gamma=\ln(\alpha)-2-f(Z) \tag{3.76}$$

with $f(Z)$ the Coulomb correction function of Davies et al. (1954) and α either equals to $2\epsilon_1\epsilon_2/k$ for no screening or equals to $111Z^{-1/3}/\xi$ for complete screening.

From the interaction matrix, the general Stokes vector for the emitted photon is found to be:

$$\begin{pmatrix} I\\ Q\\ U\\ V\end{pmatrix}=\begin{pmatrix} I\\ D\\ 0\\ -S_1L-S_2T\end{pmatrix} \tag{3.77}$$

where S_1 is the electron spin in the plane of interaction along the z axis and S_2 is the electron spin in the plane of interaction along the x axis. It shows that the bremsstrahlung radiation produced by an unpolarized beam of electrons is partially polarized perpendicular to the plane of interaction and that circularly polarized bremsstrahlung can only arise from a polarized electron.

3.2.10 Atomic recombination

When electrons and ions are confined in a hot[10] plasma, with electron temperatures exceeding 10^6 K, various collisional processes occur, primarily through electron-ion interactions. In addition to the major contribution of excitation and ionization collisional processes, recombination processes are important in determining the ionization equilibrium and the population of excited states in non-equilibrium plasmas. The *atomic radiative recombination* is the process where an incident free electron is captured by an ion of charge Z, considered at rest, to give a final ion of charge Z - 1

[10] Radiative recombination is also important in very cold, optically thin, ionized plasmas, such as the ones found in the ISM, old nova envelopes and supernovae remnants (Williams 1982; Ferland et al. 1984; Martin 1988), as it is supposed to contribute significantly to forbidden-line emission (Petitjean et al. 1990).

with the simultaneous emission of a recombination photon. Radiative recombination is the inverse process of photo-ionization, but they are usually treated in independent theoretical frameworks (Nahar 2000). Fig 3.7 shows the basic principle of photo-ionization and radiative recombination.

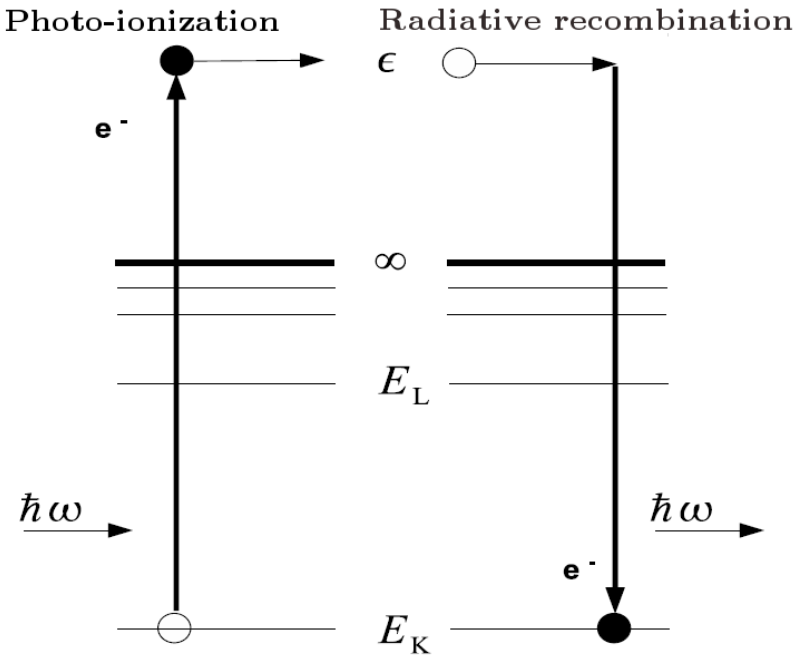

Figure 3.7: Schematic representation of the radiative recombination and its inverse mechanism, photo-ionization.

The radiative recombination cross-section can be obtained by non-relativistic dipole approximation (Hahn & Rule 1977) and fully relativistic treatments (Lee & Pratt 1975). For hydrogen-like ions one can write the photo-ionization cross section σ_{ph}:

$$\sigma_{ph} = \frac{64\pi}{3\sqrt{3}} \frac{n\xi b_0 g(E,n)}{Z^2} \left(\frac{I}{E}\right)^3 \tag{3.78}$$

with n is the principal quantum number, ξ the fine structure constant, b_0 the Bohr radius (b_0 = 5.29 $\times$ 10^{11} m), $g(E,n)$ the Gaunt factor (Karzas & Latter 1961), E the energy of the exciting electron and I the binding energy of the atomic shell from which the bound electron escapes. The above equation is also applicable to excited states of the atom, and is a good approximation for all excited atoms or ions where n is larger than the corresponding value for the valence electron. Using the Milne equation (Osterbrock 1989), it is easy to calculate the radiative recombination cross section σ_{rr} from the previous, inverse process equation:

$$\sigma_{rr}(\nu) = \frac{E^2 g_n \sigma_{ph}}{m_e^2 c^2 \nu^2} \tag{3.79}$$

where g_n is the statistical weight of the quantum level into which the electron is captured. If the radiative recombination cross section is averaged over a Maxwell distribution of electrons, the recombination coefficient R_n to level n can be obtained:

$$R_n = n_i n_e \int_0^\infty \nu f(\nu) \sigma_{rr}(\nu) \mathrm{d}\nu \tag{3.80}$$

with n_e the density of electrons, n_i the density of ions and $f(\nu)$ the Maxwellian distribution. Recombination coefficients are needed to study the ionization state of plasma departing from thermodynamic equilibrium. From the individual recombination coefficient, one can compute the total radiative recombination by summing the direct recombinations onto all atomic levels (Pequignot et al. 1991), allowing numerical simulations of the rate and intensity of the emitted photons.

Scofield (1989) derived the scattering phase function for polarized and unpolarized radiation:

$$\frac{\mathrm{d}\sigma}{\mathrm{d}\Omega} = \frac{\sigma}{4\pi} \left[\underbrace{\sum_{\lambda=0}^{\infty} B_\lambda P_\lambda \cos(\theta)}_{unpolarized\ component} - \underbrace{\sum_{\lambda=2}^{\infty} \lambda^{-1}(\lambda-1)^{-1} B_\lambda^\phi P_\lambda^{(2)} \cos(\theta)\cos(2\phi)}_{polarized\ component} \right] \tag{3.81}$$

where B_λ and $B_\lambda^{(2)}$ are the spherical Bessel functions, P_λ and $P_\lambda^{(2)}$ the Legendre functions, θ the polar angle and ϕ the azimuthal angle of the ejected photon. This scattering phase function is valid up to 100 keV, but can be simplified in the soft X-ray regime (around 1 keV):

$$\frac{\mathrm{d}\sigma}{\mathrm{d}\Omega} = \frac{\sigma}{4\pi}[1 - 2B_2 P_2 \cos(\alpha)] \tag{3.82}$$

with α the angle between the photon direction and polarization plane.

For directive incident electron beam, the polarization degree of radiative recombination can be obtained by the formula:

$$P(\theta) = \frac{\sum_{L_2=2}^{\infty} B_{L_2}(1,-1) D_{20}^{L_2}(\theta)}{\sum_{L_2=0}^{\infty} B_{L_2}(1,1) D_{00}^{L_2}(\theta)} \tag{3.83}$$

where θ is the angle between the electron momentum and the emitted photon momentum, D_{mu}^L is the rotational function, $B_{L_2}(\lambda,\lambda)$ a complex, quantum function (Wu et al. 2009) and λ, λ the two circular polarization directions of photons. Additional formulas can be found in the literature for the photon angular distribution and polarization for various helium-like ions with a non-relativistic approximation (Shen et al. 2007). Scofield (1989) calculated the photon angular- and polarization-dependent cross section for radiative recombination including contributions from multipoles and Surzhykov et al. (2001) re-investigate the radiative recombination and radiative electron capture of high-Z ions.

The topic or radiative recombination induced polarization is of a particular interest in media exposed to (non)radiative shocks, such as supernovae remnants (Laming 1990), but remains underexploited in comparisons with the previous polarization mechanisms presented so far.

3.2.11 Fluorescent emission

As seen from the previous sections, when photons scatter on atoms or molecules, they are absorbed and (lately) re-emitted in form of scattered radiations. However, when a highly energetic photon (such as X-ray radiation) scatters on an atom, its energy might be large enough to expel an electron from the inner electron shells, leaving a vacant electron position (photo-ionization). The atom is ionized and excited. As it is in an unstable state, the atom's electrons rearrange themselves to fill the gap with electronic transitions from the outer shells to the inner shells. As the physical process is exo-energetic, the atom releases the exceeding energy in terms of a UV photon if the energy transition is moderated or a X-ray photon for deeper, more energetic transitions. It is a *fluorescence emission*. It might also happen that the electronic rearrangement expels one, or more (electron cascades), electron lately called an Auger electron.

For the remainder of this paragraph, the fluorescence emission coming from transitions to the most energetic electron shell (K, with the shell index $n = 1$) is considered as an example[11] . Fig 3.8 resumes the possible radiative transmissions leading to the emission of a $K\alpha, \beta$ fluorescence photons. The most probable radiative de-excitation transition is the $2p \rightarrow 1s$ that correspond to the Kα transition between the L and K orbital angular momentum shells. This transition can be dived into two sub-transitions depending on the initial sub-shell L_2 or L_3. Those two transitions are the Kα_2 and Kα_1 emission lines respectively. The Kβ transition is associated to a transition of the kind $3p \rightarrow 1s$, thus from the M shell to the K shell. The shell transition $L_1 \rightarrow K$ is excluded from the quantum selection rules where only the transition verifying the conditions $\Delta l = \pm 1$ and $\Delta j = 0, \pm 1$ are allowed; where l and j are the orbital quantum number and the total kinetic momentum respectively.

When radiation scatters on an ionized atom (each atom has its own scattering cross section), the production of a fluorescence photon is governed by the fluorescence quantum yield that gives the efficiency of the fluorescence process. It is defined as the ratio of the number of photons emitted to the number of photons absorbed. The fluorescence yield is proportional to Z^4, with Z the atom's atomic number, so line emission is particularly high for Fe atoms and sharply decreases for lower Z-atoms. Such a behavior is confirmed by Kaastra & Mewe (1993)'s review on X-ray emission from thin plasma that gives all the fluorescence quantum yield and photon's emission wavelength necessary to include the fluorescence processes from Be to Zn ions[12] .

A particular aspect of the fluorescent emission is that the X-photons are emitted isotropically, in contrary to most of the radiative emission mechanisms. Plus, it is unpolarized if an atom is considered. However for molecules the re-emitted photon may hold an intrinsic polarization degree that dependents on the scattering molecule. But, as in the vicinity of AGN molecules can hardly survive, fluorescence emission principally impacts X-ray polarization spectra by locally decreasing the polarization degree at the emission line energies.

Now that the polarization principles and the different polarization/depolarization mechanisms

[11] Emission coming from the transitions to the L, M, N and O electron shells are also probable but results in less intense fluorescence lines, emitted at very different energies.

[12] Accurate fluorescence databases are only given for atoms with even atomic numbers Z. The reason is that nuclei with odd number of neutrons and odd number of protons tend to be less stable and thus are in minority in comparison with other, Z-even elements in any astrophysical media. Linearly interpolated fluorescence quantum yields for atoms with odd values of atomic number are given in Salem et al. (1974).

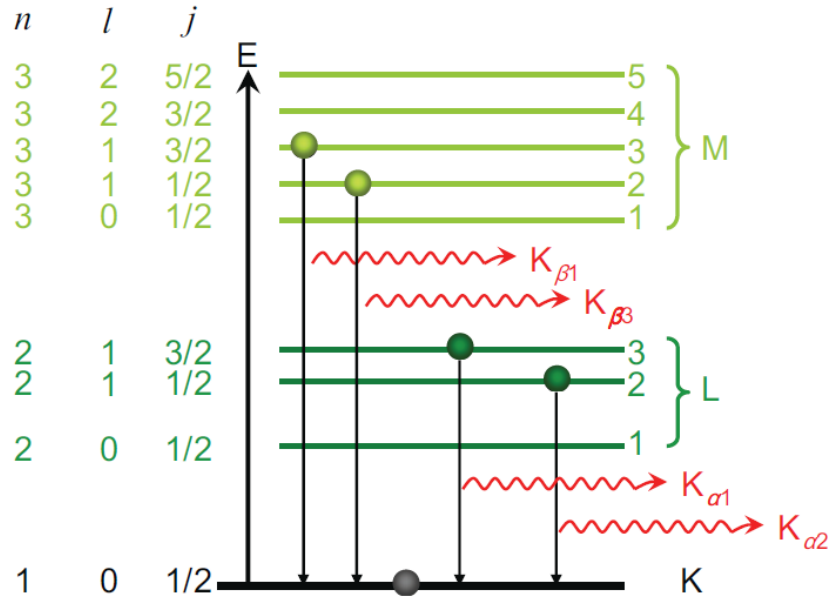

Figure 3.8: Possible radiative transitions to the K shell of an atom. The atom was previously ionized by an incoming, high energy photon.

are reminded, the last step is to generate photons in an AGN-like environment and follow the scattering-induced chaotic path of the radiation until it is absorbed or successfully escapes from the model.

3.3 STOKES: Radiative transfer and polarization

"*The computer program* STOKES *was designed to perform three-dimensional radiative transfer simulations for astronomical applications. A crucial requirement was that the code should also consider the polarization properties of the radiation. The program is based on the Monte-Carlo method and treats optical and ultraviolet polarization induced by scattering off free electrons or dust grains. Emission and scattering regions can be arranged in various geometries within the model space, the computed continuum and line spectra can be evaluated at different inclinations and azimuthal viewing angles.*"

Manual of STOKES v1.0

However, since the beginning of the thesis, STOKES has evolved. Following theoretical reminder notes on the radiative transfer and the Monte Carlo methods, the code possibilities offered on its very first released version is resumed and the improvements that led to a new public version of the code are subsequently presented. Further upgrades are examined in the last section of this chapter where the expected, forthcoming evolution of STOKES is detailed.

3.3.1 Radiative transfer

Radiative transfer is the branch of physics aimed to study the change in the properties of a light beam while it passes through a medium. It thus constitutes an important part of astrophysics since one of the few sources of information about celestial objects that we see comes from the light collected by telescopes. The study of radiative transfer allows us to establish the link between the microscopic interactions occurring between photons and atoms and the macroscopic properties of the objects studied in astrophysics. By comparing observed and simulated spectra it is possible to put constraints on the physical conditions (density, temperature, geometry, ...) prevailing in stars, galaxies or quasars.

In physics, the energy flux radiated by an extended source in a given direction, divided by the apparent area of the source in the same direction is called *Luminance*. The luminance L radiated in a time t by a source $P(\vec{r})$ in the direction $\vec{s}$ at a given frequency ν is given by:

$$L_\nu(\vec{r},\vec{s},t) = \frac{d^3\phi_\nu(\vec{r},t)}{(\vec{s}.\vec{n})dtd\Omega dS} \tag{3.84}$$

where $d\phi_\nu(\vec{r},t)$ is the monochromatic energy flux density radiated during the time dt through a surface dS oriented perpendicularly to $\vec{n}$ in a solid angle $d\Omega$. If we consider the source in a stationary state, the time-dependency might be omitted ($L_\nu(\vec{r},\vec{s},t) \rightarrow L_\nu(\vec{r},\vec{s})$). The luminance of the radiation source depends on the emission process: a black-body spectrum, a specific line emission or a power-law spectrum.

Let's now consider that the incident photon beam passes through a dense medium composed of spherical particles. The photons probably interact with the matter and three phenomena can occur (absorption, emission and scattering).

In radiative transfer theory, a semi-transparent medium is characterized by its capacity to absorb a certain amount of light $\mathrm{d}L_{\nu,a}$ coming from a luminance $L_\nu(\vec{r},\vec{s})$ along a particular distance $\mathrm{d}s$ such as:

$$\mathrm{d}L_{\nu,a}(\vec{r},\vec{s}) = -\sigma_{\nu,a}L_\nu(\vec{r},\vec{s})\mathrm{d}s \tag{3.85}$$

$\sigma_{\nu,a}$ being the absorption coefficient of the medium. As photons are absorbed, the luminance decreases, thus the minus sign.

From a corpuscular point of view, the luminance $L_\nu(\vec{r},\vec{s})$ can be associated with a photon flux N incoming with a frequency ν and passing through a portion $\mathrm{d}s$ of a medium filled with absorbing particles. The luminance variation $\mathrm{d}L_\nu(\vec{r},\vec{s})$ is thus related to the quantity of photons $\mathrm{d}N$ absorbed along the interval $\mathrm{d}s$. The absorption coefficient can be newly expressed such as:

$$\sigma_{\nu,a} = \frac{1}{\mathrm{d}s}\frac{\mathrm{d}N}{N} \tag{3.86}$$

Similarly, the same portion of medium $\mathrm{d}s$ also has the possibility to emit a certain amount of photons $\mathrm{d}L_{\nu,e}$:

$$\mathrm{d}L_{\nu,e}(\vec{r},\vec{s}) = +\sigma_{\nu,e}L_{b,\nu}(\vec{r},\vec{s})\mathrm{d}s \tag{3.87}$$

with $\sigma_{\nu,e}$ the emission coefficient of the medium at a given frequency, associated with a gain of photons and $L_{b,\nu}$ a luminance associated with the emission process.

If the system is at equilibrium (LTE[13]), then a same proportion of absorbed and emitted photons can be assumed, leading to $\sigma_{\nu,a} = \sigma_{\nu,e} = \sigma_\nu$.

The third characteristic phenomenon of thermal radiation is the phenomenon of photon scattering (if the luminance is represented using a corpuscular approach). It results in the deflection of the photon path as a consequence of shocks, when the incident flux is crossing of a thickness $\mathrm{d}s$ of a semi-transparent scattering medium. This results in a change of the luminance $\mathrm{d}L_{\nu,d}(\vec{r},\vec{s})$ according to the direction of propagation. One can discern two types of variation related to the phenomenon of scattering: a luminance gain by incoming scattering ($\mathrm{d}L_{\nu,in}(\vec{r},\vec{s})$) and the loss of luminance by outgoing scattering ($\mathrm{d}L_{\nu,out}(\vec{r},\vec{s})$). The global luminance variation linked with the scattering phenomenon is then:

$$\mathrm{d}L_{\nu,d}(\vec{r},\vec{s}) = \mathrm{d}L_{\nu,in}(\vec{r},\vec{s}) + \mathrm{d}L_{\nu,out}(\vec{r},\vec{s}) \tag{3.88}$$

A scattering coefficient $\sigma_{\nu,d}$ is associated with outgoing scatterings such as:

$$\mathrm{d}L_{\nu,out}(\vec{r},\vec{s}) = -\sigma_{\nu,d} L_\nu(\vec{r},\vec{s})\mathrm{d}s \tag{3.89}$$

and the incoming scattering radiation as to be integrated over the whole luminance directions $\vec{s'}$ deviated along $\vec{s}$:

$$\mathrm{d}L_{\nu,in}(\vec{r},\vec{s}) = +\sigma_{\nu,d}\left[\frac{1}{4\pi}\int_0^\infty\int_0^{4\pi}\Phi(\vec{s'},\vec{s},\nu',\nu)L_{\nu'}(\vec{s'})\mathrm{d}\Omega'\mathrm{d}\nu'\right]\mathrm{d}s \tag{3.90}$$

where $\mathrm{d}\Omega$ defines a solid angle fraction from which the luminance obtained by the incoming scattering can emerge. $\Phi(\vec{s'},\vec{s},\nu',\nu)$ is the scattering phase function and represents the probability density that a radiation coming from a direction $\vec{s'}$ with a wavelength ν' is scattered along the direction $\vec{s}$ with a shifted wavelength ν. In the case of non-relativistic, elastic collision, the frequency shift can be neglected ($\Phi(\vec{s'},\vec{s},\nu',\nu)$ becomes $\Phi(\vec{s'},\vec{s})$).

In order to obtain the standard integro-differential radiative transfer equation, taking into account the complexity of the physical problem (emission, absorption, scattering and frequency dependence), the total variation of the luminance passing through a semi-transparent medium with a thickness $\mathrm{d}s$ around the position r in the direction $\mathrm{d}s$ must be written. It is obtained by summing the terms related to each of the three phenomena encountered in radiation propagation and previously defined:

$$\begin{aligned}\mathrm{d}L_\nu(\vec{r},\vec{s}) &= \mathrm{d}L_{\nu,a}(\vec{r},\vec{s}) + \mathrm{d}L_{\nu,e}(\vec{r},\vec{s}) + \mathrm{d}L_{\nu,d}(\vec{r},\vec{s}) \\ &= -\sigma_{\nu,a}L_\nu(\vec{r},\vec{s})\mathrm{d}s + \sigma_{\nu,e}L_{b,\nu}(\vec{r},\vec{s})\mathrm{d}s - \sigma_{\nu,d}L_\nu(\vec{r},\vec{s})\mathrm{d}s \\ &\quad +\sigma_{\nu,d}\left[\frac{1}{4\pi}\int_0^\infty\int_0^{4\pi}\Phi(\vec{s'},\vec{s},\nu,\nu')L_{\nu'}(\vec{s'})\mathrm{d}\Omega'\mathrm{d}\nu'\right]\mathrm{d}s\end{aligned} \tag{3.91}$$

If an elastic collision at the LTE is considered and the previous equation is divided by $\mathrm{d}s$, then:

[13] The Local Thermodynamic Equilibrium hypothesis assumes that the small subsystem studied is thermodynamically stable, even if the global system is unstable. This assumptions is based on the empirical fact that 1) the relaxation time of a system is proportional to the size of the system's volume and 2) the relaxation time of thermal phenomena are much longer than the relaxation time of mechanical phenomena (such as collisions).

$$\frac{\mathrm{d}L_\nu(\vec{r},\vec{s})}{\mathrm{d}s} = \left[\sigma_\nu L_{b,\nu}(\vec{r}) + \frac{\sigma_{\nu,d}}{4\pi}\int_0^{4\pi}\Phi(\vec{s'},\vec{s})L_\nu(\vec{r},\vec{s'})\mathrm{d}\Omega'\right] - (\sigma_\nu + \sigma_{\nu,d})L_\nu(\vec{r},\vec{s}) \tag{3.92}$$

Lets define an extinction coefficient β_ν representing the beam attenuation by out-coming scattering and absorbing particles as well as the system albedo κ_ν, both wavelength-dependent:

$$\beta_\nu = \sigma_\nu + \sigma_{\nu,d} \tag{3.93}$$

$$\kappa_\nu = \frac{\sigma_{\nu,d}}{\sigma_\nu + \sigma_{\nu,d}} \tag{3.94}$$

Then, equation (3.92) can be rewritten in the form:

$$\frac{\mathrm{d}L_\nu(\vec{r},\vec{s})}{\mathrm{d}s} = \beta_\nu(1-\kappa_\nu)L_{b,\nu}(\vec{r}) + \beta_\nu\frac{\kappa_\nu}{4\pi}\int_0^{4\pi}\Phi(\vec{s'},\vec{s})L_\nu(\vec{r},\vec{s'})\mathrm{d}\Omega' - \beta_\nu L_\nu(\vec{r},\vec{s}) \tag{3.95}$$

That can also be expressed in the form:

$$\boxed{\frac{\mathrm{d}L_\nu(\vec{r},\vec{s})}{\mathrm{d}s} = \beta_\nu(S_\nu(\vec{r},\vec{s}) - L_\nu(\vec{r},\vec{s}))} \tag{3.96}$$

with:

$$S_\nu(\vec{r},\vec{s}) = (1-\kappa_\nu)L_{b,\nu}(\vec{r}) + \frac{\kappa_\nu}{4\pi}\int_0^{4\pi}\Phi(\vec{s'},\vec{s})L_\nu(\vec{r},\vec{s'})\mathrm{d}\Omega' \tag{3.97}$$

If we consider that $L_\nu(\vec{r_0},\vec{s})$ is the luminance at the point $\vec{r_0}$, then the solution of the equation (3.96) can be integrated along the optical path $\vec{r_0} \to \vec{r}$:

$$\boxed{L_\nu(\vec{r},\vec{s}) = L_\nu(\vec{r_0},\vec{s})\Gamma_\nu(\vec{r_0}\to\vec{r}) + \int_{\vec{r_0}}^{\vec{r}} S_\nu(\vec{r},\vec{s})\frac{\partial\Gamma_\nu(\vec{r'}\to\vec{r})}{\partial\vec{r'}}\mathrm{d}\vec{r'}} \tag{3.98}$$

where $\Gamma_\nu(\vec{r'}\to\vec{r})$ is the transmittance term of a semi-transparent medium between two points of space $P(\vec{r'})$ and $P(\vec{r})$ obtained with

$$\Gamma_\nu(\vec{r'}\to\vec{r}) = e^{-\tau_\nu(\vec{r'}\to\vec{r})} \tag{3.99}$$

defining $\tau_\nu(\vec{r'}\to\vec{r})$ as the optical depth[14] , a dimensionless unit obtained by integrating:

$$\tau_\nu(\vec{r'}\to\vec{r}) = \int_{\vec{r'}}^{\vec{r}}\beta_\nu(x)\mathrm{d}x \tag{3.100}$$

Considering a portion of an homogeneous medium l such as $l = \parallel \vec{r} - \vec{r'} \parallel$, then β_ν does not depend anymore on x. The previous equation can be rewritten such as:

$$\tau_\nu(l) = \beta_\nu l \tag{3.101}$$

[14] An absorbing medium is defined as optically thick if $\tau_\nu > 1$ and optically thin if $\tau_\nu < 1$. Indeed, according to the exponential form of Eq. (3.99), only a third of the initial photons escapes the medium without being absorbed if $\tau_\nu = 1$.

So:

$$\Gamma_\nu(l) = e^{-\beta_\nu l} \tag{3.102}$$

Equations (3.96) and (3.98) are the differential and the integral formulation of the radiative transfer equation[15] , respectively. They govern the interaction between matter and radiation, taking into account the optical depth and albedo of the medium. The natural next step is to solve this radiative transfer equation.

3.3.2 The Monte Carlo method

Solving the radiative transfer equation is not straightforward. At least four methods can be found through the literature (Viskanta & Menguc 1987; Modest 1993): the differential, integral, statistic and hybrid methods.

The differential method resolves the differential equation (3.96) of the radiative transfer formulation, while the integral method solves the integral equation (3.98). The hybrid methods are combinations of differential, integral and statistic methods, adapted to specific needs. In STOKES, the radiative transfer equation is solved using the Monte Carlo statistical method[16] .

The Monte Carlo method can be roughly considered as an integration method. It allows a reformulation of the problem happening when solving the radiative transfer equation in its integral form (Whitney 2011). Indeed, one of the peculiar characteristics of the Monte Carlo method is to allow simultaneous modeling of the spatial, angular and energetic dependencies by adding integrals over the considered domains; a process that would generate substantial difficulties for all other methods. To solve multiple integrals, the Monte Carlo method aims to follow the radiative transfer of photons by generating a large number of random events, where the final system state is calculated at the end of the process by averaging the values obtained. A physical phenomenon is modeled, such as the trajectory of a photon from an emission source to an absorption/detection event by a sequence of random processes. Phenomena such as emission, absorption, scattering are represented by probabilistic laws governing the behavior of photons. Thus, each radiation has its own frequency and spatial coordinate that can evolve according to the scattering process.

The Monte Carlo method is the best suited to accurately model radiative transfer, using a large number of random events that finally tend to the exact solution. In addition, it enables the computation of the uncertainty associated with each result (the error bar being associated with the standard deviation). It is therefore considered as a reference method in the field of radiative transfer modeling.

Lets denote a random number ξ associated with a uniform distribution function over the interval [0, 1] such as:

[15] For completeness and further details about the radiative transfer equations, please refer to Chandrasekhar (1960), Lenoble (1985) and Osterbrock (1989).

[16] Historically, the Monte Carlo method was developed for war purposes by J. von Neumann and S. Ulam, members of the Manhattan Project. The code was designed to study the interaction of photons, electrons and neutrons to better understand the impact of a nuclear explosion. After the Second World War, the Monte Carlo method was publicly released by Metropolis & Ulam (1949).

$$P(\xi)\mathrm{d}\xi = \begin{cases} \mathrm{d}\xi & \text{if } 0 < \xi < 1 \\ 0 & \text{outside of the interval} \end{cases} \tag{3.103}$$

Once such a ξ number chosen, it is easy to obtain a random number from a distribution function $f(x)$ using a transformation method (Press et al. 1992; Kalos & Whitlock 2008): if $y \in \{x_{min}, x_{max}\}$ is a variable whose distribution function is $f(y)$, it is possible to determine a random value x_0 from such a distribution function by generating a random number ξ and solving the following equation:

$$\xi = P(x_0) = \frac{\int_{x_{min}}^{x_0} f(y)\mathrm{d}y}{\int_{x_{min}}^{x_{max}} f(y)\mathrm{d}y} \tag{3.104}$$

where the denominator is used to normalize the cumulative distribution function $\int_{x_{min}}^{x_0} f(y)\mathrm{d}y$ such as:

$$\int_{x_{min}}^{x_{max}} P(x_0)\mathrm{d}x_0 = \int_{x_{min}}^{x_{max}} \frac{\int_{x_{min}}^{x_0} f(y)\mathrm{d}y}{\int_{x_{min}}^{x_{max}} f(y)\mathrm{d}y}\mathrm{d}x_0 = 1 \tag{3.105}$$

As x_0 ranges from x_{min} to x_{max}, ξ ranges from 0 to 1 uniformly. Thus, to sample a random variable x_0, it is just needed to call a random number generator (RNG) that uniformly samples numbers between 0 and 1, and invert Eq. 3.104 to get x_0.

The function $f(y)$ can be, in the case of a radiative transfer code, the luminance function $L_\nu(\vec{r}, \vec{s})$ or the probability $P(\tau_\nu)$ that a photon of frequency ν travels an optical depth τ_ν without interacting:

$$P(\tau_\nu)\mathrm{d}\tau_\nu = e^{-\tau_\nu}\mathrm{d}\tau_\nu \tag{3.106}$$

Thus,

$$P(\tau_\nu) = \frac{\int_0^{\tau_{\nu,0}} e^{-\tau_\nu}\mathrm{d}\tau_\nu}{\int_0^{\infty} e^{-\tau_\nu}\mathrm{d}\tau_\nu} = 1 - e^{-\tau_{\nu,0}} = \eta \tag{3.107}$$

Inverting this equation gives:

$$\tau_{\nu,0} = \log(1 - \eta) \tag{3.108}$$

where η is the uniform random deviation returned from the RNG. However, it is sometimes nontrivial to invert an analytical formula and usual mathematical functions might not solve the problem. Plus, one has to be careful when generating random numbers. If the RNG repeats itself (i.e. for the same seed number it gives the same pseudo-random value, the RNG is looping back), the statistical dispersion of the results will be erroneous and the Monte Carlo method will need more time to converge, sometimes leading to falsified results. The usual C/C++ RNG (as well as most of the other generators included in any programming language) is sophisticated enough to be used in astrophysical calculations, but may loop back after a few million iterations. More efficient RNG might be needed to avoid sequence repetitions and thus decrease the level of Poisson noise.

3.3.3 Past - Overview of the code's first version

STOKES is a C/C++ Monte Carlo radiative transfer code created by Goosmann & Gaskell (2007) that includes a treatment of the polarization.

The first version, publicly released on 2004, is able to model an emission source in the center of a model-space, radiating photons according to a power-law of the form $F(\nu) \propto \nu^{-\alpha}$, with α the spectral index. For line emission, Lorentzian flux spectra with user-defined FWHM and intensity are assumed. The geometrical shape of the emitting region can be set as point-like, cylindrical or double conical. The initial photon flux is intrinsically unpolarized.

Around the central emitting region, several absorbing and reprocessing regions can be modeled according to toroidal, spherical or hourglass-shaped geometries. These regions can be filled with either electrons or a dust grain mixture consisting of silicate and graphite (the dust model can be easily adapted to ISM, IGM or exotic dust models by the user). A radial component of the velocity field can be included for all the regions, impacting the wavelength of the reprocessed photons.

The photons are isotropically generated and then travel through the model space, undergoing multiple scattering events. The path length of the photon inside a reprocessing region is calculated using the Monte Carlo method, similarly to electron and dust scattering events where the scattering phase functions are used as probability distribution functions. Thomson and Mie scattering algorithms, using Mueller matrices coupled to a Stokes vectorial representation of the polarization, govern the polarization state of the outgoing photon according to its initial state. Dust being highly photon-absorbing in the optical and UV ranges ($\sim$ 1400 - 10000 Å), a large fraction of the photons might be destroyed by the model, leading to time-demanding runs. When photons escape from the model, a web of virtual detectors arranged in a spherical geometry is used to record the photon wavelength, intensity and polarization state. The total intensity, polarization degree P and polarization angle ψ are computed by averaging all the detected photons, at each viewing direction in polar and azimuthal directions.

Until 2013, more than 20 papers (including refereed papers, conference notes and proceedings) based on STOKES were published.

3.3.4 Present - Improvements

One of the goals of this thesis was to improve STOKES in order to release a faster, more sophisticated version of the code. Two main upgrades are presented as they are related to the version 1.2 of STOKES: an improved RNG and an imaging method. However, much more has been done on the code but as it is linked with future versions of the radiative transfer program, they are only mentioned in Sect. 3.3.5.

• **Improved random number generator**. The standard deviation of a Monte Carlo calculation is usually proportional to the square root of the number of samples. In radiative transfer modeling, enough photons need to be sampled to suppress the Poisson noise with respect to significant spectral or polarization features. In many of the models that are shown in this thesis 10^9 photons or more were therefore sampled. The generation of such long series of random numbers may run into numerical problems. In STOKES 1.0 a linear congruential generator (LCG) was used,

which is fast and efficient only for short series. For the large sampling numbers that are typically applied in the complex modeling presented here, the LCG tends to loop back on series of values it has sampled before. Therefore in STOKES 1.2, a version of the Mersenne twister generator (MTG) algorithm (Matsumoto & Nishimura 1998) is implemented. The MTG generates pseudo-random numbers using a so-called twisted generalized feedback shift register. The most common version, MT 19937, has a very high period of $2^{19937} - 1$ and provides a 623-dimensional equidistribution up to an accuracy of 32 bits. The MTG is more efficient than most other random number generators and passes the "Diehard" tests described in Marsaglia (1985). A detailed analysis of the MTG is given in Matsumoto & Nishimura (1998) and references therein. Using the MTG in STOKES substantially improves the statistics for a given sampling number of photons. Although each call of the MTG requires 20% more computation time compared to the LCG, far fewer photons are needed to obtain the same limit on the Poissonian fluctuations. Therefore, there is a significant net gain in computation time and the results converge faster.

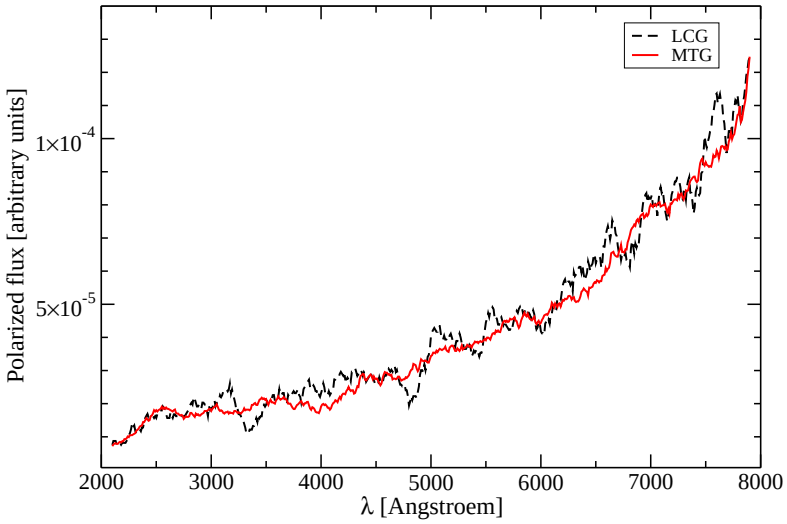

Figure 3.9: Modeling a central, isotropic source that irradiates a dusty, equatorial scattering torus with a half-opening angle of 30° (see text). The spectrum represents the polarized flux, PF/F_*, normalized to the source flux F_*, for a viewing angle of $i = 72°$. The spectra were calculated by sampling the same number of photons but using two different random number generators. *Black dashed line*: The LCG algorithm as implemented in STOKES 1.0; *red solid line*: The MTG algorithm as implemented in STOKES 1.2.

A comparison of both methods is shown in Fig.3.9. An AGN obscuring torus was modeled sampling a total of 3.10^8 photons, alternately using the LCG random number generating algorithm of STOKES 1.0 and the MTG algorithm implemented in STOKES 1.2. A large, dusty torus with an elliptical cross-section, constant density, and a V-band optical depth of $\tau_V \sim 600$ was assumed. The half-opening angle of the scattering region with respect to the symmetry axis of the torus equals

$\theta_0 = 30°$. The dust has a Milky Way composition (see section 4.2 of Goosmann & Gaskell (2007) for more details). This model illustrate the effects of the random number generator as the spectra suffer from heavy absorption and only multiply scattered photons escape from the funnel of the torus. As a result, the statistics at the particular viewing angle of $i = 72°$ tends to be low. Fig.3.9 shows that, for the same number of simulated photons, the simulation using the LCG algorithm suffers from much higher Poissonian noise. To obtain a curve as smooth as the one obtained with the MTG algorithm, LCG would have to generate a dozen times as many photons.

• **Polarization imaging**. To understand scattering by various regions in AGN it is very useful to be able to see polarization maps. These can also potentially be compared with future observations. With STOKES 1.2 it is now possible to generate polarization images. For this, each photon is spatially located before its escape from the modeling region and is projected onto the observer's plane of the sky. The resulting polarization maps can be compared to polarization imaging observations of spatially resolved objects. In unresolved objects, the model images can help to study the interplay of several scattering components.

The position of an escaping photon is projected onto a distant plane, D, which is orthogonal to the line of sight (Fig. 3.10). The photon position P is determined by its distance, r_p, from the origin O of the model space and by the two angles θ_p and ϕ_p. The center of the projection plane O' is connected to O by the segment OO', which determines the polar and azimuthal viewing angles ϕ and θ. The distance between O' and the projected photon position P' is denoted by the vector $\overrightarrow{\varrho}$. By expressing $\overrightarrow{\varrho}$ in the local frame of D, the projected photon coordinates x' and y' are obtained in the plane of the sky.

The unit vectors $\vec{e_p}$ and $\vec{e_i}$ are expressed in spherical coordinates:

$$\vec{e_p} = \begin{pmatrix} \sin\phi_p \sin\theta_p \\ -\cos\phi_p \sin\theta_p \\ \cos\theta_p \end{pmatrix} \tag{3.109}$$

$$\vec{e_i} = \begin{pmatrix} \sin\phi \sin i \\ -\cos\phi \sin i \\ \cos i \end{pmatrix} \tag{3.110}$$

while the unit vectors of the observer's plane of the sky can be written as:

$$\vec{e_{x'}} = \begin{pmatrix} \cos\phi \\ \sin\phi \\ 0 \end{pmatrix} \tag{3.111}$$

$$\vec{e_{y'}} = \begin{pmatrix} -\sin\phi \cos i \\ \cos\phi \cos i \\ \sin i \end{pmatrix} \tag{3.112}$$

The vector $\overrightarrow{\varrho} = r_p[\vec{e_p} - \cos\chi \vec{e_i}]$ is then constructed. To obtain its components in spherical coordinates, the following equations are needed:

$$\varrho_x = r_p[\sin\phi_p \sin\theta_p - \cos\chi \sin\phi \sin i] \tag{3.113}$$

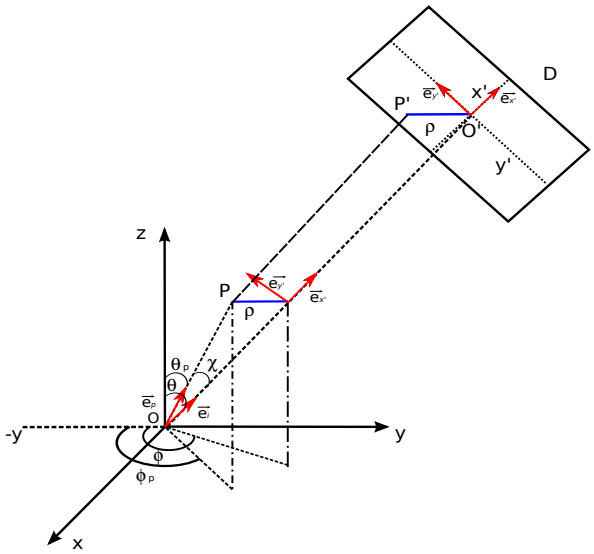

Figure 3.10: Spatial coordinates that determine the position of a photon P and its projection P' onto the plane of the sky, D.

$$\varrho_y = r_p[\cos\chi\cos\phi\sin i - \cos\phi_p\sin\theta_p] \tag{3.114}$$

$$\varrho_z = r_p[\cos\theta_p - \cos\chi\cos i] \tag{3.115}$$

with χ being the angle between $\vec{e_p}$ and $\vec{e_i}$. Using equations (3.111) and (3.112), obtain the projected coordinates $x' = \vec{\varrho}\vec{e_{x'}}$ and $y' = \vec{\varrho}\vec{e_{y'}}$ of the photon in the plane of the sky are obtained:

$$x' = -r_p\sin\theta_p\sin(\phi - \phi_p) \tag{3.116}$$

$$y' = r_p[\sin i\cos\theta_p - \cos i\sin\theta_p\cos(\phi - \phi_p)] \tag{3.117}$$

3.3.5 Future - Pushing forward the code's limits

STOKES is evolving faster than what can be published. While the version 1.2 is now on-line, much more improved versions of the code exist and are actually used to produce new scientific results. Among other features, the code is now able to compute polarization spectra in the X-ray range, from 0.8 to 300 keV, treating fluorescent emission lines of oxygen, carbon or iron. The Compton hump, due to reprocessing in low-temperature matter is properly reproduced. The temperature of the medium can be fixed by the user up to 10^9 K, while the Compton scattering matrix being

still properly computed using non-relativistic and relativistic Mueller matrices (Poutanen & Vilhu 1993; Nagirner & Poutanen 1993a,b). STOKES may be coupled to TITAN (Dumont et al. 2000) and KY (Dovčiak et al. 2004) to take into account any vertical structure of accretion disk models, with a wide range of ionization parameters, and a relativistic treatment of the photons traveling close to the potential well of a Kerr black hole. Moreover, the three components of the velocity-space are now working and are currently tested to reproduce the observed extremely asymmetric Balmer lines with the broad peak redshifted or blueshifted by thousands of $km \cdot s^{-1}$ (see Appendix D). Finally, non-axisymmetric emission and time dependency of the photon flux are implemented.

So far, the dust models of STOKES include extinction effects but no thermal re-emission after absorption of the UV/optical continuum. The inclusion of more sophisticated dust types and of dust emission in thermal or non-thermal equilibrium is a very useful next step (Draine & Weingartner 1997; Zubko & Laor 2000; Gordon et al. 2001; Misselt et al. 2001; Weingartner & Draine 2001). Adding thermal (re)emission processes emerging from complex dust distributions in STOKES will enable very robust and consistent polarization/thermal emission models to be developed for many objects from the UV to the IR bands. Plus, via the same method, it will also become possible to study the wider vicinity of an AGN. The impact of stellar clusters or star burst regions on the spectrum and polarization could be evaluated and help to improve spectroscopic methods distinguishing between AGN and stellar emission in the optical/UV. This will allow to verify past and future spectropolarimetry observations, in which the subtraction of the stellar component turns out to be ambivalent.

Furthermore, in order to understand the impact of a clumpy environment on the polarization signatures, distributions of constant-density spheres taking into account the covering and filling factors as external parameters will be implemented for torus and outflow geometries. The computation of a substantial grid of models is necessary to explore the impact of the size, density and composition of the clumps on the emerging spectral intensity and polarization as a function of the viewing directions. However the computation of large model grids or extensive modeling studies of an individual object require a fast computational method (Heymann & Siebenmorgen 2012). The computational speed of Monte-Carlo radiative transfer codes can be a problem when the reprocessing model becomes complex (this is the price to pay for the geometrical accuracy and the inclusion of multiple scattering effects). A forthcoming step will be to enable the STOKES code to also be run on GPUs (Graphic Processing Units). The GPU method is expected to make STOKES run faster than on CPUs (Central Processing Units) by a factor of at least 20.

Chapter 4

Polarization signature induced by multiple scattering in complex AGN models

In this section, we focus on polarization modeling of radio-quiet AGN that release the bulk of their radiated energy in the far UV/optical. Our goal is to infer clues about the geometry and composition of the different AGN components from the observed polarization properties. We assume that in thermal AGN the emission comes from an optically thick accretion disk (Lynden-Bell 1969b). Closely associated with the accretion disk, and situated at the outer edge of the accreted matter, is the BLR – a supposedly flattened region of high-density ($n_e \sim 10^{10}$ cm^{-3}), rapidly moving ($v \sim 0.05 - 0.001c$) gas which is optically thin in the continuum for $h\nu < 13.6$ eV (see Gaskell 2009, for a review).

Not all matter that spirals into the gravitational potential of the black hole becomes accreted. In many radio-quiet AGN strong winds are seen in the X-ray and UV spectrum (Mathur et al. 1994, 1995; Costantini 2010). Supposedly, these winds are expelled very close to the black hole and find a spatial continuation in the observed polar ionization cones. In some objects the outflowing gas can be seen as broad absorption lines (Weymann et al. 1991; Knigge et al. 2008). Immediately outside the BLR and accretion disk is the geometrically thick, dusty torus (but see Elvis 2000, 2004; Kazanas et al. 2012, and references therein for the interpretation of the equatorial obscuration as a wind). Finally, starting on a scale larger than the BLR and often extending to distances much greater than the size of the torus there is the lower-density, lower-velocity gas of the so-called "narrow-line region" (NLR).

The accretion flow at the outer accretion disk and the inner boundary of the torus funnel is difficult to assess observationally. At a distance of about a thousand gravitational radii from the black hole the accretion flow should become gravitationally unstable and become fragmented (see e.g. Lodato 2007). There are indications that the medium is continuous while being inhomogeneous in density (Elitzur 2007). In this context the interaction between the primary radiation from the accretion disk with the surrounding media causes scattering-induced polarization signatures. In a single electron- or dust-scattering event, the resulting polarization degree and position angle depend on the scattering angle (see Sect. 3.1), and therefore the resulting net polarization of the collective reprocessing in an AGN, when accurately modeled, allows us to draw conclusions about the geometry of the scattering regions. Some evidence for a flattened geometry of the matter just inside the torus comes from optical polarimetry. For many type-1 objects the $\vec{E}$-vector of the continuum radiation aligns with the projected axis of the (small-scale) radio structures (Antonucci 1982, 1983). Identifying the radio structures with collimated outflows progressing along the symmetry axis of the dusty torus (Sect. 2.2.6), such a polarization state is most easily explained by scattering in a flattened, equatorial scattering region (Antonucci 1984). The polarization state

of the radiation thus brings information about the reprocessing geometry. Based on an analysis of the polarization structure across broad emission lines, Smith et al. (2004) suggested that the equatorial scattering region may be partly intermixed with or lie slightly farther out than the BLR.

In the following subsections, we systematically examine the polarization response caused by combining different scattering regions. We built models of double-component AGN, i.e. FR I and LINERs-like galaxies (Sect. 4.2.1), "bare" (Sect. 4.2.2), or "naked" (Sect. 4.2.3) objects, to then present a multi-component model for thermal AGN and examine how the polarization spectra and images are influenced by the different AGN constituents.

4.1 Polarization signatures of individual reprocessing regions

In a model with multiple reprocessing components, theoretical polarization maps are very useful for understanding the impact of individual scattering regions. We first tested the new imaging routines of STOKES by reanalyzing some of the individual reprocessing regions presented in Goosmann & Gaskell (2007). For the remainder of this thesis, polarization is described as parallel when the $\vec{E}$-vector is aligned with the projected torus axis (polarization position angle $\psi = 90°$). Sometimes we denote the difference between parallel and perpendicular polarization by the sign of the polarization percentage, P: a negative value of P stands for parallel polarization, a positive P for perpendicular one. Finally, both the spectra and the maps show the total (linear plus circular) polarization, P. Due to dust scattering the V Stokes parameter can be nonzero, but in all our models the circular polarization was found to be a hundred times lower than the linear polarization and thus it does not have an impact on the polarization results. A proper investigation of the circular polarization emerging from our models is presented in Chap. 6.

4.1.1 Obscuring, dusty tori

The spectral properties of such a dusty scattering torus were presented in Section 4.2 of Goosmann & Gaskell (2007). For all models presented below we define an isotropic, point-like source emitting an unpolarized spectrum with a power-law spectral energy distribution $F_* \propto \nu^{-\alpha}$ and $\alpha = 1$ at the center of the torus. The inner and outer radii of the torus are set to 0.25 pc and 100 pc, respectively. The radial optical depth of τ_V measured inside the equatorial plane is taken to be ~ 750 in the V-band. The half-opening angle of the torus is set to $\theta_0 = 30°$ with respect to the vertical axis.

4.1.1.1 Wavelength-integrated polarization images

We sampled a total of 10^9 photons and modeled spectra and images at 20 polar viewing angles i and 40 azimuthal angles ϕ; i and ϕ are the viewing angles defined as in Fig. 3.10. The angle i is measured between the line of sight and the vertical z axis; ϕ is measured between the projection of the line of sight onto the xy-plane and the x axis. A fairly fine stratification in viewing angle is necessary to limit the image distortion that occurs preferentially at polar angles. The meshes of the coordinate grid have a different shape at the poles, where they are more trapezium-like, than at the equator, where they are almost square-like. The spectra are presented in terms of $\cos i$ providing an equal flux per angular bin for an isolated, isotropic source located at the center of the model space. Since the model is symmetric with respect to the torus axis, we averaged all Stokes parameters over ϕ and thereby improve the statistics. As in Fig. 4.2, we present imaging results at three different polar angles: $i \sim 18°$ (near to pole-on view), $i \sim 45°$ (intermediate viewing angle), and $i \sim 87°$

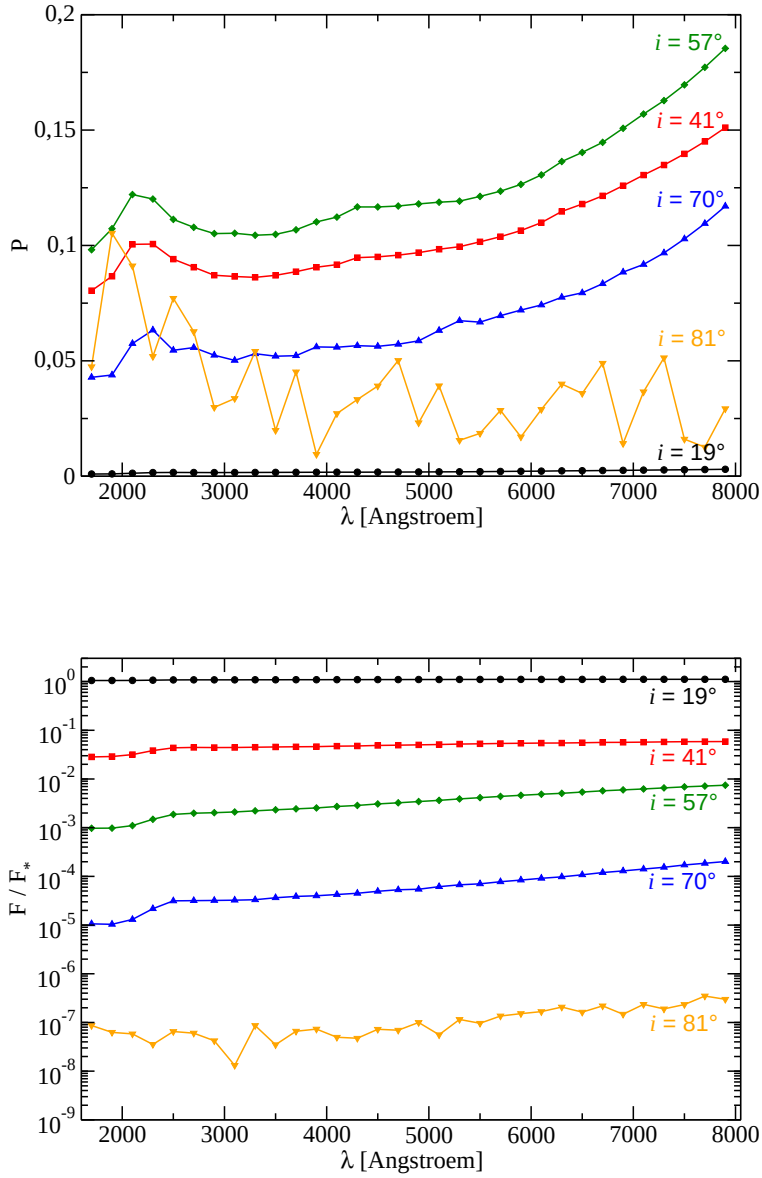

Figure 4.1: Modeling an optically thick elliptically shaped torus with $\theta_0 = 30°$ measured relative to the symmetry axis. The spatially integrated polarization P (upper panel) and the fraction F/F_* of the central flux (lower panel) are seen at different viewing inclinations, i.

(edge-on view). These lines of sight roughly represent AGN of type-1, of an intermediate type between type-1/type-2, and of type-2, respectively. We define a spatial resolution of 30 bins for the x' and y' axes so that the photon flux is recorded in 900 pixels. Each of these pixels is labeled by the coordinates x' and y' (in parsecs) and stores the spectra of the four Stokes parameters across a wavelength range of 1800 Å to 8000 Å. Ultimately, each pixel contains the same type of spectral

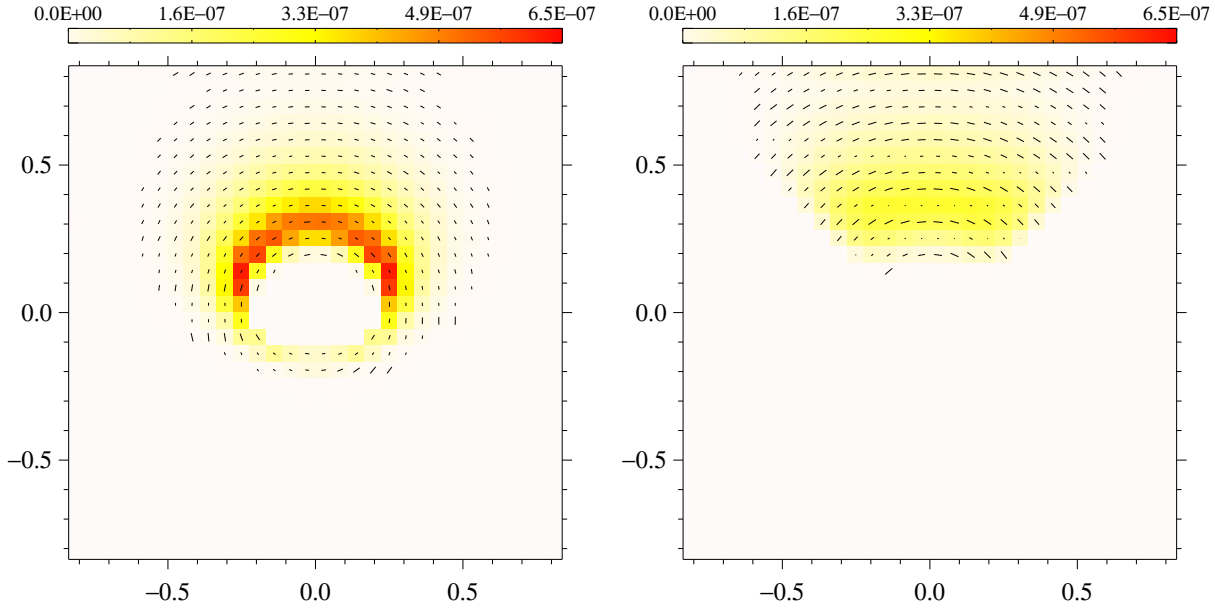

Figure 4.2: Model image of the polarized flux, PF/F_*, for a centrally irradiated optically thick, elliptically shaped torus with $\theta_0 = 30°$ measured relative to the symmetry axis; PF/F_* is color-coded and integrated over the 1800 – 8000 Å band. *Left*: face-on view at $i \sim 18°$; *right*: view at $i \sim 45°$.

information that is provided by the previous, nonimaging version of STOKES.

The polarization and flux spectra integrated over x' and y' are shown in Fig. 4.1. As expected, they agree with previous results (see section 4.2 and Fig. 6 of Goosmann & Gaskell (2007) for more details). The polarization images are shown in Fig. 4.2. Because the torus is very extended, we zoomed in on the imaging and analyzed specifically the torus funnel from which the most scattered radiation emerges. The maps simultaneously show the polarized flux, PF/F_*, the polarization position angle, ψ, and the percentage of polarization, P; ψ and P are represented by black vectors drawn in the center of each spatial bin. A vertical vector indicates a polarization of $\psi = 90°$, a slash to the right denotes $90° > \psi > 0°$, and a horizontal vector stands for an angle of $\psi = 0°$. The length of the vector is proportional to P. The Stokes parameters are integrated over all wavelengths and all azimuthal viewing angles ϕ. Note that in all images the polarized flux PF/F_* is normalized to the central flux F_* that is emitted into the same viewing direction.

When the torus is seen pole-on (Fig. 4.2 left, $i \sim 18°$), most of the polarized flux comes from its inner edge, which is most exposed to the source. The medium is optically thick, and therefore the scattering occurs mainly close to the surface of the scattering region. The unpolarized light from the source has a depolarizing effect and so does the spatial distribution of the inner edge of the torus, which is almost symmetric with respect to the line of sight. As our pole-on viewing angle $i = 18°$ is effectively off-axis (different from $i = 0°$), the shape of the scattering region is slightly deformed in the projection process and does not appear axis-symmetric. Also, due to the slight inclination, the image does not record much of the flux that is scattered off of the nearest surface of the inner torus walls.

The image in Fig. 4.2 (left) illustrates the discussion on the net polarization induced by scattering off of the inner surfaces of a dusty torus (see Kartje (1995) and Goosmann & Gaskell (2007)): the surfaces parallel to the observer's line of sight produce a polarization vector that tends toward an orientation of 90°, while the surfaces oriented perpendicularly to the line of sight produce a polarization vector at 0°. At an intermediate viewing angle (Fig. 4.2 right), the effects of extinction by dust become very strong. The inner wall opposite the observer is still visible but the walls on the side and the nearest inner surface disappear below the torus horizon. Often, the photons must undergo multiple scatterings inside the torus funnel before they escape and are observed. Because the absorption probability increases with the number of scattering events, we thus observe a lower polarized flux than at pole-on view. For a line of sight near the equator, no flux is observed owing to complete absorption by the optically thick dust. Therefore, we do not present the polarization map at an angle i of $\sim 87°$.

4.1.1.2 UV-to-optical polarization images

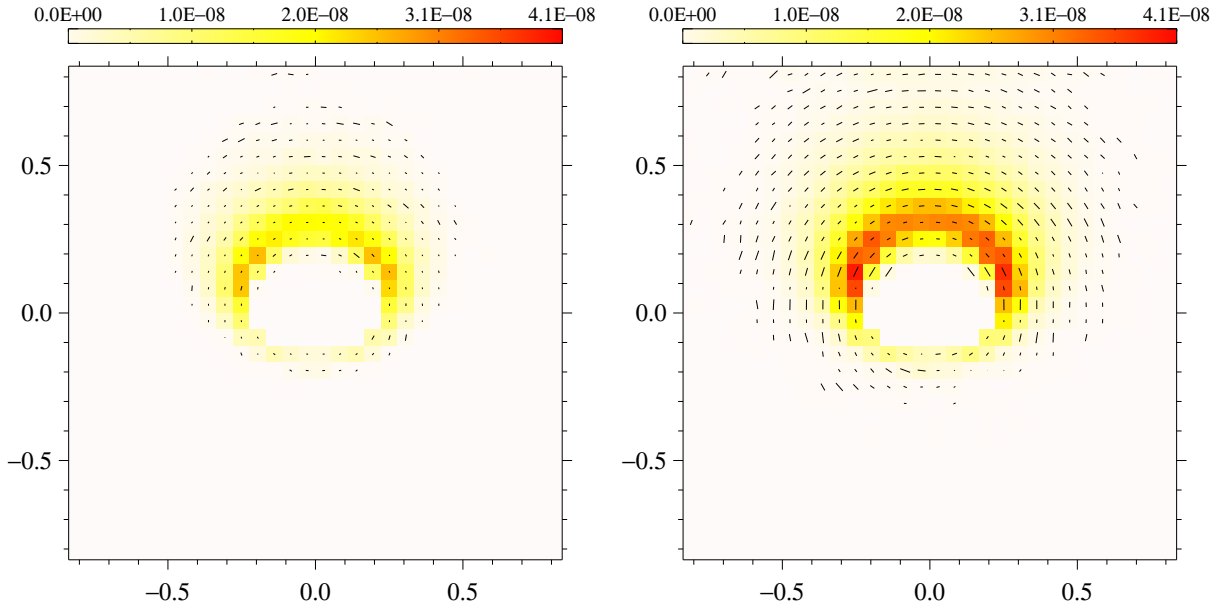

Figure 4.3: Modeled image of the polarized flux, PF/F_*, for a centrally irradiated, optically thick torus with $\theta_0 = 30°$ measured relative to the axis of symmetry; PF/F_* is color-coded and integrated over the 1800 – 8000 Å band. *Left*: face-on image at $\sim$ 2175 Å; *right*: face-on image at $\sim$ 7500 Å.

The net polarized flux coming from a given position on the torus inner walls is determined by a complex interplay between the dust albedo and the scattering phase function. Both of these properties are a function of wavelength. We therefore illustrate the wavelength-dependence of the polarization map in Fig. 4.3. The two maps are taken at the specific wavelengths of 2175 Å and 7500 Å, which correspond to a characteristic extinction feature in the UV and to a plateau region of the extinction cross-section in the optical. The spatial distribution in polarized flux differs significantly between the two wavebands, with the 7500 Å map showing a stronger PF/F_*. At 2175 Å, the scattering phase function greatly favors forward scattering over scattering to other directions. Since the torus is optically thick and its funnel is narrow, the photons are more likely

to be absorbed. At 7500 Å, the scattering phase function is less anisotropic and therefore allows scattered (i.e., polarized) photons to escape more easily from the funnel. The fact that optical photons also encounter a slightly higher albedo in the dust grains than UV photons does work in the same direction. The combination of these effects explains why the spatial distribution in polarized flux in the optical reaches out to larger distances from the central source than in the UV waveband.

4.1.2 Ionized outflows

Polar outflows are a major constituent when explaining the AGN polarization behavior. They allowed the initial discovery of Seyfert-1 nuclei in Seyfert-2 objects by means of spectropolarimetry (Antonucci & Miller 1985). An approximative geometry of the polar scattering regions corresponds to an hourglass shape with a central break where the photon source is located. It is believed that below the dust sublimation radius the polar wind is mainly composed of ionized gas whereas beyond this radius, the gas can coexist with dust. We therefore modeled an electron-filled double-cone for the ionized material closer to the source in Sect. 4.1.2 as well as a pair of more distant, dusty outflows in Sect. 4.1.3.

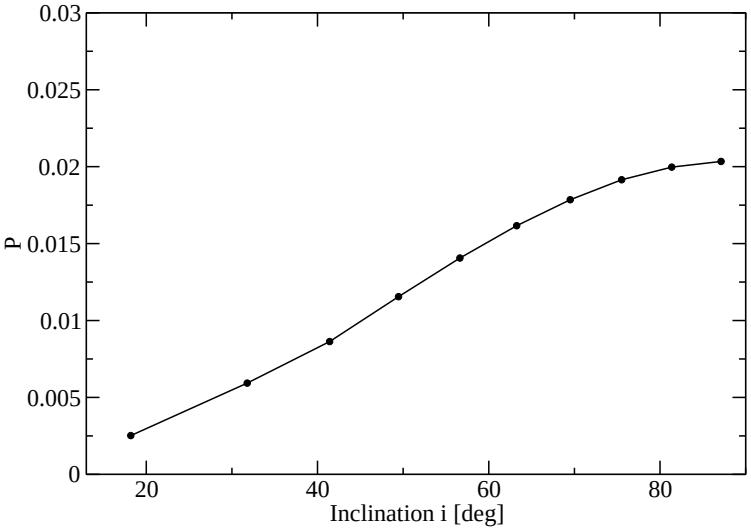

Figure 4.4: Modeling an electron-filled, scattering double-cone with the half-opening angle $\theta_c = 30°$ measured relative to the symmetry axis. The net polarization, P, is plotted versus the observer's inclination i.

Using the formalism introduced by Brown & McLean (1977), Miller & Goodrich (1990) and Miller et al. (1991) were the first to compute the polarization from an AGN double-cone composed of electrons. Based on these results, Wolf & Henning (1999) and Watanabe et al. (2003) conducted Monte Carlo simulations that also include the effects of multiple scattering that were not taken into account in the analytical formula of Brown & McLean (1977). Goosmann & Gaskell (2007)

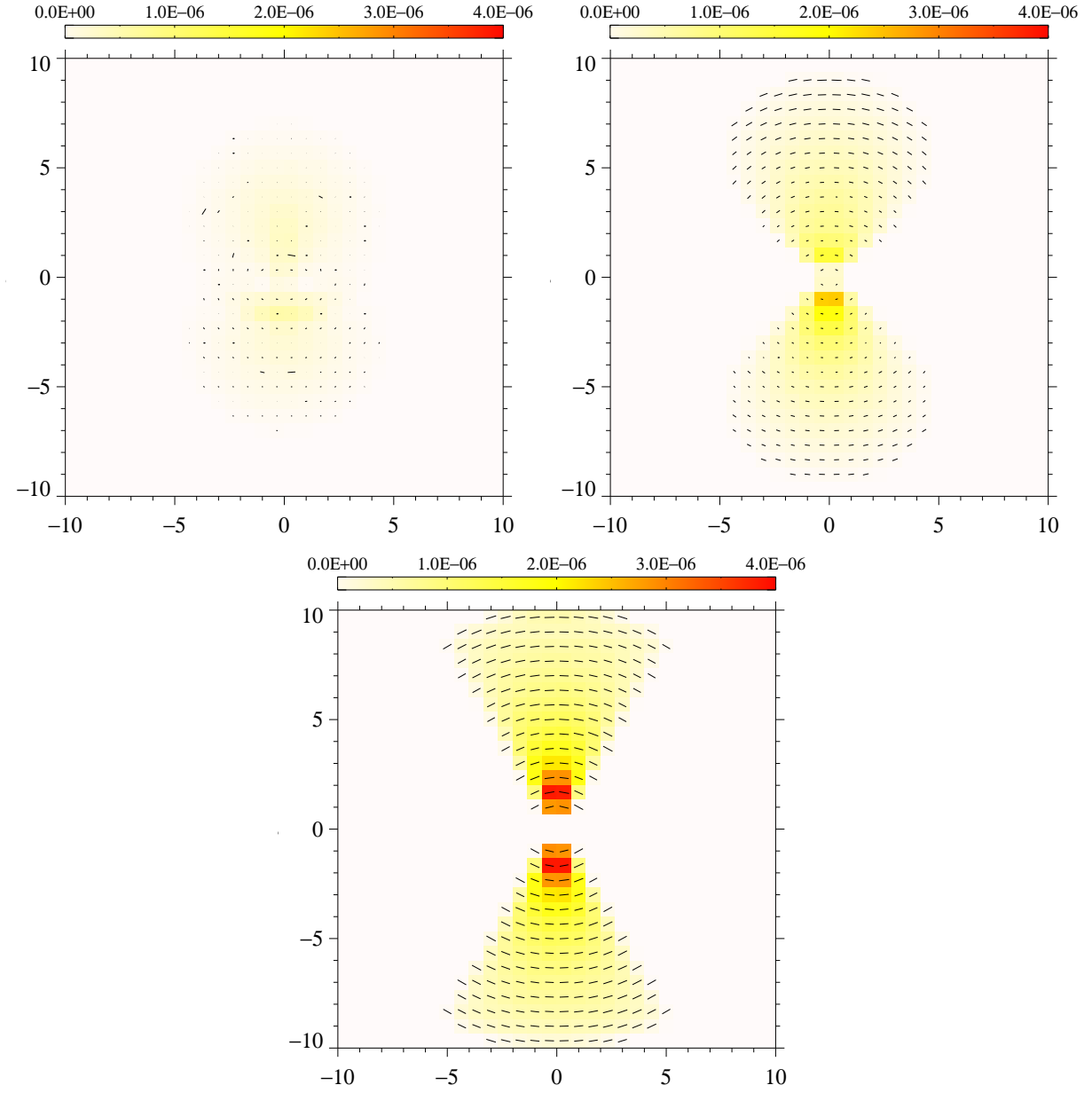

Figure 4.5: Modeled images of the PF/F_* for an electron-filled, scattering double-cone composed of the half-opening angle $\theta_c = 30°$ measured relative to the symmetry axis. The polarized flux, PF/F_*, is color-coded and integrated over the 1800 – 8000 Å band. *Top-left*: face-on image; *top-right*: image at $i \sim 45°$; *bottom*: edge-on image.

repeated and confirmed these studies. It turned out that a radial gradient of the electron density inside the double cone does not have a major impact on the resulting polarization. In most cases, a uniform density leads to very similar results. Here, we resume this investigation and add our new results for the polarization imaging.

We implemented the same polar wind characteristics as in Goosmann & Gaskell (2007) and

modeled a double cone filled with electrons. The electron density was adjusted to achieve a radial Thomson optical depth of $\tau \sim 1$ measured in the vertical direction between the inner and outer surfaces of a single cone. The half-opening angle of the double cone is 30° measured from the vertical axis. Unlike the modeling in Goosmann & Gaskell (2007), we did not restrict the emission angle of the central source but considered isotropic emission.

The resulting polarization as a function of inclination is shown in Fig. 4.4. The polarization curve is very similar to the one found in Goosmann & Gaskell (2007) (Section 5.1), but its normalization has drastically diminished. This is because of the strong dilution by the unpolarized radiation that comes directly from the source that we excluded in our previous modeling. Note that a second source of polarization dilution, not taken into account because we focused on the continuum emission, might also come from the recombination lines and continua. Such a radiative mechanism should then decrease the observed emission-line polarization and the Balmer continuum for example, and will be subject of future work.

Polarization maps are given in Fig. 4.5. From a pole-on view, the highest PF/F_* is concentrated below the (projected) center of the model space. It is dominated by photons back-scattered at the base of the far cone. Above the center, a secondary, dimmer maximum appears that originates from forward-scattering in the near cone. The slightly oval shape of the figure is a projection effect because the line of sight is inclined by 18° relative to the symmetry axis. The approximate symmetry at pole-on viewing position explains why the net polarization at this viewing angle is quite low. The distribution of polarization position angles across the image shows that the polarization produced on the left side of the line of sight partly cancels with that produced on the right side. The net ψ in the pole-on view is oriented perpendicularly to the symmetry axis. Increasing i diminishes the spatial symmetry and thereby leads to a growth of the polarized flux. There is a flux gradient along the vertical axis. Photons that penetrate farther into the cone see a larger optical depth before escaping into an intermediate or edge-on viewing direction because of the conical geometry and uniform electron density. Multiple scattering therefore diminishes the resulting polarization produced farther away from the center.

The strong radial gradient in polarized flux that we obtain in our modeling relates to the question of how strong the effect of a density gradient inside the double cone is on the net polarization (see Watanabe et al. 2003 and Goosmann & Gaskell 2007). Indeed, if the density gradient is steep near the source, the polarized flux produced at the base of the cones should diminish, but, at the same time, the polarization from the optically thinner outer parts of the cones rises because multiple-scattering becomes less important. It is thus not trivial to use polarimetry to constrain the radial density profile in conical scattering regions.

4.1.3 NLRs

Beyond the dust-sublimation radius of an AGN dust particles can survive or form. We therefore have to study the effect of dust absorption and scattering on the polarization induced by polar outflows. We used again the dust composition based on the Milky Way model (see Goosmann & Gaskell (2007) and reference therein) and defined a dusty double-cone with a half-opening angle equal to 30° from the vertical axis. The inner boundary of the scattering region was fixed at 10 pc above the source and the double cone extends to a distance of 100 pc. The optical depth in the V-band was fixed at $\tau_V \sim 0.3$.

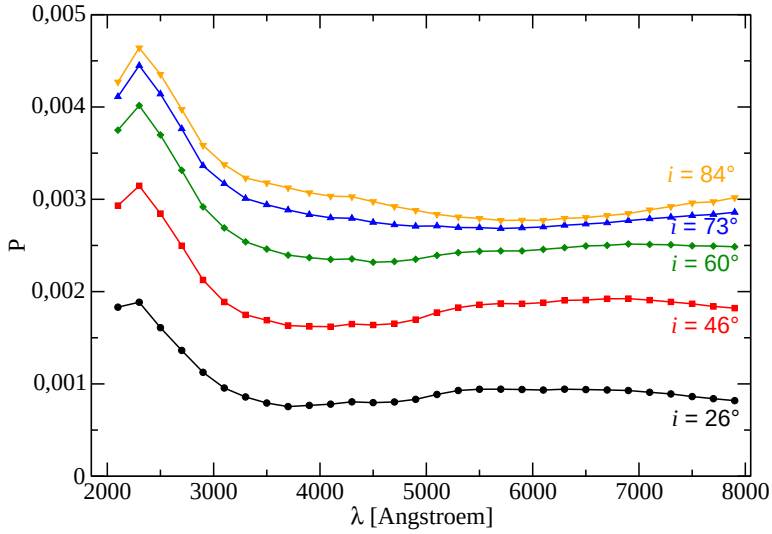

Figure 4.6: Modeling a dusty double-cone of half-opening angle $\theta_c = 30°$ measured relative to the axis of symmetry. The spectrum of the polarization percentage P is plotted for different viewing inclinations, i.

The polarization spectra are shown in Fig. 4.6. They are similar to the results of Goosmann & Gaskell (2007) (except that the Poissonian fluctuations are smoother due to better statistics with the newly implemented MTG). We show the images of the polarized flux in Fig. 4.7. Unlike the case of the double cones of scattering electrons, the face-on view shows only one spatial maximum that corresponds to forward scattering in the near cone. The dust phase function favors forward scattering over backscattering, and therefore the far cone is dominated by absorption and cannot be seen in polarized flux. However, the same characteristics of the polarization position angle, ψ, can be observed for both types of scattering media. At an intermediate viewing angle, we observe a higher polarized flux but still mainly dominated by the lower part of the upper cone. The behavior of the net polarization is again related to the spatial symmetry that changes with viewing angle, just as for the electron-scattering double cone described in Sect. 4.1.2. At an edge-on viewing position, mostly perpendicular polarization with a radial gradient is seen. Significant polarized flux still emerges close to the outer limits of the reprocessing region. For wavelengths above 2200 Å, the scattering cross section decreases monotonically so that photons can travel farther into the medium before they are scattered or absorbed.

4.1.3.1 The effects of the optical depth and wavelength

We studied the dependence of the polarization on wavelength and on the optical depth of the dusty outflows. We varied the optical depth of the medium in the V-band, τ_V, between 0.03, 0.3, and 3 and we show the imaging results in Figs. 4.8, 4.9, and 4.10, respectively. Maps are shown for an edge-on viewing angle and at wavelengths of 2175 Å and 7500 Å.

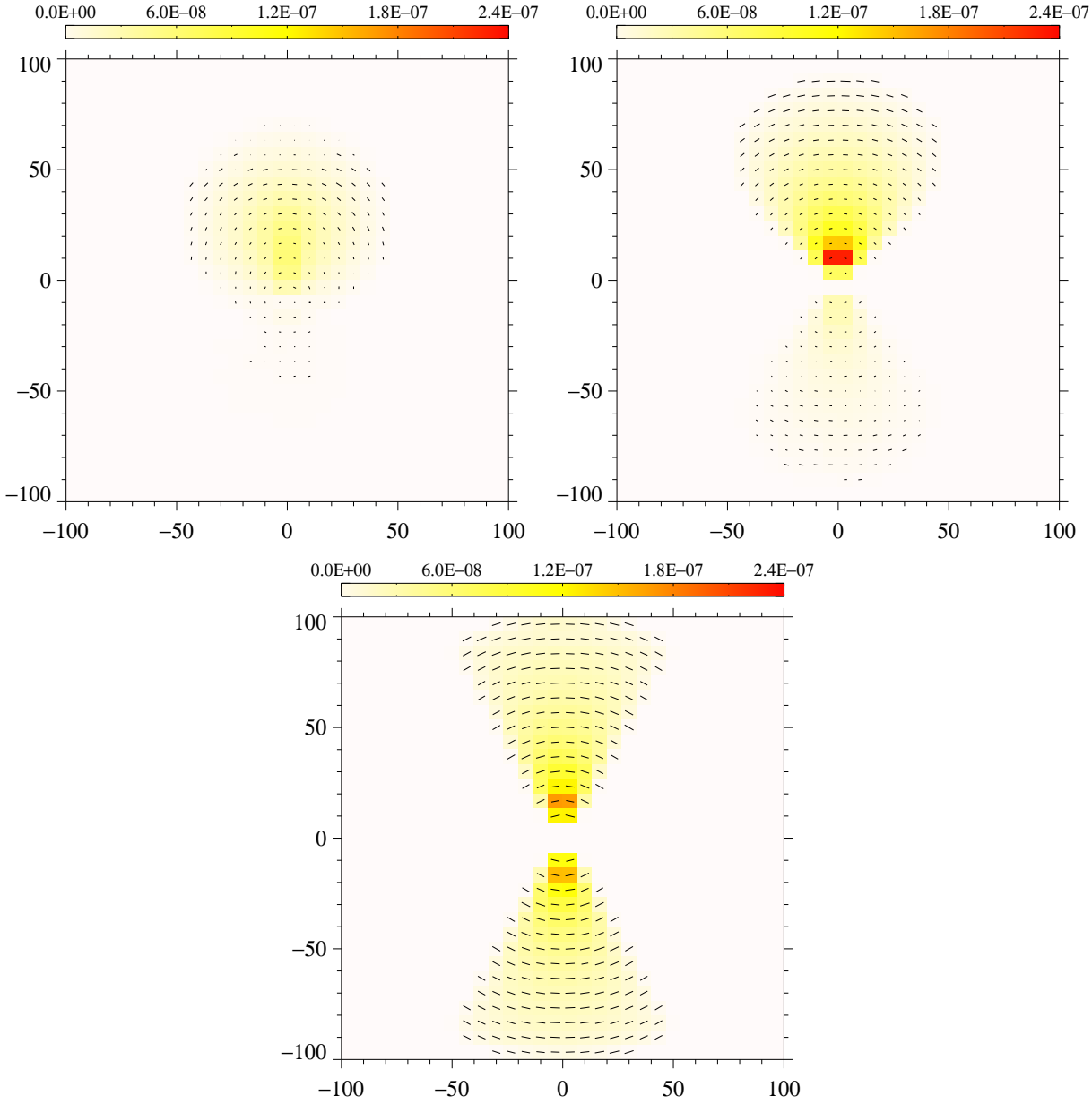

Figure 4.7: Modeled images of the polarized flux, PF/F_*, for a dusty double-cone of half-opening angle $\theta_c = 30°$ measured relative to the axis of symmetry; PF/F_* is color-coded and integrated over the 1800 – 8000 Å band. *Top-left*: face-on image; *top-right*: image at $i \sim 45°$; *bottom*: edge-on image.

It appears from the color scale of the figures that up to a range of $\tau_V < 3$ the PF/F_* increases with τ_V. As the optical depth determines the average number of scattering events before escape or absorption, increasing it leads to more scattering and therefore to more PF/F_*, at least before the optical depth becomes sufficiently high depolarizing multiple-scattering effects to become predominant. The systematic rise in PF/F_* seems to be similar at both wavelengths. Photons

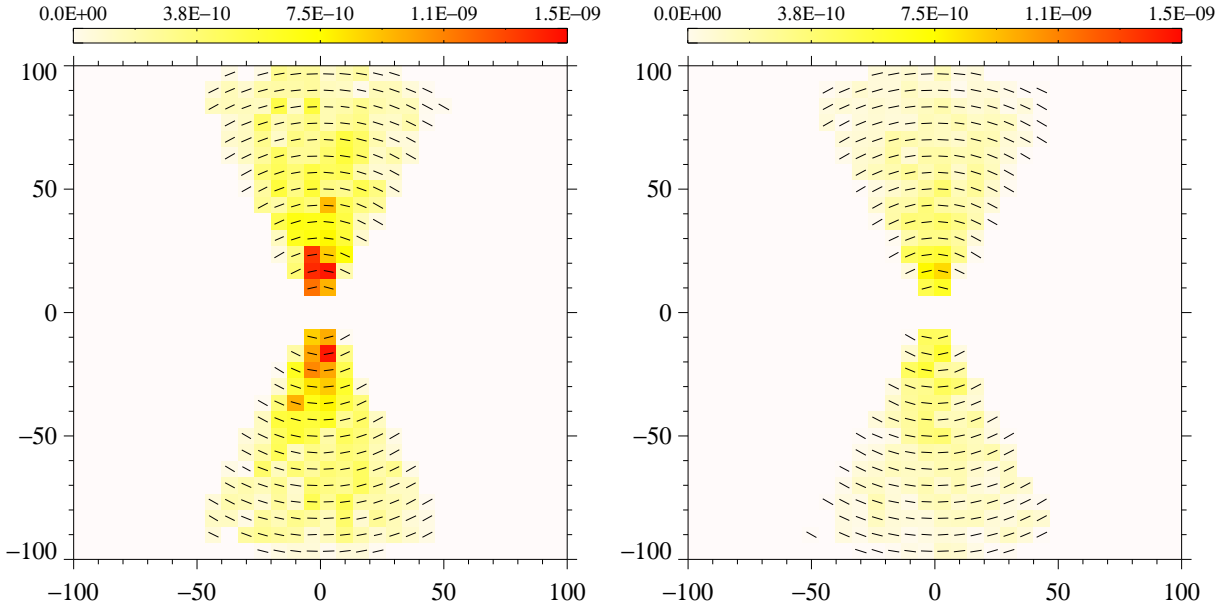

Figure 4.8: Modeled images of the polarized flux, PF/F_*, for a dusty double-cone with the half-opening angle $\theta_c = 30°$ measured relative to the symmetry axis and a radial optical depth of $\tau_V \sim 0.03$; PF/F_* is color-coded and integrated over the 1800 – 8000 Å band. *Left*: edge-on image at $\sim$ 2175 Å; *right*: edge-on image at $\sim$ 7500 Å.

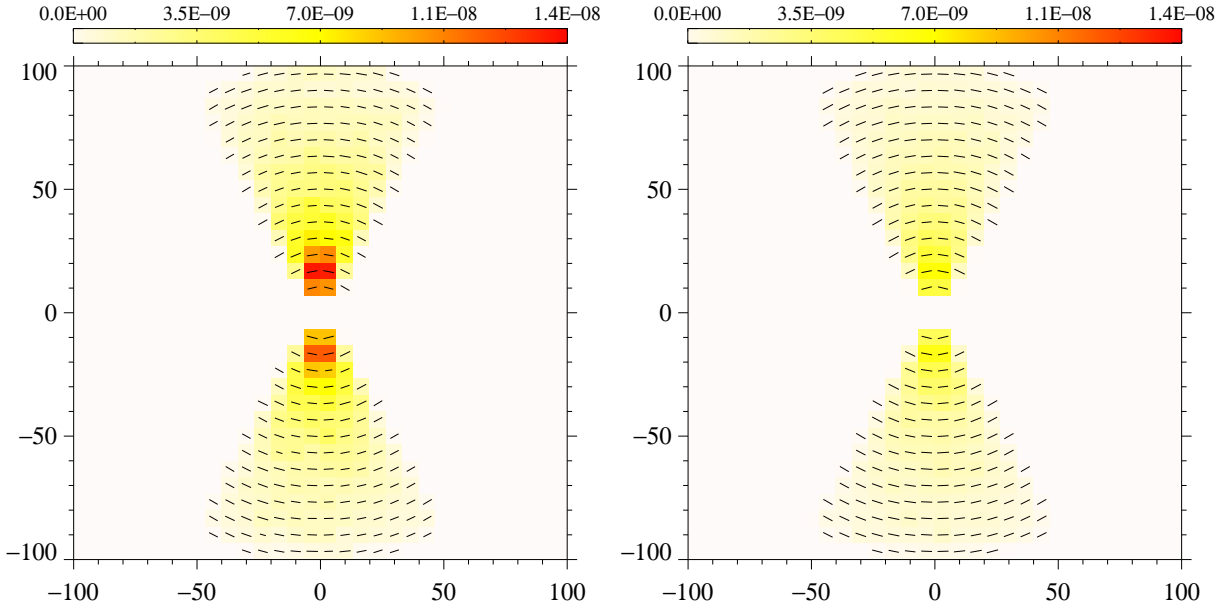

Figure 4.9: Modeled images of the polarized flux, PF/F_*, for a dusty double-cone with the half-opening angle $\theta_c = 30°$ measured relative to the symmetry axis and a radial optical depth of $\tau_V \sim 0.3$; PF/F_* is color-coded and integrated over the 1800 – 8000 Å band. *Left*: edge-on image at $\sim$ 2175 Å; *right*: edge-on image at $\sim$ 7500 Å.

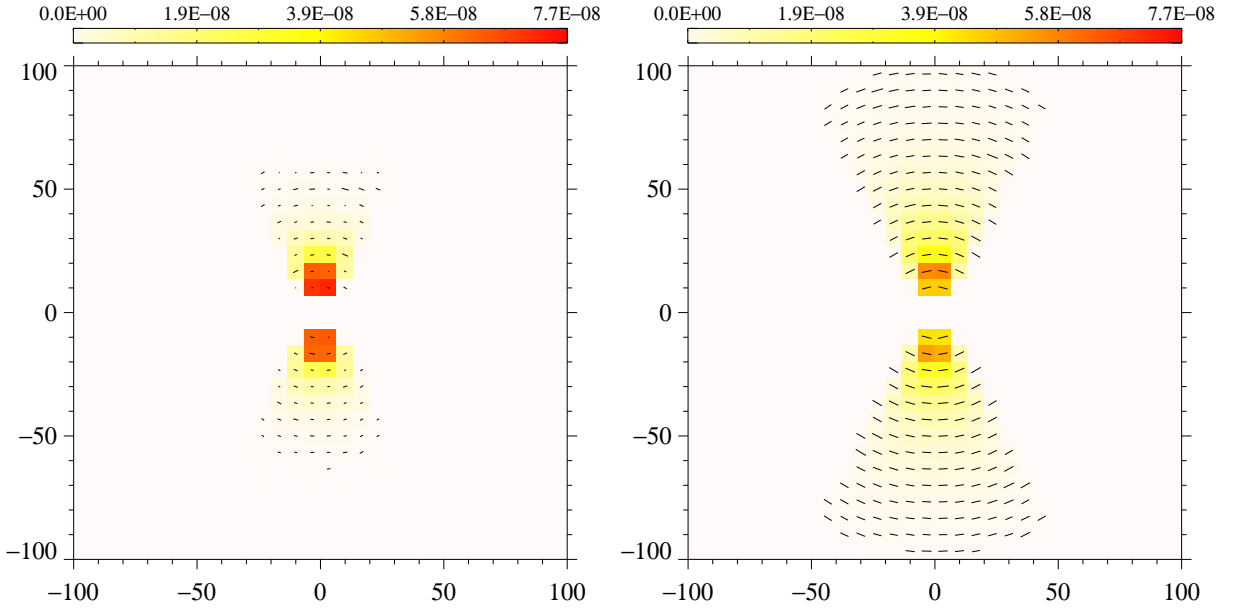

Figure 4.10: Modeled images of the polarized flux, PF/F_*, for a dusty double-cone with the half-opening angle $\theta_c = 30°$ measured relative to the symmetry axis and a radial optical depth of $\tau_V \sim 3$; PF/F_* is color-coded and integrated over the 1800 – 8000 Å band. *Left*: edge-on image at $\sim$ 2175 Å; *right*: edge-on image at $\sim$ 7500 Å.

with longer wavelengths (i.e., ∼7500 Å), pass through a larger portion of material before they are scattered and escape. This effect is related to the evolution of the extinction cross section with wavelength, as mentioned earlier.

For our modeling of the dusty outflows the optical depth is always much lower (between 0.03 and 3) than the one assumed for the optically opaque torus (∼750). The photons scattering off the outflows thus do not remain close to the surface of the scattering region but can penetrate deep into the medium before they are scattered or absorbed. At 2175 Å, the photon phase function favors forward- over backscattering. Photons that have already scattered and progressed in the direction of the observer are thus less likely to be scattered out of the line of sight. In general, the PF/F_* is therefore greater at UV wavelengths than in the optical band.

4.1.4 Radiation-supported disk

To explain the presence of parallel polarization (with respect to the projected symmetry axis), a third type of scattering region has been proposed (Antonucci 1984): a radiation-supported, geometrically thin scattering disk that lies in the equatorial plane (Chandrasekhar 1960, Angel 1969), Sunyaev & Titarchuk 1985). Most often, the geometry of a flared wedge is assumed for this scattering region (see Fig. 17 in Goosmann & Gaskell (2007) for a schematic review of the possible geometries). Following the suggestions of Goodrich & Miller (1994) and the simulations of Young (2000) and Smith et al. (2004, 2005), we showed in Goosmann & Gaskell (2007) that the flared-disk geometry can be replaced by a torus geometry without noticeable changes in polarization. This substitution is consistent for a flared-disk half-opening angle lower than 30°. Here, we simulate an equatorial scattering region using a geometrically thin torus composed of electrons with a Thomson

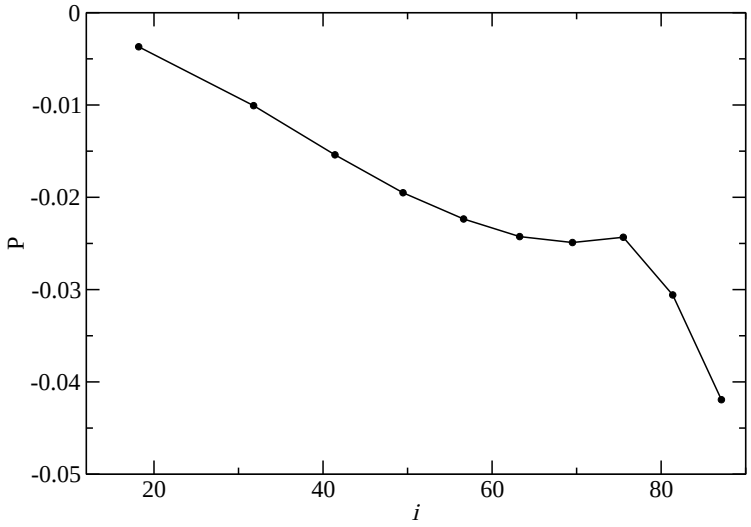

Figure 4.11: Modeling of an equatorial, electron-filled scattering disk with a half-opening angle $\theta_0 = 10^\circ$ measured with respect to the equatorial plane. Polarization P is plotted against the inclination i along the axis of the observer. Negative values for P indicate a parallel polarization.

optical depth of $\tau \sim 1$ and a half-opening angle of 10° with respect to the equatorial plane. The inner radius of the thin torus is 3×10^{-4} pc and its outer radius is 5×10^{-4} pc.

The polarization spectra as a function of the inclination i are shown in Fig. 4.11. A negative value of P indicates parallel polarization at all viewing angles. The spectra are very similar to those presented in Goosmann & Gaskell (2007) for the geometry of a flared disk. Fig. 4.12 presents the polarization maps for the simulated equatorial scattering disk. For a pole-on view, the disk is divided into concentric rings of polarized flux with polarization vectors oriented tangentially to the rings. By integrating the entire region, we obtain a polarization position angle of 90° for a nearly face-on viewing angle. The inner surface of the equatorial disk causes a lower polarized flux than the rest of the reprocessing region. The torus geometry implies that the inner region has a height (relative to the equatorial plane) that is less important than the central region. However, if the density is uniform throughout the medium; we deduce that the vertical column density is lower on the edges of the torus. Hence, the PF/F_* is greater in the central part where the vertical column density and therefore the scattering probability is maximum. When we tilt the line of sight to an intermediate position, we observe a polarized flux greater on the torus surfaces which are parallel to the line of sight. These surfaces retain a strong polarization as long as the scattering angle with respect to the observer's line of sight stays close to 90°. Surfaces orthogonal to the line of sight cause a lower PF/F_* compared to the pole-on view. Therefore, the net polarization remains parallel and is even stronger at an intermediate view than at the near face-on view. For angles i at nearly edge-on view, the scattering geometry only allows for parallel polarization for all parts of the equatorial disk.

On the PF/F_*-plots the photon source seems hidden by the medium because it is seen only

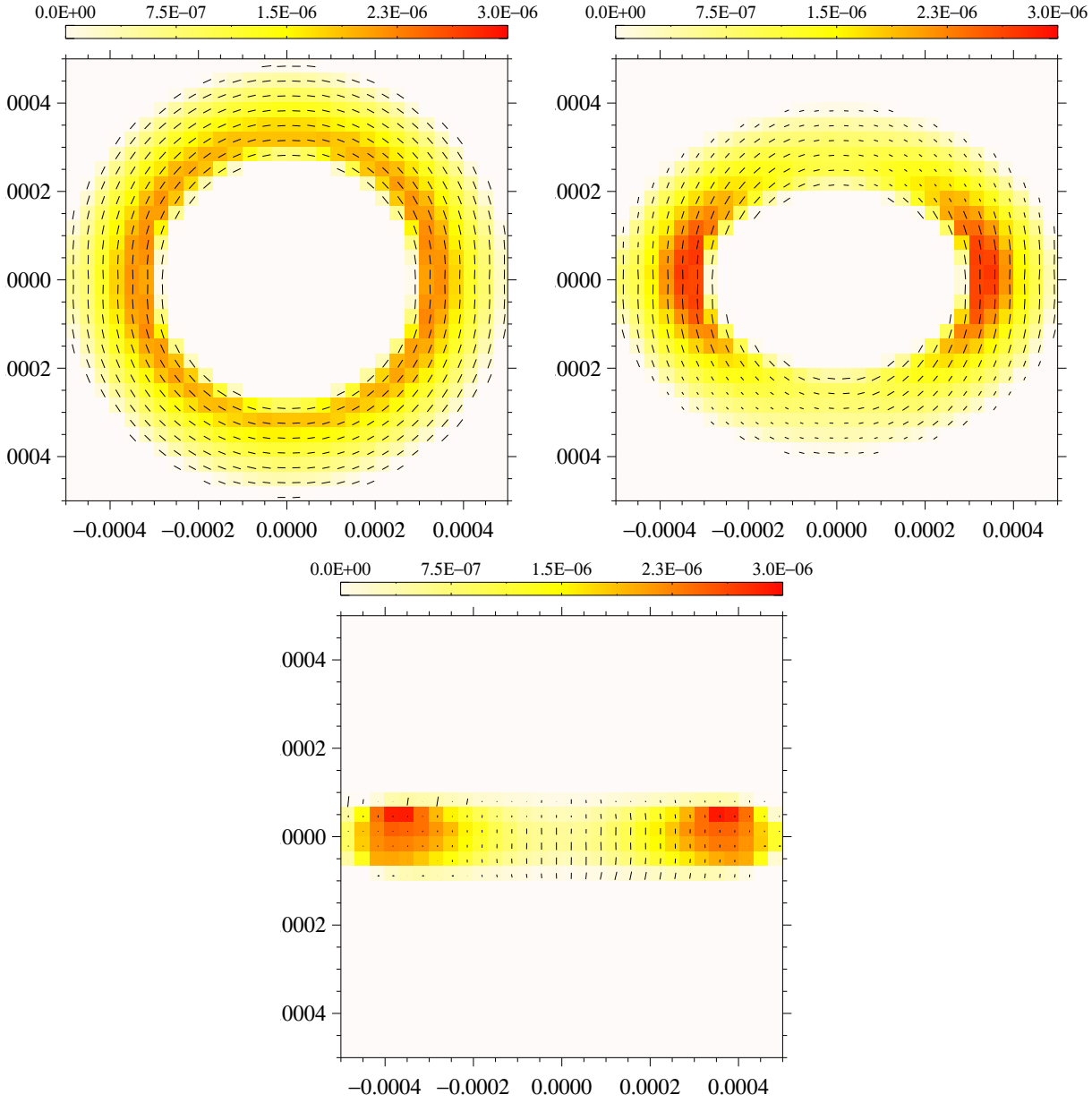

Figure 4.12: Modeled image of the polarized flux, PF/F_*, for an electron-filled, equatorial scattering disk with a half opening angle $\theta_0 = 10°$ measured with respect to the equatorial plane; PF/F_* is color-coded and integrated over the 1800 – 8000 Å band. *Top-left*: face-on image; *top-right*: image at $i \sim 45°$; *bottom*: edge-on image.

in transmission, which induces very low polarization. However, this strong, low-polarization flux dilutes more significant polarized flux coming from other areas of the scattering region. A second reason why the net polarized flux remains moderate is that at the optical depth $\tau_V = 1$ considered here multiple scattering events occur inside the medium.

4.2 Exploring the radiative coupling between two reprocessing regions

After modeling the polarization induced by individual scattering regions, we now include the effects of radiative coupling between them. Especially for significant optical depths, the coupling turns out to be important and should be properly addressed by Monte Carlo methods (see the discussions in Goosmann & Gaskell 2007 and in Goodrich & Miller 1994). We apply a step-by-step method combining first only two scattering regions at a time. Then, we approach a more complete AGN model that is composed of three individual scattering regions (see Sect. 4.3). In the following subsections we not yet include the previously studied dusty outflows because the NLR regions responsible for dust signatures in polar scattering objects are situated farther away from the central engine than the three other reprocessing regions (Marin et al. 2012c) and are investigated later in Sect. 4.4.

All three models presented here feature the same unpolarized, isotropic central source that was described previously. The first model in this section consists of an equatorial, electron-filled disk and polar, electron-filled outflows (Sect. 4.2.1). The second model is composed of the equatorial disk and an optically thick, dusty torus (Sect. 4.2.2). The last model comprises an optically thick torus and polar outflows (Sect. 4.2.3).

4.2.1 Equatorial scattering disk and electron-filled outflows

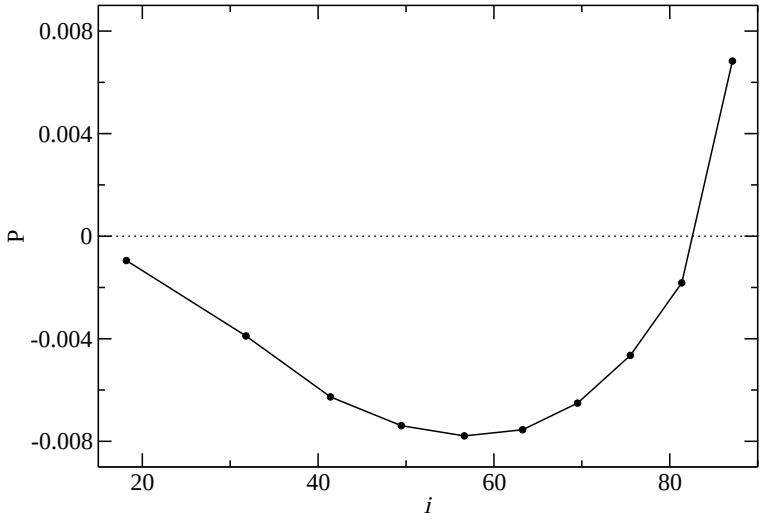

Figure 4.13: Modeling electron-filled, polar outflows with a half-opening angle $\theta_c = 30°$ relative to the symmetry axis combined with an electron-filled, equatorial disk with a half-opening angle $\theta_0 = 10°$ measured relative to the equatorial plane. The net polarization is plotted versus the inclination i of the observer.

The equatorial scattering disk was again simulated by an electron-filled, geometrically thin torus as described in Sect. 4.1.4. The polar electron-filled outflows were modeled according to

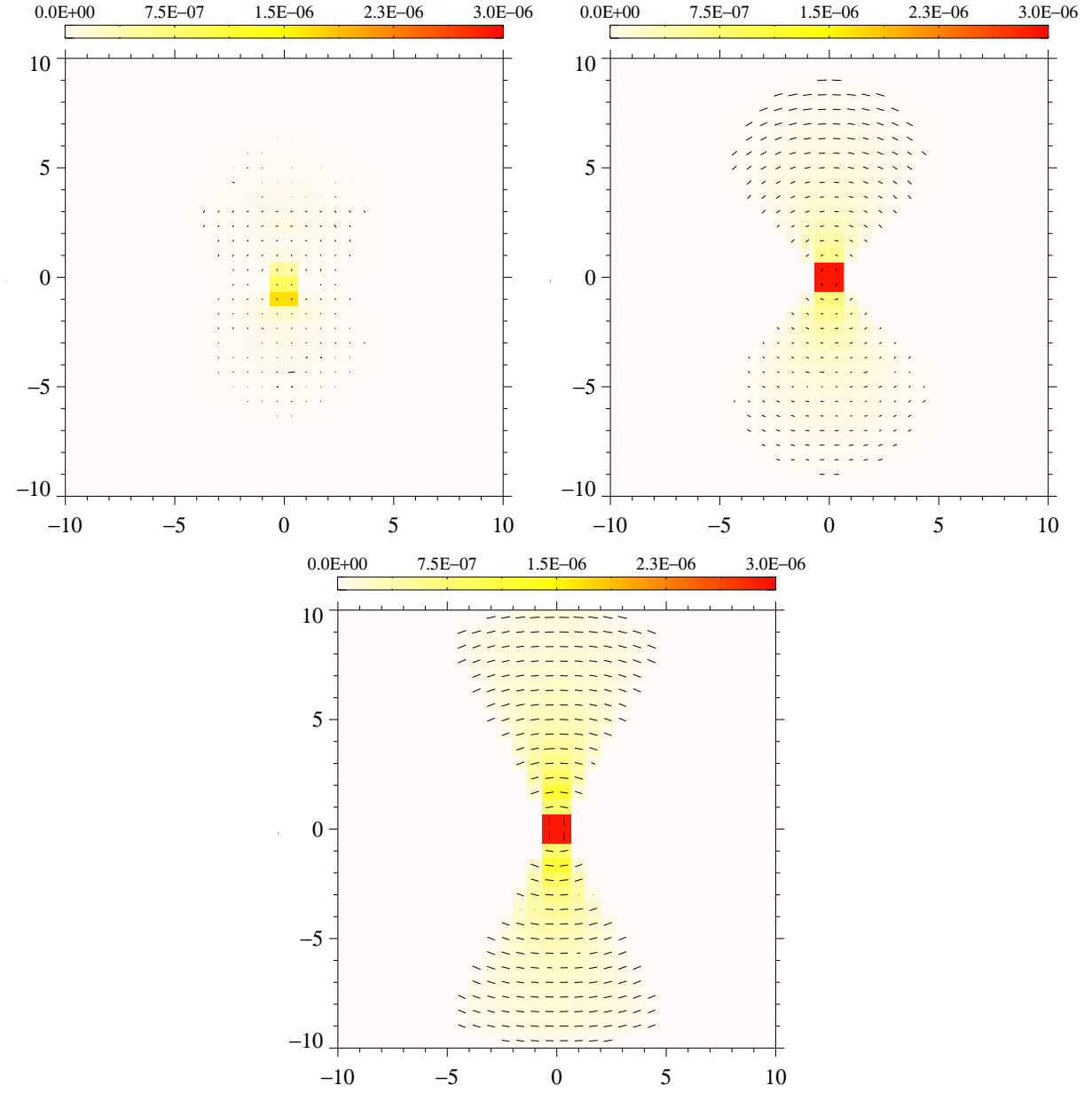

Figure 4.14: Modeled image of the polarized flux, PF/F_*, for the combination of an electron-filled, equatorial disk with electron-filled, polar outflows; The wavelength-independent PF/F_* is color-coded and integrated over the complete wavelength range. *Top-left*: face-on image; *top-right*: image at $i \sim 45°$; *bottom*: edge-on image.

Sect. 4.1.2. This model setup may be applicable to nonthermal AGN with very low toroidal absorption. This claim has been made for FR I radio galaxies (Chiaberge et al. 1999; Whysong & Antonucci 2004) and LINERs (Maoz et al. 2005).

The resulting polarization percentage as a function of the viewing angle is shown in Fig. 4.13.

At pole-on and intermediate viewing angles, P is negative (parallel net polarization). This is due to the predominance of the equatorial disk, which produces a polarization angle of $\psi = 90°$ regardless of the line of sight. At pole-on view, the parallel polarization that the photons acquire in the equatorial disk is preserved during their passage through the optically thin polar winds. Only toward the largest viewing angles the scattering polarization induced by the polar winds dominates and gives a net polarization angle of $\psi = 0°$. P is always constant in wavelength because in this particular model we only considered Thomson scattering.

The polarization maps in Fig. 4.14 further illustrate our discussion. At pole-on view (Fig. 4.14 top-left), the double cone is visible in transmission and reflection. In many areas of the image, the polarization angle is at $\psi = 0°$, however, the associated polarized flux remains weak compared to that coming from the equatorial disk, which has $\psi = 90°$. The integrated PF/F_* therefore has $\psi = 90°$. The polarization images at intermediate viewing angles (Fig. 4.14 top-right) partly agree with the results obtained for scattering in polar outflows alone (see Sect. 4.1.2). Again, the two maxima in polarized flux induced by scattering in the far and the near cone are visible and show perpendicular polarization. At the center, the impact of the equatorial disk is visible, and ψ rotates toward 90°. Finally, when seen edge-on (Fig. 4.14 bottom), the net polarization has switched to $\psi = 0°$. The scattered photons from the polar winds are now strongly polarized and dominate the net polarized flux.

4.2.2 Radiation-supported disk and obscuring torus

Next, we considered a combination of the equatorial scattering disk with an optically thick, dusty torus. The parameterization of the reprocessing regions is the same as described before (see Sect. 4.1.4 and 4.1.1, respectively). The absence of polar outflows highlights a particular subclass of thermal Seyfert-1 AGN that are characterized by a very weak or absent amount of intrinsic warm absorption (Patrick et al. 2011), a subclass also known as "bare" AGN.

Fig. 4.15 shows, from top to bottom, the polarization percentage, the spectral flux, and the normalized polarized flux as a function of wavelength. At pole-on view, the behavior of P is particularly interesting: The polarization degree is negative in the UV-band, indicating parallel polarization. With increasing wavelength, the polarization weakens and undergoes a sign inversion around 5200 Å. For longer wavelengths, the polarization becomes again significant, but is perpendicular. This behavior is due to the competition in polarized flux between the equatorial disk and the torus. The two scattering regions produce polarization at opposite signs, but the albedo and scattering phase function of the dust change systematically with wavelength. Below 5200 Å, the phase function of Mie scattering strongly promotes forward scattering over scattering toward other directions. The dust albedo in the ultraviolet is slightly lower than at longer wavelengths so that, in total, bluer photons hitting the inner walls of the torus have a higher probability to be absorbed than redder photons. In the UV, the polarized flux emerging from the equatorial disk thus predominates. Above 5200 Å, the Mie scattering phase function is less anisotropic and the polarized flux scattered off of the torus inner walls and toward a pole-on observer becomes more important. The net polarization is then dominated by the torus and is perpendicular.

At higher inclination, the equatorial scattering disk is hidden behind the torus and therefore its polarized flux with $\psi = 90°$ is not directly visible. The net polarization is now perpendicular across the whole waveband and rises toward longer wavelengths, as it does for the reprocessing of a dusty torus alone (see Fig. 4.1). The interplay between electron- and dust scattering is also visible in

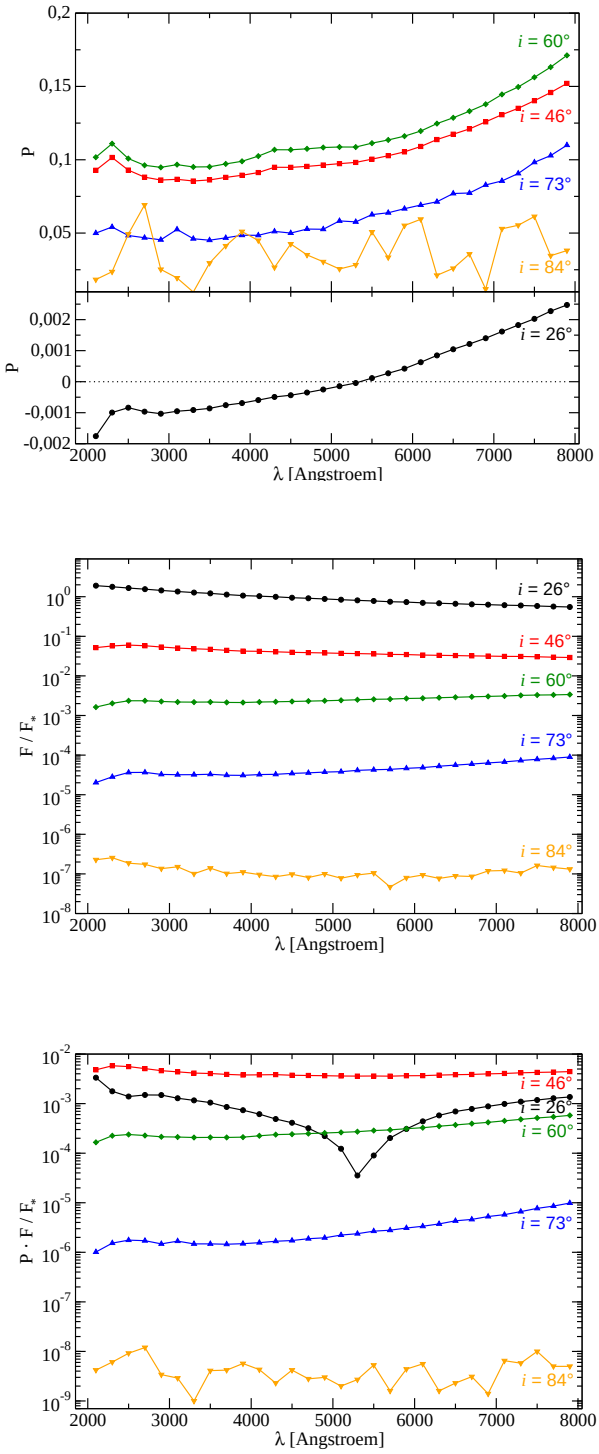

Figure 4.15: Modeling an optically thick dusty torus with the half-opening angle $\theta_c = 30°$ relative to the symmetry axis combined with an electron-filled, equatorial disk with half-opening angle $\theta_0 = 10°$ measured from the equatorial plane. *Top*: Polarization, P, as seen at different viewing inclinations, i; *middle*: the fraction, F/F_* of the central flux; *bottom*: the polarized flux P·F/F_*.

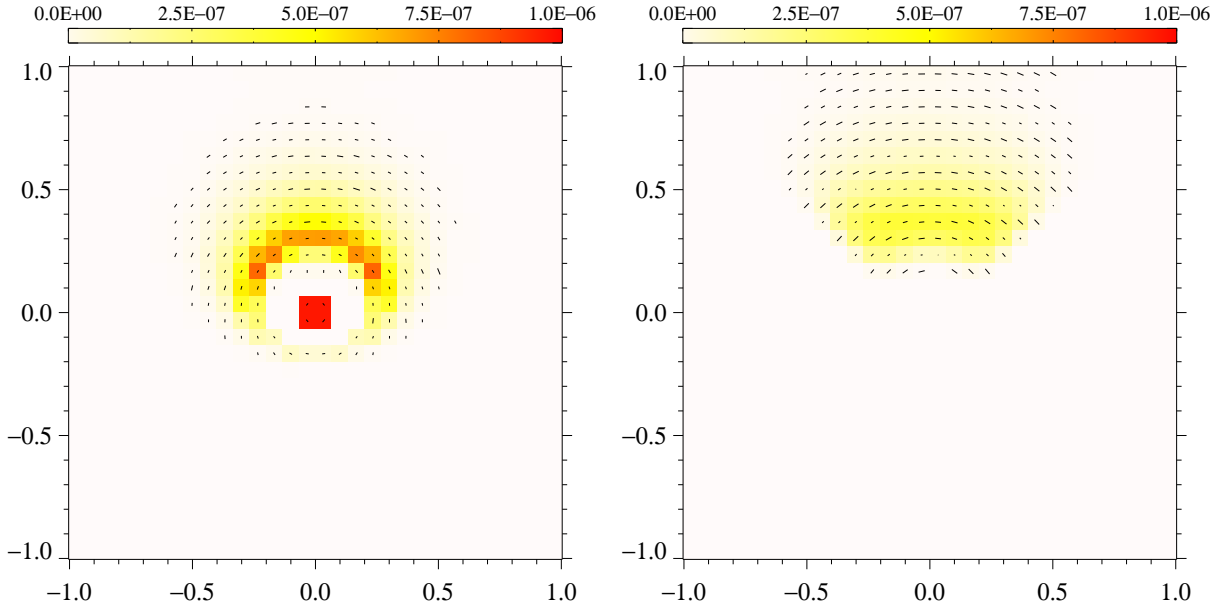

Figure 4.16: Modeled image of the polarized flux, PF/F_*, for an electron-filled, equatorial disk combined with an optically thick, dusty torus; PF/F_* is color-coded and integrated over the 1800 – 8000 Å band. *Left*: face-on image; *right*: image at $i \sim 45°$.

the F/F_* spectrum (Fig. 4.15, middle). With increasing i, the spectral slope in the optical changes gradually. This behavior is again determined by the combined effect of the wavelength-dependent albedo and scattering phase function as well as by the specific scattering geometry chosen in this model. Comparison with the spectral flux obtained for a dusty torus alone (see Fig. 4.1) reveals that the negative slope for low viewing angles is an effect of the additional electron scattering that happens inside the torus funnel. The scattering feature of carbonaceous dust in the UV is seen only at intermediate and edge-on viewing angles. At pole-on view, the feature is blended by the direct flux from the source and by scattered radiation coming from the equatorial disk.

It is instructive to also discuss the polarized flux spectrum (Fig. 4.15, bottom) for this modeling case. At pole-on view, the PF/F_* shows a minimum across the switch of the polarization position angle around 5200 Å and reduces the polarized flux by a large factor (note that when constructing the polarized flux we always take the absolute value of P). We should point out that the presence of the flip in polarization strongly depends on the exact model geometry and the scattering efficiency of the equatorial scattering disk. The strongest polarized flux occurs at a line of sight slightly below the torus horizon. Toward higher inclinations, the flux drops rapidly and so does PF/F_*.

The polarization maps are presented in Fig. 4.16. Due to the large difference in spatial scale between the two scattering regions, we restrict the mapping to the funnel of the dusty torus. At pole-on view (Fig. 4.16, left), the (wavelength-integrated) map shows that the polarized flux with $\psi = 0°$ coming from the dusty torus is almost of the same order of magnitude as the one emerging in the equatorial disk that carries $\psi = 90°$. One has to take into account that the polarized flux spectrum reported in Fig. 4.15 is integrated over all scattering surfaces; with respect to the

equatorial scattering disk, the polarized flux coming from a given position on the torus inner wall is lower, but this is compensated for by a larger integration surface. As discussed above, the exact outcome of the competition between the two components and the resulting polarization position angle depends on the wavelength. The situation is much clearer at an intermediate viewing angle (Fig. 4.16 right). Here, the polarized flux mostly emerges from the far-sided inner wall of the torus that induces $\psi = 0°$. The near-sided wall and the walls on the side of the line of sight are barely visible because they are covered by the torus body. The equatorial scattering disk is hidden in the torus funnel so that the net polarization can only be equal to $\psi = 0°$. We do not show the edge-on image for this model because almost all radiation is blocked by the optically thick torus.

4.2.3 Electron polar outflows and obscuring torus

Finally, we constructed a reprocessing model that combines the electron-filled polar outflows and the optically thick, dusty torus as presented previously in Sects. 4.1.2 and 4.1.2, respectively. This model setup would feature an AGN that (temporarily) lacks a material connection between the inner boundaries of the dusty torus and the outer parts of the accretion disk. The so-called "naked" AGN (Panessa & Bassani 2002; Hawkins 2004; Panessa et al. 2009; Tran et al. 2011) that seem to lack a BLR could fall into this category.

The spectropolarimetric modeling is presented in Fig. 4.17. The results reported in Sect. 4.1.1 show that at face-on viewing angles the polarization due to scattering off of a dusty torus is low and quite independent of wavelength. Here we obtained almost the same picture because the photons pass through the optically thin wind mostly by forward- or backward scattering. When the line of sight crosses the torus horizon, the dilution by the unpolarized source flux is suppressed and the polarization reaches higher values. With even higher inclination, there are two effects that increase the normalization of the polarization spectrum: Firstly, there are more dust scattering events necessary to escape from the torus funnel. The systematic multiple scattering sharpens the perpendicular polarization. In many other situations multiple scattering is a depolarizing effect. The polarization sharpening established here is closely linked to the narrow funnel-geometry and the high optical depth of the torus, which makes only scattering off of its surface important. The second effect relates to the outflow in which stronger polarization is produced for higher i. This is due to the shape of the polarization phase function of Thomson scattering.

In contrast to the modeling of a torus alone (see Sect. 4.1.1), here the F/F_* spectrum decreases toward longer wavelengths at all viewing angles considered; we discussed in Sect. 4.2.2 that additional electron scattering inside the torus funnel tends to decrease the spectral slope. In this respect, the polar outflows are even more efficient than the equatorial disk. The effect is again related to the change in scattering phase function from the UV to the optical waveband: the electrons inside the torus funnel scatter primary photons toward the torus inner surfaces. Since these surfaces have a receding shape toward the exit of the funnel, the scattered photons impinge it at a grazing angle. In the UV, the scattering phase function largely favors scattering into a cone of $\sim 30°$ half-opening angle around the forward direction. This gives many photons a good chance to be scattered only once by the dust and then to escape from the torus funnel. Optical photons are more often scattered to a direction that leads back into the funnel and therefore they are slightly more likely to be absorbed. This explains why the scattered spectrum of the torus is stronger in the UV than in the optical waveband (even though the albedo in the UV is slightly lower than in the optical).

As for the case of a scattering torus alone, the normalization of the F/F_*-spectrum decreases

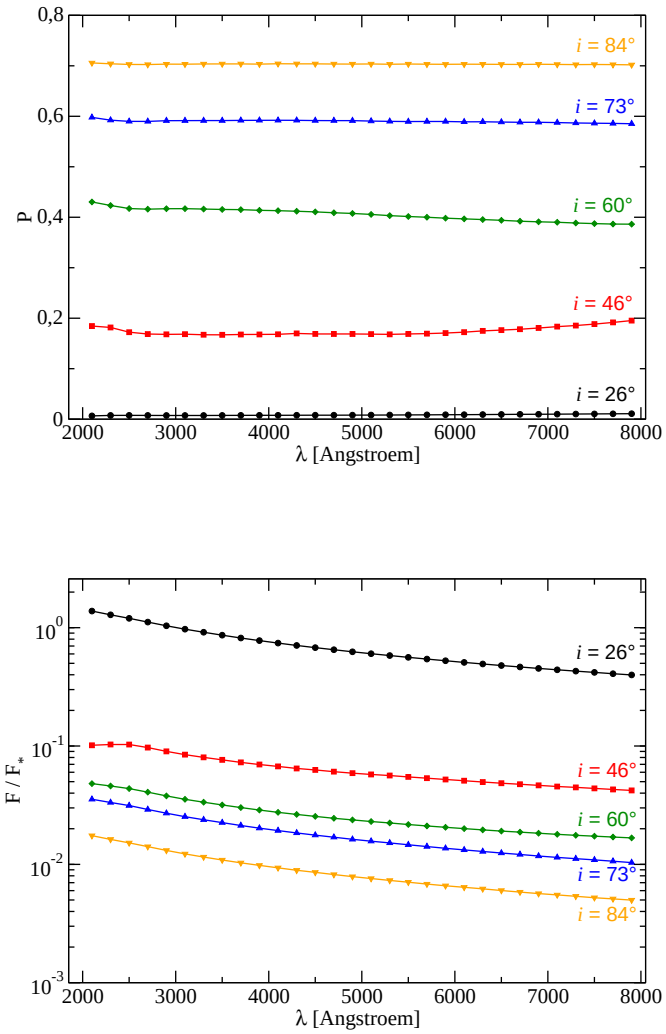

Figure 4.17: Modeling an electron-filled double cone combined with an optically thick dusty torus, both with a half-opening angle of $\theta_c = 30°$ measured with respect to the symmetry axis. Results are shown for different viewing angles i. *Top*: Polarization P; *bottom*: the fraction, F/F_* of the central flux.

toward a higher viewing angle because the visible scattering surfaces of the funnel become rapidly smaller. Also, the scattering efficiency inside the polar outflows is lower for scattering toward higher i than toward a pole-on direction. At all type-2 inclinations, a dim feature of dust reprocessing in the UV is visible and traces the radiation component that is scattered into the line of sight by the torus.

The polarization maps are shown in Fig. 4.18. At pole-on view, the spatial maximum that is related to the far cone (seen in reflection) is less extended than the one related to the near cone (seen in transmission); compared to the pole-on image of an isolated, electron-filled outflow

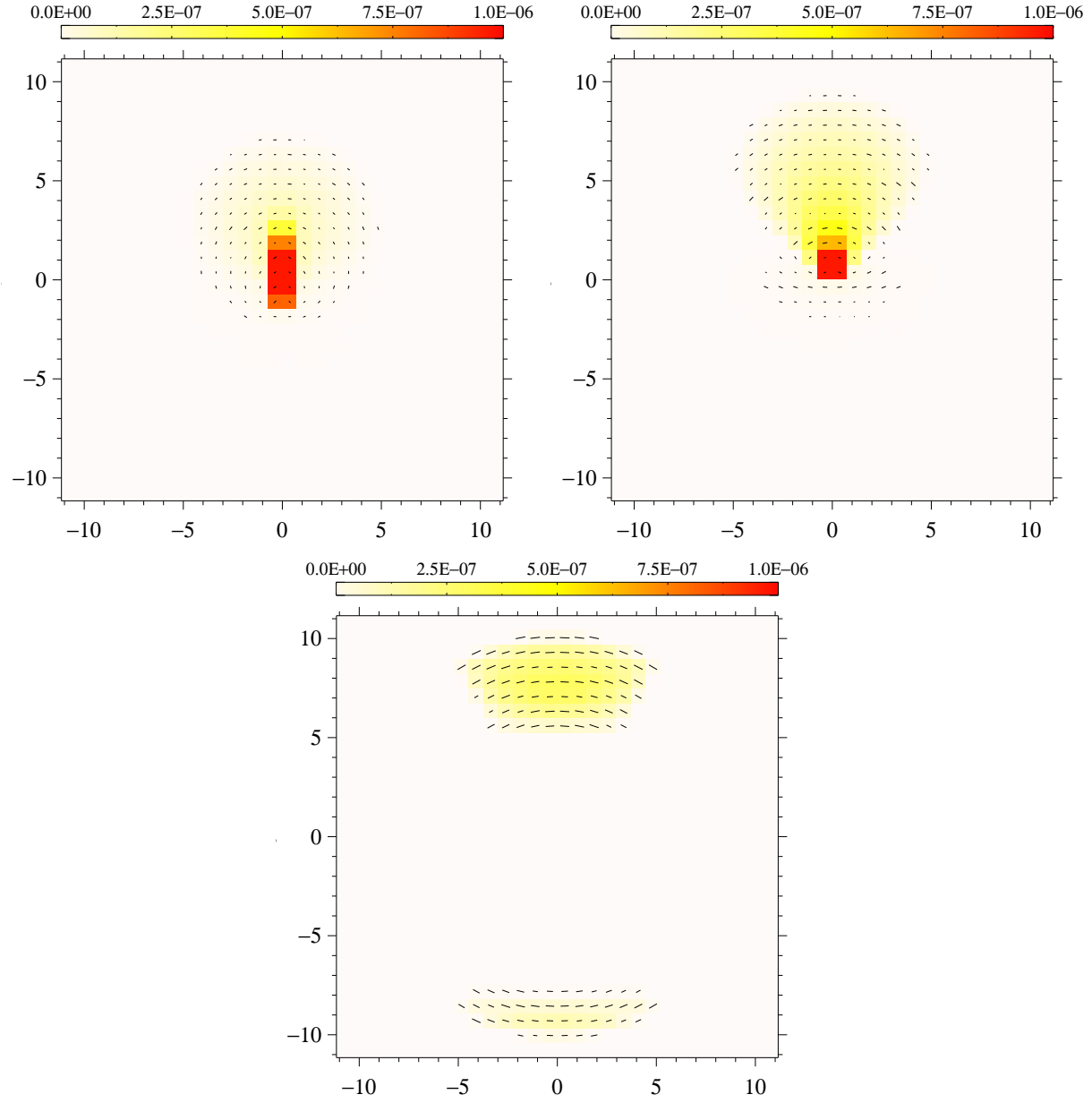

Figure 4.18: Modeling the polarized flux, PF/F_*, of electron-filled, polar outflow combined with an optically thick, dusty torus; PF/F_* color-coded and integrated over all wavelengths. *Top-left*: face-on image; *top-right*: image at $i \sim 45°$; *bottom*: edge-on image.

(see Sect. 4.1.2), the situation is reversed. This shows how the reflected flux from the far cone is partially blocked by the optically thick torus. Nevertheless, a significant polarized flux comes from the central region of the model, which is caused by the combined scattering inside the bases of the double cone and off of the inner torus walls, both producing perpendicular polarization. The two scattering regions thus reinforce each other in terms of polarization efficiency and the net polarization is, of course, perpendicular.

flared disk	dusty torus	polar outflows
$R_{\rm min} = 3.10^{-4}$ pc	$R_{\rm min} = 0.25$ pc	$R_{\rm min} = 1$ pc
$R_{\rm max} = 5.10^{-4}$ pc	$R_{\rm max} = 100$ pc	$R_{\rm max} = 10$ pc
half-opening angle = 10°	half-opening angle = 30°	half-opening angle = 30°
equat. optical depth = 1	equat. optical depth = 750	vertical optical depth = 0.03

Table 4.1: Parameters for a thermal AGN model consisting of three scattering regions. The polar outflows and torus half-opening angles are measured with respect to the vertical symmetry axis of the torus. The half-opening angle of the flared disk is measured from the equatorial plane.

At an intermediate viewing angle, the double cone is more significantly hidden and the far cone is no longer visible at all. Much polarized flux still comes from the near cone, and compared to the isolated outflow, the gradient in PF/F_* between the base and the outer regions is more shallow. This is related to the collimating effect of the torus funnel that efficiently channels photons (back) toward the outflow. Moreover, we point out the presence of a secondary scattering component coming from regions of the dusty torus that are not directly exposed to the source irradiation. When compared with the polarization map at intermediate view toward an isolated torus (see Sect. 4.1.1), this component becomes particularly visible on surfaces of the torus that are on the near side with respect to the line of sight. The photons that constitute this component have first undergone back-scattering inside the outflow and then were scattered off of the torus surface and toward the observer. This process is possible because the dusty torus has a significant average albedo of ~ 0.57 in the optical/UV band.

Finally, at edge-on view, the more distant areas of both the upper and the lower parts of the double cone are visible in reflection again. The center of the image shows no polarized flux due to the entirely opaque torus. The two extensions of the outflow scatter photons around the opaque torus and thereby produce strong polarization at a perpendicular orientation. Visualizing the polarized flux therefore enables us again to have a periscope view at the hidden nucleus.

4.3 Modeling a three-component AGN

To approach the unified AGN scheme, we built a complex model composed of three radiatively coupled reprocessing regions: around the point-like, emitting source we arranged an equatorial electron scattering disk, polar electron outflows, and an obscuring dusty torus. The parameters of the model are summarized in Table 4.1. We investigated the polarization spectra and images for this particular model and then explored the parameter space in more detail by varying the geometry and optical depths of the equatorial and polar scattering regions.

4.3.1 Spectral modeling results

The spectral results for the model described in Tab. 4.1 are shown in Fig. 4.19. At pole-on view, P is negative in the UV (parallel polarization) but of very low magnitude as the system appears to be almost axis-symmetric. Similarly to the polarization spectrum obtained for the combination of a dusty torus and an equatorial scattering disk, a sign inversion is detected between shorter and longer wavelengths. With respect to the results of Fig. 4.15 (top), the transition wavelength is shifted by the additional presence of the polar outflows. The exact wavelength at which the polarization angle switches also depends on the adopted outflow geometry and optical

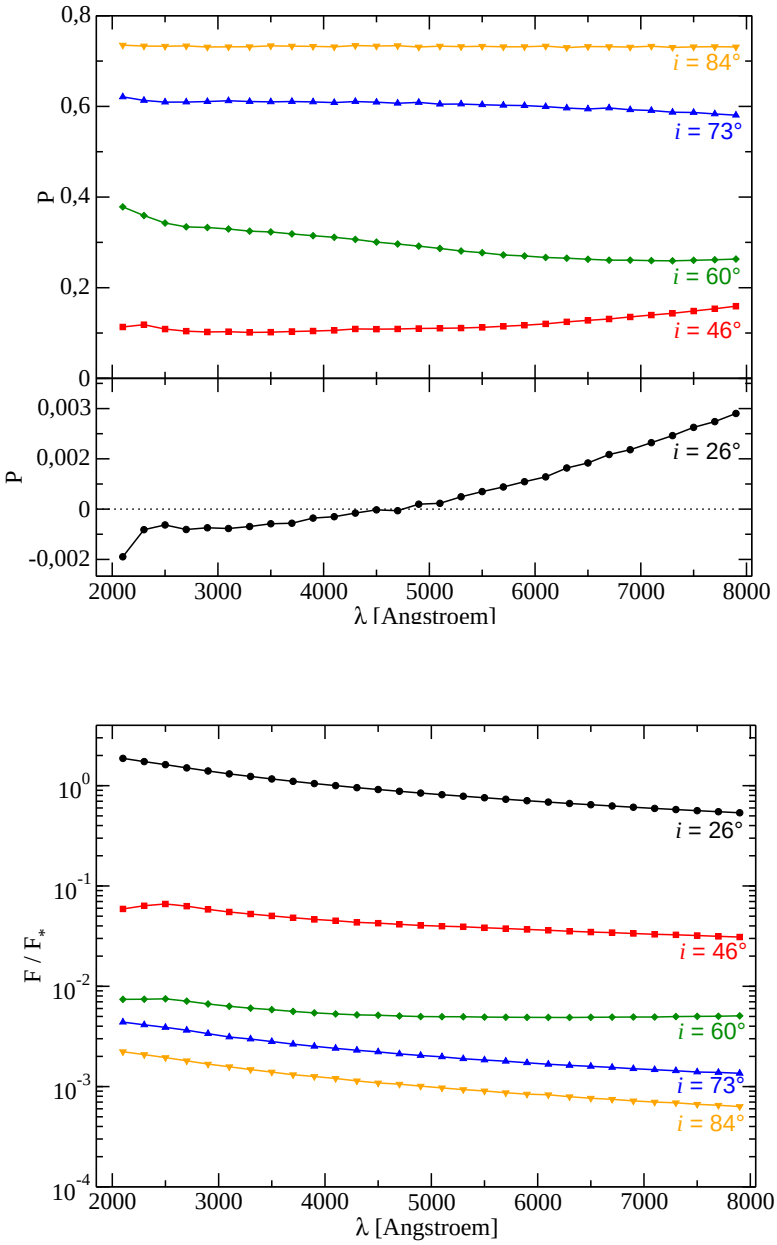

Figure 4.19: Modeling the unified scheme of a thermal AGN by three reprocessing regions (see text). *Top*: Polarization, P, as a function of viewing inclination, i; *bottom*: the fraction, F/F_*, of the central flux F_*.

depths. At intermediate viewing angles, the effects of Mie scattering are visible by a weak feature in the UV band and a slight slope of the polarization spectrum over optical wavelengths. The F/F_* spectrum also reveals the influence of wavelength-dependent dust scattering and absorption in the torus funnel by a gradually decreasing flux toward longer wavelengths, which is caused by the additional electron scattering inside the torus funnel (see the discussion in Sects. 4.2.2 and

4.2.3). A small peak of the flux around 2175 Å is caused by carbonaceous dust and visible at low and intermediate viewing angles. When i is increased even more the radiation becomes dominated by wavelength-independent, nearly perpendicular electron scattering inside the polar winds and P can achieve high values of more than 70%.

4.3.2 Wavelength-integrated polarization images

The polarization maps of our thermal AGN model are presented in Fig. 4.20. At pole-on view (Fig. 4.20, top-left), the distribution of the polarized flux is somewhat similar to the one obtained for the combination of an equatorial disk and a dusty torus only (Fig. 4.16, top-left); the effect of the polar outflows on the polarization at this viewing angle is quite small; with the strongest polarized flux coming from the equatorial scattering disk, the net polarization is parallel – as is observed in many type-1 AGN.

At intermediate viewing angles, the equatorial disk and the primary source are hidden by the optically thick torus. Nevertheless, the polarization produced at the base of the near cone (seen in reflection) is influenced by scattering inside the equatorial disk. The equatorial disk scatters a certain fraction of the primary radiation toward the outflows and induces parallel polarization. The perpendicular polarization caused by the secondary scattering inside the electron-filled double-cone is thus weakened when compared to the model that does not include the equatorial scattering disk (see Fig. 4.18, top-right).

The base of the far cone is not visible because it is hidden behind the opaque torus. Instead we detect, as in the modeling presented in Fig. 4.18 (top-right), a low polarized flux scattered off the near inner surfaces of the torus. The photons of this flux have been back-scattered from the polar winds onto the torus and then towards the observer. The overall polarization position angle at intermediate viewing angles is $\psi = 0°$.

At edge-on view (Fig. 4.20 bottom), only the most upper and lower parts of the double cone appear above and below the body of the torus, which completely hides the central region of the model. The polarization effects caused by the equatorial disk are now largely exceeded by scattering in the outflows at almost perpendicular scattering angles. The resulting net polarization is therefore perpendicular and of high degree. Note that the adopted viewing angle in Fig. 4.20 is close but not exactly equal to 90°, which explains the asymmetry between the top and bottom part of the polar winds.

In Fig. 4.21 and 4.22 we show the pole-on and edge-on polarization map at two different wavelengths, 2175 Å (UV, top) and 7500 Å (optical, bottom), respectively. For all viewing directions a higher PF/F_* is observed at 2175 Å, which is mainly caused by the larger spectral flux F/F_* in the UV because the polarization is almost wavelength-independent (see Fig. 4.20). In Sects. 4.2.1 and 4.2.2, we have explained the importance of additional electron scattering inside the funnel for the resulting polarization. The polarization maps additionally illustrate the mechanism. At pole-on viewing angles, the polarized flux in the UV comes from a larger surface area around the torus funnel showing that photons that are scattered to these positions have a higher probability to escape toward the observer than in the optical. Some of these UV photons are then scattered again in the polar outflows and are redirected toward the observer, which is why the scattered UV-flux from the winds is more significant at an edge-on view.

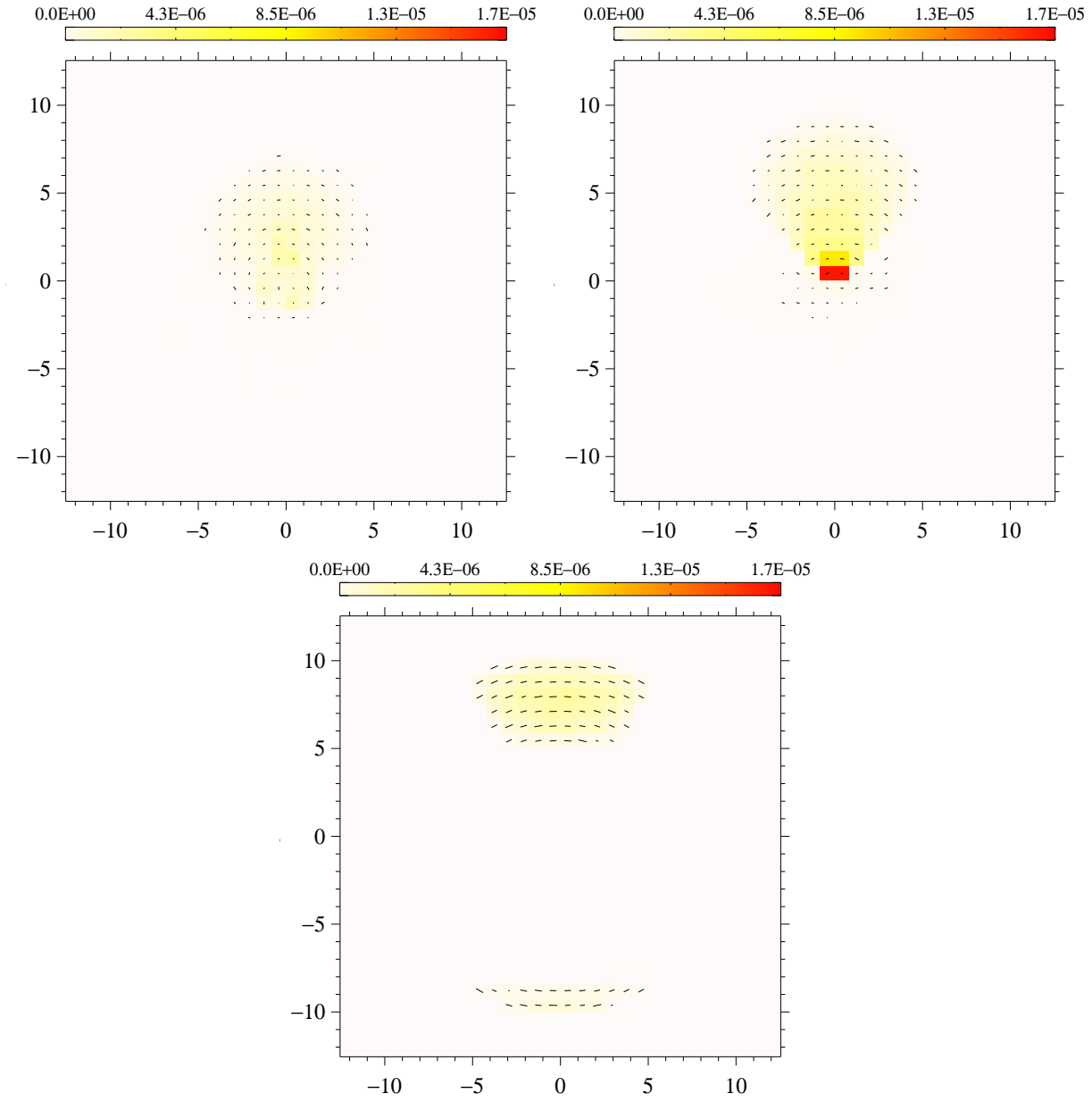

Figure 4.20: Modeling the polarized flux, PF/F_*, induced by complex reprocessing in a unified model of AGN. We combined an electron-filled, equatorial scattering disk, electron-filled polar outflows, and an optically thick dusty torus; PF/F_* is color-coded and integrated over all wavelengths. *Top-left*: face-on image; *top-right*: image at $i \sim 45°$; *bottom*: edge-on image.

4.3.3 The impact of geometry and optical depth

Starting from our base-line model of a thermal AGN, we investigated how the spectropolarimetric results depend on several crucial model parameters. We computed a grid of models by varying the half-opening angle of the dusty torus and the polar winds as well as the optical depth of the electron scattering regions. We considered a common half-opening angle of the torus and

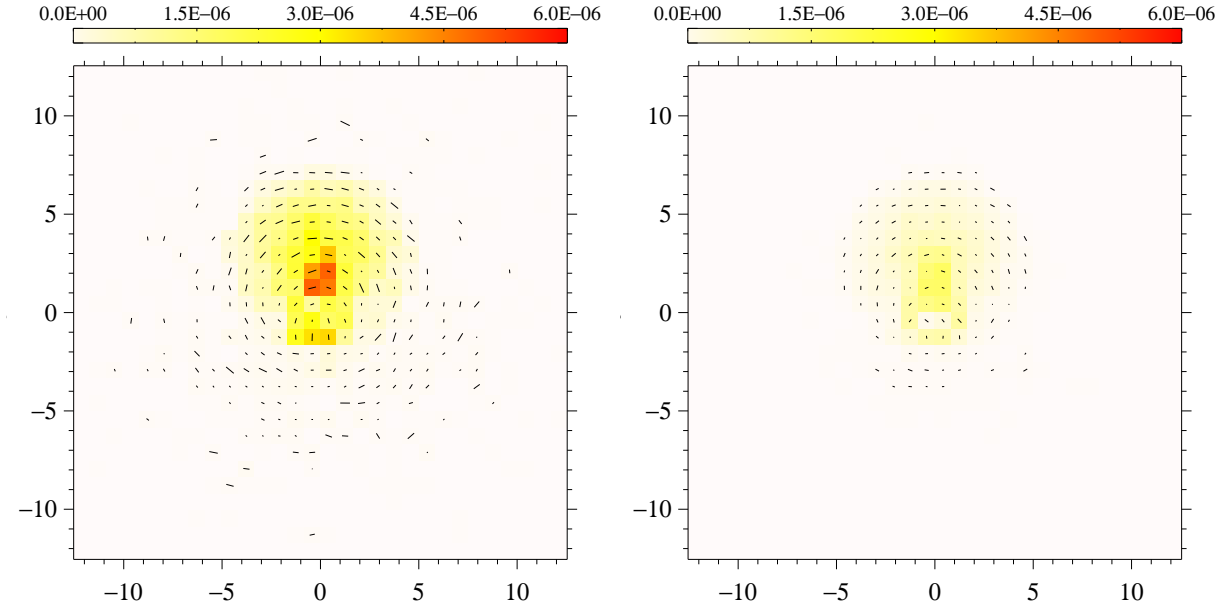

Figure 4.21: Modeling the polarized flux, PF/F_*, of an AGN composed of an equatorial scattering disk, electron-filled, polar outflows and an optically thick dusty torus; PF/F_* is color-coded and integrated over all wavelengths. *Left*: pole-on image at $\sim$ 2175 Å; *right*: pole-on image at $\sim$ 7500 Å.

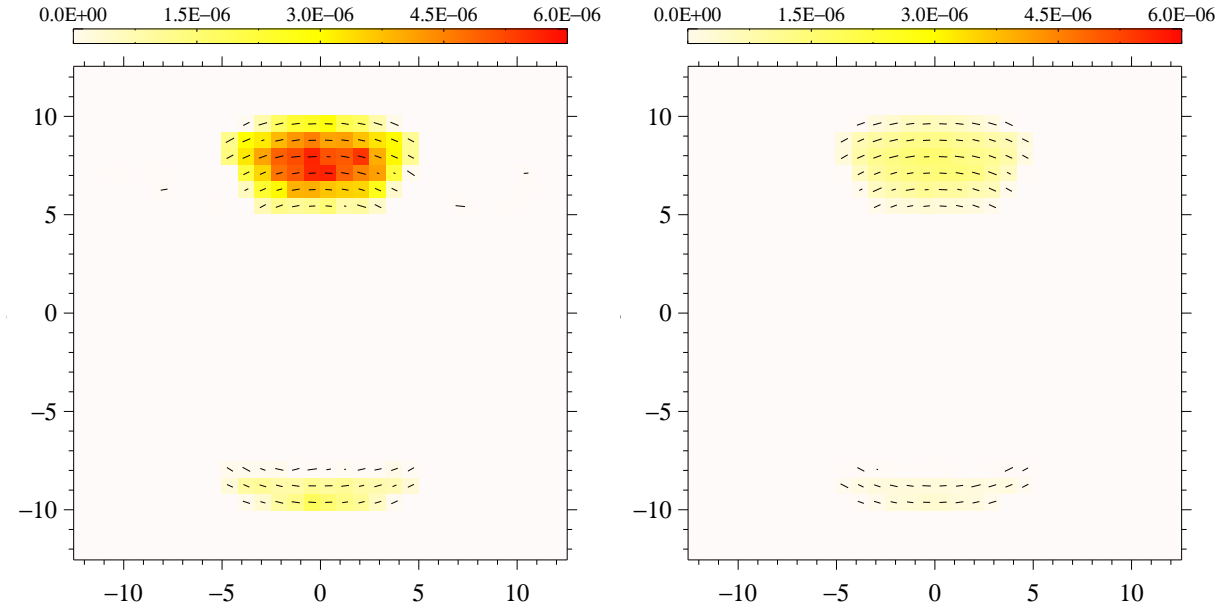

Figure 4.22: Modeling the polarized flux, PF/F_*, of an AGN composed of an equatorial scattering disk, electron-filled, polar outflows and an optically thick dusty torus; PF/F_* is color-coded and integrated over all wavelengths. *Left*: edge-on image at $\sim$ 2175 Å; *right*: edge-on image at $\sim$ 7500 Å.

the polar outflow and varied it between 30° and 60°, thereby implicitly assuming that the torus always collimates the outflow. The different optical depths assumed in the winds and the equatorial scattering regions can be interpreted as different mass transfer rates in both the accretion and the ejection flow.

A major motivation for our model grid is to explore the behavior of the polarization dichotomy between type-1 and type-2 thermal AGN. Bearing in mind the results obtained in Sect. 4.3.1, we chose a base-line model that optimizes the production of parallel polarization at type-1 lines of sight. This means in particular that we limited the spatial extension of the polar winds that produce only perpendicular polarization; in all modeling cases, the outer parts of the winds still reach out of the torus funnel but their contribution to the polarization at a type-2 viewing angle remains moderate. We also explored a broad range of optical depths for the wind reaching down to low values (0.03 – 1) and we excluded additional dusty, polar scattering regions located farther out. We studied a range of optical depths (0.1 – 5) and half-opening angles (10°, 20°, and 30°) for the equatorial scattering disk that covered its maximum efficiency to produce parallel polarization (see Goosmann & Gaskell 2007).

We present our results in Figs. 4.24, 4.25 and 4.26 for the three half-opening angles of the equatorial scattering region, respectively. It turns out that the wavelength-dependence of P is fairly low therefore the absolute value of P is averaged in our grid. The geometry of the model strongly influences the polarization response: a narrow torus and skinny polar outflows (half-opening angle of 30° from the axis) produce strong perpendicular polarization, as was discussed in Kartje (1995) and Goosmann & Gaskell (2007). A wide opening angle of the object (half-opening angle of 60° from the axis) acts in the opposite way because it weakens the perpendicular polarization coming from the polar outflows and, at the same time, the wide torus produces parallel polarization and thereby reinforces the polarization signature of the equatorial scattering disk.

Indeed for a half-opening angle of 60°, parallel polarization is detected at nearly all type-1 lines of sight. Exceptions from this rule occur for an optically and geometrically thick equatorial disk. If the half-opening angle of the disk exceeds 30°, multiple scattering sets in; then, the mechanism that produces parallel polarization becomes less effective and may lead to a polar-scattered object (see the discussion in Smith et al. 2004) with a relatively low but perpendicular polarization at

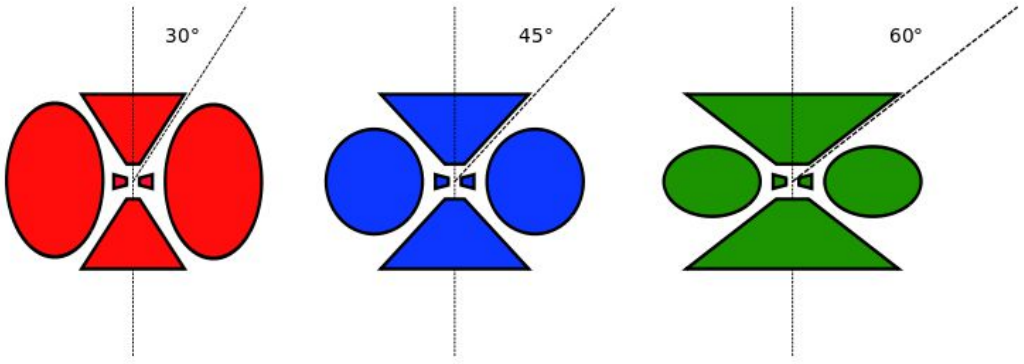

Figure 4.23: AGN model templates used for the parameter grid. The different sketches denote common half-opening angles of the torus and the polar winds of 30° (red), 45° (blue), and 60° (green).

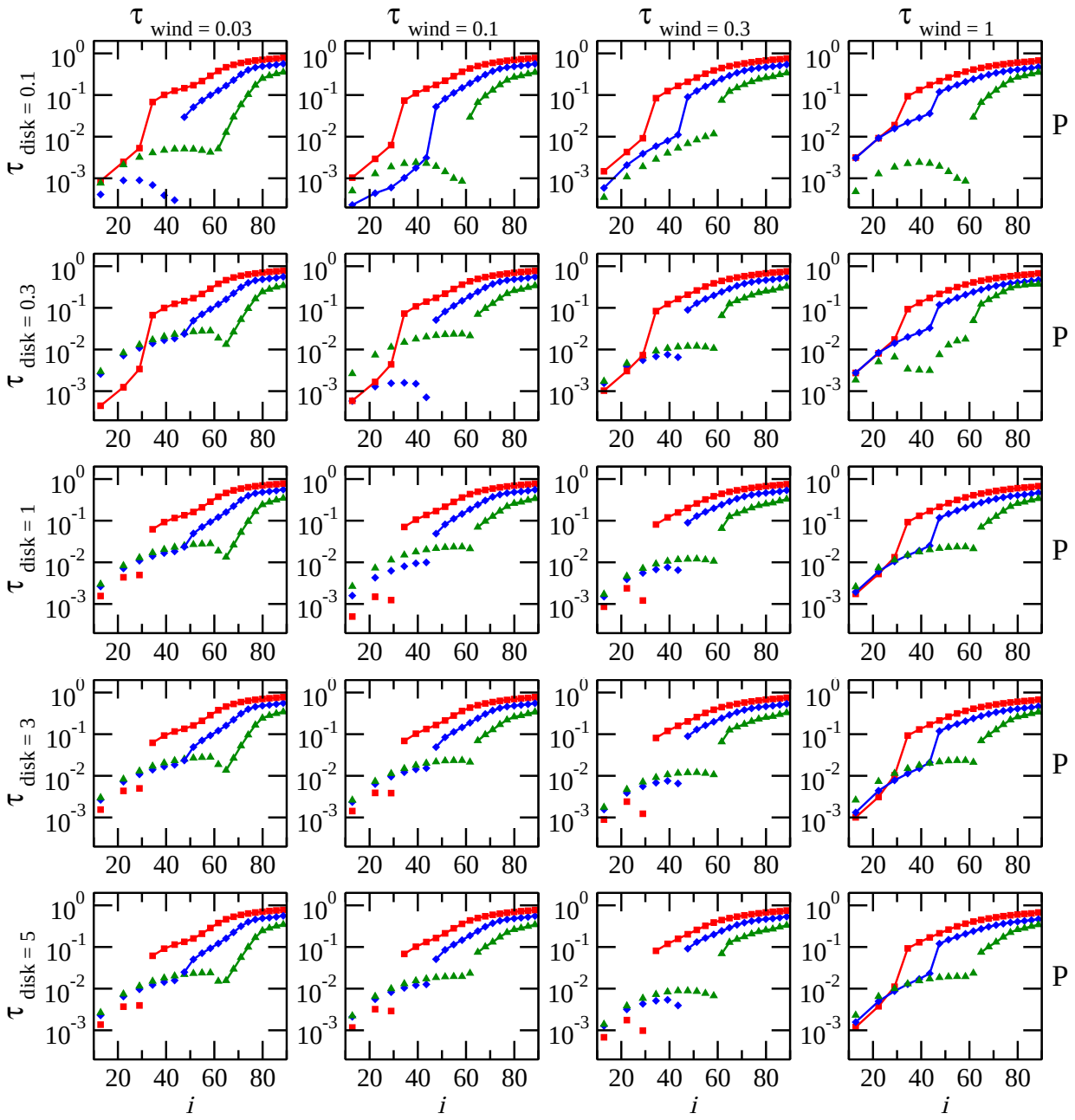

Figure 4.24: Resulting percentage of polarization, P, as a function of viewing angle, i, for a complex AGN model (see text). The half-opening angle of the equatorial scattering disk is set to 10°. *Legend:* The different curves denote common half-opening angles of the torus and the polar winds of 30° (red squares), 45° (blue diamonds), and 60° (green triangles with points to the top), see Fig. 4.23. The isolated symbols indicate a polarization position angle $\psi = 90°$ (parallel), connected symbols stand for $\psi = 0°$ (perpendicular). *From left to right*: increasing the polar outflow optical depth from 0.03 to 1; *From top to bottom*: increasing the optical depth of the equatorial disk from 0.1 to 5.

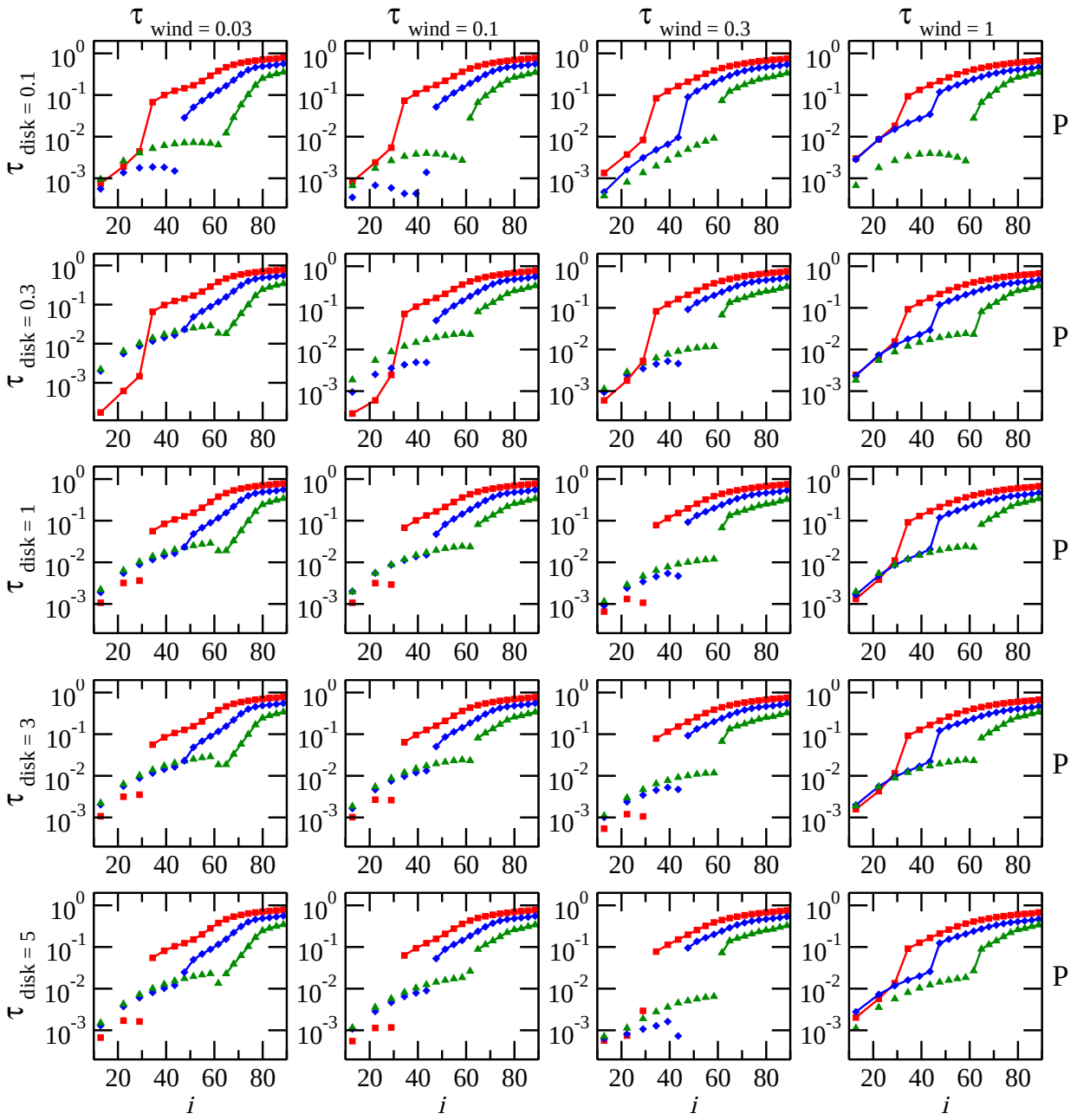

Figure 4.25: Resulting percentage of polarization, P, as a function of viewing angle, i, for a complex thermal AGN model (see text). The half-opening angle of the equatorial scattering disk is set to 20°. The legend is as in Fig. 4.24

type-1 viewing angles. This behavior occurs in particular when the optical depth of the outflow exceeds 0.3 and/or the optical depth of the equatorial disk is higher than 3.

Polar-scattered AGN are very likely to exist also for lower torus half-opening angles ($\leq 45°$ from the axis). They occur when the outflows become sufficiently optically thick ($\tau \sim 1$) or when

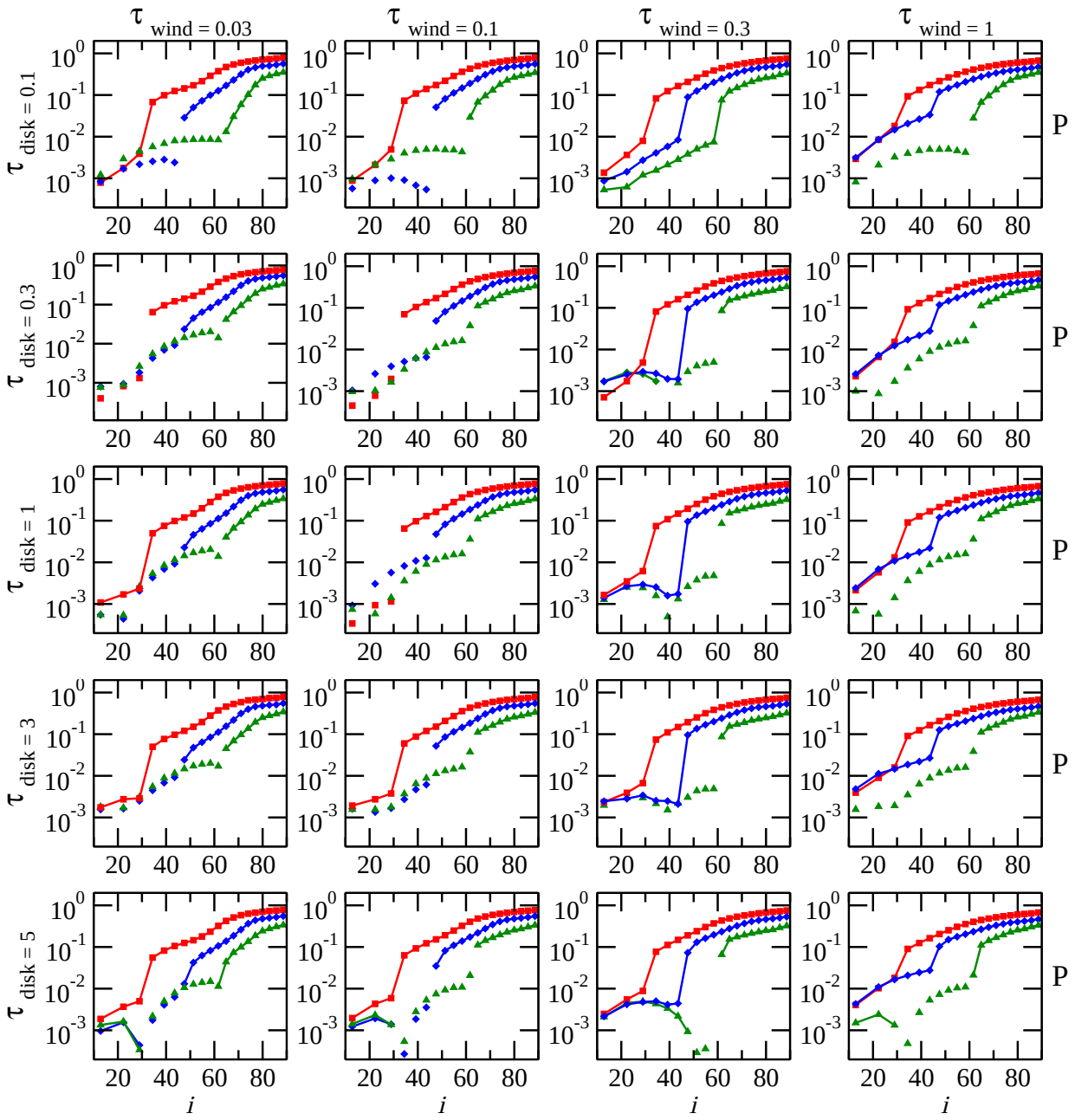

Figure 4.26: Resulting percentage of polarization, P, as a function of viewing angle, i, for a complex thermal AGN model (see text). The half-opening angle of the equatorial scattering disk is set to 30°. The legend is as in Fig. 4.24

the equatorial scattering is too optically thin ($\tau \sim 0.3$ and smaller). In all other cases, the usual polarization dichotomy is reproduced: the transition from a parallel to a perpendicular polarization angle happens when the observer's line of sight toward the primary source crosses the torus horizon. This behavior is not much affected by the geometry of the equatorial scattering disk as long as its

half-opening angle stays below 20° and the winds are not too optically thick. It turns out that the most efficient equatorial scattering geometry to induce parallel polarization in a complex type-1 AGN is obtained for a disk half-opening angle between 10° and 20°. The exact position of this optimum depends on the Thomson optical depths for equatorial and polar scattering.

With increasing type-2 viewing angle, the percentage of the perpendicular polarization rises, which is related to a more favorable scattering angle for photons coming from the polar outflows. Apart from the scattering geometry, the behavior of the polarization dichotomy depends on the Thomson optical depths of both the polar outflow and of the equatorial scattering region. The observed polarization angle at a given line of sight results from a competition between the polarization efficiency of, on the one hand, the equatorial scattering region always producing parallel polarization and, on the other hand, the polar outflows that always imprint perpendicular polarization. Owing to its significant albedo of ~ 0.57, scattering off of the opaque torus has also an important impact, but here the position angle of the polarization depends on the torus opening angle.

The polarization percentage at type-2 viewing angles as a function of the outflow's optical depth does not vary much, in particular for small or moderate opening angles of the object. The higher the Thomson optical depth of a medium, the more likely an incident photon is scattered and polarized. Up to a certain limit the polarization induced by the medium accordingly rises, but if it becomes too dense, multiple scattering starts to depolarize the radiation. Hence, increasing the wind's optical depth leads to a slightly higher P value until multiple scattering and depolarization set in and P decreases again. Investigating the impact of the flared disk's optical depth, we find that optically thin disks ($\tau \leq 0.1$) are inefficient in producing parallel polarization at type-1 views. To produce parallel polarization, the optical depth of the disk should be higher than unity. The strongest parallel polarization is obtained for a scattering disk with $1 < \tau < 3$.

Our results show that the perpendicular polarization of optically thick winds ($\tau \sim 1$) dominates over the parallel polarization coming from the equatorial disk except when the model has a large opening angle. For a more moderate and especially for a small opening angle, a net parallel polarization can be produced only when the outflows are sufficiently optically thin and, at the same time, the optical depth and the half-opening angle of the equatorial scattering region are in the right range. The interplay between polar and equatorial scattering may put constraints on the optical depth of the accretion flow if the optical depth and the geometry of the outflow in a given type-1 AGN can be estimated independently, for instance from the shape of UV and X-ray absorption lines. If it turns out that the effective optical depth in the outflow is above 0.3 and if at the same time the AGN reveals parallel polarization, we can conclude that a flattened accretion flow between the dusty torus and the accretion must be optically thick and in the range $1 < \tau < 3$.

4.4 A step further by including dusty polar outflows

As stated in Sect. 2.2.6, matter is ejected along the AGN poles in the form of an ionized outflow. Beyond the dust sublimation radius, the electron wind merges continuously with the dust grains of the host galaxy, forming the so-called low-density NLR. Capetti et al. (1999) showed that the NLR generally has a complex morphology consisting of filaments and compact emission knots (e.g. in NGC 4151) or narrow arcs (e.g. in Mrk 573). However, due to this non-trivial geometry, it may be a difficult task to obtain accurate constraints on the NLR.

So far, we have left out the NLR as it is expected to decrease the total amount of parallel polarization in type-1 AGN (see Sect. 4.3). In the following subsections, we investigate the effects

flared disk	dusty torus	ionized outflows	dusty NLR
$R_{\rm min} = 3.10^{-4}$ pc	$R_{\rm min} = 0.25$ pc	$R_{\rm min} = 1$ pc	$R_{\rm min} = 20$ pc
$R_{\rm max} = 5.10^{-4}$ pc	$R_{\rm max} = 100$ pc	$R_{\rm max} = 10$ pc	$R_{\rm max} = 70$ pc
half-opening angle = 10°	half-opening angle = 30°	half-opening angle = 30°	half-opening angle = 30°
equatorial $\tau = 0.3$	equatorial $\tau = 750$	vertical $\tau = 0.03$	vertical $\tau = 0.24$
electron scattering	Mie scattering	electron scattering	Mie scattering

Table 4.2: Parameters of the individual scattering regions in our four-component model. Note that for the polar outflow, the torus and the NLR, the half-opening angle is measured with respect to the vertical, symmetry axis of the model, while for the flared-disk the half-opening angle is taken with respect to the equatorial plane.

on the continuum polarization that can emerge from adding to our previously model an NLR-like polar scattering region that is filled with optically thin dust.

4.4.1 Spectropolarimetric signatures

To study the effect of the NLR, we presently include extended, optically thin, dusty outflows sustaining the same half-opening angle and direction as the ionized winds. However, the amount of dust associated with the NLR is difficult to constrain from the observations due to 1) a complex filamentary structure between ionized gas and dust and 2) reddening corrections in the data reduction that can be a potential source of errors as the gas to dust composition is not known (Cracco et al. 2011). Taking into account that the fraction of dust in the NLR clouds must be smaller than in the circumnuclear region and in order to allow a large fraction of the radiation to escape in a polar direction, we fix the NLR opacity to a value significantly below unity (Hoenig et al. 2012). Table 4.2 summarizes the parameters of the reprocessing regions in our models.

The resulting polarization percentage P and the fraction F/F_* of the central flux, F_*, as a function of the viewing angle for both the three-component and the four-component model are shown in Fig. 4.27. As expected, the overall polarization behavior for the model including the NLR (Fig. 4.27, top left) is different from the results obtained for the three-component model (Fig. 4.27, top right). When adding the NLR, the global amount of polarization in type-2 objects decreases due to a combination of effects; the polarized flux from the ionized outflows is diluted by the relatively weaker polarization of the flux coming from the NLR. Note that for our dust mixture (Mathis et al. 1977) the theoretical polarization degree produced by a single Mie scattering event reaches a maximum value of 35% at 8000 Å, while for electron scattering P is as high as 100%. The dilution from polar Mie scattering in the NLR is particularly efficient at edge-on viewing angles and P decreases by a factor of ~ 3 in comparison to the three-component model. Additional depolarization occurs because the photons passing through the NLR have to undergo more scattering events before they escape from the model region. Due to the wavelength-dependence of Mie scattering, the presence of the NLR also has an effect on the spectral shape of P.

Apart from the polarization, the bottom of Fig. 4.27 shows that the total (polarized + non-polarized) spectrum F/F_* decreases towards longer wavelengths in both models. This is another signature of the wavelength-dependent Mie scattering cross section and phase function. Also, a faint scattering feature at 2175 Å due to the carbonacious dust component is visible. When the NLR is included, the additional polar dust scattering increases the total flux scattered towards edge-on inclinations.

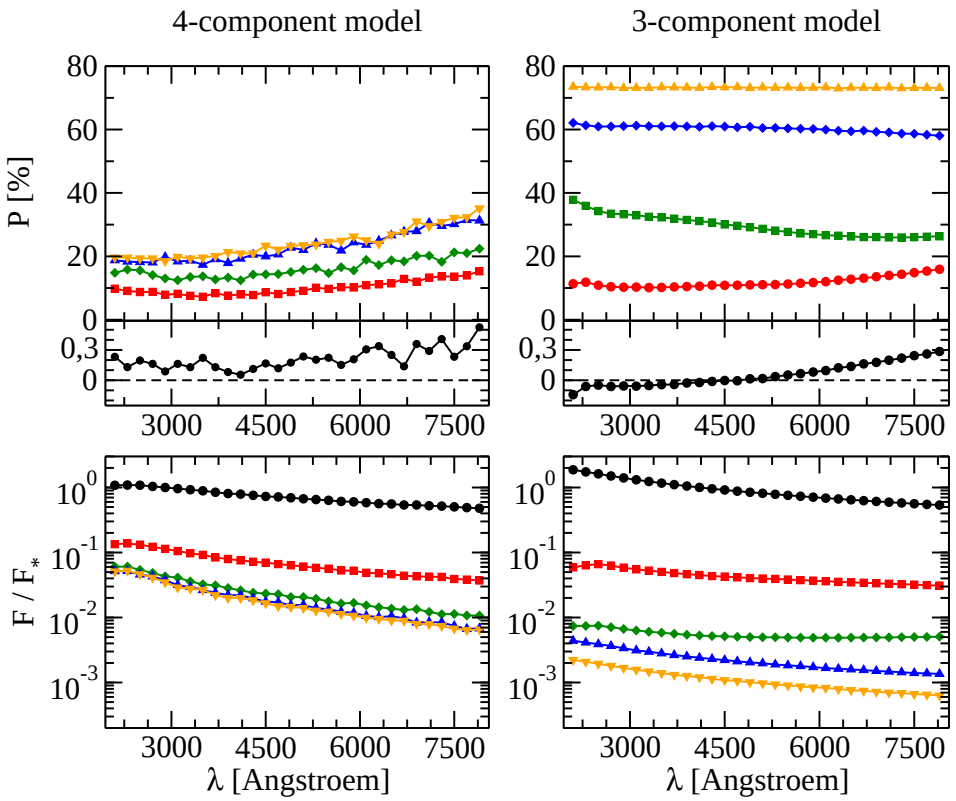

Figure 4.27: Modeling the unified scheme of a thermal AGN. *Left column*: the four-component model as described in the text. *Right column*: the three-component model as in Sect. 4.3.1. Both figures show the polarization percentage, P, as a function of viewing inclination i measured from the torus symmetry axis, and the fraction, F/F_*, of the central flux, F_*; Legend: $i = 84°$ (orange triangles with points to the bottom), $i = 73°$ (blue triangles with points to the top), $i = 60°$ (green diamonds), $i = 46°$ (red squares), $i = 26°$ (black circles).

For type-1 objects our modeling shows that the additional dust scattering in the NLR can switch the $\vec{E}$-vector from a parallel to a perpendicular polarization state. While for the three-component model the polar view exhibits parallel polarization below 4500 Å (Fig. 4.27, top right, lower panel), the polarization is perpendicular across the whole wavelength range in the four-component case (Fig. 4.27, top left, lower panel). Given the resulting weak percentage ($< 0.5\%$) of the perpendicular polarization, this model setup is coherent with the so-called *polar scattering dominated* AGN (Smith et al. 2002b). Such type-1 AGN present a perpendicular, optical polarization rising towards the blue that Smith et al. (2002b) explained by dust extinction along a line of sight passing through the upper layers of the torus material. Our model qualitatively produces a similar wavelength-dependent polarization, but at a much lower viewing angle. However, the relatively low optical depth of the polar dust scattering does not reproduce the full extend of the observed rise in P towards the blue end of the spectrum.

4.4.2 Wavelength-integrated polarization maps

The polarization maps of our thermal, four-component AGN model are presented in Fig. 4.28. At the pole-on view (Fig. 4.28 top-left), the polarization map is saturated by the polarized flux originating from the emitting source (center of the map). Photons have traveled through both the electron and dusty winds and then carry a higher polarized flux than photons reprocessed on the torus inner walls and then scattered to the borders of the NLR. Thus, the pole-on polarization map shows a bright central polarized flux knot. At greater distances, the polarized flux is lower and photons have a smaller P. The integrated polarization angle is perpendicular as expected from Fig. 4.27 results.

At an intermediate view (Fig. 4.28 top-right), the most important polarized flux source is coming from the ionized winds identified by its perpendicular and constant P. The second (in terms of intensity) polarized flux is the NLR cloud which extend up to 70 parsecs. Both the polarized flux and P are smaller than in the ionized outflows. Finally, we detect a low polarized flux scattered off the near inner surfaces of the torus. Back-scattered from the polar outflows (both the ionized wind and the NLR) onto the torus and then towards the observer, those photons highlight the tori shape and then can put constraints on its spatial extension. The overall photon polarization angle is perpendicular.

At an edge-on view (Fig. 4.28 top-right), the emitting source is totally hidden by the dusty structure. Similarly to the intermediate viewing angle polarization map, most of the polarized flux is originating from the small ionized outflows. However, contrary to the expected behavior inferred in Watanabe et al. (2003), Goosmann & Gaskell (2007) and in Sect. 4.1.2, the polarized flux is higher in the cone upper part. It is due to the presence of the NLR and its dusty composition as Mie scattering phase function promotes forward and backward scattering. Photons that escape from the ionized wind have a chance to scatter on the NLR wind base and being backscattered to the ionized wind. As a result, a higher incident flux impinges on the upper part of the ionized outflows and thus produces a greater polarized flux. We finally note that the integrated photon polarization angle remains perpendicular.

4.4.3 Extensive grids of parameters

It is now interesting to look at the impact of dusty outflows on the spectropolarimetric signatures of our grid of models. Re-using the four-component model of a thermal AGN (Tab. 4.2), we computed the same grid as in Sect. 4.3.3 for four different NLR optical depths ranging from 0.03 to 1. The different optical depths assumed in the dusty winds can be interpreted as different ISM densities around the AGN central engine. We considered that the half opening angle of the NLR outflow is the same as the ionization cones, as it is a collimated extension of the inner AGN polar winds. Since NLR scatterers are enhancing the detection of perpendicular polarization, we opted for an electron-filled equatorial disk that maximizes the production of parallel polarization. To do so, we choose to fix the half opening angle at 10° and the optical depth at unity. Our main motivation here is to extrapolate new constraints on the NLR clouds.

The spectropolarimetric grid of the four-component model is presented in Fig. 4.29. Considering an optically thin NLR ($\tau_{NLR} \leq 0.1$), polar dust scattering is not found to impact the resulting polarization position angle. The polarization dichotomy is preserved between type-1 and type-2 inclinations. However, while being smaller than for a NLR-free model, the net polarization signal tends to increase with increasing values of τ_{wind}: for ionization cones with low opacity and for lines-of-sight close to the equatorial plane, P is lower than in Fig. 4.24 by a factor ~ 2.8. When the ionization cones optical depth is rising, so do P. For $\tau_{wind} = 1$, the polarization signal is only lower

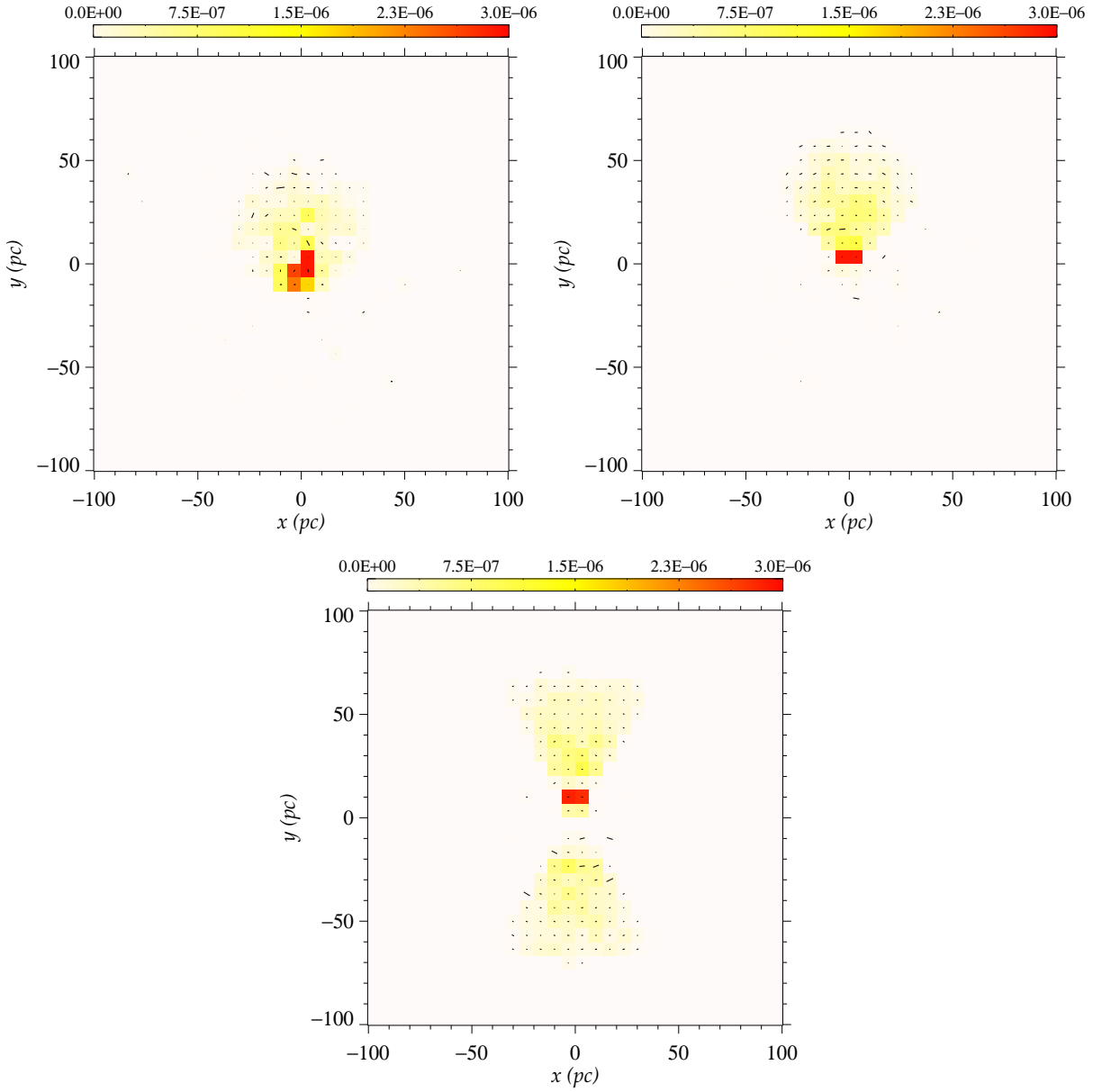

Figure 4.28: Modeling the polarized flux, PF/F_*, induced by complex reprocessing in a unified model of AGN. We combine an electron filled, equatorial scattering disk, an optically thick dusty torus, electron filled polar outflows and extended optically thin dusty polar NLR. PF/F_* is color-coded and integrated over all wavelengths. *Top-left*: face-on image; *top-right*: image at $i \sim 45°$; *bottom*: edge-on image.

by a factor ~ 1.2. This trend is also seen for $\tau_{NLR} > 0.1$, but the poloidal dust is now impacting the polarization dichotomy. For geometrically thick dusty torus ($\theta = 30°$), parallel polarization tends to disappear when the opacity of the ionized wind is superior to 0.1 at $\tau_{NLR} = 0.3$. For higher NLR opacities, medium-sized torus configurations ($\theta = 45°$) also present perpendicular photon position angle at polar inclinations. The resulting polarization degree at large NLR optical depths is lower

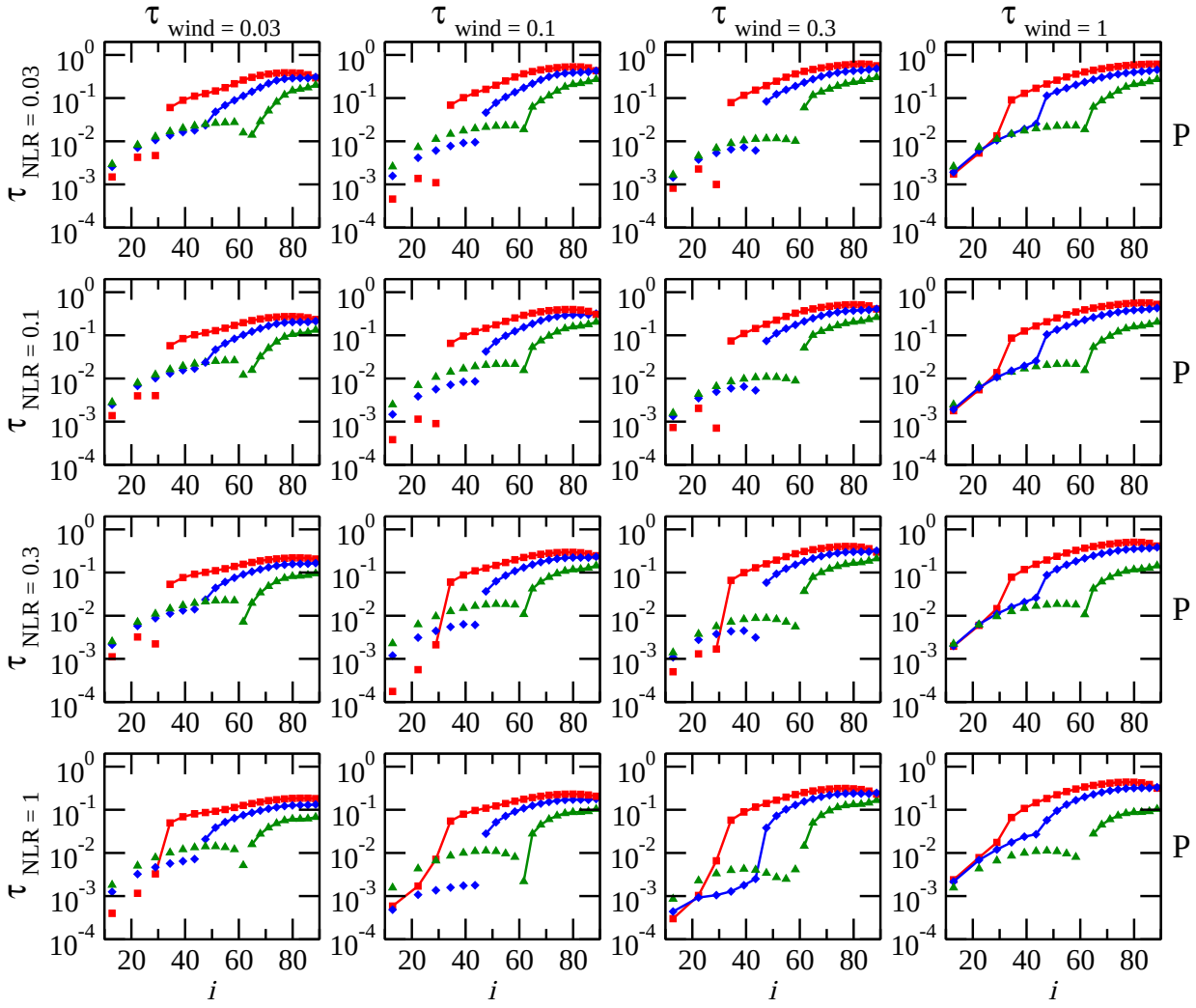

Figure 4.29: Resulting percentage of polarization, P, as a function of viewing angle, i, for a complex AGN model (see text). The half-opening angle of the equatorial scattering disk is set to 10° and its optical depth to unity. *Legend:* The different curves denote common half-opening angles of the torus and the polar winds of 30° (red squares), 45° (blue diamonds), and 60° (green triangles with points to the top). The isolated symbols indicate a polarization position angle $\psi = 90°$ (parallel), connected symbols stand for $\psi = 0°$ (perpendicular). *From left to right*: increasing the polar outflow optical depth from 0.03 to 1; *From top to bottom*: increasing the optical depth of the NLR clouds from 0.03 to 1. The figure must be compared to the model with the same parameters but no NLR, resumed hereafter and extracted from Fig. 4.24.

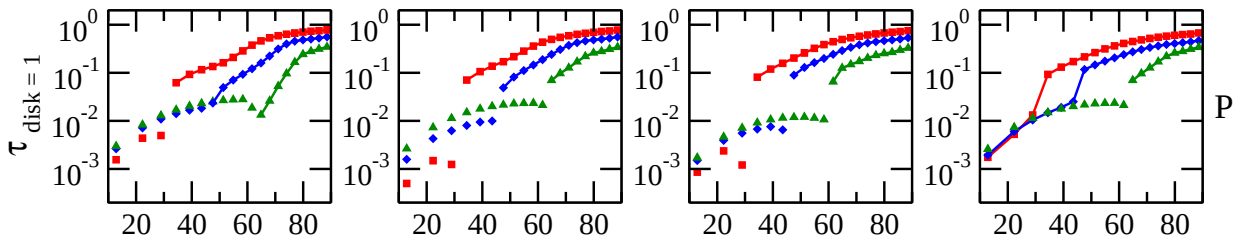

than for $\tau_{NLR} \leq 0.1$, down to 17 % for type-2 orientations, $\tau_{wind} = 0.03$.

Similarly to our conclusions in Sect. 4.4.1, adding a NLR cloud to our previous model tends to diminish the resulting polarization degree, particularly at type-2 inclinations. However, its impact onto the polarization dichotomy strongly depends on the NLR opacity. At $\tau_{NLR} \leq 0.1$, parallel polarization is preserved at polar viewing angles. A rotation of the polarization position angle starts for bulk torus configurations at $\tau_{NLR} \sim 0.3$. For high opacities, only geometrically thin dusty torus are able to maintain a polarization dichotomy between type-1 and type-2 viewing angles. Our conclusions are thus in agreement with the torus geometrical predictions derived in Sect. 4.3.3 and with the NLR opacity limit ($\tau_{NLR} < 1$) of Hoenig et al. (2012).

4.5 Summary and discussion

An important motivation of the work presented in this chapter has been to investigate the net polarization caused by radiative coupling between the continuum source and different reprocessing regions of an AGN.

We considered electron scattering in an equatorial disk and in polar outflows as well as dust reprocessing by an obscuring torus and an NLR-like cloud. At first approach, it is reasonable to assume that the torus funnel collimates both the electron and dusty polar outflows, which simplifies this multi-parameter problem. As a result, five parameters remain: the half-opening angles of the equatorial disk and of the torus/winds as well as the optical depths of the two electron scattering regions and of the NLR. The torus was always considered to be optically thick. Apparently the net polarization as a function of the viewing angle is most sensitive to the half-opening angle of the system and to a lesser extent on the geometry of the scattering disk, at least as long as it does not exceed a half-opening angle of 20° measured from the equatorial plane. A thicker equatorial disk favors multiple scattering and a partial disappearance of the parallel polarization. The optical depths of both electron scattering and of the dusty wind have a significant impact once they exceed ~ 0.3. Our modeling shows that including multiple scattering effects inside a given scattering region and between several scattering regions is important.

In the general case of a unified model, it is possible to reproduce the observed dichotomy of the polarization angle for thermal AGN within a limited range of geometries and optical depths:

(1) A flat, equatorial scattering region with $1 < \tau < 3$ is required to generate the observed parallel polarization in type-1 AGN. This indicates that the accretion flow at the outer edge of the accretion disk in Seyfert-1 galaxies is optically thick.

(2) A wide half-opening angle ($\sim 60°$) for the torus helps to produce parallel polarization, whereas narrow tori and/or a higher optical depth of the polar outflow produce polar-scattering-dominated AGN (the same AGN show perpendicular polarization when seen at a type-1 viewing angle).

(3) At type-2 viewing angles, all cases we modeled produced perpendicular polarization that often is significantly stronger than the observed polarization percentage. Again, a wide half-opening angle of the torus and the wind help to lower this discrepancy with respect to the observations. It is likely, though, that a more significant moderation of the perpendicular polarization is caused by a clumpy structure.

(4) Detailed observations and modeling of the polarization spectrum may give hints on the presence of an equatorial electron scattering inside the torus funnel. We found that the equatorial scattering region leads to a more concave polarization spectrum than dust scattering

off the inner torus walls alone. Consequences of this polarization behavior are investigated in further details in the end of Sect. 4.5.2.

When compared to the observed optical/UV polarization, our systematic modeling can thus put constraints on certain AGN properties, as we discuss in more detail in the following sub-sections, after a brief review of previous modeling codes.

4.5.1 Comparison with previous modeling work

There are several radiative transfer codes that include optical/UV polarization and that are applied in AGN research. Some of them only refer to continuum polarization (see e.g. Brown & McLean 1977; Manzini & di Serego Alighieri 1996; Kartje 1995; Wolf & Henning 1999; Watanabe et al. 2003) while others include details about the polarization of spectral lines (see e.g. Young 2000; Wang & Zhang 2007). Earlier works often applied semi-analytical or single-scattering methods. With greater computational power, Monte Carlo methods that include multiple scattering and more arbitrary geometries became suitable. In this section, we relate and compare our results to previous modeling work that is similar to ours.

To our knowledge, Wolf & Henning (1999) were the first and so far the only authors to simulate polarization images in the context of AGN. Their Monte Carlo code is based on earlier work by Fischer et al. (1994) which was also an important inspiration during the early development of STOKES. In their application to AGN, Wolf & Henning (1999) included Mie scattering by two types of dust and electron scattering. Several reprocessing regions were investigated and gave rise to theoretical spectra and images of the intensity and polarization as a function of the viewing angle.

The AGN model adopted by Wolf & Henning (1999) is composed of (1) an obscuring dusty torus, (2) an electron-filled inner region and bi-conical outflow, and (3) an outer, dusty, bi-conical outflow. The authors showed that multiple scattering has an impact on the polarization as soon as the optical depths involved are higher than 0.1. A comparison to the geometry that we adopted in our work is not straightforward as there are differences in the details. For instance, the dusty torus employed by Wolf & Henning (1999) includes a cylindrical funnel. However, in our modeling we found a similar dependence of the polarization percentage on the viewing angle and also a good match in polarization images. We would like to point out that Wolf & Henning (1999) also investigated the effects of electron scattering inside the torus funnel. Their figure 13 shows that the resulting polarization spectrum becomes more concave for more centralized distributions of electrons. This agrees with our results and in Sects. 4.2.2 and 4.2.3 we gave an explanation of the effect based on the Mie scattering phase function and scattering geometry. Note that Kartje (1995) also considered the effects of additional electron scattering inside the torus but he did not vary the geometry of the electron distribution.

By also including a discussion on the net polarization angle as a function of viewing direction, we here extend the modeling performed by Wolf & Henning (1999), who did not discuss the polarization dichotomy. Producing parallel polarization for type-1 objects must be very hard in their adopted geometry as it lacks an equatorial scattering disk. Equatorial scattering, however, is included in the Generic Scattering Model (GSM) by Young (2000) and was subsequently applied by Smith et al. (2004) to explain strong, yet systematic variations of the polarization across broad emission lines. In addition to the interesting dynamical constraints that the model provided for the BLR, it also predicts a sequence in viewing angle for the continuum polarization. This sequence runs from type-1 AGN with parallel polarization to the so-called polar scattering dominated type-1

objects with perpendicular polarization (see Sect. 4.5.3.2) and ends at the type-2 AGN, again with perpendicular polarization.

The GSM analytically combines the polarized flux from the equatorial and polar scattering regions in a semi-analytical manner assuming single scattering. In Smith et al. (2004), the authors chose a Thomson optical depth of 0.2 for both electron scattering regions, a torus half-opening angle of 45° and an equatorial scattering disk with a half-opening angle of 20° or 30°. This configuration produced the strongest polarized flux with parallel polarization at type-1 viewing angles. Our Figs. 4.25 and 4.26 indicate that for a comparable case modeled with STOKES, the resulting polarization at type-1 viewing angles is somewhat low compared to the observed range of generally $\sim 0.3\% - 1.3\%$ (see Table Smith et al. 2002b) or can even adopt a perpendicular polarization angle. One should take into account, however, that in our model we used a different geometrical shape for the equatorial scattering disk, a uniform density in all scattering regions, and we also considered the effects of multiple dust and electron scattering. Therefore, a comparison between both modeling schemes is not straightforward. We agree with Smith et al. (2004) in that a fairly flat equatorial scattering disk is required (half-opening angle <= 20°), but we prefer it to have a higher optical depth. Moreover, we found that systems with a torus half-opening angle significantly larger than 45° are better suited to produce the observed amount of parallel polarization in type-1 objects. We discuss the implications of our modeling on the polarization dichotomy in more detail in the following section.

4.5.2 Polarization at type-1 and type-2 viewing angles

In Sect. 4.3.3 and Sect. 4.4.3, we showed that for all modeling cases the polarization detected at a type-2 angle is strong and perpendicular. Even the most efficient equatorial scattering cannot force the net polarization to be parallel. If a thermal type-2 object with parallel polarization is observed, it cannot be explained by our current model and a possible re-interpretation then would be that the small-scale radio axis does not coincide with the symmetry axis of the dusty torus and/or the outflow.

The modeled perpendicular polarization at type-2 viewing angles covers a range of 17% to 80% for edge-on viewing angles. This would exclude the vast majority of Seyfert-2 galaxies that were analyzed by Kay (1994) and mostly showed polarization up to only 10%. Under the reasonable assumption that the distribution of viewing directions toward Seyfert galaxies is uniform, our modeling therefore suggests that the half-opening angle of most Seyfert-2 galaxies should be large, i.e., at least 60°. This conclusion would be consistent with the evolution model for Seyfert galaxies and the type-1/type-2 number counts given by Wang & Zhang (2007) but exceed those by Schmitt et al. (2001). On the other hand, it is not clear that the assumption of a universal half-opening angle for all dusty tori is realistic.

The situation is different for Seyfert-1 galaxies. The spectropolarimetric data collected by Smith et al. (2002b) and Smith et al. (2004) show low polarization percentages mostly staying below 1%. However, it can have a parallel, perpendicular and sometimes also intermediate position angle. On the modeling side, the situation is equally ambiguous: narrow (i.e., geometrically thick) tori and outflows favor the production of perpendicular polarization for type-1 AGN while systems with wide (i.e., geometrically thin) tori and winds more likely produce type-1 AGN with parallel polarization, even when the outflows are optically thick. For the case of narrow tori, ionized outflows with an electron optical depth ranging from 0.03 to 1 still allows us to produce parallel net polarization at a type-1 viewing angle. Denser ionized winds ($\tau_V \geq 1$) then switch the polarization to perpendicular. Adding a polar, dusty outflow to the picture is a second method to produce

perpendicular polarization at type-1 inclinations if the dust opacity is superior to 0.3 for narrow tori. Intermediate-sized tori may present a constant parallel photon polarization angle is the NLR optical depth is equal to unity. In any case, the resulting polarization percentage is low and therefore matches the observed values quite well.

However, it is noteworthy to point out that some peculiar type-1 AGN like Mrk 231 (Gallagher et al. 2005) and many Warm Infrared Ultraluminous AGN in the survey of Hines (1994) show a relatively high polarization degree, of up to 4%. Our grid of models is indeed unable to reproduce this high percentage of polarization despite the extended space of parameters. This indicates that the clue to this high polarization level must be different from the usual optical depth and half-opening angle considerations. In blazar AGN, synchrotron emission can produce degrees of polarization superior to 30% in the UV/optical range while being strongly variable in time (Smith 1996). The amount of polarization is lower for extra-galactic, non-blazar, radio-loud objects, as in the case of OI 287 which exhibits $P \sim 8\%$ (Angel & Stockman 1980). In addition to the lack of polarization variability in time, Rudy & Schmidt (1988) and Goodrich & Miller (1988) proved with spectropolarimetric observations of OI 287 that the emission lines are polarized in a similar way to the continuum, ruling out a synchrotron origin. In addition to scattering, dichroic extinction might also increase the level linear polarization in face-on AGN if the dust grains are aligned by magnetic fields. Kartje (1995) showed that for not too optically thick ($\tau_V \leq 10$) dusty torii with partially aligned grains, the expected percentage of polarization might rise by 1.5%. Yet, in denser torii, scattering and dichroic extinction will partially cancel, causing P to increase more slowly. As our models present optically thick torii ($\tau_V = 750$), dichroic extinction will not be sufficient to explain the high polarization percentages detected in Gallagher et al. (2005) or Hines (1994). A third explanation may come from IRAM PdBI observations of the extended outflows in Mrk 231. Cicone et al. (2012) discovered a possible extension of the CO(1-0) transition blue wing a few arcseconds to the north, which remains unexplained. If we assume that the ionized polar outflows sustain the same half-opening angle and direction as the massive AGN-driven winds that can be considered as a naturally extended, dust mixed extension (Antonucci 1993; Cracco et al. 2011), the polar outflows in Mrk 231 might be nonaxisymmetric, similarly to NGC 1068 (Raban et al. 2009; Goosmann & Matt 2011b). Because the system is seen from the pole, the overall picture would be less symmetric due to the winds inclination and then create an higher polarization degree. However, while the explanation of the high P detected in particular type-1 AGN might be an addition of the last three mechanisms proposed above, it is important to recognize that we have restricted the analysis in this chapter to axially-symmetric situations while real AGN are certainly messier and simple asymmetry could be the explanation. The significant long-term variability of the degree of polarization in Mrk 231 while the angle stays constant is qualitatively similar to what Gaskell et al. (2012) discussed for NGC 4151. As with NGC 4151, polarimetric reverberation mapping could give important information about the location of the main scattering region responsible for the relatively high polarization in Mrk 231.

The equatorial scattering region is important for determining the net polarization position angle for a type-1 view. If the half-opening angle of the system is intermediate or small ($< 45°$ from the axis), equatorial scattering with sufficient Thomson optical depth can still lead to parallel polarization at a type-1 viewing angle. The degeneracy between the impact of the torus/winds on the one hand and the equatorial scattering region on the other must be resolved by taking into account additional observables. We mentioned before that the analysis of UV and X-ray absorption lines in a type-1 AGN may constrain the optical depth in the outflow, but possibly the spectral slope of the polarization can also give a hint at the amount of equatorial scattering. When comparing the polarization spectra for a type-1 AGN in Fig. 4.15 and Fig. 4.19 to that in Fig. 4.17, it turns

out that electron scattering inside the polar cones produces a flat polarization spectrum, whereas dust equatorial scattering inside the torus funnel or the NLR winds induces a concave shape in P. Comparing the broad-band continuum shape of the spectral flux to the polarization percentage can thus help to detect electron scattering that occurs deep inside the torus funnel. This type of modeling can help to explore the nature of AGN that intrinsically seem to lack a BLR in more detail.

In our modeling of AGN polarization, we saw that poloidal dust is only impacting the production of parallel polarization when it is optically thick ($\tau_{NLR} \geq 1$). However, we assumed a favorable condition: the spatial extension of the ionization cones is relatively small. Still, under these favorable condition it turned out that the torus half opening should be quite large and the optical depth of the equatorial scattering region has to be about $1 - 3$ to maximize the percentage of parallel polarization in type-1 views. Lower ($\tau < 0.3$) optical depths will lead to the disappearance of parallel signatures and higher values ($\tau > 3$) will decrease P through multiple scattering (depolarization) effects.

4.5.3 Constraining particular AGN classes

4.5.3.1 Bare and naked AGN

The orientation unification model Antonucci (1993) explains the observed differences between type-1 and type-2 Seyfert galaxies as originating from orientation effects, but it is now recognized that orientation is not the whole explanation (Antonucci 2012). For example some Seyfert-1 AGN show weak or even no intrinsic warm absorption along the observer's line-of-sight (Weaver et al. 1995; Patrick et al. 2011). These "bare" AGN allow a direct observation of the central engine.

Hawkins (2004) reported the presence of "naked" Seyfert-2 AGN, resulting from a survey of about 800 quasars and emission line galaxies. This new subclass is characterized by the weakness or even absence of the BLR and is coupled to strong optical variability, suggesting that the inner regions are not hidden anymore by an obscuring medium. Those unabsorbed Seyfert-2 galaxies, which are part of a more general class called "nonhidden BLR" type-2 AGN = NHBLR type-2s (Gliozzi et al. 2007), were mostly studied in the X-ray domain (Panessa et al. 2009; Gliozzi et al. 2010), i.e., without the help of spectropolarimetric tools.

For both of these subclasses of AGN, spectropolarimetric measurements are not available and the absence of the cited reprocessing regions is based on X-ray analyses. In this chapter, we presented a modeling case (see Sect. 4.2.3 for the naked model and Sect. 4.2.2 for the bare case) that can be compared to optical and UV observations. Such a broadband spectropolarimetric comparison can bring more information about the real nature of naked and bare AGN as well as constrain the real morphology of these particular galaxies.

As is discussed at length in Antonucci (2012), it is often not clear whether the failure to detect a hidden BLR in polarized flux means that the AGN in a nonthermal AGN lacking a big blue bump and BLR or whether the failure is due the absence of a suitable scattering region to give us the needed periscopic view of the central regions. Polarization modeling can help us assess these two possibilities.

4.5.3.2 Polar-scattering-dominated AGN

A particular group of Seyfert-1 galaxies are known as *polar-scattering-dominated AGN* (Smith et al. 2002b). In these type-1 objects the resulting polarization angle is perpendicular and relatively weak. In our reprocessing model, polar-scattering-dominated AGN generally have more strongly

collimated outflows and tori with steep inner surfaces. Possibly, these objects also reveal a low polarized flux induced by (inefficient) equatorial scattering. However, if the polarization induced by equatorial scattering is strong, i.e., the equatorial scattering region is geometrically thin and has an optical depth of $1 < \tau < 3$, then the outflows must have a sufficiently column density to still produce a net polarization that is perpendicular.

Spectropolarimetric observations show that the optical polarization of polar-scattered AGN typically rises toward the blue. According to Smith et al. (2004), this wavelength-dependence is caused by dust extinction occurring along a line of sight that passes very close to the torus horizon, while still denoting a type-1 viewing angle. Material form the uppermost layers of the torus then produces a visible extinction of $1 < A_{\rm V} < 4$ and causes the gradient in P. Our modeling shows this trend only for a torus half-opening angle of 45°. It leads to the very opposite spectral slope of P for more narrow tori. Thus, also the observed visible extinction in polar-scattering-dominated AGN indicates that the dusty torus should be rather wide than narrow. Note that for a torus half-opening angle of 60° no polar-scattering-dominated AGN exist in our model, even when adding polar dust scattering.

We return to this problem in Chap. 7 when we analyze in more detail the wavelength-dependence of our models also for clumpy media (see below) and different prescriptions for the dust. We have shown already that the polarization spectrum is quite sensitive to the dust composition and grain size distribution (Goosmann et al. 2007a,b).

4.5.4 More general geometries for the reprocessing regions

We have investigated the effects on our model results when one deviates from the adopted standard scales and geometry of certain scattering regions. This includes, in particular, the size of the obscuring torus and the geometrical shape of the equatorial scattering ring. We verified that a more compact torus with the same geometry and half-opening angle does not significantly alter the results. The same holds true when we replaced the toroidal scattering ring in the equatorial disk with a flared disk.

Our modeling assumed a uniform constant density across a given scattering region. This a considerable simplification. Observations of ionized outflows in AGN show that the winds should be at least partially fragmented. Using the spectropolarimetric capacities that were available on *HST*, Capetti et al. (1995) obtained spectropolarimetric and polarization imaging data of NGC 1068 in the UV. The authors detected a clumpy structure in polarization percentage and position angle. In most AGN, the ionized outflows cannot be spatially resolved and the polarized flux from a clumpy structure is integrated and only gives a net polarization for the entire outflow. By following this principle, Ogle et al. (2003) measured an average optical depth for the ionized outflows of NGC 1068 from spatially resolved X-ray observations with the HETGS onboard *Chandra*. The ratio of scattered X-ray continuum and emission line flux from the central region of the AGN gave an estimate of the Thomson optical depth of 0.27 ± 0.08. This confirmed the hypothesis that X-ray, NLR, and the optical/UV/X-ray reprocessing regions are likely to coincide.

There are more and more indications from observations and modeling in the IR that the obscuring torus should also have a clumpy structure (Nenkova et al. 2008b,a, 2010; Schartmann et al. 2008; Hönig & Kishimoto 2010; Heymann & Siebenmorgen 2012). For the future, a clumpy torus will be important to add to our modeling. We currently conduct preliminary studies for the expected optical/UV polarization of a centrally irradiated torus with a fragmented structure. So far, we find that, on the one hand, the normalization of the polarization spectra is significantly lower, while its spectral shape does not change much compared to the case of a uniform density

torus. On the other hand, a clumpy torus allows more flux to escape from the central funnel, even at type-2 viewing angles that are strongly obscured by a uniform-density torus. Since the polarization efficiency is measured by the polarized flux emerging from the torus, we therefore expect that the torus remains an important scattering region even when it has a fragmented structure. Nonetheless, the lower polarization produced by a clumpy torus should lead to a weaker net polarization detected at type-2 viewing angles (see Sect. 4.3). This would help to bring our modeling results to better agreement with the observed spectropolarimetric data for Seyfert-2 galaxies (Kay 1994).

More general considerations about a clumpy but continuous accretion flow are currently discussed in the literature (see Elitzur 2007, and references therein for an overview) and therefore should be considered systematically in modeling work such as the one presented here. The clumpy nature of the dusty torus might also resolve the known problem that a geometrically thick torus lacks stability against self-gravity and therefore cannot be in hydrostatic equilibrium. The torus could rather be interpreted as a dynamical region of flowing, optically thick clouds. However, our modeling results and the observed parallel polarization in type-1 AGN as well as the moderate perpendicular polarization in type-2 objects argue against a geometrically thick torus (see Sect. 4.5.2).

Finally, we emphasize that in this work we always assumed the axes and half-opening angles of the dusty torus and the ionized outflows to be identical. A multi-wavelength analysis performed by Raban et al. (2009) suggests, however, that the bi-conical outflow in NGC 1068 should be inclined by $\sim 18^\circ$ with respect to the axis of the obscuring torus. The collimation effect on the ionized outflows might thus not be an obvious (although greatly simplifying) assumption in our modeling. We will investigate the consequences of this misalignment for the observed polarization spectra and images in the next chapter (Chap. 5). This work is part of a multi-wavelength modeling attempt that also includes predictions for future X-ray polarimetry observations of NGC 1068 (Goosmann & Matt 2011b). Some preparatory work on the optical/UV polarization signatures of the misaligned outflows in NGC 1068 at different azimuthal and polar viewing angles can be found in Marin et al. (2012a).

The results presented in this chapter have been partially published in Marin et al. (2012c) and Marin & Goosmann (2012). An extended publication, exploring the polarization signal induced by the NLR, is in preparation.

Chapter 5

The continuum polarization of NGC 1068

NGC 1068 is considered as one of the best examples of archetypal, thermal Seyfert-2 galaxies. According to the most straightforward interpretation of the unified scheme of AGN (Antonucci 1993; Urry & Padovani 1995, resumed in Sect. 2.3), the innermost regions of NGC 1068 are hidden by optically thick, circumnuclear matter usually designated as a "dusty torus". Jaffe et al. (2004) and Wittkowski et al. (2004) provided support for the presence of this obscuring media around the core of NGC 1068 by spatially resolving the direct emission coming from a torus-like structure. Using the MID infrared Interferometric instrument at the VLT, Raban et al. (2009) estimated the torus to be a compact (0.45×1.35 pc) region; a size coherent with the torus observations of the Circinus galaxy (radius $r < 2$ pc, Packham et al. 2005) or Centaurus A ($r < 2$ pc, Radomski et al. 2008). We saw in Sect. 2.2.6 that the circumnuclear dust is thought to collimate the ejected winds to a double-cone shape (the ionization cone, Osterbrock & Mathews 1986); the principal hypothesis being that the polar outflows sustain the same half-opening angle as the dusty torus. However, a recent interferometric campaign on NGC 1068 carried out by Raban et al. (2009) showed that the polar winds (represented as a bi-conical structure) are inclined with respect to the obscuring torus axis. Hence, the general picture of polar outflows became more complex.

When it comes to geometrical considerations, polarization has proven to be a solid tool to investigate the structure and composition of complex objects such as AGN (Kartje 1995; Young 2000; Goosmann & Gaskell 2007; Marin et al. 2012c). In this context, NGC 1068 is one of the best case studies, as it was the first Seyfert-2 galaxy in which scattered broad lines were discovered using spectropolarimetric measurements (Antonucci & Miller 1985), strengthening the idea that Seyfert-2 AGN hold hidden Seyfert-1 nuclei. Extending the spectropolarimetric exploration of NGC 1068 allows us to investigate its complex morphology in more details.

Starting at high energies, Goosmann & Matt (2011a,b) explored the 1 to 60 keV polarization signature of tilted outflows in NGC 1068. They showed that the misalignment of the ejection winds can be detected by a rotation of the polarization position angle between soft and hard X-rays. But the lack of flying X-ray polarimeters (see Chap. 9) compels us, for now, to focus on other wavelengths. Moving down to the UV and optical wave bands, the polarization spectra of NGC 1068 show a nearly constant percentage of polarization P and polarization angle ψ over more two decades (Angel et al. 1976; Axon et al. 1996); but, those observations were not used to constrain the geometry of the polar winds. Polarization maps from the HST were used to identify the location of the hidden nucleus (Capetti et al. 1995; Kishimoto 1999) and served as a base-ground information to reconstruct a three dimensional picture of NGC 1068. Despite the remarkable attempt of Kishimoto (1999), no one has yet constrained the polar outflow's tilting

angle using spectropolarimetry only. Das et al. (2006) pointed out the complexity of the problem by suggesting that the polar outflows of NGC 1068 may lean out of the plane-of-the-sky, introducing an unknown azimuthal angle.

In this chapter, we use the method presented in Chap. 4 to investigate the complex geometry of NGC 1068. We first explore a correlation between the X-ray hydrogen column density and the optical depth of dust grains in order to be coherent over the three energy ranges (X, UV and optical). Using the constraints on the size and geometry of the reprocessing regions found in the literature, we conduct radiative transfer calculations of the polarization signature in the 1400 – 8000 Å spectral band. We then compare our polarization results to data obtained by the *HST* and the Lick telescopes. To tune our azimuthal angle parameter, we examine the polarization dependence of the model over a wide range of azimuthal viewing angles towards the ionized winds. Along with this, we examine the impact of dust scattering on the polarization spectra while adopting three different dust mixtures. Compiling all our results with previously published constraints, we present a set of new geometrical parameters for NGC 1068.

5.1 A model of NGC 1068 from broadband observations

Little is known about the dust composition in the circumnuclear torus of AGN (Li 2008). However its dimensions and geometry, the density distribution, and the dust grain properties may be inferred from mid-infrared spectral energy distributions (SED, Mor et al. 2009). Such diagnoses help us to determine the dust composition in type-2 quasi-stellar objects (QSOs) using the presence (or absence) of silicate and polycyclic aromatic hydrocarbon (PAH) emission features (Sturm et al. 2006). From the unified model we know that the torus must be optically thick to prevent radiation from escaping along the equatorial plane (Antonucci 1993) but more detailed characteristics, such as the total optical depth at edge-on line-of-sights, remain unclear (Hönig & Kishimoto 2010). To estimate the density of the dust, we opted for a new approach, presented in Sect. 5.1.1, before summarizing the model setup in Sect. 5.1.2.

5.1.1 The correlation between the optical depth of dust and hydrogen

Operating the Copernicus satellite to survey the spectral region near L_α (1170 - 1270 Å) and to measure column densities of interstellar H_1 toward a hundred of stars, Bohlin et al. (1978) obtained a mean ratio between the total column density of neutral hydrogen and the color excess (Eq. 5.1).

$$< N(H_1 + H_2)/E(B-V) > \; = \; 5.8 \times 10^{21} \text{ atoms cm}^{-2} \text{ mag}^{-1} \tag{5.1}$$

We opted for a dust-dominated torus composition as the hottest inner part of the dust system is still at a lower temperature than the dust sublimation limit (Jaffe et al. 2004). Thus, we do not take into account possible ionized dust components in our model. To correlate the dust optical depth in the optical/UV waveband to the hydrogen column density in the X-ray domain, we used Eq. 5.1 to calculate the torus composition in terms of dust densities. X-ray absorption being primarily caused by H_1, H_2 and metals like carbon, nitrogen and oxygen, our main assumption requires universal ratios of element abundances. Following Evans (1994), we first substituted in Eq. 5.1 the color excess $E(B-V)$ by the visual extinction A_V divided by the reddening R_V (Eq. 5.2).

$$A_V = R_V \times E(B-V) \tag{5.2}$$

Then we used the ratio of total-to-selective extinction to replace A_V by the optical depth in the V band τ_V.

$$A_V = 1.086 \times \tau_V \tag{5.3}$$

The dust grain density n was finally calculated using the definition of the optical depth, with σ_{ext} being the dust extinction cross-section and l the extension of mater in one cone along the observer's line-of-sight.

$$\tau_V = \int_0^l \sigma_{ext} \times n \times dx \tag{5.4}$$

To calculate the dust grain density, we assumed the hydrogen column density of NGC 1068's torus to be superior to 10^{25} atoms/cm^2 (Goosmann & Matt 2011b and references therein). The dust extinction cross-section is taken from the internal computation of STOKES (Goosmann & Gaskell 2007), based on the results from Mie scattering theory (Bohren & Huffman 1983; Draine & Lee 1984). The reddening was fixed to an average value of 5.55 ± 0.15 (Gaskell et al. 2004), according to AGN extinction curves based on the composite spectrum of 1018 radio-quiet AGN (Francis et al. 1991) and 72 radio-loud quasars (Baker & Hunstead 1995, 1996a,b). The V-band photoelectric photometry measurement by Daltabuit et al. (1976) indicates that the magnitude of NGC 1068 lies around 10.21. From this set of parameters, Eq. 5.1 gives a corresponding dust grain density of 3.1×10^{-4} atoms/cm^3 ($\tau_V \sim 860$).

5.1.2 Asymmetric model setup

In our model, derived from the results of Raban et al. (2009), NGC 1068 is powered by a central, isotropic, point-like source emitting unpolarized radiation with a power-law shape $F_* \propto \nu^{-\alpha}$. Observations of NGC 1068 pointed out that the photon index α varies between 0.88 (Antonucci et al. 1994) and 1.5 (Antonucci & Miller 1985), depending on the details of the data reduction process and the AGN activity. To be coherent with the results of Goosmann & Matt (2011b), we opted for $\alpha = 1$. Along the equatorial plane, an electron-filled, flared disk responsible for the parallel polarization observed in type-1 objects (Antonucci 1984), surrounds the central source. At a greater distance along the same equatorial plane, an obscuring, optically thick dusty torus blocks the radiation from escaping along edge-on directions. We assume the winds to be hourglass-shaped, optically thin and filled with electrons[1] . According to Raban et al. (2009), the polar winds do not sustain the same half-opening angle as the torus: the winds are tilted by an angle $\theta = 18°$ from the symmetry axis of the torus. We also take into account the arguments of Das et al. (2006), implying that the bi-conical structure of the AGN may lay out of the plane-of-the-sky, extending our setups to a more complex, three-dimensional geometry. Unfortunately, a measurement of the outflow's radial velocities by Axon et al. (1998) showed that Doppler velocities are not suited to determine the azimuthal viewing angle of the observer, as blueshifted and redshifted clouds were detected in both, upper and lower parts of the polar winds. In a first attempt, we thus arbitrarily fixed the wind's azimuthal angle to $\phi = 18°$. Finally, according to Goosmann & Matt (2011b), we also adopted two different optical depths ($\tau_V \sim 0.03$ and 0.3) to model the polar outflow's response to the incident continuum. The obscuring torus is filled with standard (Mathis et al. 1977) "Milky Way" dust, already presented in Goosmann & Gaskell (2007) and recalled in Table 5.2. According

[1] A precise description of the X-ray model can be found in Goosmann & Matt (2011b). Complementary informations about the UV/optical modeling of NGC 1068 are presented in Marin et al. (2012a).

flared disk	**dusty torus**	**polar outflows**
$R_{\rm min} = 3.10^{-2}$ pc	$R_{\rm min} = 0.1$ pc	$R_{\rm min} = 0.3$ pc
$R_{\rm max} = 5.10^{-2}$ pc	$R_{\rm max} = 0.5$ pc	$R_{\rm max} = 1.8$ pc
half-opening angle = 20°	half-opening angle = 60°	half-opening angle = 40°
equat. optical depth ~ 1	equat. optical depth ~ 860	polar tilting angle = 18°
		azimuthal angle = 18°
		vertical optical depth ~ 0.03 or 0.3

Table 5.1: Parameters for a model of NGC 1068 consisting of three reprocessing regions. The polar outflows half opening and polar tilting angles, as well as the torus half-opening angle, are measured with respect to the symmetry axis of the torus. The half-opening angle of the flared disk is measured from the equatorial plane. The azimuthal inclination of the outflows is measured from the plane-of-the-sky in a clockwise direction.

to Sect. 5.1.1, the grain density is equal to 3.1×10^{-4} atoms/cm^3. The parameters of the model are summarized in Table 5.1 and a three-dimensional sketch of NGC 1068, seen at a typical type-2 line-of-sight and including both the polar and azimuthal angles of the wind, is presented in Fig. 5.1.

In the model space of STOKES, θ represents the tilting angle of the polar outflows measured with respect to the torus axis. i is defined as the observer's inclination, defined with respect to the same axis. Finally, ϕ is the azimuthal coordinate for an observer rotating in a clockwise direction around the vertical axis of the AGN. As in the previous chapter, the polarization spectra computed by the code are recorded in terms of polarized flux PF/F_* (normalized by the total flux of the primary source F_*), percentage of polarization P and polarization position angle ψ.

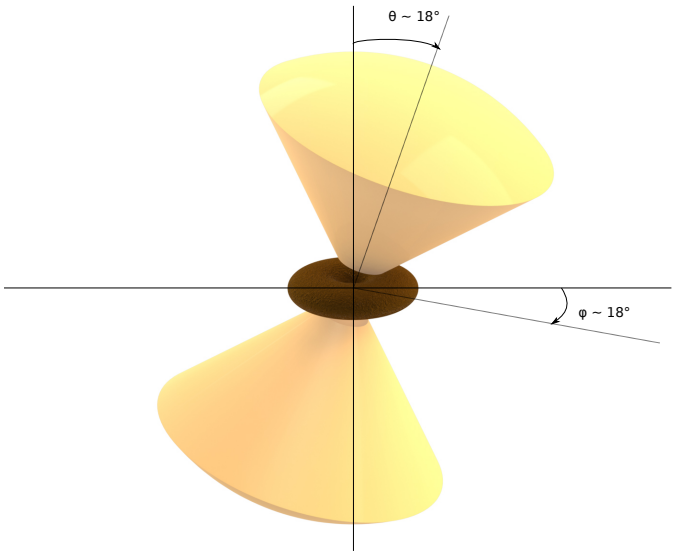

Figure 5.1: Three dimensional model of the reprocessing geometry in NGC 1068. The model is seen at an inclination $i \sim 70°$ with $\theta = 18°$ and $\phi = 18°$. *Credits: Alix Videlier.*

5.2 UV and optical continuum polarization of NGC 1068

5.2.1 Spectropolarimetric and imaging results

In Fig. 5.2, we present the polarization degree P and polarization position angle ψ for two optical depths of the polar outflows (*dashed line* $\tau_V \sim 0.3$, *plain line* $\tau_V \sim 0.03$). We set the observer's viewing angle to a typical type-2 line-of-sight according to Hönig et al. (2007) who found, by applying a clumpy torus radiative transfer model to infrared data, that NGC 1068 is seen at an inclination of $i \sim 70°$.

Fig. 5.2 (top) shows the total (linear plus circular) polarization. P is constant for both models in the 3500 – 8000 Å range, where Thomson scattering exceeds Mie scattering, which dominates at shorter wavelengths. In the 1400 – 3500 Å waveband, the phase function of dust scattering becomes more and more asymmetric, and this change in scattering geometry produces a stronger UV tail in terms of polarization degree. The difference in P between the two models is directly related to the amount of Thomson scattering. Increasing the optical depth of the ionized wind leads to an increase of P until multiple scattering effects start to dominate and depolarize at very high τ_V. The average P on the 3500 - 8000 Å band is equal to 12.9 % (polar outflows $\tau_V \sim 0.03$) and 33.9 % ($\tau_V \sim 0.3$). When integrating the polarization signal over the whole wavelength domain, P increases to 14.2 % ($\tau_V \sim 0.03$) and 34.7 % ($\tau_V \sim 0.3$). The amount of polarization is thus a direct tracer of the optical depth in the polar winds of AGN.

The polarization position angle, Fig. 5.2 (bottom), is wavelength-independent, with ψ = -19.3° for both optical depths. Interestingly, this value differs from the one found in Sect. 4.3, were ψ was equal to 0° (Marin & Goosmann 2011; Marin et al. 2012c). The difference arises from the symmetry break of the model, as the outflow's last scattering surfaces are no longer parallel to the projected torus axis. ψ roughly aligns with the tilting angle of the outflows, producing a polarization position angle different from zero. This allows the observer to put constraints on the inclination of the wind with respect to the torus axis (Marin et al. 2012a).

Polarization maps are shown in Fig. 5.3. The 30 x 30 pixel maps compile the spectra of the four Stokes parameters across a wavelength range of 1400 – 8000 Å. Each pixel is labeled by its coordinates x and y (in parsecs). The polarized flux PF/F_* is color-coded and a vector drawn in black at the center of each pixel represents the ψ and P values. A vertical vector indicates a photon polarization angle of 90°, a slash to the right denotes $90° > \psi > 0°$, and a horizontal vector stands for an angle of 0°.

Both polarization maps ($\tau_V \sim 0.3$, left and $\tau_V \sim 0.03$, right) show that the polarized flux is concentrated in the vicinity of the torus funnel which is hiding the innermost regions of the AGN. The equatorial reprocessing region is not visible due to circumnuclear obscuration but still impacts the overall polarization signal as can be seen from the orientation of the polarization vectors at the bases of the ionized winds. Complex reprocessing in the central region of the model tends to orientate the polarization vectors alongside the vertical axis of the torus, which is the expected parallel signature of the equatorial, reprocessing region (Marin et al. 2012c). At larger distances from the torus funnel, the polarization angle rotates to an orientation that is perpendicularly to the symmetry axis of the winds, high-lightening the orientation of the titled region. The inclined winds also show a polarized flux gradient, as previously discussed in Watanabe et al. (2003), Goosmann & Gaskell (2007) and Marin et al. (2012c). This gradient is much stronger in the case of the optically thicker model with $\tau_V \sim 0.3$, which also presents a higher P, as mentioned above. Finally, due to the system inclination, the upper part of the bi-conical structure shows a slightly stronger polarized flux than the lower part. With $\theta = 18°$ and $\phi = 18°$, the upper cone of the wind leans closer to

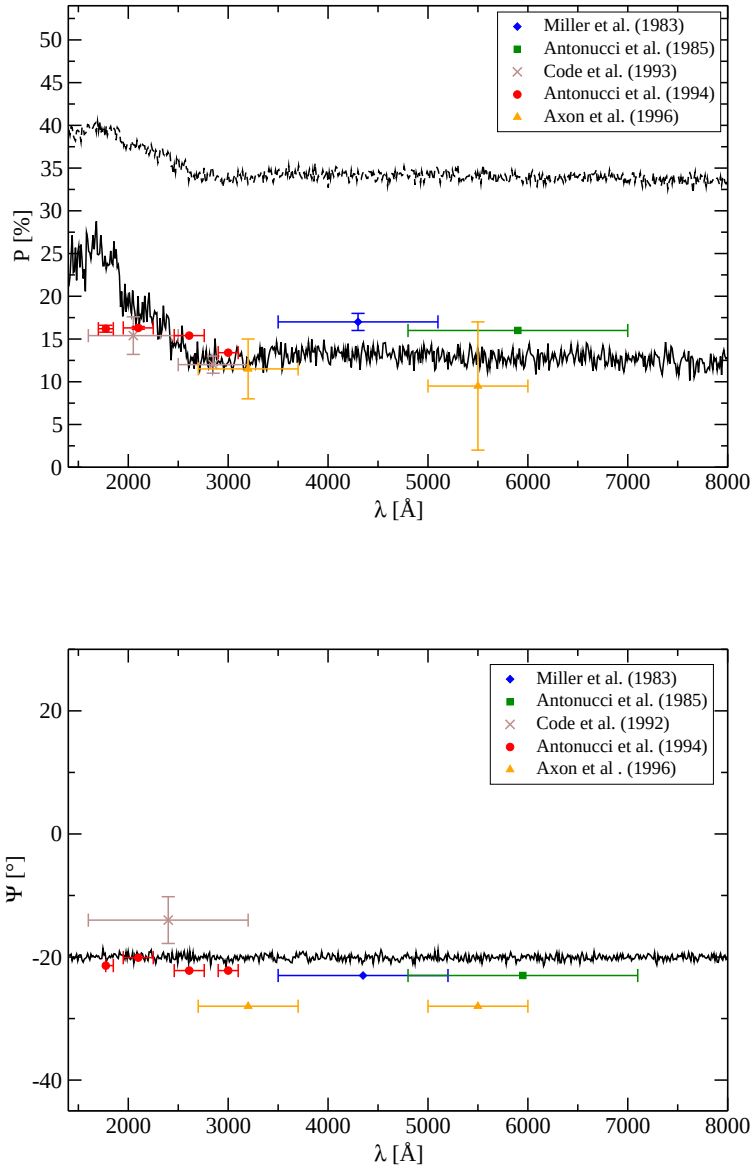

Figure 5.2: Modeling NGC 1068, with a viewing angle of $i \sim 70°$, $\theta = 18°$, $\phi = 18°$ and two different optical depths for the polar outflows (*dashed line* $\tau_V \sim 0.3$, *plain line* $\tau_V \sim 0.03$). Spectropolarimetric observations of NGC 1068 by Miller & Antonucci (1983); Antonucci & Miller (1985); Code et al. (1993); Antonucci et al. (1994) and Axon et al. (1996) are reported on the spectra. *Top*: Percentage of Polarization (linear + circular) P; *Bottom*: Polarization Angle ψ.

the observer (see Fig. 5.2) and exposes a larger portion of the wind basis, from which the strongest polarized flux comes.

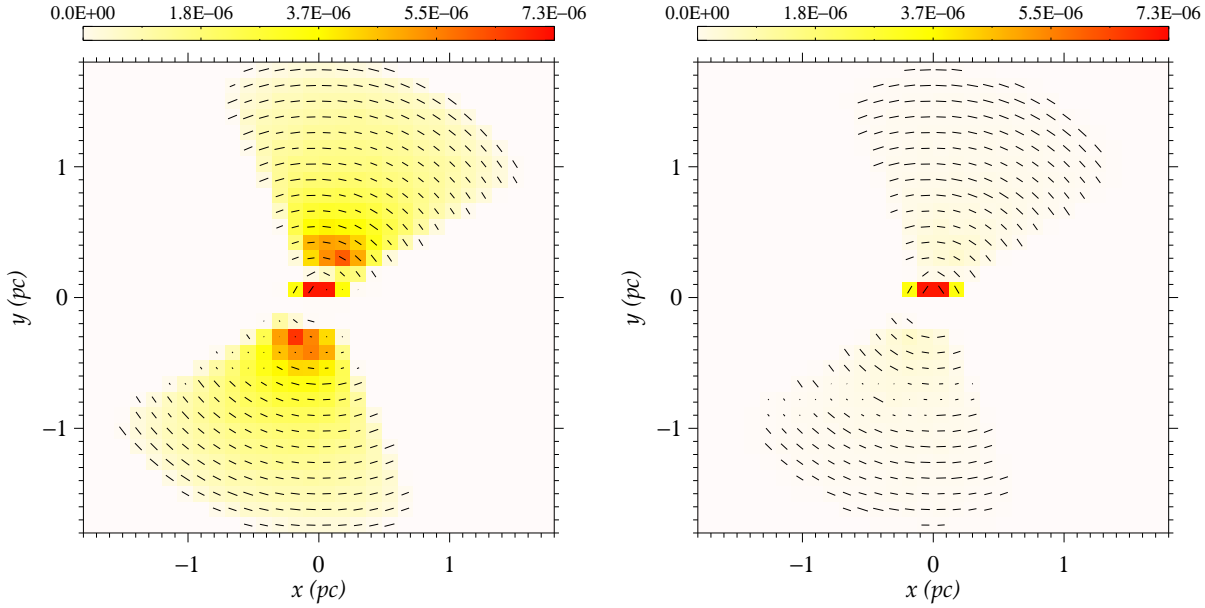

Figure 5.3: Modeled polarization images of NGC 1068 at a viewing angle of $i \sim 70°$, with $\theta = 18°$, $\phi = 18°$. The polarized flux, PF/F_*, is color-coded and integrated over the 1400 – 8000 Å band. *Left*: Polar outflows $\tau_V \sim 0.3$; *right*: Polar outflows $\tau_V \sim 0.03$

5.2.2 Comparison with observations

NGC 1068 has been regularly observed for the past three decades using the *Hubble Space Telescope* (*HST*) spectropolarimetric and polarization imaging capabilities (Antonucci et al. 1994; Capetti et al. 1995; Axon et al. 1996), the Lick 3m Shane telescope Image Dissector Scanner (Miller & Antonucci 1983) modified for simultaneous spectrophotometry and spectropolarimetry (Antonucci & Miller 1985) or the Wisconsin Ultraviolet Photo Polarimeter Experiment (Code et al. 1993). For all those observations, ψ can be determined with respect to the radio axis of NGC 1068, whereas in our simulations, ψ is measured relative to the equatorial plane. Taking into account that 1) the inner radio structure of NGC 1068 suggests an ejection axis inclined by 10° with respect to the North-South direction (Wilson & Ulvestad 1982; Miller & Antonucci 1983), and 2) the bi-conical structure of the winds is also titled by 18°, we then correct the observational ψ by adding a negative offset of 118° (90° + 10° + 18°).

Miller & Antonucci (1983) found a polarization position angle ψ = -23° in the 3500 – 5200 Å wavelength band associated with a wavelength-independent continuum polarization of 16 ± 2 %, indicating electron scattering as the main polarization mechanism. Antonucci & Miller (1985) found again that the non-stellar continuum is polarized at ∼ 16 %, independently of the wavelength, along with a photon position angle of ψ = -23°. Code et al. (1993) presented the first UV spectropolarimetric observation of NGC 1068. In their communication, a constant percentage of polarization (∼ 16 %) associated with an abnormally low position angle of -14° was found, later discussed by Antonucci et al. (1994). Shortward of 2700 Å, Antonucci et al. (1994) confirmed the results of Antonucci & Miller (1985), but with a slightly different value of ψ (-21°). The 2400 – 2700 Å polarization mapping campaign by Capetti et al. (1995) revealed that the inner AGN region is dominated by scattered radiation with an average polarization of 20 %, and matter knots

in the polar winds capable of increasing P to a local value as high as 30 – 65 %. Axon et al. (1996) confirmed the previous results by a spectroscopic study of NGC 1068 in the UV (2700 – 3700 Å) and in the optical (5000 – 6000 Å) bands, finding a ψ close to $-28°$.

Looking at the polarization spectra (Fig. 5.2 top), the optically thin ($\tau_V \sim 0.03$) polar winds tend to reproduce the nearly wavelength-independent signal measured in the soft-UV and optical wave bands. The UV-tail (1400 – 2500 Å) shows a high polarization degree ($P \sim 26$ %) induced by the dust model, which seems to be in disagreement with the observations. However, one must note that in this waveband, the presence of several emission lines (e.g. He II] λ1640, C III] λ1909, C II] λ2326 and Ne IV] λ2423) makes the measurement of the polarization continuum quite difficult, thus it is often excluded from the interpretation (Antonucci 1984)). Increasing the optical depth by a factor of ten ($\tau_V \sim 0.3$) allows us to reproduce the knot's polarization ($P \geq 30$ %) observed by Capetti et al. (1995) and Axon et al. (1996). This suggests that the outflowing medium is optically thin with an average value of $\tau_V \sim 0.03$, but that it also contains some higher density regions responsible for bright knots with stronger polarization. The ψ spectra (Fig. 5.2 bottom) bring an additional information: the wavelength-independent ψ is $\sim 6.3°$ lower than the observed polarization angle of NGC 1068, indicating that the inferred non-axisymmetric geometry is still not properly adjusted.

An intermediate conclusion would be that our model already reproduces the expected behavior of both the polarization degree and the photon polarization angle, using $\theta = 18°$, $i = 70°$ and $\tau_V \sim 0.03$ (winds), but a better tuning of the azimuthal angle is still necessary to match the observed polarization angle. The importance of the dust mixture must also be considered as so far it fails to reproduce the observed polarization degree in the UV-tail.

5.2.3 Investigating the dependence on the azimuthal angle

We now determine the variations of both the polarization degree and the polarization position angle with respect to the azimuthal viewing angle at $i \sim 70°$.

Fig. 5.4 (top) shows that the (2500 – 8000 Å)-integrated percentage of polarization of NGC 1068 is nearly constant (~ 15.8 %) for $0° \leq \phi \leq 180°$. In this range, the lower part of the bi-conical winds is partly hidden by the obscuring torus, thus much less contributing to P. However, the upper part of the polar outflows has a maximal contribution to the overall polarization degree, being more strongly exposed to the observer. From 180° to 360°, the upper part of the wind is now at the rear of the model and a fraction of the torus funnel can be directly seen without transmission through the winds. The scattered radiation coming from the equatorial scattering region dilutes the polarization signal from the wind down to ~ 8.8 % at $\phi = 270°$ (when the upper part of the polar outflows is at a maximal distance from the observer). This effect is visible on the polarization maps (Fig. 5.3), where the base of the upper cone shows a bright polarized flux associated with a polarization position angle influenced by the reprocessed radiation coming from the equatorial, flared disk. The contribution to polarization from the lower part of the bi-conical winds is small, as it is partially hidden by the dusty torus.

The polarization angle ψ as a function of ϕ (Fig. 5.4, bottom) varies between -20 and 20°. Related to the azimuthal orientation of the cones, the model might look like asymmetric ($\phi = 0°$ or 180°) or symmetric ($\phi = 90°$ or 270°) with respect to the projected axis of the torus. In the first case, the system lies in the plane-of-the-sky and ψ traces the inclination of the bi-conical structure. When the system is slightly rotated, ψ tends to vary according to the projected wind geometry, until the two cones align with the projected axis of the torus. The model becomes symmetric and produces a photon polarization angle $\psi = 0°$, as expected from theoretical modeling of type-2 AGN

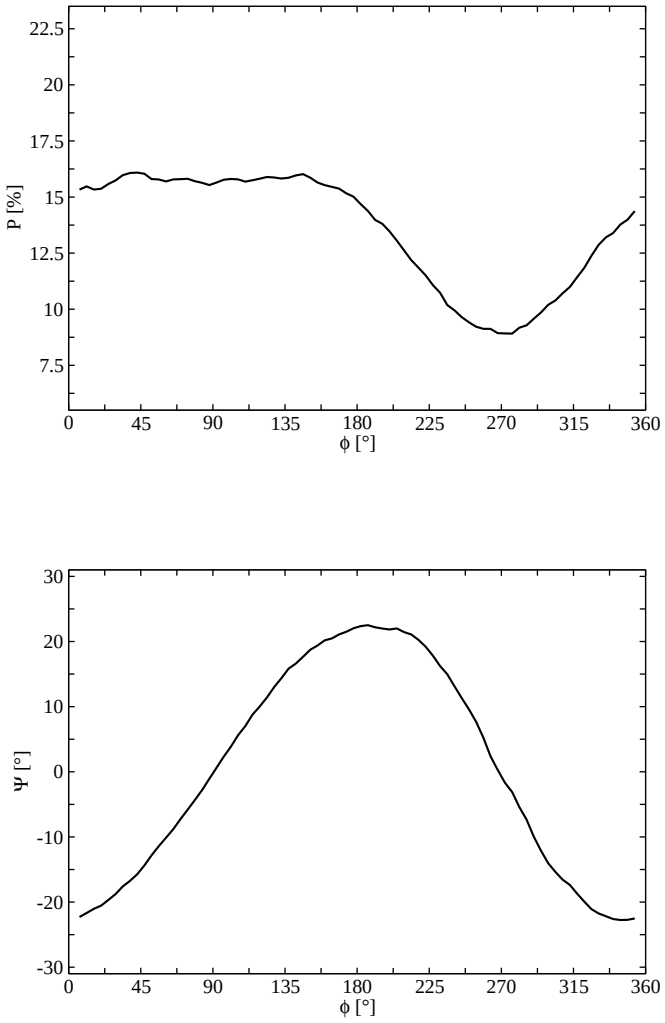

Figure 5.4: Polarization response of NGC 1068. $\theta = 18°$, $i \sim 70°$ and ϕ circles around the model. Polar outflows τ_V is set to 0.03. *Top*: Percentage of Polarization (linear + circular) P; *Bottom*: Polarization Angle ψ.

(see Chap. 4).

Using the orientation-dependent polarization properties of our model, we can now constrain the azimuthal parameter to obtain the expected level of polarization, as well as the correct polarization angle. Degeneracies are removed by the different behaviors of P and ψ, probing that the polarization degree and the polarization position angle are two valuable, independent variables that can be used as discriminating a tool (see Chap. 9). As the polarization percentage computed in Fig. 5.2 (top) lies already within the error bars of the observations for $\tau_V = 0.03$, only ψ needs to be adjusted. The $\sim 6.3°$ difference in ψ between our model and the observations finally vanishes when the wind's azimuthal angle is increased between $40° - 50°$, leaving P unchanged.

5.2.4 Importance of the dust grain model

The exact composition of dust in the circumnuclear tori of AGN remains unknown (Li 2008). To model the scattered flux and polarization of nuclear radiation, Wolf & Henning (1999) assumed various types of dust grains having a size distribution proportional to a^s (a being the grain radius and s a power-law index). Composed of ortho- and para-graphite[2] as well as silicate, a particular dust composition called "Milky Way" was derived by Mathis et al. (1977) taking our own galaxy as a sample. This dust prescription was then used in Goosmann & Gaskell (2007), Marin et al. (2012c) and in the work presented here.

Hönig & Kishimoto (2010) presented a three-dimensional radiative model using a clumpy, dusty torus to model the impact of the dust mixture on the IR spectrum of AGN. They found that a standard interstellar medium "ISM" dust composition appears to be in overall agreement with observed IR SEDs. Finally, Gaskell et al. (2004) presented a third kind of dust composition called "AGN" dust, and derived from the reddening of the broad emission lines and continua of radio-loud and radio-quiet AGN.

In order to check the validity of our previous results, we computed the polarization signal of our NGC 1068 model ($i = 70°$, $\phi = 18°$) using the three dust mixtures previously stated. The dust compositions and parameters are summarized in Tab. 5.2.

Name identifier	para-graphite	ortho-graphite	silicates	a_{min}	a_{max}	grain size index s
Milky Way	12.5%	25%	62.5%	0.005 μm	0.25 μm	-3.5
AGN	5%	10%	85%	0.005 μm	0.2 μm	-2.05
ISM	15%	32%	53%	0.025 μm	0.25 μm	-3.5

Table 5.2: Composition and main physical properties of the dust grain compositions used in our models

In Fig. 5.5, the polarization degrees are found to be slightly different from one dust model to another, with the "Milky Way" model used a reference. Focusing on the polarization results for a polar outflow with $\tau_V \sim 0.03$, we find that both the "ISM' and "AGN" present lower polarization degrees in the optical band, as well as larger polarization variations in the UV-tail. More precisely, the "AGN" model shows an optical, wavelength-independent polarization degree which is ~ 5 % below the reference level, and a steeper UV-tail with P varying from 7.5 % to 27.5 %. The "ISM" grains also produce a steep UV-tail, with P rising from 10.1 % to 26.4 % in the 2400 – 3000 Å waveband, but its optical polarization is found to be wavelength-dependent (~ 1.3 % lower than the "Milky Way"). As the observed polarization should be wavelength-independent and showing a rather small polarization variation in the UV-tail (Code et al. 1993; Antonucci et al. 1994), both the "ISM' and "AGN" models can be excluded from the choice of suitable dust mixture in the modeling of NGC 1068. The results from Fig. 5.5 thus comfort our choice using a standard "Milky Way" dust model for the remainder of this manuscript.

Looking at an optically thicker polar wind ($\tau_V \sim 0.3$), our previous results hold while the energy-dependent behavior of the "ISM" model appears less accentuated, as electron polar scat-

[2] Graphite is a highly anisotropic material. Radiative transfer codes simplify the problem of radiative transfer between the partially aligned dust grains by assuming an ovoid morphology for graphite, with a major and a minor axis. The terms ortho- and para-graphite refer to the two axis, either perpendicular or parallel to the basal plane (the plane parallel to the lateral or horizontal axis). Specific dielectric functions are associated to ortho- and para-graphite grains (Draine & Lee 1984).

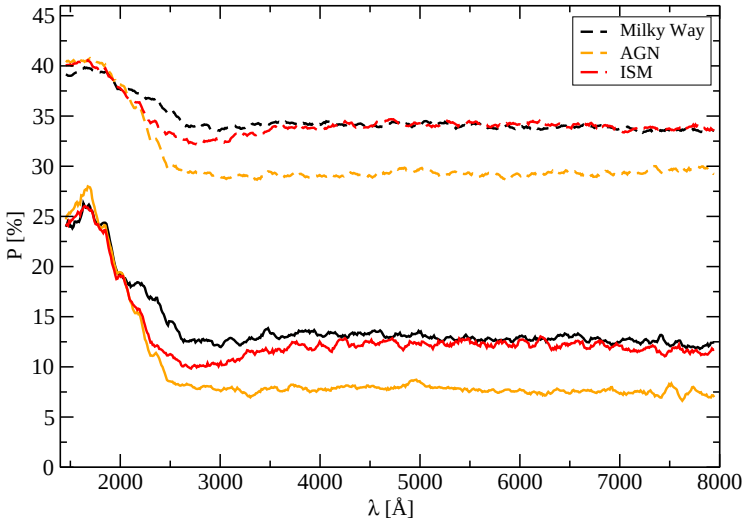

Figure 5.5: Modeling the polarization degree of NGC 1068, with a viewing angle of $i \sim 70°$, $\theta = 18°$ $\phi = 18°$ and different dust grain models. The optical depth of the polar outflows are set to 0.03 (*plain line*) and 0.3 (*dashed line*). *Legend*: Milky Way model in *black*, AGN model in *red* and ISM model in *orange*.

tering predominates and tends to smooth out the dust signatures. The differences in the optical polarization degree between the three models are smaller and the UV-tail variations less accentuated. However, the "AGN" dust grain model still produces a strong P variation at shorter wavelengths, a characteristic feature that can be detected in further observations to diagnose the real dust composition.

Note that Fig. 5.5 does not show the polarization angle spectra, as all the dust models reproduce the same ψ = -19.3° value, as expected from Fig. 5.2 (bottom).

5.3 Summary and discussion

In this chapter, we constructed a polarization model of NGC 1068 based on the X-ray model developed by Goosmann & Matt (2011b) and subsequently adapted to the UV and optical wavebands using Bohlin et al. (1978)'s formula. We took into account the angular offset of the winds suggested by Raban et al. (2009) and Das et al. (2006) to improve the consistency of our model. Finally, varying the wind azimuthal angle, we fit the observed level of (linear + circular) polarization and photon polarization angle.

Our model successfully reproduces the expected percentage of polarization as well as the photon polarization angle reported by the literature, taking into account:

(1) Inclined polar outflows with a tilting angle of $\theta = 18°$ with respect to the projected symmetry axis of the obscuring torus, and a $40° \leq \phi \leq 50°$ azimuthal angle with respect to the plane-of-the-sky. In this region of the parameter space, the upper part of the wind is closer to the observer than the lower part.

(2) An electron-filled, optically thin, continuous polar outflow with $\tau_V \sim 0.03$. This outflow is assumed to be ionized by the central AGN source and dominated by Thomson scattering.

(3) A typical Seyfert-2 observer's viewing angle of $\sim 70°$.

(4) An optically thick ($\tau_V \sim 860$) equatorial torus filled with standard "Milky Way" dust.

(5) The presence of an equatorial, geometrically thin, optically thick ($\tau_V \sim 1$), electron-scattering region representing the accretion flow at the outer edge of the accreting disk.

We find that a "Milky Way" dust model is favored to the "ISM" and "AGN" models when modeling the continuum polarization of NGC 1068. It correctly reproduces the increase of polarization in the UV band and a wavelength-independent polarization degree in the optical domain. We reproduce the high continuum P detected by several authors in punctual, dense matter knots using a wind optical depth $\tau_V \sim 0.3$. This hint points toward a fragmented medium, and we discuss the complex geometry of the outflow, as well as the presence of denser regions in the wind in the following subsections.

5.3.1 The complex geometry of the outflows in NGC 1068

Das et al. (2006) and Raban et al. (2009) where the first to suggest that the polar outflows of NGC 1068 break the symmetric picture of AGN. Das et al. (2006) measured the kinematics of the Narrow Line Region (NLR) to infer the misalignment of the winds with respect to the radio-jet. Doing so, they modeled the polar outflows of NGC 1068 using wind geometries leaning out of the plane-of-the-sky. By investigating the alignment of the maser disk with respect to the dusty torus and the radio jet, Raban et al. (2009) came to the conclusion that the bi-conical structure of the winds is inclined with respect to the radio axis. However, the first hints on the misalignment of the polar winds with the torus axis can even be found in previous work done by Kishimoto (1999). Using archival UV imaging polarimetry data of the *HST*, and assuming that the UV polarization is dominated by electron scattering, Kishimoto (1999) derived a three-dimensional map of the structure in NGC 1068. In their cartography, the fluxes form the southern clouds are found to be systematically lower than those of the northern part. Based on this observational evidence (Gallimore et al. 1994; Macchetto et al. 1994) the authors suggested that the southern region of NGC 1068 must face an absorption excess.

According to our model, this excess is possibly due to the back-leaning cone which, situated farther away from the observer's, presents a lower polarized flux in the polarization maps (Fig. 5.3). The projected southern outflow, being partially covered by the circumnuclear dust, radiates much less photons and thus can appear as more obscured than its northern counter-part. Due to the system inclination, the upper side of the torus funnel is partially visible, allowing radiation reprocessed off the equatorial disk to illuminate the northern cone base. Fig. 5.3 clearly shows this trend without invoking any foreground absorption on the observer's line-of-sight.

If we generalize our model to the global AGN picture, it implies that a possible symmetry break must be considered when investigating the outflows of Seyfert-like galaxies. This asymmetry may thus be detected by an anomalously high percentage of polarization, such as discussed in Marin et al. (2012c) for the Seyfert-1 galaxy Mrk 231.

5.3.2 Fragmentation of the winds

Our NGC 1068 model showed that using a continuous and homogeneous polar outflow with $\tau_V \sim 0.03$, it is possible to reproduce the observed level of polarization after fine tuning of the

wind's three-dimensional orientation. It also showed that the very high P values found by Capetti et al. (1995) and Axon et al. (1996), when observing the dense matter knots in the extended NGC 1068 outflows, can be reproduced with an optically thicker geometry (i.e. $\tau_V \sim 0.3$). The spatially resolved *Chandra* High Energy Transmission Grating (HETG) observations and modeling of NGC 1068 by Ogle et al. (2003) corroborate the presence of an ionized region sustaining $\tau_V \sim 0.27 \pm 0.08$. Thus, the best modeling approach would be to consider optically thick ($\tau_V \sim 0.3$) clumps immersed in an optically thin ($\tau_V \sim 0.03$) continuous medium.

In a future work we aim to explore the polarization signature emerging from a fragmented ionization cone composed of optically thick ($\tau_V \sim 0.3$) clouds. Multiple scattering between clumps should lead to polarization levels close to the one observed in Fig. 5.2, as the high polarization degree produced in the knots may be balanced by depolarization effects induced by multiple scattering. A preparatory work, based on the impact of different cloud distributions onto polarization is explored in Chap. 7, and will be used in a future work to build a more complex model of NGC 1068.

5.3.3 Detection of circular polarization in NGC 1068

Along this chapter, we examined the production of total (linear + circular) polarization, but the amount of circular polarization can be neglected in comparison with linear polarization (Landstreet & Angel 1972; Gehrels 1972). The detection of optical circular polarization in Seyfert-like galaxies is challenging as this expected amount due to scattering is very low ($\ll 1$ %). While Nikulin et al. (1971) claimed to have measured a very large degree of circular polarization (~ 1 %) in NGC 1068, their results were never confirmed by other authors (Gehrels 1972; Landstreet & Angel 1972; Angel et al. 1976).

To check the validity of our dust model as well as the overall parametrization of NGC 1068, a further investigation of the circular polarization signal must be considered. Two main mechanisms are responsible for the production of circular polarization: multiple Mie scattering on asymmetric distributions of spherical or randomly aligned dust particles, and transmission of light by aligned dust grains, a process known as dichroic extinction (see Sect. 3.2.6). STOKES, handling multiple scattering in a user-defined dust medium, is already able to take into account the first mechanism. We thus examine the amount of circular polarization induced by Mie scattering in AGN tori in the next chapter.

The results presented in this chapter have been partially published in Marin et al. (2012a). A publication exploring the complex geometry of NGC 1068 is in preparation.

Chapter 6

Exploring the circular polarization induced by AGN tori

To understand the impact of circumnuclear absorption and scattering on the AGN spectropolarimetric signatures, numerous modeling of radiative transfer in dusty tori has been conducted in the UV and optical bands. Kartje (1995) developed a Monte Carlo code to track the polarization induced by dust scattering in a uniform-density, toroidal region. He found that it can produce substantial polarization, up to 30 %, depending on the observer's viewing angle. Wolf & Henning (1999) investigated the radiative transfer in the AGN unification scheme and confirmed that dust scattering in the optically thin NLR is responsible for the wavelength dependence of the linear polarization. Young (2000), using his General Scattering Model (GSM), reproduced the continuum polarization of Mrk 509. To reproduce the near infrared continuum polarization of Mrk 1210, Mrk 463E and NGC 1068, Watanabe et al. (2003) investigated a polarization model for dust scattering in a torus with the same grain size distribution as in the Galactic diffuse interstellar medium. Goosmann & Gaskell (2007) explored the effect of the shape of the torus inner edge as well as different opacities and half-opening angles on the polarization continuum. Finally Marin et al. (2012c) coupled the dusty, circumnuclear region with several other AGN reprocessing media such as the polar, ionized outflows and investigated how the torus geometry and composition impact on the polarization signature of a complex AGN model (see Chap. 4).

All of these previous attempts to study and determine the impact of the dusty torus on the AGN polarization signal were undertaken focusing on the linear polarization induced by Mie and Thomson scattering. While being more difficult to observe due to its intrinsically small degree of polarization ($\ll 1$ %), circular polarization induced by Mie scattering on spherical or randomly aligned dust particles can bring new information directly related to the dust composition. However, the search for optical, circular polarization in Seyfert nuclei gave nearly no results (Landstreet & Angel 1972; Gehrels 1972); for instance Gehrels (1972) found a degree of circular polarization close to 0.01 ± 0.18 % for NGC 4151 and 0.11 ± 0.14 % for NGC 1068, a type-1 and a type-2 Seyfert galaxy, respectively. Both of these measurements suffer from large error bars. Due to a level of instrumental noise similar to the sources degree of circular polarization and a non-mastered correction method for instrumental depolarization (Gehrels 1972), observational campaigns were abandoned and the recorded circular polarization data remain questionable.

To determine the degree of circular polarization that can be produced in the circumnuclear, dusty region of radio-quiet AGN and to compare it with the few near-UV and optical continuum polarization measurements from the literature, a new investigation of the torus spectropolarimetric signature is necessary. Theoretical modeling of dust scattering that has been done so far either only considered the first order scattering approximation and/or was restricted to linear polarization. In

this chapter, we aim to investigate for the first time the circular polarization induced by multiple Mie scattering events on an optically thick dusty torus filled with three different mixtures of dust used in previous work to fit the torus spectral and polarimetric signatures.

6.1 Producing circular polarization

6.1.1 Circular polarization from multiple scattering

In STOKES, the photon's polarization is recorded using the Stokes formalism $\vec{S} = (I, Q, U, V)^{\mathrm{T}}$ as illustrated in Bohren & Huffman (1983). A detailed description of the polarization properties of the radiation and its transformation during scattering events can be found in this manuscript (Chap 3, Sect. 3.1), and in Goosmann & Gaskell (2007), based on the previous work of Fischer et al. (1994). In addition to this description, we want to recall that the total polarization P computed in STOKES is a combination of the linear P_{lin} and circular P_{circ} polarization.

In this formalism, P is calculated by

$$P = \frac{\sqrt{Q^2 + U^2 + V^2}}{I} \tag{6.1}$$

And P_{lin} is equal to

$$P_{\mathrm{lin}} = \frac{\sqrt{Q^2 + U^2}}{I} \tag{6.2}$$

While P_{circ} is derived as

$$P_{\mathrm{circ}} = \frac{V}{I} \tag{6.3}$$

where the V-parameter of the Stokes vector traces the intensity of the circular polarization.

The linearly polarized, UV and optical continuum observed in AGN originates from thermal processes including electron and dust scattering (Angel et al. 1976; Bailey et al. 1988). But, to produce circular polarization, multiple Mie scattering on spherical, asymmetric distributions or randomly aligned dust particles is the main mechanism in the UV/optical waveband (Angel & Martin 1973; Serkowski 1973), as electron scattering leaves V unchanged (Goosmann & Gaskell 2007). Based on the study of VY Canis Majoris (VY CMa), Serkowski (1973) and Angel & Martin (1973) demonstrated that the light crossing a medium filled with spherical or any sort of randomly aligned particles with a size comparable to the radiation wavelength is linearly polarized at the first scattering (Q and/or $U > 0$). Then a second scattering on a dust particle introduces ellipticity, provided that the incident electric vector is not perpendicular or parallel to the scattering plane ($U \neq 0$). It follows that radiative transfer modeling of AGN tori must contain multiple scattering to take into account second order scattering and thus variations of the V-parameter inducing circular polarization.

6.1.2 Spectropolarimetric signatures of the torus

To simulate the circular spectropolarimetric response of an optically thick dusty torus, we defined an isotropic, point-like source emitting a spectrum with a power-law spectral energy distribution $F_* \propto \nu^{-\alpha}$ and $\alpha = 1$. As circular polarization emerges from Mie scattering of linearly polarized photons, the input spectrum polarization state ranges from an unpolarized state (P_{source} = 0 %) to a maximally intrinsic polarization (P_{source} = 100 %). We defined the linear polarization level using a positive value for the U-parameter of the Stokes vector in order to produce ellipticity (see previous paragraph). The initial polarization is linearly oriented at 45° with respect to the

meridian, a configuration maximizing the production of circular polarization (see Sect. 3.1.2). Surrounding the emission source, we modeled a circumnuclear torus with an inner radius of 0.1 pc and an outer radius of 0.5 pc. The torus is set to match the geometrical sizes derived for the archetypal Seyfert 2 galaxy NGC 1068, as determined by Raban et al. (2009). According to the unified model (Antonucci 1993) that implies an optically thick, obscuring region to preserve the observed type-1/type-2 dichotomy, the radial optical depth of $\tau_{\rm V}$ measured along the equatorial plane is taken to be ~ 500 in the V-band. The half-opening angle of the torus is set to $\theta_0 = 60°$ with respect to the vertical axis, to be coherent with the parametrization of Goosmann & Matt (2011b) for the dusty torus in NGC 1068. The torus is filled with typical "Milky Way" dust (Tab. 5.2, Chap. 5) defined by Wolf & Henning (1999) and used by Goosmann & Gaskell (2007), Marin & Goosmann (2011), Marin et al. (2012a) and Marin et al. (2012c) to model dusty tori.

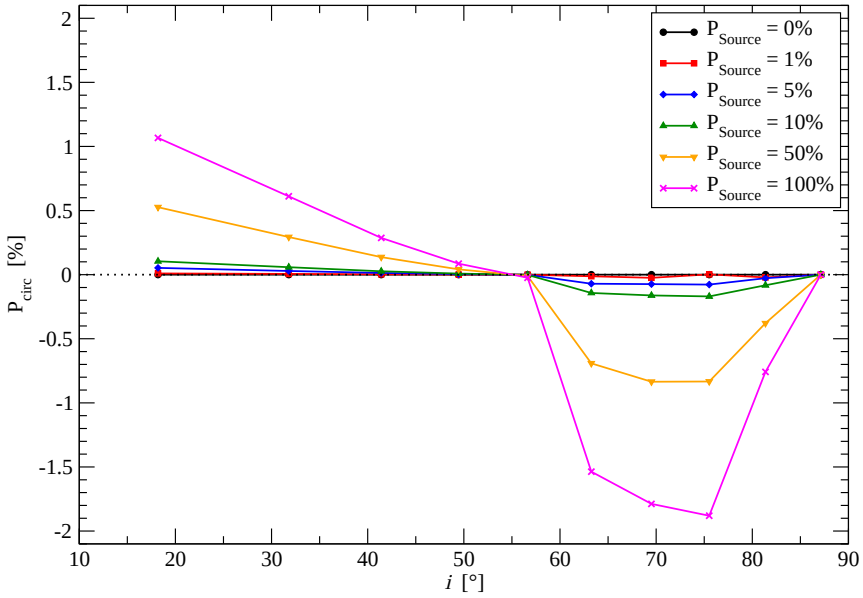

Figure 6.1: Modeling a dusty torus with $\tau_V \sim 500$ and a half-opening angle $\theta_0 = 60°$ measured relative to the axis of symmetry. A "Milky Way" dust model is considered. The circular polarization $P_{\rm circ}$ is plotted for different viewing inclinations, i, according to its initial polarization state. *Legend*: $P_{source} = 0$ % (black dots), 1 % (red squares), 5 % (blue diamonds), 10 % (green triangles), 50 % (yellow inverted triangles) and 100 % (magenta crosses).

The integrated, 3000 – 8000 Å, circular polarization $P_{\rm circ}$ emerging from the dusty torus model is presented in Fig. 6.1. Conventionally, a positive value of $P_{\rm circ}$ denotes a right-handed circular polarization, and a negative value stands for left-handed $P_{\rm circ}$. Note that if the U-parameter of the incident Stokes vector was defined to be negative, the resulting circular polarization would be inverted. For an unpolarized input spectrum, the resulting circular polarization is equal to zero, as left- and right-handed polarization are equally created by scattering events and cancel each other. Thus, if the initial photon flux is not polarized neither by an intrinsic emission mechanism

nor by previous scattering events, no circular polarization can emerge from a uniform dusty torus. However, when considering polarized radiation sources, circular polarization is created. For type-1 viewing angles, $P_{\rm circ}$ is positive and decreases with inclination. Photons, scattered off the torus funnel, carry a right-handed circular polarization that is maximum at polar viewing angles. As the orientation of the system increases, less photons are able to escape from the torus inner walls. The polarization spectra pass through a minimum value when the observer's viewing angle is equal to the torus half-opening angle. $P_{\rm circ}$ then switches to a negative value and photons escaping from the torus carry a left-handed polarization signal, due to backscattering events inside the torus funnel. The absolute value of $P_{\rm circ}$ rises with inclination, with a maximum value around $i \sim 75$ °, and strongly decreases along equatorial directions due to the torus obscuration. At type-1 viewing angles, $P_{\rm circ} \sim 1$ % at maximum for $P_{source} = 100$ %; along type-2 viewing angles, $P_{\rm circ} \sim 2$ % for the same polarization input. However, such a high initial polarization is incompatible with theories and observations. According to Chandrasekhar (1960) and Sobolev (1963), radiation emerging from an electron plane-parallel slab, representing the emitting accretion disk, has a maximum intrinsic parallel polarization of 11.7 % when viewed edge-on. If the disk is inclined (warped disks, Nayakshin 2005; Martin 2008; Bartko et al. 2009), it might produce the necessary initial polarization, linearly oriented at 45° with respect to the meridian. Using this constraint, a dusty torus can produce a circular polarization degree up to 0.1 % along the polar directions, and up to 0.2 % at typical type-2 viewing angles.

One must note that our results are only applicable for an initial polarization vector defined with its U-parameter > 0 and Q-parameter $= 0$. The polarization orientation ψ, defined as $\psi = \frac{1}{2}\tan^{-1}(\frac{U}{Q})$ (see Sect. 3.1.2), is equal to $\pm 45°$ (with respect to the meridian) for $U = \pm 1$ and $Q = 0$. When $U = 0$ and $Q = \pm 1$, ψ is equal to 0° (perpendicular polarization) or 90° (parallel polarization). Intermediate Q and U states give intermediate ψ values. To produce a maximum degree of circular polarization, the Mueller matrix for Mie scattering implies a polarization position angle as close as possible to 45°, but it is hard to find an explanation for a source to solely produce linear polarization oriented at 45°. From now on, we keep in mind that the rest of this chapter is considering a theoretical approach, rather than a close-to-reality scenario.

6.1.3 Circular polarization emerging from different dust grain models

As stated in Chap. 5, Sect. 5.2.4, the exact composition of the dusty environment in AGN is poorly constrained. To check the impact of the grain composition on the modeled circular polarization degree, we now test the three different dust models presented in Tab. 5.2.

It appears that the "AGN" and "ISM" dust models produce the same amount of wavelength-integrated circular polarization as the "Milky Way" prescription (see Fig. 6.2). $P_{\rm circ}$ is lower than 0.12 % for type-1 inclinations, and close to 0.2 % for type-2 viewing angles, taking into account $P_{source} = 10$ %. No particular features distinguish the "Milky Way" dust model from the "AGN" and "ISM" models. At $i \sim 75°$, all the models produce the same, maximum amount of circular polarization as the photons scatter multiple times before escaping from the torus funnel, thus carrying a maximum polarization degree, independently of the model. We prove here that there are no deep differences in circular polarization signatures for the three dust mixtures examined, indicating that linear polarization studies are more suitable to discriminate between different dust models (see Chap. 5, Sect. 5.2.4).

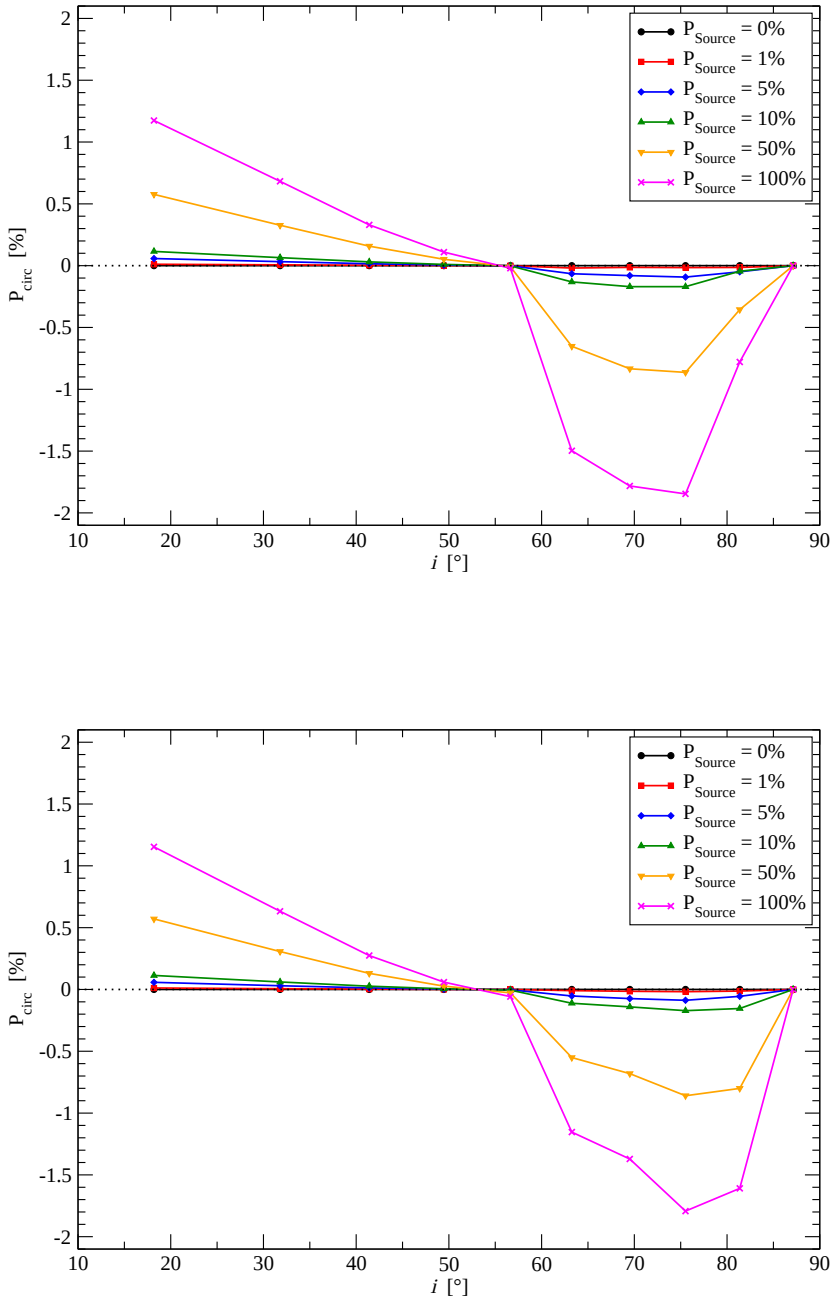

Figure 6.2: Modeling a dusty torus with $\tau_V \sim 500$ and a half-opening angle $\theta_0 = 60°$ measured relative to the axis of symmetry. An ISM (top) and AGN (down) dust models are now considered. The circular polarization $P_{\rm circ}$ is plotted for different viewing inclinations, i, according to its initial polarization state. *Legend*: $P_{source} = 0$ % (black dots), 1 % (red squares), 5 % (blue diamonds), 10 % (green triangles), 50 % (yellow inverted triangles) and 100 % (magenta crosses).

6.2 Comparison with the circular polarization in NGC 1068

As presented in Chap. 5, NGC 1068 is considered as one of the best examples of archetypal, thermal Seyfert-2 galaxies and gave rise to the discovery of broad line signatures in its scattered polarization spectrum (Antonucci & Miller 1985). Being relatively close (14.4 Mpc, Bland-Hawthorn et al. 1997) and luminous (1.5×10^{11} $L_{\odot}$, Bock et al. 2000), NGC 1068 was extensively observed during the past three decades in linear polarization. But, to my knowledge, only three attempts to measure the amount of optical, circular, continuum polarization were published. Nikulin et al. (1971) measured $P_{\rm circ}$ with the stellar magnetograph of the 104-inch Crimean reflecting telescope and found a value of 0.98 ± 0.12% in the 4000 - 5800 Å band. Gehrels (1972), using the Steward 229-cm reflector with the Wollaston polarimeter of Gehrels & Teska (1960), did not confirm the level of $P_{\rm circ}$ found by Nikulin et al. (1971). Over the same energy band, they found a polarization degree of 0.11 ± 0.14 % which they considered as not meaningful. Finally, Angel et al. (1976) detected a circularly polarized, optical continuum, with $0.04\ \% \leq P_{\rm circ} \leq 0.18\ \%$, using the 90 inch telescope of Steward Observatory.

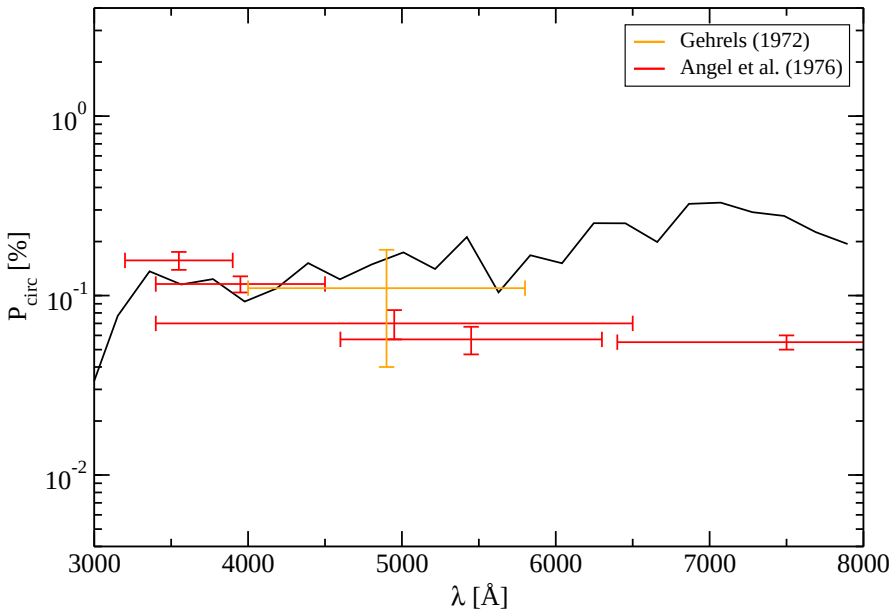

Figure 6.3: Modeling the circular polarization of NGC 1068 using a uniform dusty torus with $\tau_V \sim 500$, $i \sim 70°$ and a half-opening angle $\theta_0 = 60°$ measured relative to the axis of symmetry. The torus is filled with a "Milky Way" dust grain model. NGC 1068 spectropolarimetric observations by Gehrels (1972) and Angel et al. (1976) are reported on the spectra.

In Fig. 6.3, we plotted the circular polarization originating from our isolated, optically thick, dusty torus filled with a "Milky Way" dust mixture. The emitting source is set to a polarized state with $P_{source} = 10$ % (linearly oriented at 45° with respect to the meridian). As stated in Sect. 6.1.2, the geometry of our model matches the torus size constraints of NGC 1068 and, in

order to be coherent with observational evidences, we opted for a system inclination of $i \sim 70°$ (Hönig et al. 2007). The resulting $P_{\rm circ}$ is plotted versus the photon wavelength. In comparison with Gehrels (1972) and Angel et al. (1976), the model shows the expected level of $P_{circ} \sim 0.1$ % but fails to reproduce the increase of polarization in the 3500 – 4000 Å band observed by Angel et al. (1976). The "Milky Way" model is globally wavelength-independent and presents an increase of P_{circ} in the red part of the spectrum; a behavior not observed in NGC 1068. However, as demonstrated by Gehrels (1972) and Antonucci & Miller (1985), the detection of optical circular polarization in Seyfert galaxies is challenging and the observations might suffer from too much background and instrumental pollution to correctly account for any spectral tendencies. A new observation of the optical, polarized continuum of NGC 1068 would be needed to verify the results of Angel et al. (1976).

It is interesting to note that the modeled wavelength-dependent polarization signature is in agreement with the measurement by Gehrels (1972), Serkowski (1973) and Angel & Martin (1973) of the ellipticity of VY CMa that was found to increase in the red tail. While being a massive and luminous ($6 \times 10^4 < \mathrm{L}_\odot < 5 \times 10^5$) red super-giant star, VY CMa is embedded in a large, optical, asymmetric circumstellar environment (Wittkowski et al. 2012), somewhat similar to the geometry of AGN. This shows that our model can be applied to other classes of astrophysical objects, while the dust composition and geometry must, of course, be adapted to the individual case.

6.3 Summary and discussion

We have conducted accurate modeling of the circular polarization emerging from circumnuclear, dense matter that obscures a central irradiation source. The scattering region was filled either with "Milky Way", "AGN" or "ISM" dust, and its dimensions were set according to size constraints of the torus in NGC 1068.

We found that, if the input spectrum is not intrinsically polarized, the resulting circular polarization emerging from multiple scattering inside the torus funnel is equal to zero as left- and right-handed polarization cancel each other. However, if we consider a theoretical model in which the radiation source is already linearly polarized and oriented at 45° with respect to the meridian, then circular polarization can be introduced. According to the maximal level of polarization that an inclined, ionized accretion disk can produce, P_{circ} can be as high as 0.2 % along type-2 viewing angles. In this condition, our scenario matches the observed level of circular polarization detected in NGC 1068.

Surprisingly, the different dust models investigated in this chapter do not show strong differences in the resulting circular polarization. Thus, in contrast to linear polarization (see Chap 5, Sect. 5.2.4), circular polarization cannot be used to discriminate between different grain prescriptions.

If we consider that a uniform, torus model is a correct approximation, then circular polarization induced only by Mie scattering is not enough to reproduce the degree of circular polarization observed by Gehrels (1972) and Angel et al. (1976) in NGC 1068 . Other mechanisms must be considered to achieve and a solid explanation must be found to explain why the irradiating source has an intrinsically polarized spectrum, with its polarization position angle preferentially oriented at 45°.

6.3.1 Other mechanisms responsible for optical circular polarization

6.3.1.1 Dichroic extinction in radio-quiet AGN

An alternative mechanism to produce circular polarization is transmission of light by aligned dust grains, a process known as dichroic extinction (please refer to Chap 3, Sect. 3.2.6 for more details). Dichroic extinction is one of the mechanisms responsible for the interstellar linear (Wood 1997) and circular (Martin 1974) polarization in the Milky Way. Aligned dust grains acquire two distinct absorption cross-sections along the particle's vertical and horizontal symmetry planes, resulting in polarization vectors of a scattered radiation aligned parallelly or perpendicularly to the symmetry axis of the grain, respectively. The scattering efficiency is not isotropic, as radiation can "see" different scattering cross-section, even if the reprocessing region is symmetric. In the context of active galaxies, this scattering mechanism can considerably increase the level of linear polarization in AGN (Kartje 1995). It may be partly responsible for the polarization of type-1 AGN when the observer's line-of-sight crosses the NLR, believed to be constituted of both ionized matter and interstellar dust (Marin & Goosmann 2012 and references therein). However, the impact of dichroic extinction on optical circular polarization of AGN in the context of complex reprocessing between different media was never studied and remains a goal for further development of STOKES.

6.3.1.2 Synchrotron emission in radio objects

In radio jets, optical circular polarization is produced during the emission of synchrotron radiation in an intense magnetic environment. While the synchrotron emission has an intrinsically high degree of linear polarization, it also contains a small fraction of circular polarization (Legg & Westfold 1968) which depends on the magnetic field, the angle between the field and the observer's line-of-sight, and the emitted frequency (Saikia & Salter 1988). The polarization of blazar AGN can be observed in the optical band for low frequency break BL Lac objects (LBL) and at UV wavelengths for the high frequency break BL Lac objects (HBL) (Ulrich et al. 1997), with HBL being generally less polarized than LBL in the optical band (Jannuzi et al. 1993). The amount of optical circular polarization in radio-loud objects is lower than 1 % but some peculiar objects, such as 3C279 (Rieger & Mannheim 2005), show an unexplained high $P_{\rm circ} > 1$ %. In any case, the optical synchrotron emission overwhelms the production of Mie-induced circular polarization from the dusty heart of the blazars.

Many experiments have been performed to measure the amount of circular polarization at larger wavelengths, especially in the radio domain (Weiler & Raimond 1977; Weiler & de Pater 1980, 1983; Komesaroff et al. 1984). Judging from the atlas of Weiler & de Pater (1983), no radio sources exceed 0.5 % in circular polarization. Besides, less than 40 % of the 120 sources observed show circular polarization at even 2σ detection. This indicates that the detection of circular polarization in radio galaxies is tricky even at radio wavelengths.

6.3.2 Fragmented tori

As stated in most of the previous chapters, our modeling assumed a uniform constant density across the torus, which is a considerable simplification. There are numerous hints indicating that the dusty torus surrounding the AGN core should be fragmented (Tristram et al. 2007; Nenkova et al. 2008b,a; Hönig & Kishimoto 2010; Heymann & Siebenmorgen 2012). Based on previous tests, we argue in Marin et al. (2012c) that a clumpy structure should lead to a weaker net polarization detected at type-2 viewing angles. This statement will be verified in the next chapter, where cloudlet

distributions will finally replace bulky, reprocessing regions. However, our previous statement solely concerns the total polarization, where linear polarization dominates by a factor of 100 the net circular polarization. The clumpiness of the torus should play in favor of the circular polarization as more scattering is needed for photons to escape from the circumnuclear region, thus leading to an increase of $P_{\rm circ}$. Further tests are necessary to assess this statement and to model the circular polarization emerging from a clumpy structure. This type of modeling is time-consuming in terms of statistics and STOKES requires computational improvements in order to reach this goal.

The results presented in this chapter have not yet been published. A paper is in preparation.

Chapter 7

Enhancing the complexity with fragmented reprocessing media

The topic of fragmentation became famous in the very beginning of the twentieth century, when Jeans (1902) investigated the stability of a uniform, self-gravitating nebula. His linear analysis of the gravitational stability of a spherical medium lead to the discovery that beyond a critical mass (or radius), any formation mechanism should lead to a fragmented medium if the initial amount of gas is spread over large (i.e. astronomical) distances. The initial formulation of Jeans (1902) was improved half a century later, when (Hunter 1962) solved the exact equations for hydrodynamical instabilities. Recognized as a ubiquitous phenomenon in astrophysics, the fragmentation of dense media was soon investigated by non-linear analyses, where the impact of radiation and the cases of non-uniform media were subsequently explored by Arny (1966).

The work done by Arny (1966) is particularly interesting for the field of AGN physics because he proved that a non-uniform medium, immersed in a radiation field, can dislocate itself without requiring any magnetic forces. The fact that the large-scale magnetic environment in AGN is believed to be negligible, taking into account that most of the detected media are neither uniform nor symmetrical, and that the central engine is irradiating the whole system from the infrared to the X-ray band, it is quite a straightforward conclusion that most of the AGN components should be fragmented. In particular, the supposed bulk circumnuclear torus, shielding the SMBH along the equatorial plane, is quite debated as the torus size invoked by the unified model (Antonucci 1993; Lawrence 1991), typically from 0.1 to 100 parsecs, is inconsistent with self-gravitational stability. A fragmented dynamical state is thus a natural possibility.

In this chapter, we first resume the few observational and numerical hints pointing toward fragmented media in AGN. We particularly focus on the dusty torus, the outflowing winds and the more distant accretion flow as there are direct and indirect proofs that they should be clumpy. We then build fragmented models and investigate their spectropolarimetric signatures in comparison with the uniform scattering regions explored in Chap. 4. We ultimately gather all the fragmented regions in a complex AGN model assembling more than 4500 reprocessing clumps.

7.1 Hints for clumpy structures in AGN

Most of the previous chapters of this thesis already mentioned that there is an increasing number of hints indicating that some of the reprocessing regions in AGN should be fragmented. Optical/UV observations of NGC 1068's NLR by Capetti et al. (1995) revealed the presence of two knots of different luminosity in the outflowing gas that can be attributed to inhomogeneities of the medium. Similar results are found by other studies at similar (Capetti et al. 1997) or longer

wavelengths (Packham et al. 1997), strengthening the idea that the AGN outflows may not be a continuous flow.

There is less direct evidence for a clumpy structure of the dusty torus. Most of the suppositions about the fragmented nature of the circumnuclear matter comes from numerical simulations. Based on Pier & Krolik (1992, 1993) suggestions about the nature of the obscuring, equatorial region, Nenkova et al. (2002) undertook IR modeling of a distribution of clumps around a central irradiating source. They successfully reproduced the 10 μm silicate feature, the width of the far-IR emission peak and the Spectral Energy Distribution (SED) of both type-1 and type-2 objects. Similar work, at different wavelengths, was conducted to reproduce or examine the behavior of a fragmented torus (Risaliti et al. 2002; Nenkova et al. 2008b,a, 2010; Schartmann et al. 2008; Hönig & Kishimoto 2010; Heymann & Siebenmorgen 2012).

If we take into account reverberation mapping observations of the BLR (Netzer & Laor 1993; Suganuma et al. 2006; Gaskell et al. 2007), the low ionization gas region of the BLR should coincide with the dust sublimation radius of the dusty torus (see Chap. 4). In this hydrodynamical picture, the torus is thought to be a smooth continuation of the accretion flow. It further implies that the BLR zone contains self-shielding clouds that become hotter towards smaller radii of the outer accretion disk (Gaskell et al. 2007).

7.2 Impact of fragmentation on the polarization signature of individual reprocessing regions

The overall picture of AGN becomes more complicated adding clumpy instead of uniform reprocessing regions. Radiative transfer calculations take much more time as extensive multiple scattering must be considered. Also, the complex radiative interactions between two consecutive clumps are different from scattering inside a homogeneous medium, especially when one considers polarization as part of the process, as the geometry of the model is very different (see Fig. 7.1).

7.2.1 Building a fragmented model

To investigate the impact of fragmented reprocessing media, we now re-compute the polarization of isolated, uniform scattering regions presented in Chap. 4, namely the dusty torus, the polar winds and the hot accretion flow. We conserve the model geometry but replace the region by three clumpy distributions of 500, 1000 and 2000 spheres. These clouds are distributed uniformly inside the scattering region. Doing so, we evaluate how the filling factor of the model components affects the polarization behavior. The filling factor $\mathcal{F}$, ranging from 1 to 0, can be evaluated by summing up the volume of the clumps and dividing the total by the volume of the same, unfragmented reprocessing region. For the remainder of this chapter, the clumps are modeled using constant density spheres of equal radius. The total optical depth along the observer's viewing angle strongly depends on the filling factor: for the 500-sphere models, 1 to 3 clumps can (partially) obscure a line-of-sight crossing the cloud distribution, and up to 10 clumps can hide the irradiating source in the 2000-sphere models.

Similarly to most of our previous modeling, we define an isotropic, point-like source emitting an unpolarized spectrum with a power-law spectral energy distribution $F_* \propto \nu^{-\alpha}$ and $\alpha = 1$ at the center of the model. We maintain the convention established in the previous chapters: a negative value of P stands for parallel polarization with respect to the vertical axis of the model space, a positive P for perpendicular one.

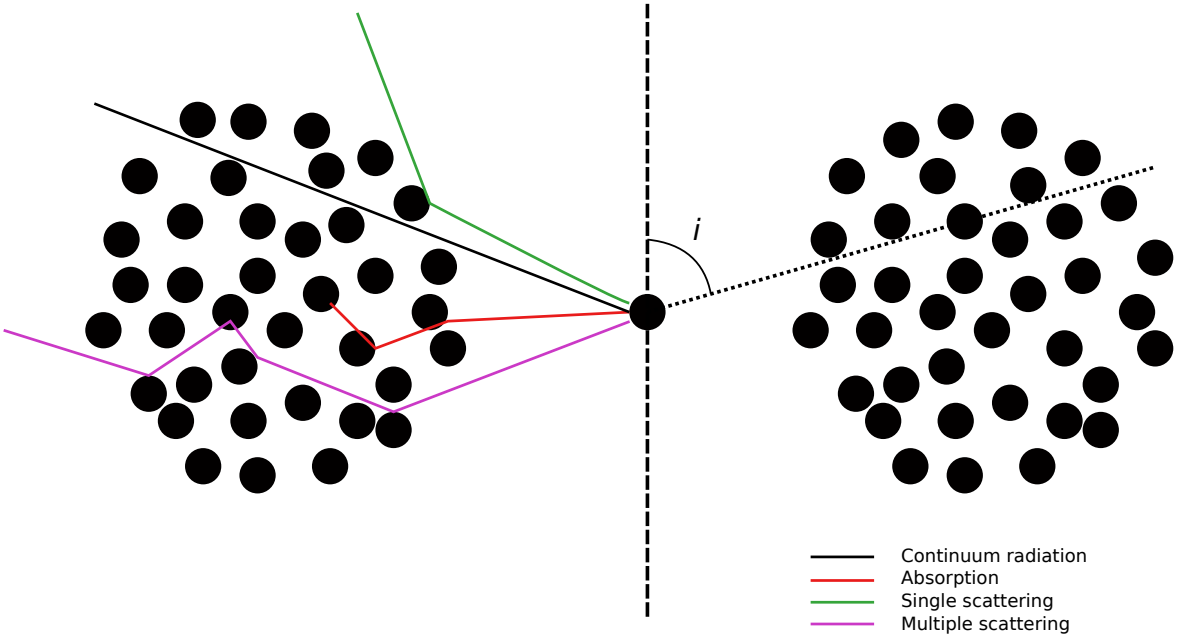

Figure 7.1: Schematic view of a fragmented region. Clumps are shielding each other from the central source, but gaps between the spheres allow part of radiation to escape from the model, even along equatorial directions where obscuration is most efficient (in the case of a circumnuclear torus).

7.2.2 Clumpy torus model

The first model corresponds to a uniform obscuring dusty torus ($\tau_{dust} = 750$) situated along the equatorial plane of the model. The inner and outer radii of the fragmented torus are set to 0.25 pc and 100 pc, respectively, the half-opening angle is set to $\theta_0 = 30^\circ$ and the model spheres are filled with dusty grains based upon the Milky Way mixture (see previous chapters). Each clump has a radius $\mathrm{R}_{sphere} = 2.35$ pc and is optically thick, with $\tau_{dust} = 200$.

The fractions F/F_* of the central flux for a uniform model, as well as three sphere distributions: 500 ($\mathcal{F} = 0.06$), 1000 ($\mathcal{F} = 0.13$) and 2000 spheres ($\mathcal{F} = 0.25$), are presented in Fig. 7.2 (top). In comparison with a uniform torus model, the 500-sphere model shows a similar behavior in terms of flux versus inclination. The flux is maximum for viewing angles close to the polar directions as the observer is looking directly through the torus funnel. As the inclination of the system increases, the radiation flux becomes partly obscured by the dust clumps and thus decreases. At an equatorial viewing angle, $i \sim 81^\circ$, 500 spheres are not sufficient to block photons escaping from the central source; thus the flux is still quite high for a type-2 model. The spectral shape is more curved in the blue tail in comparison with the uniform model since, at larger wavelengths, photons may scatter between clumps before escaping or being absorbed. This behavior is opposite to our previous uniform model. When increasing the number of clumps, the filling factor of the model

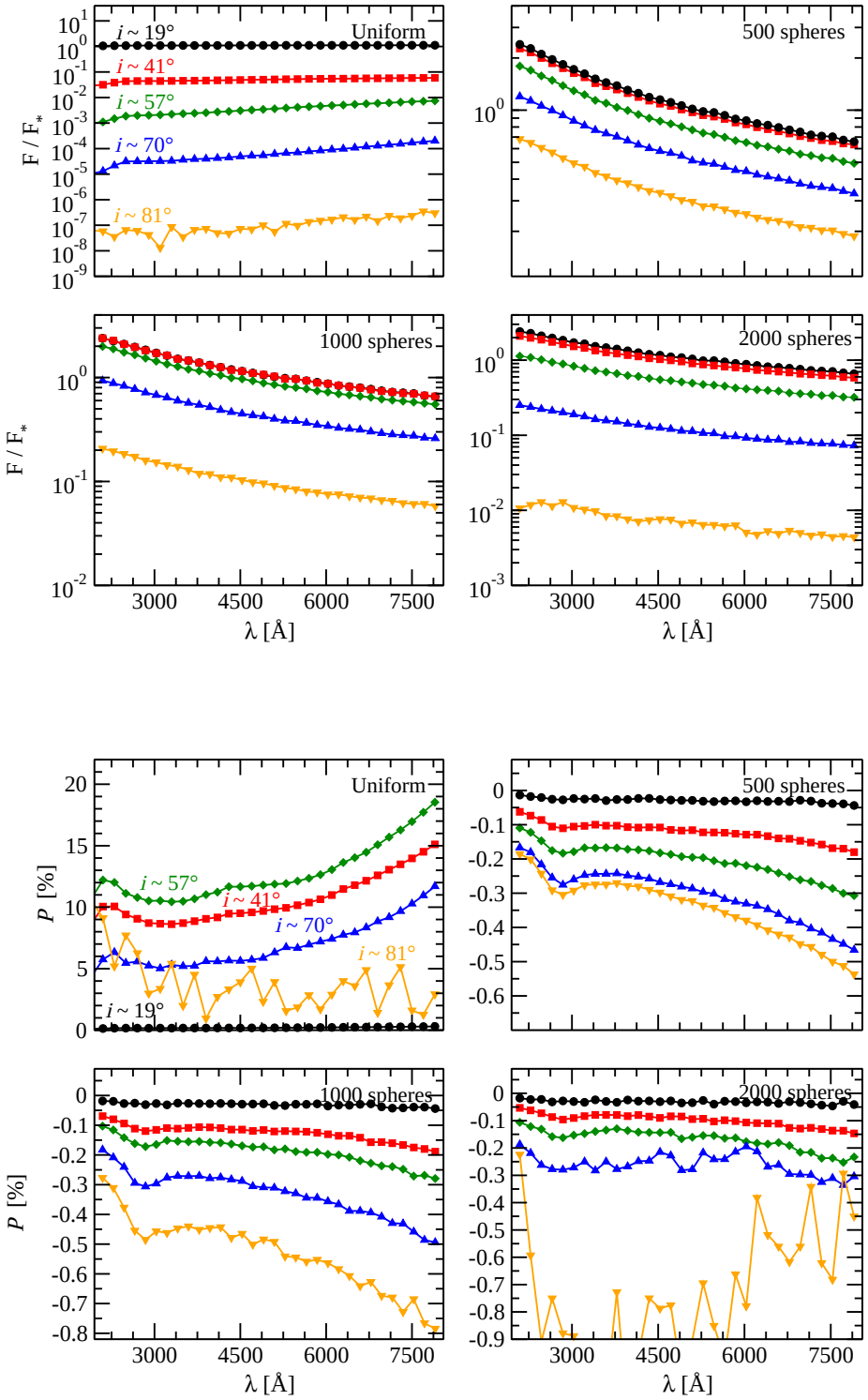

Figure 7.2: Modeling an optically thick, elliptically shaped, fragmented torus with $\theta_0 = 30°$ measured relative to the symmetry axis. The fraction F/F_* of the central flux (upper panel) and the spatially integrated polarization P (lower panel) are seen at different viewing inclinations, i, from 2000 to 8000 Å. The reader is cautioned to notice the change in scale between the four models.

rises and the partial covering of the source becomes more important. Less flux is observed at type-2 inclinations as it is more obscured. The flux at type-1 inclinations remains maximum as there is no absorption along the line-of-sight. Finally, with a 2000-sphere configuration it is possible to reduce the flux coming from the inner source at equatorial views but it is impossible to completely cancel the incoming flux due to multiple scatterings between the clumps. It indicates that, for a clumpy torus, some optical AGN flux should be detected at high inclinations, if not drowned in the star light of the host galaxy.

The polarimetric signatures of a clumpy torus (Fig. 7.2, bottom panel) are much more surprising. For a 500-sphere distribution, the polarization degree is about ten times lower than for a uniform model and negative (i.e. parallel to the projected symmetry axis of the torus). However, the spectral shape of polarization is greatly similar to our previous results: the 2175 Å feature is properly reproduced as well as the increase of polarization in the red tail of the spectra. A minimum P is detected for polar viewing angles, as photons can easily escape from the torus funnel, and the polarization rises with inclination but does not decrease when the observer's line-of-sight crosses the torus horizon. The absolute value of P keeps increasing until it reaches a maximum at $i \sim 81°$. As there are empty spaces between the clouds, one or two scattering events are enough for the radiation to escape along the equatorial plane, which is much easier than for a uniform model. The net polarization percentage is thus much higher along the equator than at lower inclinations. A similar behavior is seen for the 1000-sphere model, where P rises close to 1 % for a type-2 inclination. Finally, when the cloud distribution starts to properly cover the central source, a large part of the photons becomes absorbed and the few ones escaping carry a large P. But, coupled to a small F/F_*, the resulting polarized flux is expected to be negligible.

The behavior of a fragmented torus model is thus quite different from the usual, uniform donut-shaped model, but some characteristics such as the spectral shape and the graphite peak are conserved. The parallel orientation of the photon position angle is explained by the small number of clouds at the torus maximum height. Most of the cloudlets are concentrated along the equatorial plane, and scattering then preferentially produces parallel polarization (see Sect. 4.1.4). Changing the morphology of the torus boundaries (i.e. reducing the external radius and increasing the half-opening angle) might affect the photon polarization angle and will be explored in the future.

7.2.3 Fragmented polar outflows

Investigating the clumpiness of AGN outflows may lead to the most observer-friendly predictions that we can realize, as direct comparisons can be undertaken with past detections from the HST, when the polarization imaging camera was functional. We now look at two different realizations of the winds, the first one using electron-filled spheres to mimic the ionized winds and the second one using dust clouds to represent the more extended NLR.

7.2.3.1 Ionization cones

We modeled an hourglass-shaped scattering region filled with electron spheres of a radius $R_{sphere} = 0.27$ pc and optical depth $\tau_{elec} = 0.3$ (in comparison, the uniform model had $\tau_{elec} = 1$). The half-opening angle of the double cone is 30° measured from the vertical axis. The filling factor for a 500-sphere distribution is equal to $\mathcal{F} = 0.06$, $\mathcal{F} = 0.12$ for 1000 spheres and $\mathcal{F} = 0.24$ for 2000

spheres. Finally, the emitting source is not restricted to radiate along a favorite direction aligned with the cones but emits isotropically.

We find that the fraction F/F_* of the central flux (Fig. 7.3, upper panel) is very similar between a uniform and a fragmented model using a low filling factor. Less flux is detected when the observer's viewing angle passes through the ionized outflow, but due to the elastic scattering the flux difference between type-1 and type-2 viewing angles is not important. When the cloud distribution is higher, multiple scattering is enhanced even when considering optically thin scattering clouds. A larger fraction of the flux is deviated from the polar direction and F/F_* decreases.

The polarization degree spectra (Fig. 7.3, bottom panel) strengthen our observations. A 500-sphere model reproduces the integrated polarization degree that we found for a uniform model, with a maximum P at equatorial viewing angles. The shape of P with respect to the system's inclination is quite similar too. For 1000 and 2000 spheres, as there are more scattering targets, the resulting polarization percentage increases up to a factor of 3. The inclination dependence is preserved but P becomes more important. The polarization position angle is positive for all the models as the spheres are situated mainly along the vertical axis of the model.

A model of fragmented winds is able to reproduce the same amount of positive polarization degree, as well as the same P-dependency versus inclination, as a uniform model if the filling factor of the wind is small. Denser cloud distributions produce higher polarization degrees due to multiplication of scattering targets. Uniform models are then a good approximation for real systems containing few gas clouds.

7.2.3.2 NLR winds

We now consider a fragmented outflow consisting of dusty spheres with $R_{sphere} = 2.7$ pc and $\tau_{dust} = 0.2$ (previous uniform model: $\tau_{dust} = 0.3$). The filling factor of the 500-sphere distribution is equal to $\mathcal{F} = 0.06$, $\mathcal{F} = 0.12$ for 1000 spheres and $\mathcal{F} = 0.24$ for 2000 spheres. The clouds are optically thin in order to represent the NLR clouds detected farther away from the irradiating source, where dust can form and survive. We follow the assumption established in Sect. 4.4 of Chap. 4 and consider that the dusty double-cone sustains the same half-opening angle as the ionized outflows, $\theta_{op} = 30°$ from the vertical axis. The inner and outer boundaries of the reprocessing region were fixed to 10 pc and 100 pc above the source, respectively.

The F/F_* spectra produced by scattering on a small number of spheres (Fig. 7.4 upper panel) reproduces the expected flux behavior: there is an equal amount of photons reaching observers whose lines-of-sight are not crossing the NLR horizon, and the flux is slightly absorbed at pole-on directions. The graphite peak signature is marginally detectable when considering a 500-sphere distribution but once looking at a denser cloud distribution, the 2175 Å absorption becomes more apparent and the flux of radiation escaping from the model at $i \sim 19°$ decreases. The 1000-sphere distribution is found to be the closest one to the uniform model.

The polarization percentage induced by a fragmented model with a low amount of scattering targets is in the same range as for a uniform model (Fig. 7.4 lower panel). According to the scattering phase function of polarization, a maximum polarization degree is observed for equatorial viewing angles, with the 2175 Å peak occuring also in polarization percentage. As the observer's

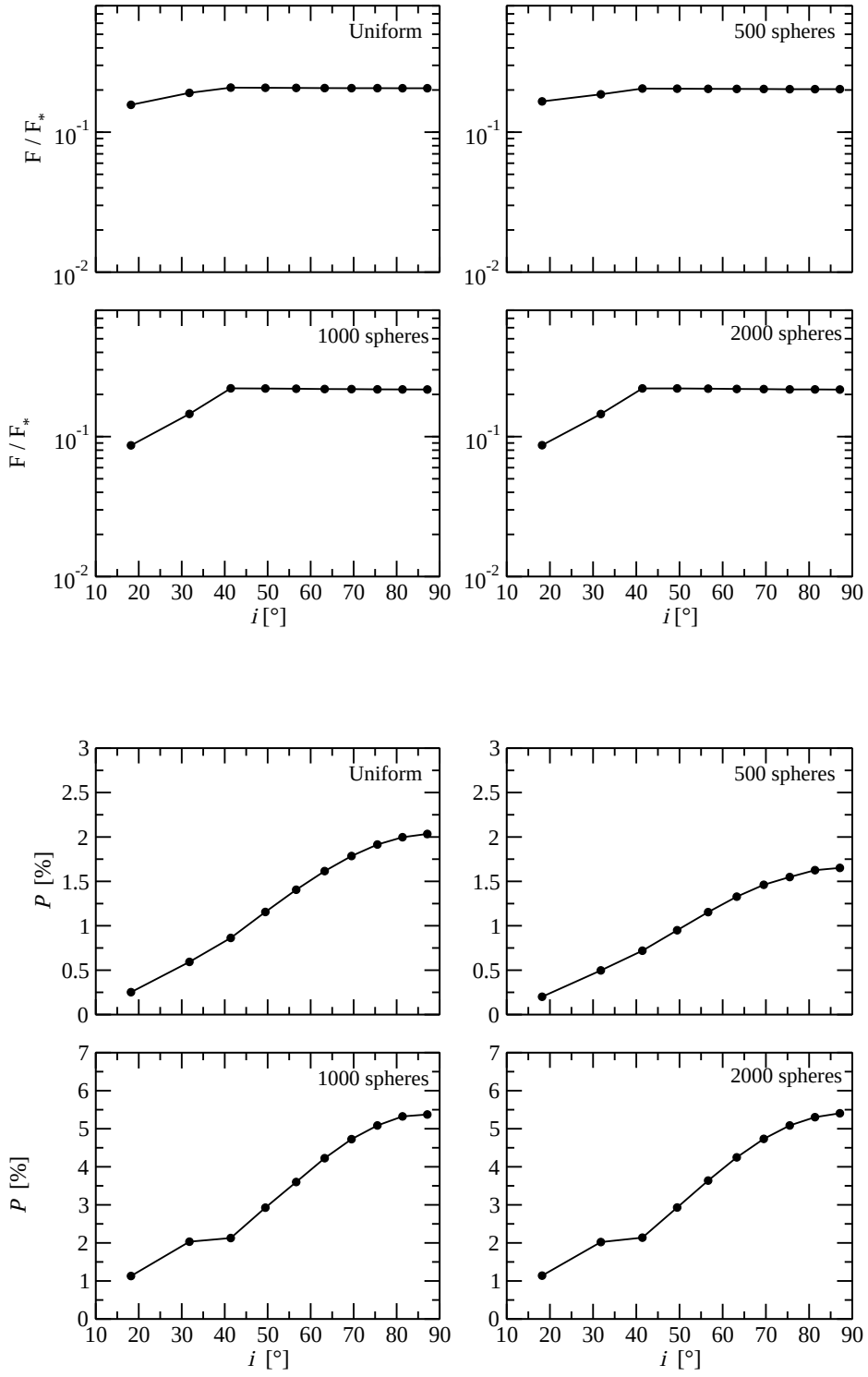

Figure 7.3: Modeling an electron-filled, fragmented, scattering double-cone with $\theta_0 = 30°$ measured relative to the symmetry axis. The fraction F/F_* of the central flux is integrated from 2000 to 8000 Å (upper panel) and the spatially integrated polarization P is plotted versus the observer's inclination i (lower panel). The reader is cautioned to notice the change in scale between the four models.

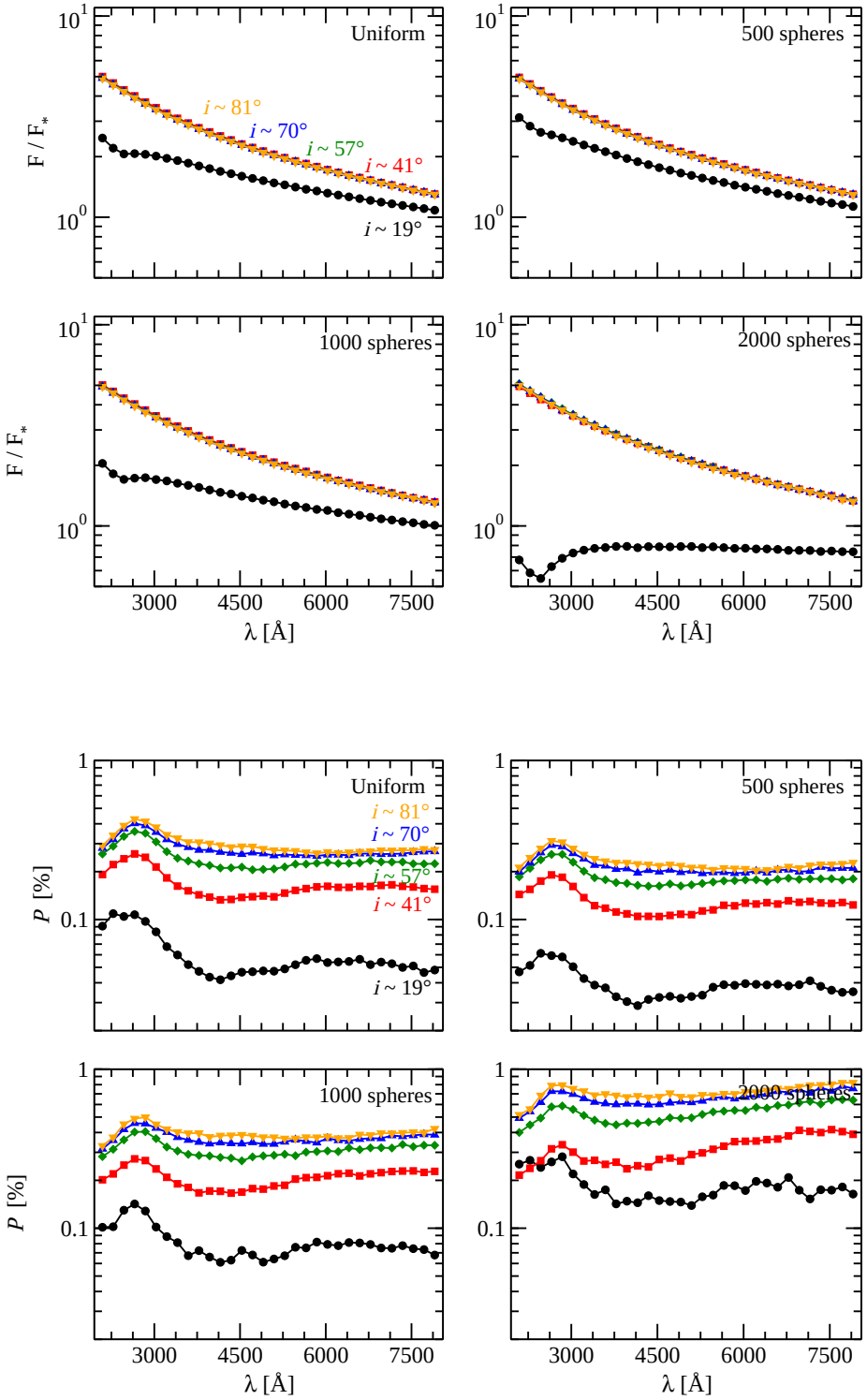

Figure 7.4: Modeling an optically thin, dusty, fragmented double-cone with $\theta_0 = 30°$ measured relative to the symmetry axis. The fraction F/F_* of the central flux (upper panel) and the spatially integrated polarization P (lower panel) are seen at different viewing inclinations, i, from 2000 to 8000 Å. The reader is cautioned to notice the change in scale between the four models.

line-of-sight gets closer to the polar direction, P decreases as absorption by dust grains limits the transmission of photons through the gas. For a 500-sphere distribution, P is slightly lower than for a uniform model, but for 1000 clouds of gas, the models are very similar, as expected from Fig. 7.4 (upper panel). For a 2000-sphere distribution, P is higher than for a uniform model as the more important number of scattering targets coupled to an higher escape probability between the gas cloudlets enhance the polarization degree.

It is interesting to note that a polar distribution of spheres does not strongly impact the resulting polarization degree in comparison with a uniform model. Taking into account a low-to-moderate amount of clumps, one can use a continuous outflow model as a good approximation. This result does not apply to equatorial distributions of gas (see Fig. 7.2).

7.2.4 Disrupted accretion flow

The last scattering region to be examined is the accretion flow between the torus and the accretion disk, simulated by a fragmented equatorial scattering region composed of electron spheres with $R_{sphere} = 1.17 \times 10^{-5}$ pc and $\tau_{elec} = 0.3$ (in the previous uniform model, τ_{elec} was set to unity). The clouds sustain a half-opening angle of 10° with respect to the equatorial plane and are distributed between 3×10^{-4} pc and 5×10^{-4} pc. The filling factor of the 500-sphere distribution is equal to $\mathcal{F} = 0.06$, $\mathcal{F} = 0.13$ for 1000 spheres and $\mathcal{F} = 0.25$ for 2000 spheres.

Equatorial obscuration by a distribution of ionized clouds only impacts equatorial lines-of-sight (Fig. 7.5 upper panel). When radiation passes through the model, it escapes more easily from a fragmented model with a low number of scattering targets than from a uniform reprocessing region. Thus, the observed flux is higher along the equator for sparsely populated models. When the number of gas spheres increases, the partial covering of the source also increases, so the flux recorded at $i > 75°$ diminishes. But, due to multiple scattering and the gaps between clouds, the amount of photons reprocessed along the equator is still higher than for a uniform model, even when considering a maximum number of spheres.

As photons more easily escape from a fragmented model, the fraction of reprocessed radiation is lower, so the polarization degree (Fig. 7.5 lower panel) decreases. The general tendency is the same in comparison with a continuous accretion flow, with a maximum polarization degree detected at equatorial inclinations, but its percentage is much lower. A fragmented medium also reproduces the parallel orientation of the photon polarization angle, similarly to a clumpy dusty torus model. To increase P, equatorial obscuration must be higher, and only starting at 2000-sphere the model can approximatively reproduce the polarization signature of the uniform case.

7.3 AGN modeling with clumpy structures

Now that the isolated reprocessing models are investigated, our last step is to construct a three-component model to approach the unified scheme of AGN. To do so, we gather three fragmented regions around the central emitting source. First, the equatorial electron-dominated flow is modeled using 2000 spheres in order to maximize the production of parallel polarization at polar viewing angles (see Sect. 7.2.4). Then, at greater distances, a fragmented torus reduces the flux coming from the inner part of the AGN. We opted for another 2000-sphere model to enhance the partial covering factor of the source (see Sect. 7.2.2). Finally, the torus collimates ionized

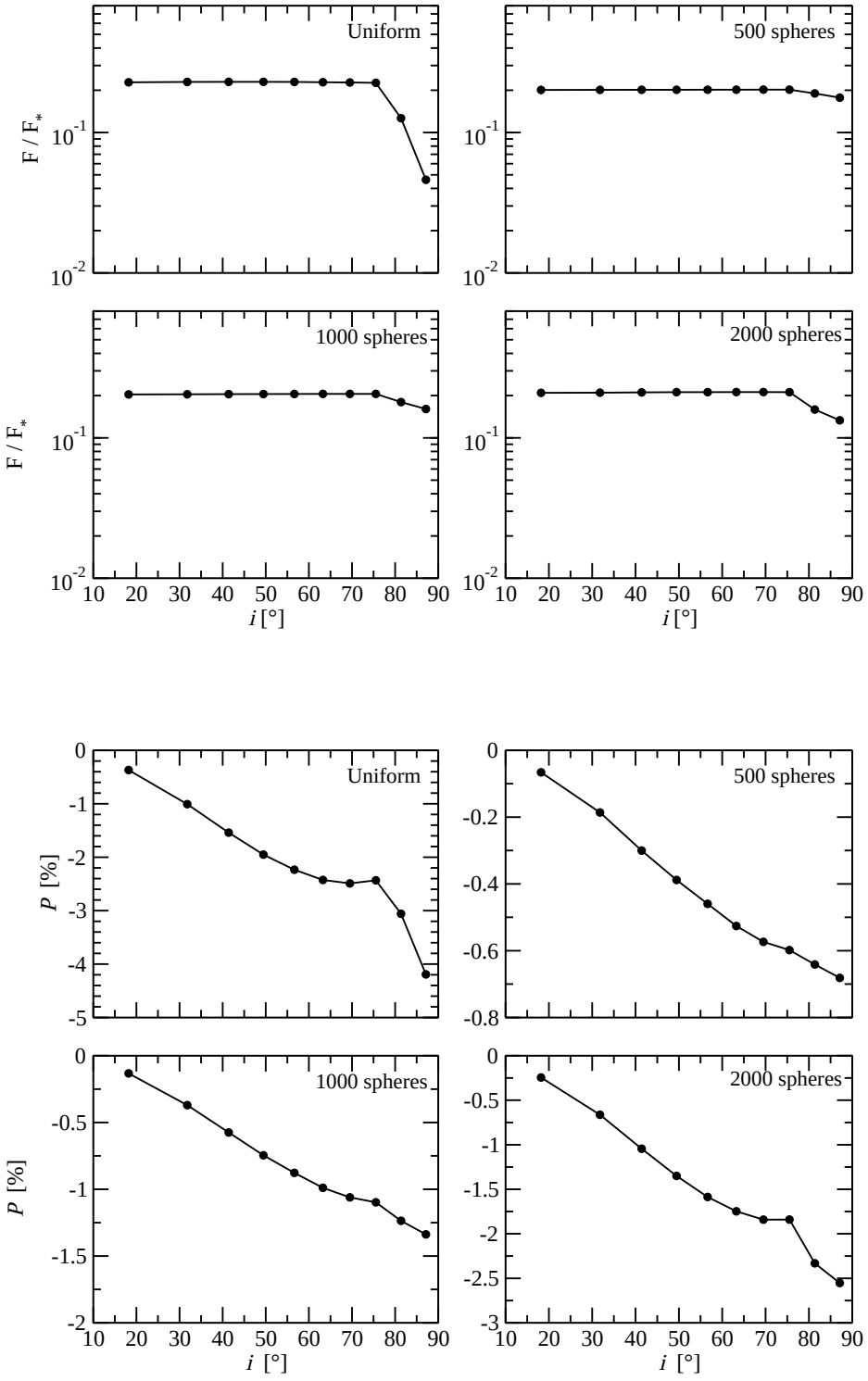

Figure 7.5: Modeling of an equatorial, electron-filled, fragmented scattering disk with a half-opening angle $\theta_0 = 10°$ measured with respect to the equatorial plane. The fraction F/F_* of the central flux (upper panel) and the spatially integrated polarization P (lower panel) are seen at different viewing inclinations, i, integrated over 2000 to 8000 Å. The reader is cautioned to notice the change in scale between the four models.

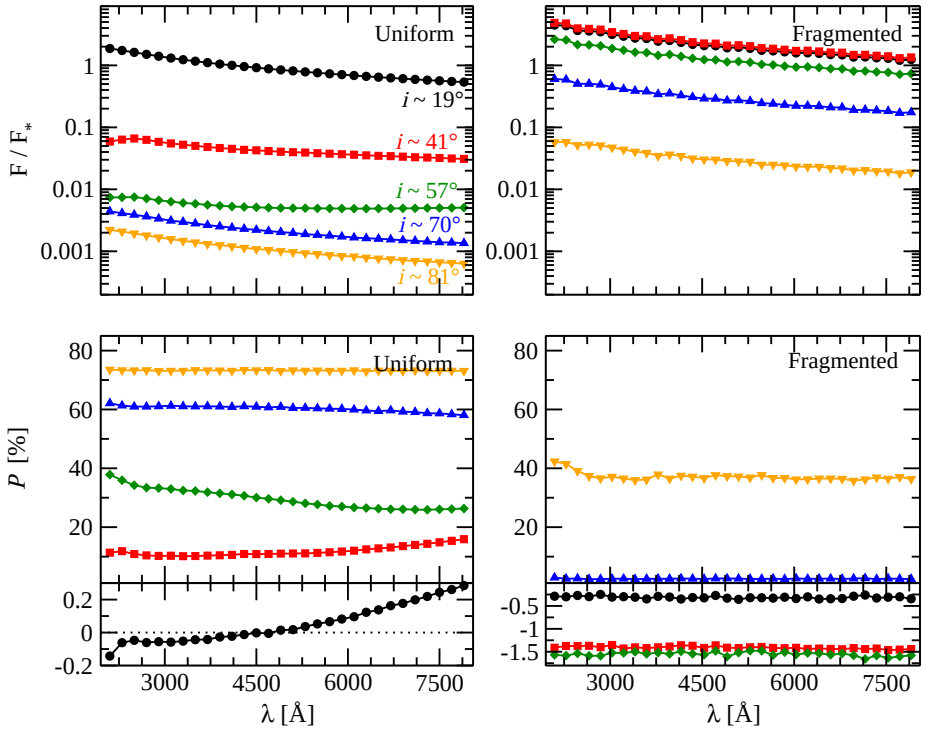

Figure 7.6: Modeling the unified scheme of a thermal AGN by three fragmented reprocessing regions (see text) The fraction F/F_* of the central flux is plotted from 2000 to 8000 Å (upper panel) and the spatially integrated polarization P is plotted versus the observer's inclination i (lower panel). The reader is cautioned to notice the change in scale between the two models.

outflows composed of only 500 spheres, as we saw in Sect. 7.2.3.1 that the differences between a uniform and a fragmented model is negligible for small numbers of clumps.

The fraction F/F_* of the central flux is found to be different, in terms of intensity, between a uniform model (Fig. 7.6, top-left) and its fragmented counterpart (Fig. 7.6, top-right). The amount of radiation in the polar direction is maximum and higher than for a continuous model since the empty spaces between the optically thin clouds inside the outflow are large. The flux is seen in transmission and has not suffered many scattering events. When the viewing angle increases, F/F_* slowly decreases, but not as fast as in the uniform case. Part of the photons previously trapped by the inner walls of the dusty torus are now able to escape, largely contributing to the flux. As soon as the inclination of the system crosses the torus horizon, the flux decreases sharply, but is still 100 times larger than in the uniform case. Along the equatorial plane, where a minimum amount of radiation is detected, photons escape from the model by orthogonal scattering in the winds as well as direct transmission through the circumnuclear matter. The resulting type-2 F/F_* is then much higher for a fragmented model than for a continuous one.

Fragmentation strongly influences the resulting polarization signatures of an AGN model.

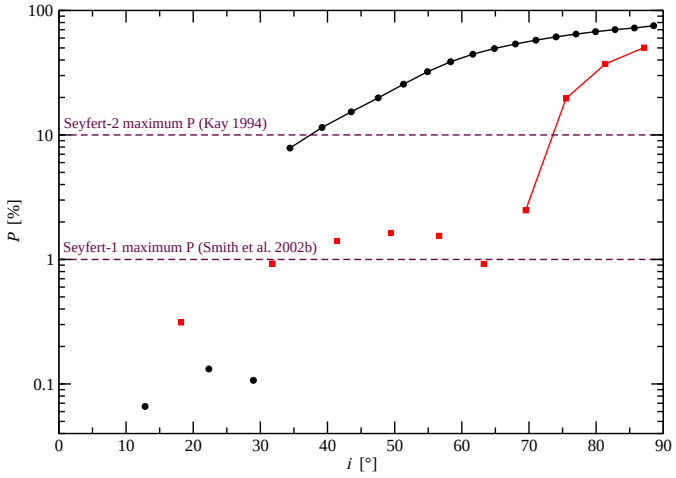

Figure 7.7: The spatially integrated polarization P of a uniform AGN model (black dots) and its counter-part using clumpy distributions (red squares) are plotted at different viewing inclinations, i. The isolated symbols indicate a polarization position angle $\gamma = 90°$ (parallel), connected symbols stand for $\gamma = 0°$ (perpendicular).

In the uniform case (Fig. 7.6, bottom-left), parallel polarization was only detected at viewing angles close to the pole ($i \sim 19°$), but in the case of a clumpy model (Fig. 7.6, bottom-right) parallel polarization is detected up to $i \sim 57°$. Such an inclination coincides with a viewing angle passing directly through the torus clumps without suffering too much absorption. There is a dual contribution from the accretion flow and from the dusty torus that are both producing negative polarization. The levels of P range from 0.5 % to 2 % for type-1 AGN. When the observer's line-of-sight crosses the bulk of the dusty torus, where there is a maximum density of spheres, the photon position angle switches from parallel to perpendicular orientation. Most of the flux is seen by orthogonal scattering in the ionized winds, only producing 0° (perpendicular) polarization angles. P is much lower for $i \sim 70°$ in the fragmented case ($P \sim 2$ %) than in the case of a uniform model ($P \sim 60$ %). Finally, at an extreme type-2 inclination, the polarization degree is maximum, with $P \sim 40$ %. For all the viewing angles, P is found to be approximatively wavelength-independent, as expected from spectropolarimetric observations.

If we consider that P is totally wavelength-independent, we can integrate the polarization percentage over 2000 – 8000 Å and more easily compare the uniform and fragmented models. In Fig. 7.7, the two morphologically-similar cases are plotted versus inclination. As stated above, the type-1 polarization degree is much higher for a fragmented model than for a uniform one. The multiplication of scattering targets enhances the production of polarization and as photons can more easily escape from the polar outflows and from the equatorial dust region, many more photons can reach a type-1 observer. At type-2 viewing angles, P is still high, but significantly lower than for the uniform-density model. It is interesting to note that the shape of the integrated polarization versus inclination is the same from one model to another, with a polarization hump

in the type-1 angle domain. The fragmented model is very similar, in shape, to a model with a geometrically thiner, constant-density, obscuring torus with a much wider half-opening angle of 60° (Figs. 4.24, 4.25 and 4.26 in Chap. 4). This implies that a flat torus is not necessary if we consider it to be fragmented. Finally, a fragmented AGN model also reproduces the observational polarization dichotomy, potentially even in a better way than a uniform model.

We also added to Fig. 7.7 the rough limits on the polarization percentage detected for type-1 (Smith et al. 2002b) and type-2 (Kay 1994) AGN. While an AGN model constituted of uniform reprocessing media creates a too weak polarization signal at type-1 inclinations ($\sim$ 10 times lower than the polarization limit) and a too large P for type-2 objects ($\sim$ 8 times), a fragmented model is found to be much closer to the observations. The polarization degree produced at type-1 inclinations lies in the observational range of Smith et al. (2002b); however, P is still a little bit too high at type-2 viewing angles. This is primarily due to the efficiency of orthogonal scattering in the polar outflows, giving rise to a large polarization percentage, with the contribution from photons transmitted through the circumnuclear dust being marginal.

7.4 Summary and discussion

We modeled a set of isolated clumpy structures and ran Monte Carlo simulations in order to compare their resulting polarization signatures with the uniform models analyzed in Chap. 4. We created three different model cases using cloud distributions of 500, 1000 and 2000 spheres of constant radius and density, corresponding to the respective filling factors: $\mathcal{F} \sim 0.06$, $\mathcal{F} \sim 0.13$ and $\mathcal{F} \sim 0.25$.

We found that equatorial distributions of clumps, either for a dusty torus or an ionized accretion flow, tend to decrease the net polarization percentage, independently of the cloud density. The resulting polarization position angle is parallel for type-1 and some type-2 viewing angles. A residual photon flux always manages to escape from the central parts of the model even when considering an observer's line-of-sight passing through the highly-covered equatorial region. Moreover, this equatorial flux is carrying an important polarization degree that might be detected if not diluted by star-light emission. In the case of scattering regions constructed along the polar directions, the impact of fragmentation is reduced: a small number of clouds is able to perfectly reproduce the polarization behavior of uniform models. Increasing the cloud distribution only results in increasing the net polarization percentage. Like in the uniform density case, also fragmented outflows solely produce perpendicular polarization angles.

Combining the radiation supported electron region with the dusty torus and the polar outflows, we then modeled an AGN only made of clumpy structures. Such a model, with a torus half-opening angle of 30°, produces a strong polarization percentage ($\sim$ 1 %), associated with parallel polarization, at inclinations up to $i \sim 60°$. When the observer's line-of-sight passes through the central part of the equatorial dusty matter, polarization increases and switches from parallel to perpendicular orientation. A large P ($\sim$ 40 %) is found at edge-on viewing angles, but it is significantly lower than what was found for an AGN model built with uniform reprocessing regions and better reproduce the observed polarization dichotomy.

7.4.1 Further modeling

So far, we explored the impact of fragmentation onto polarization by running models with the same morphology as in Chap. 4. We restricted ourselves to a unique clump geometry per scattering region and fixed a uniform optical depth for all its clouds. Future work must explore a

wider variety of morphologies, increasing or decreasing the clumps opacity, filling factors, as well as the half-opening angles. It is particularly important to test to which extend a circumnuclear distribution of absorbing gas produces parallel polarization. If it is found that a clumpy torus always produces parallel polarization position angles, then the need for a radiation-supported, geometrically thin scattering disk that lies in the equatorial plane of AGN (Antonucci 1984) may disappear.

We also found that a sphere distribution with a low filling factor is sufficient to reproduce similar spectral and polarimetric results than for a continuous ejection flow. It might be interesting to explore lower filling factors as well as lower optical depths, however our models are already in agreement with the measurement of the optical thickness of dense matter knots in NGC 1068 ($\tau_V \sim 0.27 \pm 0.08$, Ogle et al. 2003). We will run further tests to include such a clumpy distribution into the NGC 1068 model investigated in Chap. 5.

Finally, there is a hybrid option that we consider to explore in the future: mixing an optically thin continuous medium with denser clumps. In this case, the continuous medium might be seen as an interclump medium (surrounding an inhomogeneous distribution of compact knots. As the interclump medium would be much less dense than the clumps, its impact on the polarization should be weak but the model would anyway be closer to reality.

7.4.2 An alternative solution to fragmentation

In a large part of this manuscript, we considered smooth dusty tori (i.e continuous dust distributions that change either slowly or not at all with distance from the AGN engine). Here, we investigated the case of circumnuclear obscuration using a fragmented medium. Both of the two models have failures and successes in reproducing peculiar aspects of AGN observations (Vollmer et al. 2004; Dullemond & van Bemmel 2005; Feltre et al. 2012).

However, there is a third, less known competitor: bulk tori maintained by nuclear starbursts. In this scenario, supernovae (SNe), from nuclear star-bursts situated within the inner 100 pc of low-luminosity AGN (LLAGN), couldput out enough energy to keep up the scale height of the dusty torus (Fabian et al. 1998). The bulky torus is essentially supported from the inside by SN energy boosts and is then neither smooth nor fragmented, but has a "Swiss cheese" or "sponge-like" structure. The proposed scenario of Fabian et al. (1998) was investigated in detail by Wada & Norman (2002) using three-dimensional hydrodynamical simulations. The authors assumed a toroidal geometry around the SMBH in which the energy input from SNe is in equilibrium with the turbulent energy dissipation. Doing so, they infer new constraints on the inclination of LLAGN as the torus half-opening angle seems to be correlated with the SMBH mass. But one must keep in mind that, according to Krolik & Begelman (1988), stirring by supernovae processes might not be strong enough to compete with the tidal disruption of the circumnuclear gas.

The results presented in this chapter have not yet been published. Several papers are in preparation.

Chapter 8

Investigating disk-born winds

According to the unified scheme, many of the observational characteristics of AGN can be explained by an inclination effect rather than intrinsic composition differences (see Sect. 2.3). However, the exact morphology of the inner AGN region remains highly debated due to a wide panel of observational emission and absorption line features. While cylinder-like, rotating reprocessing regions where initially used to model the broadening of the emission lines in Seyfert-1 objects (see Osterbrock 1991 for a review), it is now admitted that the morphology of the broad line region is by far more complex (e.g. Davidson & Netzer 1979; Mathews & Capriotti 1985; Shields 1977; Eracleous 2006; Gaskell 2009). In this picture, the central, ionizing source is surrounded by a roughly spherical distribution of clumps in Keplerian motion, situated at the outermost areas of the accretion disk (Gaskell & Goosmann 2013). Similar assumptions about the clumpy nature of the narrow line regions (Capetti et al. 1995; Ogle et al. 2003) increase the difficulty of the challenging but necessary goal of drawing a unifying model for the sub-parsec region of quasars.

In this context, Elvis (2000) developed a model to explain the wide variety of emission and absorption features in AGN spectra, assuming a simple, but remarkably well-determined, outflowing structure. The model presented by Elvis (2000) assumes a flow of warm, highly ionized matter (WHIM) that is launched from an accretion disk over a small range of radii and then bent outward and driven into a radial direction by radiation pressure (see Fig. 8.1 and Elvis 2000). Certain aspects of this empirically derived structure can be directly tested from number counts of type-1 and type-2 AGN or from the relative number of broad absorption line (BAL) versus narrow absorption line (NAL) objects. The wind structure surrounds the irradiating accretion disk and gives rise to a reprocessing spectrum that varies with the disk luminosity and the viewing angle of the observer. Time-resolved spectroscopy therefore is a powerful tool to test the model against the observations, but this technique may not be sufficiently sensitive to the outflow geometry and dynamics.

To extend the comparison of the outflow model to the observations somewhat further, spectropolarimetric data of AGN can be explored. In the optical/UV band, the polarization of radio-quiet AGN is mostly determined by reprocessing and strongly depends on the scattering geometry. We expect BAL objects to be generally more highly polarized than non-BAL QSOs (Ogle et al. 1999) and NAL Seyfert-like galaxies to show parallel polarization associated with polarization degrees inferior to unity (Smith et al. 2002b). Hence, when a detailed polarization model is provided, the polarization thus constrains the geometry and the composition of reprocessing and scattering media. This continues to be very relevant in AGN research where geometry is a key parameter for unification theories (Antonucci & Miller 1985; Antonucci 1993; Elvis 2000).

In this chapter, we model the polarization properties produced by radiative reprocessing inside the structure of quasars as suggested by Elvis (2000). We focus on the continuum polarization at optical and ultraviolet wavelengths and we test if the outflow model can reproduce the observed dichotomy with respect to the polarization position angle (Antonucci 1983, 1984; Smith et al. 2002b). We present and analyze spectropolarimetric simulations of disk-born outflows for different model parameters, discuss our results and relate them to the observational constraints.

8.1 Model geometry

To run STOKES with the structure for quasars as proposed by Elvis (2000), we construct continuous outflow regions that can be filled with electrons or dust or a combination of the two at uniform density. Assuming a uniform density certainly is an oversimplification and we are going to release this condition in future work. For now, we only perform the most basic polarization test of the wind model. For all models presented in this chapter, the equatorial emitting region is defined as an isotropic, disk-like source emitting an unpolarized spectrum with a power-law spectral energy distribution $F_* \propto \nu^{-\alpha}$ and $\alpha = 1$. The model geometry is summarized in Fig. 8.1: the wind arises from the accretion disk at a distance $r_1 = 0.0032$ pc (10^{16} cm) and is bent into a direction of $\theta = 60^\circ$ relative to the model symmetry axis. The range of radii where the flow arises from the accretion disk is parametrized by $r_2 = 0.00032$ pc (10^{15} cm). Finally, the half-opening angle $\delta\theta$ of the wind is set to 3° and the flow extends up to $r_3 = 0.032$ pc (10^{17} cm). Note that the column of ionized matter arises from the disk at a distance r_1 from the central source, but the emitting region extends up to $2r_1$.

8.2 The warm, highly ionized medium

8.2.1 Testing the electron-dominated outflows

We assume that the WHIM is mainly composed of ionized gas with a Thomson optical depth τ of the order of unity along the conical outflowing direction. This wind extends out to several parsec and can be associated with the typical "ionization cones" seen in Seyfert-2 galaxies (Capetti et al. 1995; Axon et al. 1996; Osterbrock 1991). To investigate the scattering properties and the resulting spectra and polarization from the WHIM, we first consider a uniform-density, continuous medium made of electrons. The Thomson optical depth at the wind base and inside the conical, outflowing direction are set to $\tau_1 \sim 0.02$ and $\tau_2 \sim 2$, respectively. Such an optical depth is in agreement with observational measurements (Packham et al. 1997; Ogle et al. 2003) and also suggested by polarization modeling work on NGC 1068 (Miller et al. 1991; Young et al. 1995; Goosmann & Matt 2011b).

In Fig. 8.2, we plot the simulated spectropolarimetric results across the 2000 – 8000 Å wave band and as a function of the observer's viewing angle. We consider three different lines-of-sight: one along typical Seyfert-1 (polar) inclinations (9°), one passing through the outflowing wind (61°), and one along an extreme Seyfert-2 (equatorial) inclination (89°). The inclination of the system is defined with respect to the symmetry axis of the model. The type-1 and type-2 lines of sight do not cross the extended wind and the fraction F/F_* of the central flux, F_*, remains similar for both inclinations. At intermediate inclinations, however, a significant fraction of the radiation is scattered out of the line-of-sight by the optically thick wind. The polarization percentage at all three viewing directions is wavelength-independent, as it is expected for Thomson scattering, and the polarization position angle is $\psi = 90^\circ$ (parallel polarization) for all cases. The polarization

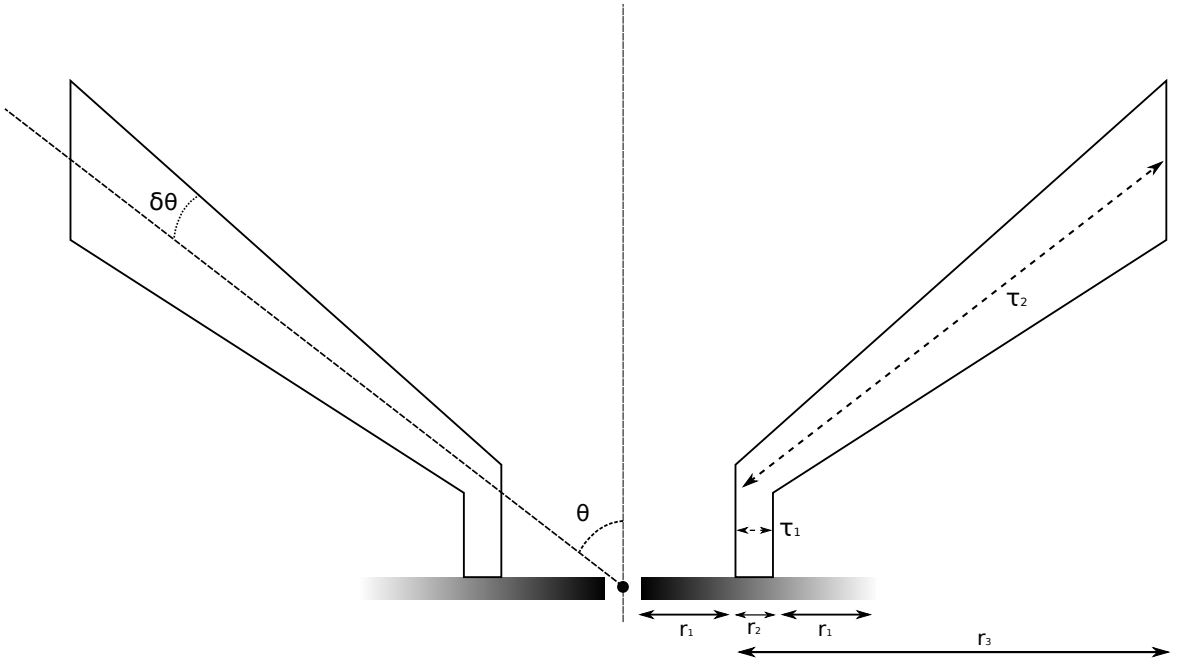

Figure 8.1: Schematic view of the structure proposed by Elvis (2000) and implemented in the STOKES model. The outflow arises vertically from the accreting disk and is bent outward by radiation pressure along a 60° direction relative to the model symmetry axis. The half-opening angle of the wind extension is 3°. The radial optical depths of the wind base and of the outflowing material are set to by τ_1 and τ_2 respectively.

percentage P is very low at type-1 viewing angles and then rises with i. It increases to 0.05 % when looking through the extended wind and then further to about 0.3 % for an edge-on line-of-sight.

The corresponding polarization images are shown in Fig. 8.3. The 60 × 60 spatial bins compile the polarization properties integrated across the whole wave band of 2000 – 8000 Å. Each pixel is labelled by its projected coordinates x and y (in parsecs) with respect to the center of the model space. The polarized flux PF/F_* is color-coded and the orientation and length of a vector drawn in black at the center of each pixel represent the ψ and P values, respectively.

Inspection of the polarization images is helpful to understand the net polarization properties as a function of the viewing angle: at a polar viewing direction (Fig. 8.3, top-left), the central source irradiates the outflow funnel, which causes a weak polarized flux in the vicinity of the model center. However, the spatial distribution of polarization position angles remains close to being symmetric with respect to the center and therefore the resulting net polarization at a low viewing angle is very low. The polarization is also strongly diminished by the diluting flux coming from the continuum source that is directly visible at low inclinations. The resulting polarization position angle at $\psi = 90$ is determined by the geometry as the wind is rather flat ($\theta = 60°$) and therefore favors scattering close to the equatorial plane. Equatorial scattering produces parallel polarization and was suggested early-on to play an important role in producing the polarization properties of type-1 AGN (Antonucci 1984).

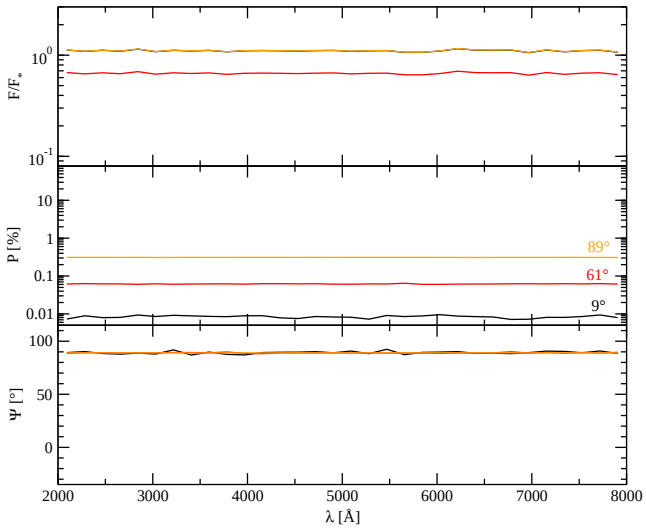

Figure 8.2: Modeling an electron-filled structure for quasars outflow using a uniform model such as in Fig. 8.1, seen at different viewing inclinations, i (black: 9° – red: 61° – orange: 89°). *Top*: the fraction, F/F_* of the central flux; *middle*: polarization, P; *bottom*: polarization angle, ψ.

At $i = 61°$ (Fig. 8.3, top-right) the line-of-sight passes through the extended winds. The net polarized flux now comprises a strong component seen in transmission. While the wind base is optically thin, the scattering optical depth along the line-of-sight is significant and the latter thus contributes strongly to the net polarization. The interface between the inner funnel of the torus and the extended winds is traced by a sharp gradient in polarized flux. The inner (outer) surfaces of the upper (lower) part of the outflow are visible in reflection, but due to their low optical depth in the poloidal direction the scattering is inefficient and does not produce much polarized flux.

Finally, the equatorial view of the model at $i = 89°$ (Fig. 8.3, bottom) allows us to recover the edge-on morphology of the system. The polarized flux emerging from the wind base and its extensions is significantly higher than at the intermediate view. The boundaries of the extended winds trace out an X-shaped structure that extends far out and produces strong polarization. These regions have a higher polarization efficiency because they present a significant optical depth along the line of sight and favor a scattering angle around 90° with respect to the extended continuum source.

8.2.2 Exploring different bending and opening angles of the wind

We continue our investigation by exploring different angles θ and $\delta\theta$ of the wind. To obtain a more narrow cone with respect to the default parametrisation used in Sect. 8.2.1, it is necessary to lower the bending angle θ while the wind extensions become thicker when increasing the half-opening angle $\delta\theta$. We systematically explore the response in polarization for a range of both angles and summarize the results in Fig. 8.4. Since the polarization of electron scattering is wavelength-independent we now plot the wavelength-integrated polarization degree as a function of the viewing angle. Note that we apply a sign convention for P that expresses the orientation of the polarization position angle: for positive P, the $\vec{E}$-vector is perpendicular to the wind axis, while for negative P the polarization is parallel (intermediate orientations of the net polarization are impossible due to

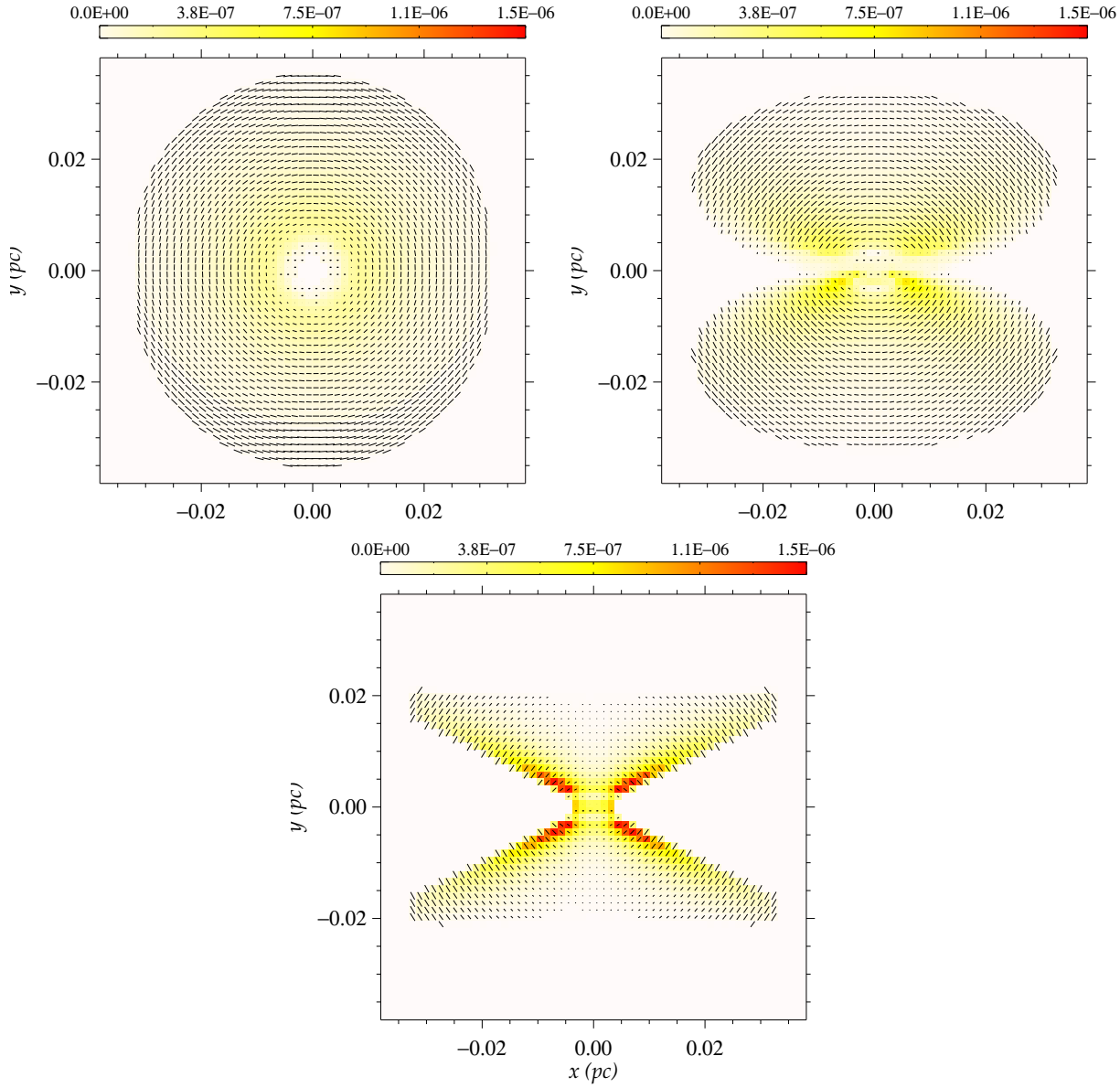

Figure 8.3: Modeled images of the PF/F_* for an electron-filled, scattering outflow as presented in Fig. 8.1. The polarized flux, PF/F_*, is color-coded and integrated over the wavelength band. *Top-left*: image at $i \sim 9°$; *top-right*: $i \sim 61°$; *bottom*: $i \sim 89°$.

symmetry reasons).

For $\theta = 75°$ the model produces polarization degrees that are low at small viewing angles and moderate, up to 15 %, for higher inclinations. The normalisation of P rises with $\delta\theta$. There is no dichotomy for the polarization angle as the $\vec{E}$-vector is always parallel to the projected axis. The case of $\theta = 60°$ with $\delta\theta = 3°$ is discussed in the previous section. It turns out that increasing $\delta\theta$ can change the dichotomy of the polarization position angle and even produce three or four different regimes at low, intermediate and large viewing angles. The polarization then turns out

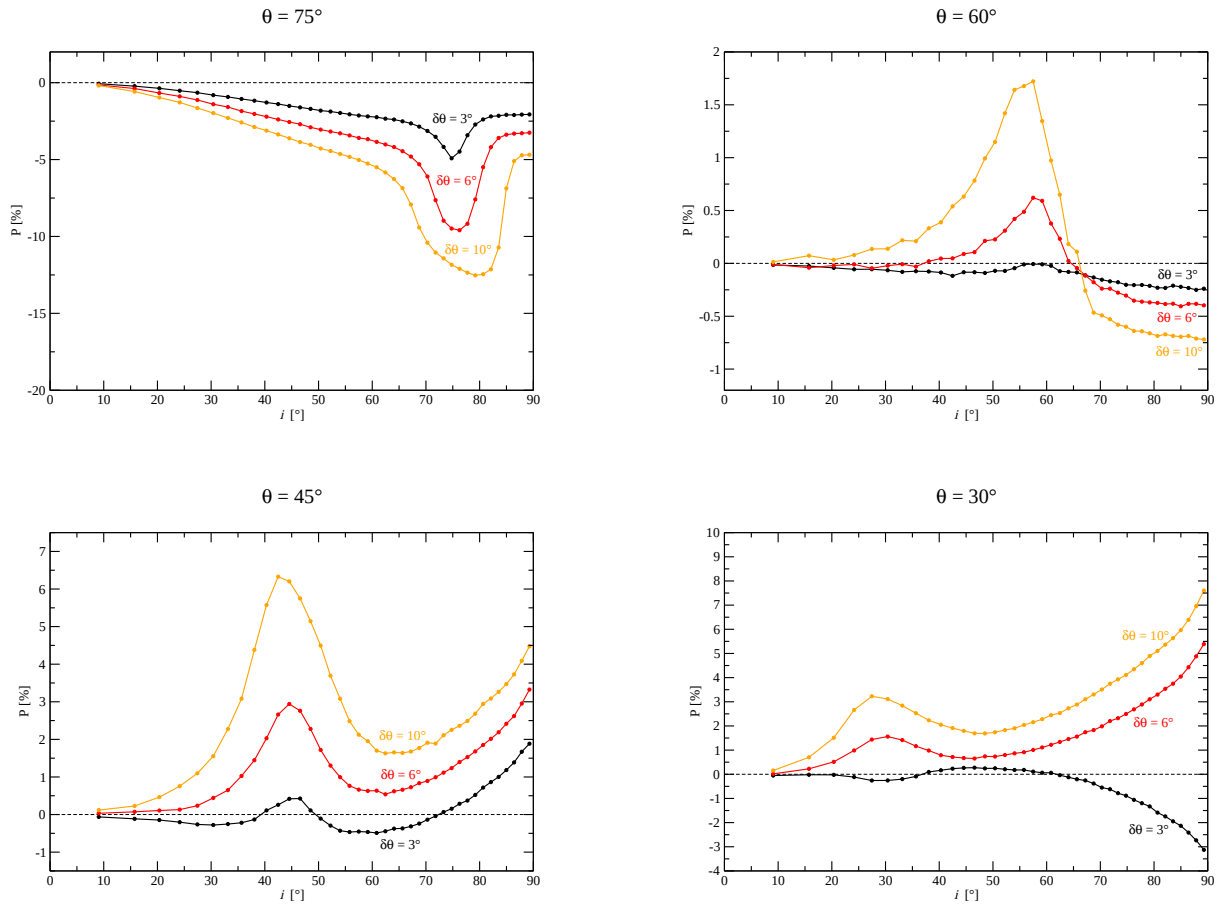

Figure 8.4: Investigating the polarization response of the quasar's structure according to the observer's viewing angle i, at four different wind bending angles θ and three outflows opening angle $\delta\theta$ (black: $\delta\theta = 3°$ – red: $\delta\theta = 6°$ – orange: $\delta\theta = 10°$). *Top-left*: $\theta = 75°$; *top-right*: $\theta = 60°$; *bottom-left*: $\theta = 45°$; *bottom-right*: $\theta = 30°$.

to be parallel for a face-on and edge-on view and perpendicular along a line-of-sight through the wind. Further narrowing the bending angle to $\theta = 4°$ increases the trend to have multiple regimes for the polarization angle that now occur even for the smallest opening angle of $\delta\theta = 3°$. It also reinforces the polarization degree for parallel polarization until an optimum is reached and the trend is inverted (see the case of $\theta = 30°$).

An important motivation for the model by Elvis (2000) was given by the observed number distribution of quasars with narrow, ionized absorption lines in the UV and X-ray band versus BAL- and non-NAL objects. The BAL objects are assumed to be seen along the conical wind, the NAL objects on a line of sight that crosses the optically thin wind base. Quasars with NALs are type-1 AGN and therefore preferentially have a parallel polarization in the optical. Interestingly, there is a parameter range for which our modeling allows for the existence of parallel polarization at low inclinations (non-NAL, type-1 AGN with low parallel polarization) and high-inclinations

(NAL, type-1 AGN with significant parallel polarization). In between these inclinations the line of sight points toward a BAL objects with considerable perpendicular polarization.

An interesting challenge to the wind model by Elvis (2000) is the presence of obscured, type-2 AGN without narrow absorption lines and a ubiquitous perpendicular polarization. These objects may be accounted for by adding dust shielding at certain inclinations to the model. The dust may exist on the far-side of the wind where the temperature drops below the sublimation temperature. We are going to investigate to such scenarios in the following.

8.3 Dust in the wind

The structure for quasars analyzed here may also account for the extended narrow line regions found at greater distances from the central engine. They are supposed to be the extensions of the ionized outflow, beyond the sublimation radius where dust can survive. However, the presence of dust originating close to the accretion disk remains theoretically possible according to Czerny & Hryniewicz (2012), who proved that dust can be formed in accretion disk atmospheres. Dust rises similarly to the electronic disk-born wind, but is soon evaporated by the central irradiation source (Elvis 2012). Knowing that dust may be more abundant in low-luminosity AGN (LLAGN) than in quasars (Edelson et al. 1987), Elvis (2000) suggested that a part of the BAL flow may be obscured by a dust region that is still close to the active nucleus. It is a natural explanation of the absence of BAL in Seyfert-like galaxies and fits in with the observed presence of dusty NLR clouds at larger distances from the irradiation source.

8.3.1 A pure absorbing wind model

Before investigating the impact of dusty NLR clouds on the WHIM, we aim to explore the polarization signatures of a purely absorbing media. To do so, we use again a typical Milky Way dust prescription (Wolf & Henning 1999), together with the same geometry as for the WHIM model considered in Sect. 8.2. As one of the goals of the wind model by Elvis (2000) is to overcome the need for an obscuring torus around the equatorial plane of the AGN (Antonucci & Miller 1985; Pier & Krolik 1992), we first opted for an optically thick model, with $\tau_1 \sim 36$ and $\tau_2 \sim 3600$. This model is not necessarily physical as such a dense absorbing medium may not form or survive so close to the accretion disk.

The spectropolarimetric signatures of a dusty model are presented in Fig. 8.5. The fraction F/F_* of the central flux differs from the electron-filled model, the flux in the polar and intermediate viewing angles being weaker than at equatorial inclination, where part of the emitting disk is unobscured. The combination of an extended, disk-like radiating source and a thin optical depth in the poloidal direction of the outflow results in a great escape probability and the resulting polarization degree is then higher for lines-of-sight passing through the dust medium ($P < 0.1$ %). Due to dilution by the emitting source ($i \sim 9°$) or absorption along the line-of-sight ($\sim i$ 89°), the degree of polarization at polar and equatorial angles is lower ($P < 0.01$ %). We also observe that the percentage of polarization is no longer wavelength-independent and rises towards the red side of the spectrum. It is a consequence of the Mie scattering phase function which becomes less anisotropic at longer wavelengths. A larger fraction of photons can then escapes at higher wavelengths and thus P increases and the dust-induced polarization position angle is equal to 0°.

In Fig. 8.6, we present the simulated polarization cartography of the same model. At a polar viewing angle (Fig. 8.6, top-left), the funnel of the outflow is illuminated by the central source,

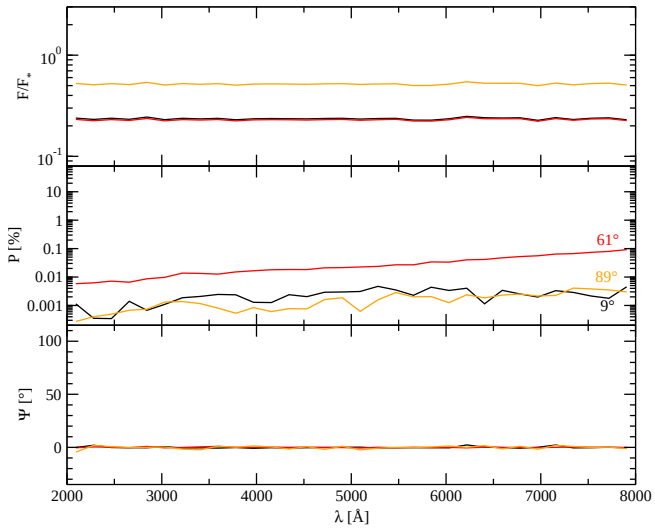

Figure 8.5: Modeling a dust-filled structure for quasars using a uniform, dusty model such as in Fig. 8.1, seen at different viewing inclinations, i (black: 9° – red: 61° – orange: 89°). *Top*: the fraction, F/F_* of the central flux; *middle*: polarization, P; *bottom*: polarization angle, ψ.

and multiple forward and backward scattering events are responsible for the high polarized flux detected in the vicinity of the emitting region. The illumination decreases with distance from the source and nearly no polarized flux is detected in the most extended parts of the outflows. The spectropolarimetric pattern is similar to the polarization maps produced for an isolated dusty torus (Marin et al. 2012a) and appears not to be distinguishable by polarization imaging.

At intermediate inclinations (Fig. 8.6, top-right), the flux mainly comes from scattering events on the lower part of the model, where photons escape from the geometrically thin outflow ($\delta\theta = 3°$) and are reprocessed. Due to the important optical thickness along the wind flow, all of the polarized flux is absorbed at the wind base. The overall shape of the model is of a double-cone, with a maximum polarized flux detected in the wind bases. However, the flux gradient, as seen from previous modeling of hourglass-shaped outflows (Marin et al. 2012a), is less intense due to the hollow geometry of the model.

Finally, along the equatorial viewing angle (Fig. 8.6, bottom), the outflow is nearly invisible as it absorbs most of the input photon flux. However, a large fraction of radiation can escape by transmission through the equatorial medium and collaborate to rise the polarization degree detected in type-2 viewing angles. A few photons are detected on the northern part of the map, due to rare backscattering events on the top-end of the upper wind, since the inclination of the model is not exactly 90°.

8.3.2 BAL obscured outflows

We simulate the BAL obscuring wind using our previous WHIM model (see Sect. 8.2) and adding two cylindrically shaped extinction regions to the outer edge the flow. The dusty wind originates at $r_3 = 0.032$ pc and is of moderate optical depth ($\tau_3 \sim 1$) in order to allow the radiation to partially escape along intermediate viewing angles. The model is summarized in Fig. 8.7. The dust composition and grain size distribution represents an average dust type of our Milky Way (see

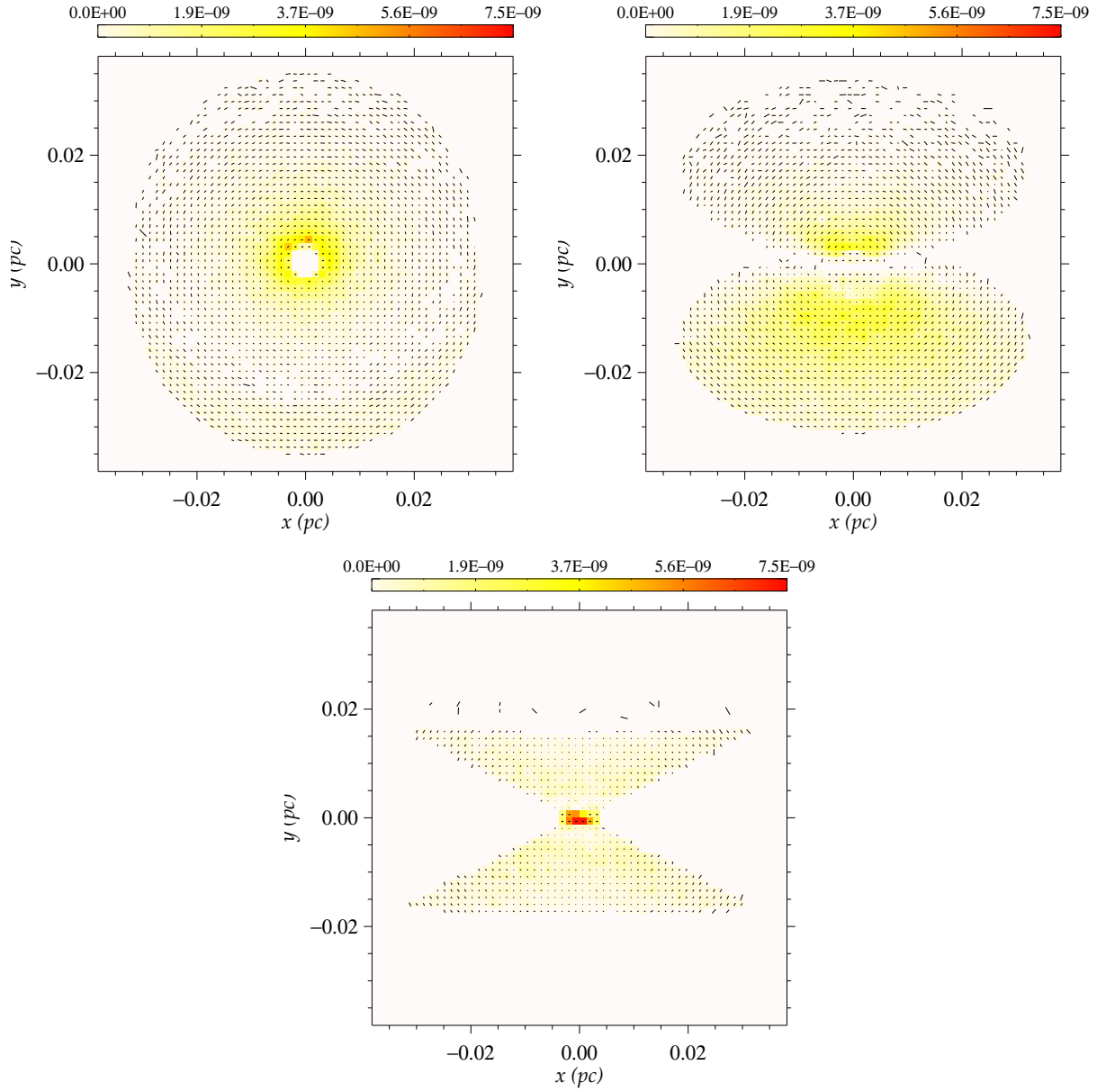

Figure 8.6: Modeling the polarized flux, PF/F_*, induced by complex reprocessing in a unified model of AGN. We combine an electron filled, equatorial scattering disk, an optically thick dusty torus, electron filled polar outflows and extended optically thin dusty polar NLR. PF/F_* is color-coded and integrated over all wavelengths. *Top-left*: face-on image; *Top-right*: image at $i \sim 60°$; *Bottom*: edge-on image.

Mathis et al. 1977; Wolf & Henning 1999; Goosmann & Gaskell 2007).

The resulting total flux spectra for polar and equatorial viewing angles (Fig. 8.8) are similar to those for the WHIM model (Fig. 8.2), indicating that Thomson scattering is the predominant reprocessing mechanism occurring at these inclinations. The impact of the dust on F/F_* remains marginal except when the observer's line-of-sight crosses the outflowing direction ($i = 61°$). The

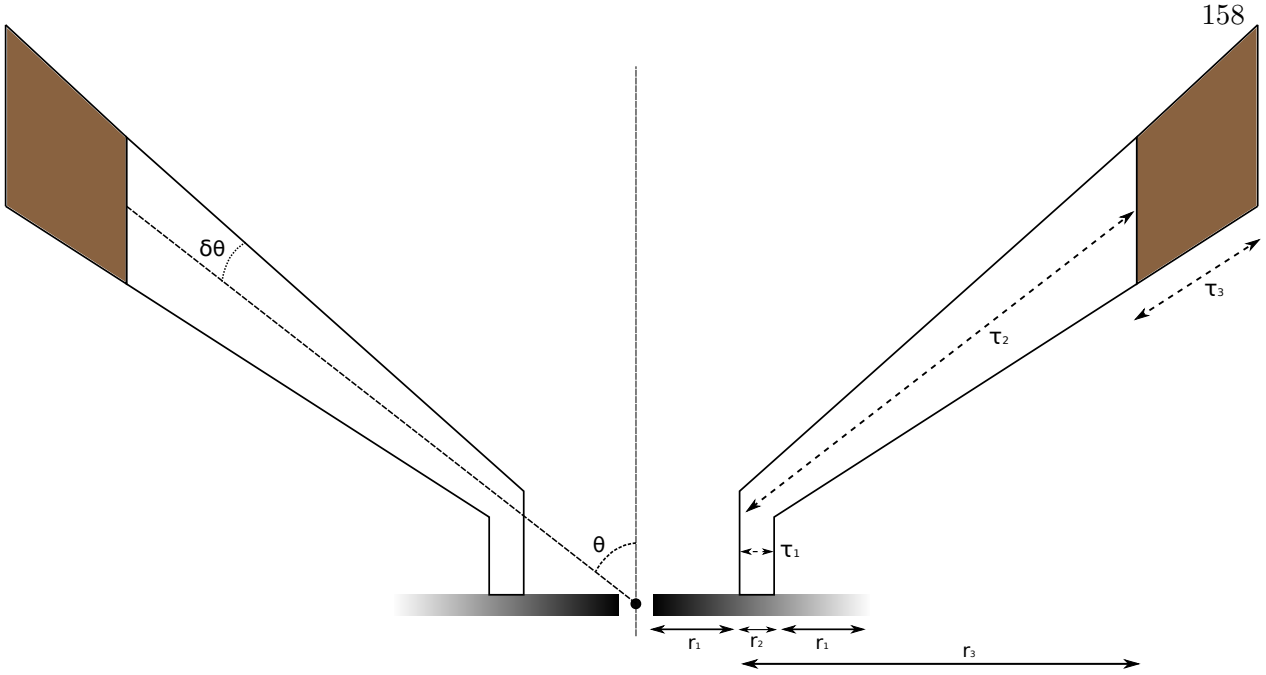

Figure 8.7: Investigating the presence of dust in low luminosity objects. The brownish medium represents the dusty medium, preventing the BAL from being seen in Seyfert-2 galaxies.

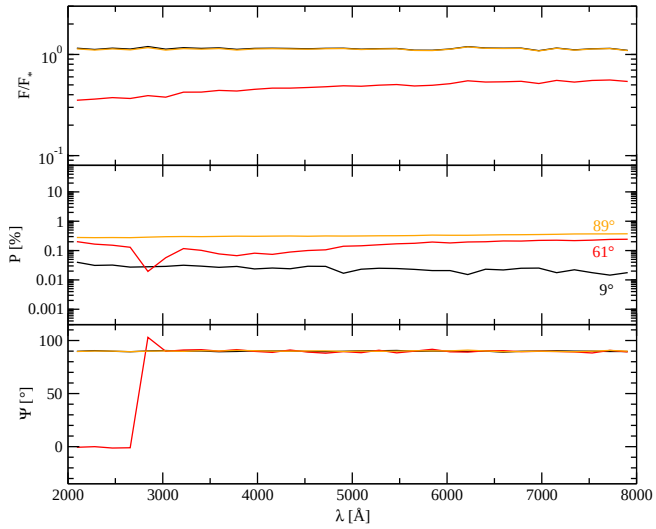

Figure 8.8: Modeling an obscured structure for quasars outflow where BAL are seen through a dusty medium of $\tau_{dust} \sim 1$. The model, presented in Fig. 8.7, is seen at different viewing inclinations, i (black: 9° – red: 61° – orange: 89°). *Top*: the fraction, F/F_* of the central flux; *middle*: polarization, P; *bottom*: polarization angle, ψ.

flux then becomes wavelength-dependent and increases towards the red, but with respect to the

pure WHIM case it does not suffer from heavy absorption due to the moderate opacity of the dusty wind. The impact of the dust clouds is particularly visible in the percentage of polarization. At polar inclinations, P remains below 0.05 % and is nearly wavelength-independent. At equatorial inclinations, P is at its maximum ($\sim$ 0.3 %) and again wavelength-independent. However, at an intermediate inclination, the escaping radiation crosses the dust atmosphere and presents the characteristic wavelength-dependent polarization signal. The net polarization degree is higher than for the pure WHIM model as photons have to scatter into the line-of-sight; P drops from 0.2 % to 0.02 % in the blue part of the spectrum and then rises back to 0.2 % in the red. This peculiar dip is connected to a switch of the polarization position angle, from 0° to 90°, as the Mie scattering phase function becomes more forward-dominated and the overall scattering geometry thus changes towards shorter wavelengths. At all other inclinations and wavelengths of the system the polarization position angle is perpendicular.

8.4 A two-phase medium

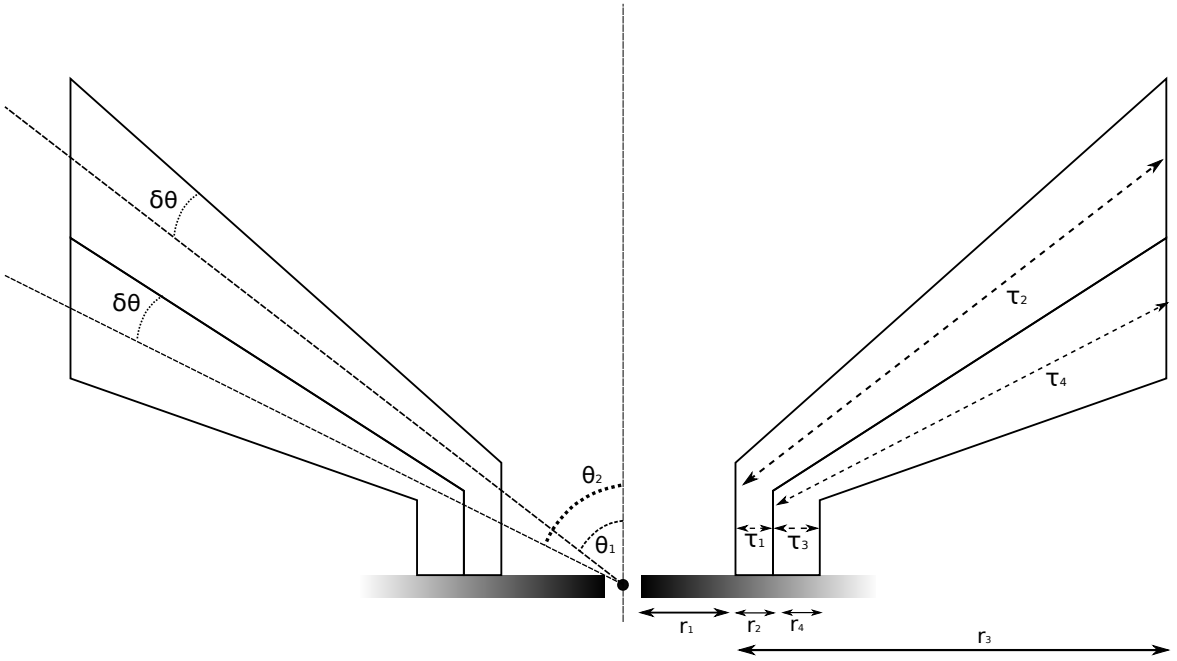

Figure 8.9: A two-phased medium where the cool WHIM outflow is composed of dust.

An important test of the structure for quasars is to reproduce the polarization position angle dichotomy observed in AGN (Antonucci 1983, 1984); our results in Sect. 8.2.2 have proven that a pure WHIM is yet inadequate to explain the switch in polarization position angle between type-1 and type-2 AGN. In the context of Seyfert-2 AGN, the additional presence of dust close to the equatorial plane is suggested as a physical possibility (Czerny & Hryniewicz 2012). Shielded from the full continuum by the WHIM, dust can rise from the disk and survive long enough to impact the

radiation across a significant solid angle around the equatorial plane. Such an absorbing medium would be less ionized than the high ionization BEL region, giving rise to low-ionization line emission, such as in NGC 5548 where the Mg II lines are thought to arise from several light-months away from the irradiating source (Elvis 2000). However, the equatorial dust should also suppress the parallel polarization signal at intermediate and equatorial viewing angles.

In the following, we investigate the polarization properties of a two-phase structure, where the highly ionized inner flow protects a cold absorbing flow arising farther away from the continuum source. Such a medium should be optically thin at some viewing angle in order to allow for the detection of NAL signatures above the equatorial dust lane, but not too optically thin to prevent the detection of parallel polarization at other inclinations.

8.4.1 Modeling two-phase outflows

We adopt the morphology derived by Elvis (2000) for NGC 5548 to explain the high/low ionization BEL regions. Of course, dust would not survive in the BLR, so the dusty wind we define here actually needs to be farther away from the center or remain cold by efficient shielding in the WHIM and BLR. The model geometry is presented in Fig. 8.9 and we fix $\tau_1 \sim 0.02$, $\tau_2 \sim 2$, $\tau_3 \sim 40$ and $\tau_4 \sim 4000$. The bending angle of the WHIM, $\theta = \theta_1$, is equal to 60° and $\theta_2 = \theta_1 + 2\delta\theta$. Similarly to our previous modeling, $\delta\theta = 3°$. According to Elvis (2000), $r_1 = 0.0032$ pc (10^{16} cm), $r_2 = 0.00032$ pc, $r_3 = 0.032$ pc and $r_4 = 0.00608$ pc.

To consider a more physical emission geometry, we replace the radiating disk by a point-like source. With the flux intensity decreasing like r^{-3} from the center, most of the radiation comes from the inner part of the emitting disk. When comparing different realisations of the modeling, we find, however, that the size of the emission region does not have a major impact on the spectropolarimetric results. We now also include the fact that the inner accretion flow allows for Thomson scattering and we define a geometrically flat, flared-disk region, with optical depth $\tau \sim 1$ along the equator. This reprocessing region was proposed early on by Antonucci (1984) to explain the presence of parallel polarization in type-1 AGN, and a complete description of its polarization properties can be found in Goosmann & Gaskell (2007). The flared morphology is in agreement with the theory of accretion disks (Shakura & Sunyaev 1973) and will strengthen the production of parallel polarization, with a maximum polarization degree of up to a few percent (Marin et al. 2012c).

The spectropolarimetric modeling results are plotted in Fig. 8.10. Interestingly, the polar viewing angle shows a maximal and wavelength-independent flux in comparison with other inclinations, as expected from observations of radio-quiet, type-1 AGN. The impact of dust is visible by absorption and anisotropic scattering processes in intermediate and equatorial inclinations, where the obscured flux is a hundred times lower than at polar lines-of-sight. The percentage of polarization is minimal for polar inclinations ($P \approx 0.01$ %) and maximal for equatorial viewing angles ($P \approx 10$ %). Along the direction of the outflow, the polarization ranges around 1 %, is wavelength-independent, and oriented parallel to the projected axis of the model. The position angle is the same at other inclinations and the expected polarization dichotomy is still not reproduced. Therefore, the two-phase model needs to be further refined.

8.4.2 Investigating different opening angles

Similarly to Sect. 8.3, we now explore a broader range of morphological parameters (θ, $\delta\theta$) in order to discriminates between more realistic and less favorable realizations of the two-phase

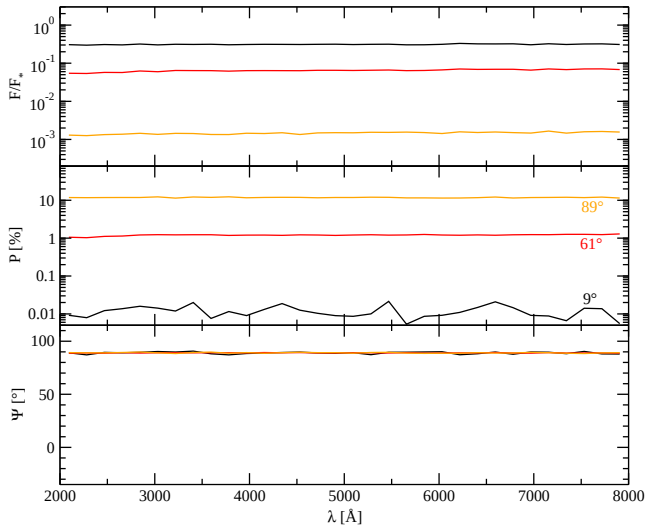

Figure 8.10: Modeling a two-phased quasars outflow where the cool WHIM outflow is composed of an optically thick dust medium, using a uniform model such as in Fig. 8.9, seen at different viewing inclinations, i (black: 9° – red: 61° – orange: 89°). *Top*: the fraction, F/F_* of the central flux; *middle*: polarization, P; *bottom*: polarization angle, ψ.

wind model. As seen from Fig. 8.10, the polarization continuum is close to being wavelength-independent, thus we also plot the wavelength-integrated polarization degree as a function of the viewing angle. The sign convention is preserved from Sect. 8.3.

For $\theta = 60°$ (Fig. 8.11), the model uniformly creates negative (parallel) polarization for the whole range of half-opening angles, with moderate polarization degrees at low inclinations, increasing up to 12 % at equatorial viewing angles. The parametrisation is non compatible with the expected polarization dichotomy. However, the case of $\theta = 45°$ is more interesting as it correctly reproduces the variation of the polarization position angle between type-1 and type-2 inclinations. The transition between negative to positive polarization is a function of the half-opening angle of the model, but is comprised between $i \sim 34°$ and $i \sim 42°$. Negative [positive] polarization degrees reach up to 1.2 % [25.6 %] for the flattest flow geometry ($\delta\theta = 3°$) and the polarized flux tends to decrease when the observer's line-of-sight is reaching the equatorial plane ($P = 16.3$ %). Finally, for $\theta = 30°$, the polarization dichotomy also appears but the regime transition occurs between $i \sim 15°$ and $i \sim 24°$, which is unrealistic according to the observed distribution of AGN types and individual observations of Seyfert-1 inclinations, such as for ESO 323-G077 ($i = 45.0°$, Schmid et al. 2003) or NGC 5548 ($i = 47.3^{+7.6}_{-6.9}$, Wu & Han 2001). Moreover, the polarization degree for models with $\theta = 30°$ can be as high as 62 % at equatorial inclinations, a behavior far from polarimetric observations of obscured AGN (Kay 1994).

Our immediate conclusions are coherent with the ones derived from electron-filled outflowing models presented in Sect. 8.3: a model with a wind bending angle $\theta = 60°$ unsuccessfully reproduce the polarization dichotomy, but a change in the flow geometry can solve this issue. In particular, for $\theta = 45°$, both the transition between parallel and perpendicular polarization at acceptable inclinations and polarization degree close to observed quantities are emerging.

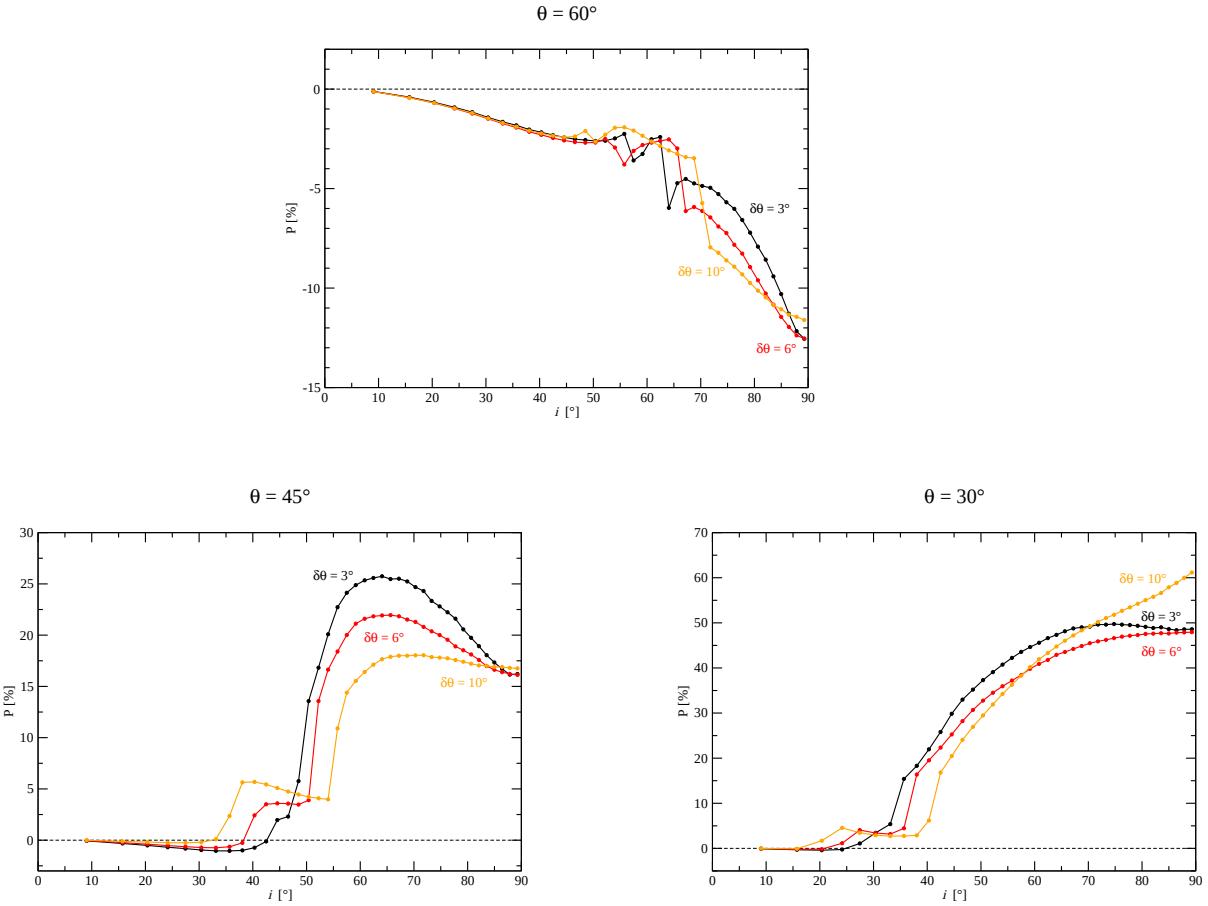

Figure 8.11: Investigating the polarization response of the dual quasar's structure according to the observer's viewing angle i, at three different wind bending angles θ and three outflow's opening angle $\delta\theta$ (black: $\delta\theta = 3°$ – red: $\delta\theta = 6°$ – orange: $\delta\theta = 10°$). *Top*: $\theta = 60°$; *bottom-left*: $\theta = 45°$; *bottom-right*: $\theta = 30°$.

8.4.3 Exploring a range of dust optical depths

It remains a challenge to the double-wind model to reproduce the observed levels of polarization. With respect to the results of Sect. 8.4.2, the polarization degree should be reduced by a factor of five at type-2 inclinations, and by a factor of two at intermediate viewing angles. The cold, absorbing medium shielded by the WHIM may play a decisive role in this.

In our first test, we fixed the absorbing equatorial optical depth to 40, which may be an upper limit for the medium opacity. A wider range of τ_{dust} is now investigated in Fig. 8.12, using $\tau_{dust} = 40$, 4, 1 and 0.4. The figure shows a series of intermediate cases between our results for an optically thick dust layer explored in the previous Sect. 8.4.2 and the pure WHIM case (Sect. 8.2).

As seen from Fig. 8.11, at high optical depths of the dust, the scenarios of Fig. 8.12 have similar polarimetric properties to the multi-component torus models investigated in Marin et al. (2012c). The polarization dichotomy is reproduced but the polarization degree at type-2 inclinations

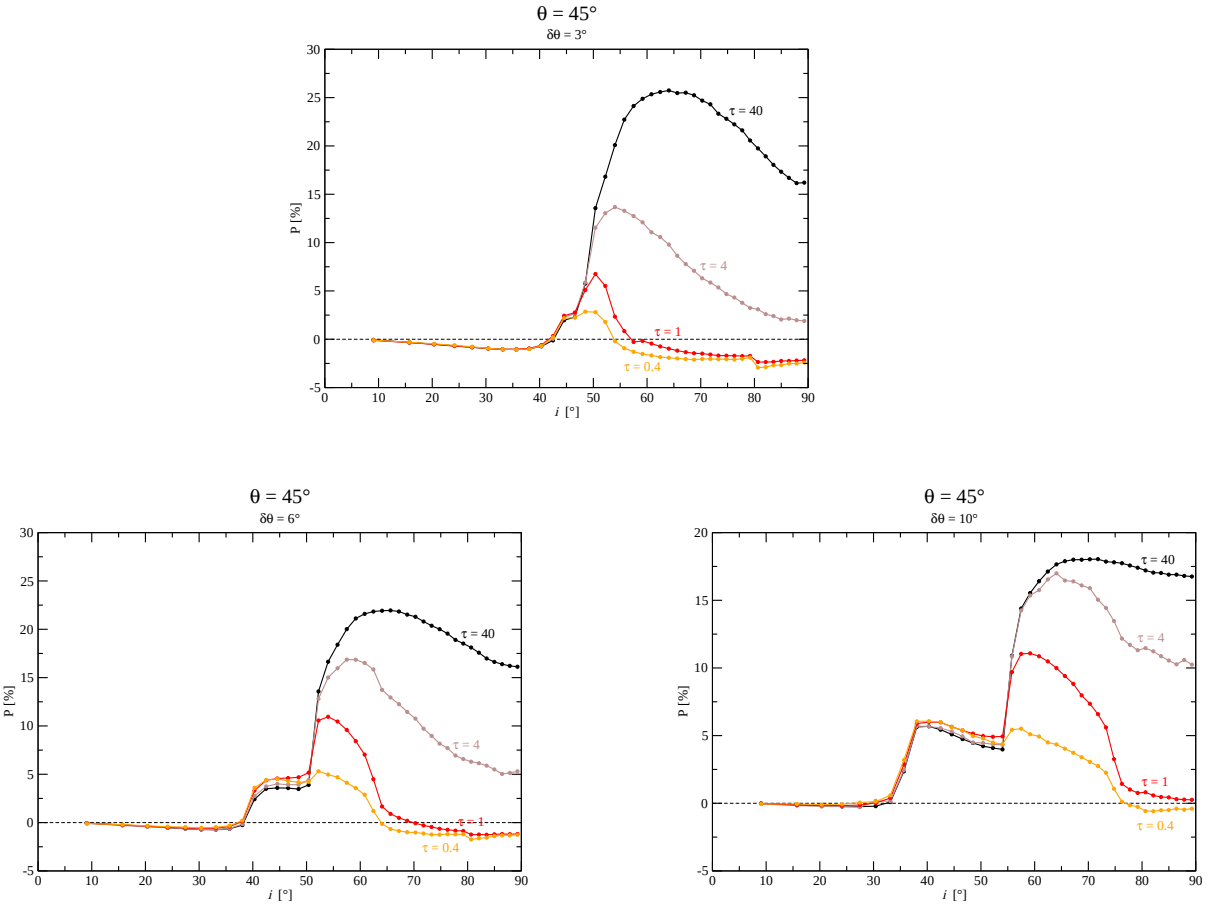

Figure 8.12: Investigating the polarization response of the dual quasar's structure with a bending angle $\theta = 45°$ according to the observer's viewing angle i, varying the outflow's opening angle $\delta\theta$ and the dust equatorial optical depth τ (black: $\tau_{dust} = 40$ – brown: $\tau_{dust} = 4$ – red: $\tau_{dust} = 1$ – orange: $\tau_{dust} = 0.4$). *Top*: $\delta\theta = 3°$; *bottom-left*: $\delta\theta = 6°$; *bottom-right*: $\delta\theta = 10°$.

is higher than observed P levels (Kay 1994). Decreasing the dust optical depth ($\tau = 4$) diminishes the overall P as photons can now escape from the dusty funnel by transmission through the dust wind. The polarization dichotomy is preserved down to τ approximatively equals unity, where the multiple regimes for parallel and perpendicular polarization reappear. However, they leave a higher covering factor for the observed number density of type-2 AGN and the resulting polarization degree at equatorial viewing angles is lower and thus closer to the observed range. Our modeling excludes optically thin dust environments ($\tau < 1$) as they automatically generate perpendicular photon polarization angles at equatorial inclinations.

The impact of the model morphology is essentially visible at intermediate and equatorial viewing angles, where the observer's line-of-sight is crossing the dust material. For type-1 objects, the polarization degree is found to be parallel, with $P < 2$ %, slightly increasing with i. Around 45°, P remains stable for a few i, depending on the half-opening angle of the outflow. Such a

polarization plateau ($P \sim 3$ – 5 %) is a strong observational prediction that could help to estimate the averaged $\delta\theta$ of BAL-quasars. For higher inclinations, P rises as backscattered photons from the WHIM funnel strongly contributes to the polarization flux. When the internal structure becomes hidden by the cold, outer dust layer, P starts to decrease until it reaches a minimal value along type-2 inclinations (below 10 % at $\tau \leq 4$).

We thus find that for $\theta = 45°$, and $\delta\theta = 3°$–$10°$, and moderate optical depths of the dust with $1 < \tau \leq 4$, the double-wind model seems to rather well reproduce the observed continuum polarization. It gives strong observational predictions on the geometrical opening angles of the outflow, as well as the amount of cold dust that can survive so close from the emitting source. However, it is important to investigate if the physical and geometrical changes to the model of Elvis (2000) proposed are realistic and in agreement with number counts of different AGN types.

8.5 Summary and discussion

We tested to which extend the WHIM model of Elvis (2000) can reproduce the observed polarization dichotomy with respect to the polarization position angle, as well as the expected level of polarization percentage in type-1 and type-2 AGN. A pure Thomson scattering model with $\theta = 60°$ and $\delta\theta = 3°$ only produces parallel polarization. For low-luminosity objects, Elvis (2000) predicts that the amount of polarization along the outflow's direction, where a layer of dust prevents the detection of BAL, would be below 0.5 %. Our modeling agrees with this claim but adding dust to the outer parts of the conical outflows still does not produce the polarization dichotomy. Finally, a double-layered wind again only produces parallel polarization as well as too high polarization percentages at type-2 viewing angles.

Exploring different sets of morphological and opacity parameters, we then found that small modifications help to match the modeling results with polarization observations. A key point is to slightly lower the bending angle of the winds to allow for the presence of perpendicular polarization at type-2 viewing directions. Perpendicular polarization at intermediate and equatorial lines-of-sight emerges naturally when photons travel through geometrically thick regions with an optical depth equal or larger tha unity.

For the pure WHIM model we found parametrisations that may correspond to the observed polarization dichotomy between non-NAL/NAL (type-1) AGN and obscured BALQSO's or Seyfert-2 galaxies. However, the solid angle of the sky covered by Seyfert-2 galaxies may require additional dust obscuration that we also tested. Both, the observed polarization dichotomy and polarization degrees can be reproduced if we consider a dual wind model with $\theta = 45°$ and include equatorial scattering in the accretion flow. The half-opening angle $\delta\theta$ of the flow then normalises the polarization degree as well as the maximum inclination at which parallel polarization is still detected. The opacity of the outer (dusty) wind may also be adjusted to decrease the polarization degree at equatorial inclinations; the maximum polarized flux is then observed along the outflowing direction. To match with spectropolarimetric observations, the dust optical depth along the equator should be close to unity.

8.5.1 Discriminating between different wind models

The question of discriminating between different wind models was raised by Elvis (2000, 2002b,a) discussing wind properties for the X-ray range. We here add a brief discussion about the UV/optical properties of the ionization cones and narrow line regions seen in Seyfert-2 like galaxies.

The first conical models were based upon the geometrical shape of the extended narrow line regions that are supposed to be the natural extension of the ionized outflows. The assumed morphology is an hourglass-shaped, bi-conical region with the emitting source situated at the cone base.

The resulting polarization rises from face-on towards edge-on viewing angles and uniquely produces perpendicular polarization angles, independently of the filling medium (either electrons or dust grains, Goosmann & Gaskell 2007). Typically, P can be as high as 20 % for ionized or dusty winds. However, the wind structure of Elvis (2000) presents a very different polarization pattern: in contrast to polar outflows, the hollow winds can produce polarization et parallel and perpendicular position angles. Compared with the model presented in Fig. 8.11 and Fig. 8.12, the polarization degree is small ($P < 5$ %) at both polar and equatorial viewing angles. The maximum polarization degree is reached for lines-of-sight crossing the outflow, with $5 < P < 25$ %, depending on the model's dust opacity and half-opening angle. The two-phase model succeeds to reproduce the polarization degree expected from the polarized continuum of BAL quasars (Cohen et al. 1995; Goodrich & Miller 1995; Ogle 1998).

The low-luminosity version of the wind with dusty extensions leads to $P <$0.5 % as predicted for non-BAL objects (Berriman et al. 1990). Moreover, Elvis (2000)'s two-phase model may produce a polarization position angle that varies from 90° at pole-on views to 0° at equatorial views, which is in agreement with the observed polarization dichotomy. Depending on the parametrization, it is also possible to create $\psi = 0°$ photons at polar inclinations – a phenomenon observed in some Seyfert-1 galaxies that were named *polar scattering dominated* AGN by Smith et al. (2002b).

8.5.2 Polarization upper limits from Seyfert-atlases

Compared to the modeling results for AGN winds, the observed polarization degrees are generally found to be significantly lower. In the atlas of Seyfert-2 galaxies presented by Kay (1994), a large polarization degree was detected for Mrk 463E ($P = 10.29 \pm 0.18$ % after starlight correction, $z = 0.050$ Veron-Cetty & Veron 1987), but finding such highly polarized type-2 AGN is quite uncommon. The majority of the observed Seyfert-2 galaxies show lower P values, usually below 3 % (Miller & Goodrich 1990; Kay 1994). Most Seyfert-1 galaxies have very weaker polarization degrees, usually below 1 % (Smith et al. 2002b, 2004), except for exceptional, high-polarization objects where P can reach up to 5 % (see Mrk 231 in Goodrich & Miller 1994 and Fairall 51 in Smith et al. 2002b).

The diversity of detected polarization degrees is a difficult assess in the modeling. Simulations of simple and isolated (Miller & Goodrich 1990), or complex and radiatively coupled (Marin et al. 2012c; Marin & Goosmann 2012) reprocessing regions in AGN tend to create too large polarization degrees at equatorial viewing angles and not enough polarization at polar inclinations. The outflow model evaluated in this chapter seems to be able to overcome these difficulties when taking into account a two-phase wind structure. High polarization degrees at a perpendicular polarization position angle can be reached if the inclination of the system is close to the bending angle of the quasar wind; low P values are produced when the observer's line-of-sight is close to the equatorial plane. As the proposed set of outflow half-opening angles lies between 3° and 10°, the ratio of high-P to low-P AGN remains small, which is coherent with the few high-P Seyfert-2 galaxies detected. As for Seyfert-1 galaxies, the structure is able to produce parallel polarization as high as 2 % (Fig. 8.11), while preserving the observational evidence of higher P values for equatorial viewing angles than at polar inclinations (Fig. 8.11 and Fig. 8.12).

8.5.3 The test case of the Seyfert galaxy NGC 5548

NGC 5548 is one of the best laboratories for testing AGN models (Rokaki et al. 1993) and an important reference for Elvis (2000). How does the wind model hold against spectropolarimetric measurements of the object? The Seyfert-1 galaxy ($z = 0.0174$) shows a continuum polarization degree of 0.67 ± 0.01 % associated to a position angle of $\psi \sim 45.6 \pm 0.6$ ° (Goodrich & Miller 1994)[1] . To compare our modeling predictions to the measured polarization position angle, the observed ψ needs to be related to the position angle of the radio axis of NGC 5548 (157°). The angular difference of 111° is roughly perpendicular.

According to Goodrich & Miller (1994), perpendicular polarization indicates that polar electron scattering is the dominant scattering mechanism. However, Wu & Han (2001)'s estimation of the inclination towards NGC 5548 ($i = 47.3° \ ^{+7.6}_{-6.9}$) implies that the polarization degree should be significantly higher than the observed value. Our model presented in Fig. 8.9 can explain the polarization degree and the polarization position angle of NGC 5548 in the context of the wind model for a bending angle of 45°. It strengthens the idea that AGN winds do not need to be fully filled by reprocessing matter; a hollow geometry may be then considered as more likely.

8.5.4 The morphology of the outflow in IC 5063

Located in the southern hemisphere, IC 5063 ($z = 0.011$, Morganti et al. 2007) is a Seyfert-galaxy that is famous to be the first AGN where a fast outflow of neutral hydrogen was detected (Morganti et al. 1998). Among other characteristics, its *Hubble Space Telescope* image shows an ionized structure extending out to 15 kpc in a remarkable, X-shaped morphology (Morganti et al. 2003). However, spectroscopic and spectropolarimetric images of solid double cone models (Wolf & Henning 1999; Marin et al. 2012c) show that the scattering region re-emits uniformly to the irradiation source and the peculiar behavior of IC 5063 cannot be visually explained using uniform or fragmented polar winds. The idea that AGN winds may be hollow came while observing the 3-dimensional velocity field of the line-emitting gas over 1 kpc in NGC 1365 (Hjelm & Lindblad 1996). The flow pattern of such a wind then naturally creates an X-shaped signal in the imaging.

The WHIM model investigated in this chapter (Fig. 8.3 bottom) successfully reproduces[2] the X-shaped morphology of IC 5063, as well as the bright flux spot in the AGN inner regions detected by Morganti et al. (2003). It indicates that Thomson scattering is still a dominant mechanism at large distances from the central source of IC 5063 and it tends to support the idea that quasar outflows are hollow structures. However, not all AGN where hollow winds are suggested show an X-shaped morphology (see for instance NGC 2992 in Veilleux et al. (2001) or NGC 1068 in Crenshaw & Kraemer (2000)). A possible complication here may be that the amount of dust in the extended narrow line regions in high and thus prevents direct imaging of the hollow wind signatures.

8.5.5 The tilted outflow of NGC 1068

NGC 1068 is considered to be one of the most archetypical examples of thermal Seyfert-2 galaxies. According to the simplest approach in AGN unification models (Antonucci 1993; Urry & Padovani 1995), the central region of NGC 1068 is hidden by optically thick, circumnuclear matter usually designated as a dusty torus. It is then a direct consequence of the circumnuclear dust that

[1] In comparison, Smith et al. (2002b) found $P \sim 0.69 \pm 0.01$ % and $\psi \sim 33.2 \pm 0.5$ ° for NGC 5548.

[2] The *Hubble Space Telescope* image presented by Morganti et al. (2003) is based on total flux only, while our Fig. 2.3 shows the polarized flux (total flux × polarization degree). We checked that the X-shape morphology is also reproduced in total flux, a straightforward conclusion as Thomson scattering is wavelength-independent.

the radiation of the central engine escapes non-isotropically along the polar regions. It forms the so-called ionized winds that farther out interact with the interstellar medium of the host galaxy and give rise to narrow emission lines (Osterbrock & Mathews 1986). It is a common hypothesis that as a consequence of the collimation effect by the circumnuclear dust the polar outflows sustain the same half-opening angle as the dusty torus. This assumption is derived from the assumed axisymmetry of the unified model. However a recent study on NGC 1068 carried out by Raban et al. (2009) showed that the polar winds (represented by a bi-conical structure) are most likely inclined with respect to the obscuring torus axis. In the context of this work, several models of tilted outflows (Das et al. 2006; Goosmann & Matt 2011b; Marin et al. 2012a) are being developed – but the off-axis outflow may also be explained by the structure for quasars if the radiation pressure field is not isotropic. In this case, the bending of the flow becomes non-axisymmetric and the extended outflow would appear tilted with respect to the symmetry axis of the system.

The results presented in this chapter have been published in Marin & Goosmann (2013a) and in Marin & Goosmann (2013b,c).

Chapter 9

X-ray polarimetry: the complementarity of multi-wavelength observations

The interplay between radio and optical observations, that lead to the discovery of quasi-stellar objects (see Sect. 2.1, Chap. 2) is one of the best examples of multi-wavelength complementarity. Following surveys of AGN where based upon the comparison between radio detection and photographic techniques in the optical to find sources with compact, blue nuclei. Optical spectroscopy was then used to identify and classify the samples according to their absorption and emission line widths (Weedman 1977). Today, the search for AGN has extended the wavebands of interest and large-scale X-ray, optical, and near-IR surveys (Sanders & Mirabel 1996; Skrutskie et al. 1997) reveal larger populations of quasars than were discovered by radio/UV techniques alone.

Knowing that polarization is a powerful tool to probe the unresolved and obscured parts of AGN, one would like to explore polarimetric signals over a large spectral range. Nowadays, polarization can be measured from the radio domain to the GeV band:

- In the radio domain, polarimetry can be achieved by rotating the antenna to record the Stokes vector. Radio observations are particularly suitable to investigate magnetic fields in AGN jets by tracing polarized synchrotron emission as well as Faraday rotation.

- In the infrared band, one can obtain polarization measurements by splitting the photon beam using birefringent gratings (Packham et al. 2008) or rotating waveplates. As scattering is less important than at optical/UV wavelengths (Wood 1997; Wood & Jones 1997), polarimetry is particularly useful to reveal magnetic fields in the dusty, circumnuclear quasar regions.

- In the optical/UV, birefringent beam-splitters are used to separate the ordinary from the extraordinary beam. For the AGN case, this waveband is of particular interest as it led to the discovery of hidden Seyfert-1 nuclei in Seyfert-2 objects, revealing the broad, polarized signatures of emission lines (Antonucci & Miller 1985).

- Even if there are no polarization-dedicated instruments in the Gamma-ray range, there were a few attempts to measure polarization from Gamma Ray Bursts (GRB) and SNR using the spectrometer aboard *INTEGRAL* (McGlynn et al. 2007; Dean et al. 2008) and the 9-element Ge spectrometer array of the Ramaty High Energy Solar Spectroscopic Imager *RHESSI* (Smith et al. 2002a). Many Gamma-ray emission and radiative transfer processes are expected to produce linearly polarized photons (Lei et al. 1997) that could trace both the emission geometry and mechanisms.

Yet, there is no flying X-ray polarimeter. This is surprising as the number of bright sources emitting in the 0.1 – 100 keV is large, from Sun-like stars, where X-ray are produced in the solar corona (Guedel et al. 1997), to AGN, X-ray binaries and ultra-luminous X-ray sources (ULX, Winter et al. 2006) where X-ray emission is a product of accretion. We know, since the observations of Tindo et al. (1972) and Nakada et al. (1974), that hard X-ray polarization can emerge from solar flares. X-ray polarization induced by synchrotron emission was also measured from supernova remnants (Novick et al. 1972; Weisskopf et al. 1978b), but the X-ray polarization emerging from fainter sources, such as AGN, has not yet been measured.

In this last chapter of the manuscript, we intend to investigate what could be the AGN polarization signature that can emerge from the 1 – 100 keV band. We aim to show that there is important work that can be done with X-ray polarimetry as a new, independent and complementary tool to spectral and timing analyzes. We particularly focus on a strongly debated topic of X-ray astrophysics (i.e. the relativistic reflection versus complex absorption scenarios that are proposed to explain the iron line broadening in Seyfert 1 AGN) and present strong observational predictions for a future spectropolarimetric X-ray mission.

9.1 AGN modeling from the optical to the X-ray domain

To be coherent with our previous work throughout this manuscript, we now present a composite, multiple-scattering and reprocessing model of AGN from which spectropolarimetric fluxes are computed simultaneously in the optical/UV and in the X-ray band. Our model setup is based on the classical, axis-symmetric unified scheme of AGN (Urry & Padovani 1995) and we are particularly interested in the polarization properties as a function of wavelength and viewing direction. If we assume that the radio structure is stretched along the symmetry axis of the torus, our modeling allows us to test if we can reproduce the observed dichotomy (Antonucci 1983, 1984; Smith et al. 2002b) between polar and edge-on photon polarization angle in the X-ray regime.

We consider a compact continuum source of unpolarized photons being emitted isotropically according to a power-law $F_\nu \propto \nu^{-\alpha}$ with index $\alpha = 1$. For the optical/UV part (1600 Å – 8000 Å) we assume the continuum source to be very compact and quasi point-like. For the X-ray range (1 keV – 100 keV), we adopt a lamp-post geometry and include X-ray reprocessing of the primary radiation by the underlying disk. The primary source is located at low height on the disk axis subtending a large solid angle with the disk.

The source region is surrounded by a geometrically and optically thin scattering annulus with a flared shape. This radiation-supported wedge plays a major role as it produces a parallel polarization signature in type-1 view by electron scattering (see e.g. Chandrasekhar 1960, Angel 1969, Antonucci 1984, Sunyaev & Titarchuk 1985). At larger radius an optically thick, elliptical dusty torus surrounds the system. It shares the same symmetry plane as the flared disk and is responsible for the optical obscuration at type-2 views. The torus funnel supposedly collimates a mildly-ionized, optically thin outflow stretched along the symmetry axis of the system. The polar wind has an hourglass shape and is centered on the photon source. Parameters defining the shape and the composition of the three/four reprocessing regions are summarized in Tab. 9.1. The dust model used for the torus at optical/UV wavelengths is based on a prescription for Galactic dust as described in Goosmann & Gaskell (2007). In the X-ray band, we assume neutral reprocessing for the torus and for the accretion disk. Details of this reprocessing model can be found in Goosmann & Matt (2011b).

irradiated accretion disk	flared disk	dusty torus	polar outflows
(only present for X-rays)	$R_{\rm min} = 0.02$ pc	$R_{\rm min} = 0.1$ pc	$R_{\rm min} = 0.3$ pc
$R_{\rm disk} = 0.0004$ pc	$R_{\rm max} = 0.04$ pc	$R_{\rm max} = 0.5$ pc	$R_{\rm max} = 1.8$ pc
$h_{\rm disk} = 3.25 \times 10^{-7}$ pc	half-op. angle = 20°	half-op. angle = 60°	half-op. angle = 40°
vertical opt. depth >600	equat. opt. depth = 1	equat. opt. depth = 750	vertical opt. depth = 0.03
neutral reproces.	electron scat.	Mie scat./neutral reproces.	electron scat.

Table 9.1: Parameters of the different model components. The accretion disk is only present when modeling the X-ray range. The elevated primary X-ray source is located on the disk axis and subtends a half-angle of 76° with the disk. Note that for the polar outflow, the half-opening angle is measured with respect to the vertical, symmetry axis of the torus, while for the flared-disk the half-opening angle is taken with respect to the equatorial plane.

In the top panels of Fig. 9.1, we present the total flux, F, for the two wavebands considered. The fluxes are normalized to the pure source flux, F_*, that would emerge along the same line-of-sight if there were no scattering media. The results for the polarization percentage, P, and for the polarization angle are combined in the bottom panels of Fig. 9.1. We adopt the usual sign convention for the polarization percentage that is recalled in the figure caption.

9.1.1 Results for the optical/UV band

At face-on and edge-on view, the optical flux is wavelength-independent indicating that electron-scattering in the equatorial flared-disk and in the polar outflows dominates. At intermediate viewing-angles, the impact of the wavelength-dependent dust scattering emerges, mostly around the λ_{2175} feature in the UV. This little bump at 2175 Å in the flux spectrum is due to scattering by carbonaceous dust in the torus.

The model reproduces the observed polarization dichotomy. The signature of the flared-disk is visible exceeding the effects of the polar outflow and producing low degrees of parallel polarization towards face-on viewing angles. At higher inclination, the equatorial scattering is hidden by the dusty torus and polar scattering dominates causing perpendicular polarization. The variations of P with wavelength at intermediate viewing angles indicate that the dusty torus also has a significant impact on the polarization. The rise in P towards the UV at $i \sim 76°$ is a combined effect of multiple scattering inside the torus funnel and of the wavelength-dependent polarization phase function that is associated with Mie scattering by Galactic dust.

9.1.2 Results for the X-ray band

The X-ray spectrum shows typical features of neutral reprocessing – the iron Kα and Kβ fluorescence lines at 6.4 keV and 7.1 keV and their absorption edges, the Compton hump, and strong soft X-ray absorption at intermediate viewing angles are prominent spectral features. The fluorescent line emission and the Compton reflection hump around 30 keV are present at every line of sight.

An important result of our modeling is that we predict a polarization dichotomy also for the X-ray band. At all viewing directions below the torus horizon, P is positive implying perpendicular polarization. But towards a face-on view, the electron scattering in the equatorial flared disk predominates and produces a net parallel polarization. A peculiar feature appears at $i \sim 73°$, where P changes from positive to mildly negative values around the Compton hump. This behavior

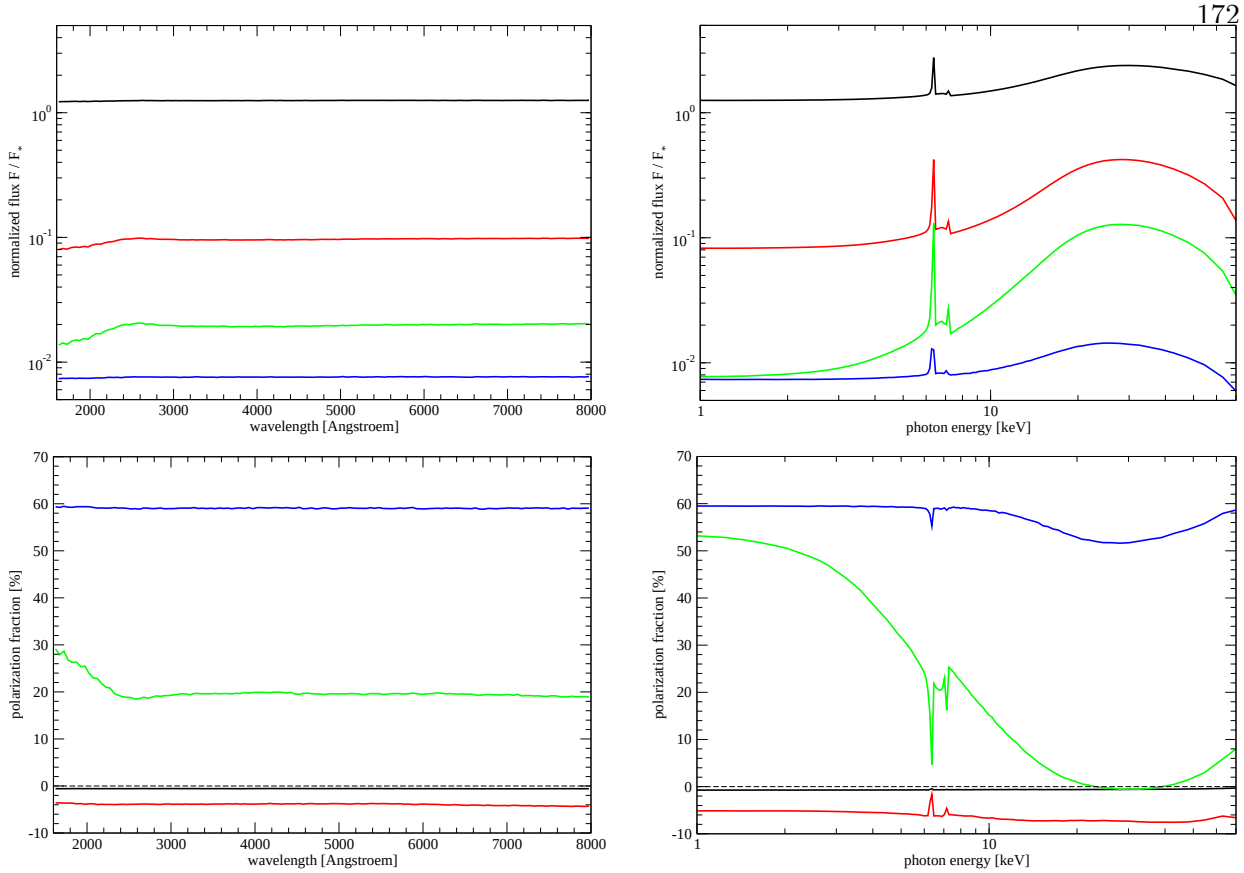

Figure 9.1: Modeling the radiative coupling between the different axis-symmetric reprocessing regions. The normalized spectral flux is shown in the top panels, the polarization properties are shown below. A negative P denotes a "type-1" polarization (parallel to the projected symmetry axis) and a positive P stands for a "type-2" polarization (perpendicular to the axis). The transition at $P = 0$ is indicated by dashed lines. Four different viewing angles, i, are considered: a face-on view at $i \sim 18°$ (black), a line-of-sight just below the torus horizon at $\cos i = 0.63°$ (red), an intermediate type-2 view at $i \sim 76°$ (green), and an edge-on view at $i \sim 87°$ (blue). Left: optical/UV energy band. Right: X-ray band.

is due to the competition between parallel and perpendicular polarization emerging from different reprocessing regions of the model. Around 30 keV, the effect of the flared disk becomes less important than the Compton scattering in the other regions. Explaining this behavior in detail is not trivial as several factors have to be taken into account, one of them being the angle-dependent scattering phase function. But also the energy-dependence of the electron scattering cross-section has an effect as it favors soft X-ray photons to scatter more than hard X-ray photons. Higher energy photons therefore pass more easily through the optically thin, equatorial scattering region without interacting. This partly explains the disappearance of the parallel polarization at higher photon energy.

This thesis mainly focuses on the continuum polarization emerging from multiple reprocessing. However, *STOKES* can handle radiative recombination and fluorescence emission, as shown in

Fig. 9.1. To illustrate the importance of atomic processes imprinting emission and/or absorption features on the polarized continuum, we now examine, until the end of this manuscript, the possible polarization degree and position angle that can emerge across the famous 6.4 keV iron line

9.2 Is X-ray polarimetry powerful enough to discriminate between absorption and reflection scenarios in type-1 Seyfert galaxies?

With the launch of *Astro-C/Ginga*, Fe Kα emission lines in Seyfert galaxies started to be regularly detected (Pounds et al. 1990). After the initial discovery in MCG-6-30-15 (Tanaka et al. 1995), systematic surveys of radio-quiet, type-1 active galactic nuclei (AGN) showed that some objects have extremely broadened and distorted iron lines (see e.g. Reeves et al. 2006; Nandra et al. 2007; de La Calle Pérez et al. 2010; Patrick et al. 2011). Associating the X-ray fluorescent line with the Compton reflection hump above 10 keV, George & Fabian (1991) showed that both components can arise from reprocessing in the same medium. However, the actual location of this scattering material is actively discussed as two competing scenarios attempt to explain the apparent broadening of the iron line's red wing.

On the one hand, the reprocessing medium is thought to be the accretion disk (Fabian et al. 1989) surrounding the supermassive black hole. Reflection of hard X-rays off the inner disk, reaching down to the innermost stable orbit, produces fluorescent emission, subsequently broadened by general relativistic and Doppler effects (Miniutti et al. 2003; Reynolds et al. 2009). Integrating the reprocessed emission across the disk constitutes the blurred line that is sensitive to the spin of the SMBH. By fitting observational 4–7 keV band spectra with relativistic reflection models, the spin parameter can then be constrained (Fabian et al. 1989; Laor 1991; Dovčiak et al. 2004; Brenneman & Reynolds 2006; Dauser et al. 2010).

On the other hand, the fluorescent emission may also come from more distant matter situated along the observer's line-of-sight (Yaqoob & Padmanabhan 2004; Page et al. 2004). In this scenario, an evolving complex absorption due to clouds of absorbing gas, partially covering the central AGN source, is responsible for both the flux variability and the apparent broadening of the Fe line. Continuum radiation transmitted and scattered through circumnuclear medium carves out the extended red wing, which leads to systematically lower measurements of the SMBH spin than obtained by the relativistic reflection method (Inoue & Matsumoto 2003; Miller et al. 2008, 2009).

In order to discriminate between the two scenarios, it has been suggested that sufficiently accurate X-ray spectroscopy is needed, so that the shape of the underlying continuum is precisely distinguished from the iron line. This requires to extend the spectral range to cover also the Compton hump, i.e. over a few tens of keV. With the recent *NuSTAR* observation of NGC 1365, a nearby galaxy ($z = 0.005$) hosting a type-1.8 AGN, Risaliti et al. (2013) indeed gave advantage to reflection-dominated models using temporal and spectral analyzes. However, Miller & Turner (2013) also claim that the excess emission above 10 keV, the spectral shape and the time-invariant iron red-wing of NGC 1365 can be reproduced using absorption-dominated models. A similar discussion raised upon the archetypal, bright MCG-6-30-15 Seyfert galaxy, whose extended red wing is well-established from long observations with *XMM-Newton* (Wilms et al. 2001; Fabian et al. 2002) and *Suzaku* (Miniutti et al. 2007).

In this dual context, we aim to explore an independent path suggesting future X-ray polarimetry observations as a discriminating tool between the two scenarios. It is not the scope of

this section to produce an accurate spectral fit to the X-ray data of the two major examples MCG-6-30-15 and NGC 1365. We rather assimilate prescriptions for reflection and absorption models that have been presented before and, based on these models, we compute the predicted X-ray polarization as a function of the observer's viewing angle.

9.2.1 Exploring models for MCG-6-30-15

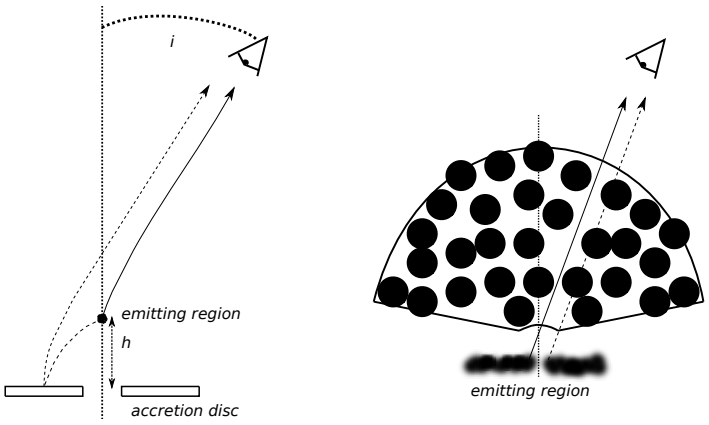

Figure 9.2: Schematic view of the scenarios considered for MCG-6-30-15. *Left*: reflection with a lamp-post geometry and light-bending. *Right*: partial covering with a clumpy wind.

9.2.1.1 The relativistic reflection model

We first consider relativistic reflection from a cold accretion disk illuminated by an elevated lamp-post on the disk axis. The method is described in detail in Dovčiak et al. (2011). A grid of local reprocessing models, i.e. taken in the frame of the rotating accretion disk, was computed with the Monte-Carlo radiative transfer code *NOAR* (Dumont et al. 2000) providing the re-emitted intensity as a function of incident and re-emission angle. We defined an isotropic, point-like source emitting an unpolarized spectrum with a power law shape $F_* \propto \nu^{-\alpha}$ and $\alpha = 1.0$. The accretion disk is approximated by a constant density slab with cosmic abundances. Compton scattering, photo-absorption and iron line fluorescent emission are included in the computation of the locally re-emitted spectra. The local polarization is computed using the transfer equations of Chandrasekhar (1960). Since the reprocessing medium is optically thick, the reprocessing predominately occurs very close to the irradiated surface of the slab and thus the approximation is sufficiently accurate. The local, polarized reflection spectra are then combined with the *KY*-code (Dovčiak et al. 2004) conducting relativistic ray-tracing between the lamp-post, the disk, and the distant observer (see Fig. 9.2, left). The height of the lamp-post is fixed at 2.5 $R_{\rm G}$, where $R_{\rm G} = GM/c^2$, and an extreme Kerr black hole with the dimensionless spin $a = 1$ and a mass of $M = 1.5 \times 10^6 {\rm M}_\odot$ is assumed.

Our choice of parameters is in good agreement with the assumptions of Miniutti & Fabian (2004). We point out though that in our approach the primary source is not off-axis, which should have an impact on the resulting polarization. Models of a patchy corona (see e.g Galeev et al. 1979; Haardt et al. 1994) presume that the off-axis sources should be anchored to the disk by magnetic field loops and thus co-rotate in Keplerian motion. In the relativistic reflection model, the X-rays

are emitted very close to the black hole and we thus estimate the maximum orbital time-scale occurring in a corona with the radial size $R_{\rm C} = 50 R_{\rm G}$ to;

$$T_C = 317 \times \frac{M}{10^7 M_\odot} \left[\left(\frac{R_{\rm C}}{R_{\rm G}} \right)^{1.5} + a \right] [s] \approx 17 \; ks. \tag{9.1}$$

This time span is by a large factor lower than the minimum exposure time for an observation of MCG-6-30-15 with a near-future X-ray polarimeter (see Sect. 9.3.3). The observed polarized flux due to a single, off-axis source is thus integrated over many Keplerian orbits. For this reason, the primary emission region should appear axis-symmetric in near-future X-ray polarimetry. So would the irradiation pattern due to a central lamp-post as assumed in our modeling.

The expected X-ray polarization for a non axis-symmetric, clumpy irradiation pattern of the accretion disk was studied by Schnittman & Krolik (2010a), who obtain polarization percentages across the 2–10 keV band that are significantly higher than the results obtained by Dovčiak et al. (2011) for the lamp-post geometry. Aside from the different coronal geometry, this is also related to different assumptions about the ionization of the accretion disk. When assuming a radially structured surface ionization (Ballantyne et al. 2003) we expect the local percentage of polarization to increase compared to a neutral disk because the efficiency for electron scattering rises with ionization. For the same black hole spin, the resulting integrated polarization observed at infinity must therefore increase as well.

Finally, here we do not include any intrinsic polarization of the primary radiation. Such polarization may occur if the primary spectrum emitted by the lamp-post is indeed due to inverse Compton scattering of UV/X-ray photons coming from the disk. This effect may thus strengthen the net polarization observed at infinity.

In summary, the net polarization percentage predicted by our lamp-post model with unpolarized primary radiation and a cold accretion disk is likely to be conservative.

9.2.1.2 The complex absorption model

An alternative approach to explain the broad red-wing of the Fe Kα line in MCG-6-30-15 and its lack of variability with respect to the continuum was given by Miller et al. (2008). The authors first suggested a model of absorbed, non-relativistic reflection combined with variable partial covering of the primary source. In the following, Miller et al. (2009) even proposed a pure absorption scenario. This model supposedly is in-line with evidence for high-column density, partial covering absorption found in other AGN (Turner et al. 2009; Reeves et al. 2009; Risaliti et al. 2009). It contains five absorbing zones with the ionized zones 1–3 being required to reproduce the narrow absorption lines in the *Chandra* and *XMM-Newton* grating data. The spectral curvature in the 1–10 keV band is caused by the low-ionization zones 4 and 5 covering the continuum source by 62 % and 17 %, respectively. We therefore focus on these two zones when modeling the expected polarization. The absorbers 1–3 fully cover the source and they thus represent an additional, low optical depth of $0.0002 < \tau_{\rm c} < 0.06$ with respect to Compton scattering that we could add to zones 4 and 5. However, given the large optical depth of zone 4 ($\tau_{\rm c} \sim 1.5$) and its predominant covering factor, it turns out that the impact of zones 1–3 is very limited and that we can safely neglect them.

Using the latest version of the *STOKES* code, we model a geometrically thin, static, disk-like source emitting an isotropic, unpolarized primary spectrum between 1 and 100 keV using the same power law slope of $\alpha = 1.0$ as for the relativistic modeling presented in Sect. 2.1. This setup is close to the approach of Miller et al. (2009). The emitting, central cylinder radially extends up to

0.05 pc and may represent a so-called hot inner flow. Note that in the absorption scenario we do not assume the accretion disk to reach down to the ISCO as otherwise, we would expect again the signs of relativistic reflection. The disk may be truncated at larger radii and thus it presents a low solid angle to the emission region and an eventual reprocessing component remains weak.

Between the source and the observer, a conical, neutral absorber with a height of 1.8 pc along the vertical axis, a half-opening angle of 75°, cosmic element abundances, and a Compton optical depth of either $\tau_c \sim 1.5$ or $\tau_c \sim 0.02$ is defined (Fig.9.2, right). This parameterisation is a good match to the modeling of zone 4 and zone 5 as given in Miller et al. (2009), except that our computations also include reprocessing. The actual modeling in *STOKES* is done for a uniform density cloud and the clumpiness is included by re-normalising the resulting Stokes fluxes in such a way that 62 % of the primary emission in the case of zone 4 and 17 % in the case of zone 5 are incident onto the cloud while 21 % of the source flux reach the observer directly.

9.2.1.3 Resulting polarization signatures

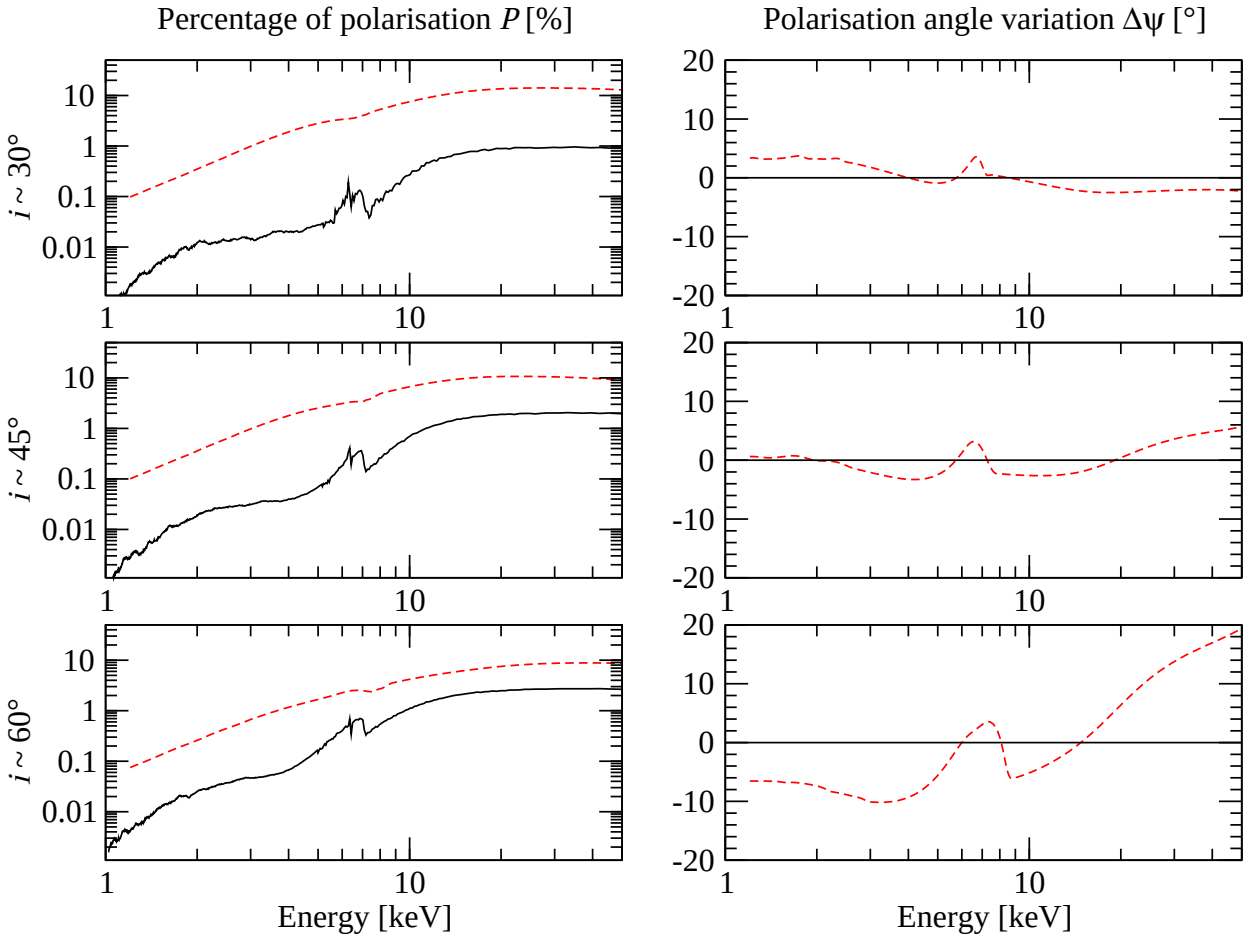

Figure 9.3: Percentage of polarization P and variation of the polarization angle $\Delta\psi$ with respect to its mean as a function of the energy. Three particular MCG-6-30-15 viewing angles i are considered: 30°, 45° and 60°. *Legend*: a fragmented absorption region (plain line) and a relativistic reflection model with an extreme Kerr SMBH with $a = 1$ (red dashed line).

In Fig. 9.3, we plot the resulting polarization as a function of photon energy at a viewing angle of 30°, 45° and 60°. No circular polarization can occur in this model setup, so P designates only linear polarization and $\Delta\psi$ the rotation of the polarization position angle with respect to a convenient average of the polarization position angle over the depicted energy band. The actual normalisation of the polarization angle with respect to the disk axis is not of primary interest as we cannot determine it from the observations.

It appears that in comparison with the absorption model, relativistic reflection produces a polarization percentage P in the 10-50 keV band that is at least by a factor of fifteen higher (Fig. 9.3, left). At lower energies, P decreases gradually down to 0.1 % for the reflection scenario while for the absorption model P drops much more drastically below 5 keV. In the relativistic case, the spectral shape of P is determined by the net integration of the polarization over the accretion disk. The fast motion of the accreting matter and strong gravity effects near the SMBH induce a rotation of the polarization angle that depends on the position on the disk and on the inclination of the observer. In contrast to this, the energy dependence of P for the absorption scenario is related to the polarization phase function of electron scattering. A large fraction of the radiation has undergone mostly forward scattering and thus only produces weak polarization.

Additionally, the primary spectrum of the continuum source favors the emission of soft X-ray photons and thus it causes strong dilution of the transmitted flux by unpolarized radiation at low energies. In the reflection scenario, a significant part of the primary flux is bent down to the disk and the dilution is less efficient.

As the viewing angle increases from 30° to 60°, P varies differently in both scenarios. In the relativistic reflection case, P decreases by a factor of ~ 1.3 as the polarization contribution from the inner and outer parts of the disk produce differently oriented and partly cancelling polarization. In the absorption case, P increases with viewing angle; when taken between 5 and 8 keV it is by a factor of ~ 6 higher at 60° than at 30°. Nonetheless, the polarization percentage for relativistic reflection always remains significantly higher than for the absorption scenario.

The variation of the polarization angle (Fig. 9.3, right) puts additional constraints on the origin of the broad iron line: in the absorption case, $\Delta\psi$ exhibits no variation. The relativistic model, however, induces energy-dependent variations in $\Delta\psi$ that increase with viewing angle and that are particularly strong across the iron line. This behavior is related to the energy dependent albedo and scattering phase function of the disk material. Note that at a viewing angle of 60° the variation of $\Delta\psi$ in the 2–10 keV band is larger than 10°. At an inclination of 30°, which is more probable for MCG-6-30-15, the variation is still around 5°.

9.2.2 Exploring models for NGC 1365

We illustrate the predictive power of X-ray polarimetry in the case of NGC 1365 by comparing the two prescribed reflection (Risaliti et al. 2013) and absorption (Miller & Turner 2013) models, based on which we run Monte Carlo radiative transfer simulations of the 1–100 keV polarization. The input spectrum of both models has a power-law shape $F_* \propto \nu^{-\alpha}$ with a spectral index $\alpha = 1.2$ (Risaliti et al. 2009, 2013; Miller & Turner 2013). The intrinsic flux is unpolarized and emitted isotropically.

9.2.2.1 The relativistic reflection model

In the reflection scenario the apparent broadening of the Fe Kα line is a consequence of rapid motion and general relativistic effects close to the SMBH. In this case, a neutral or partially ionized accretion disk is illuminated by an elevated lamp-post. The method is already described in Dovčiak

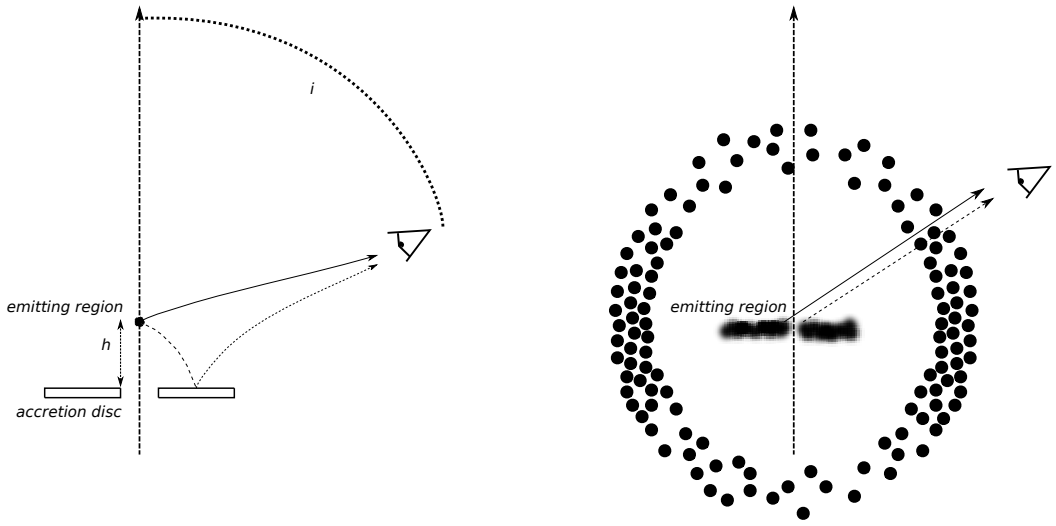

Figure 9.4: Schematic view of the two scenarios considered for NGC 1365. *Left*: reflection with a lamp-post geometry and light-bending. *Right*: partial covering with circumnuclear absorbers.

et al. (2011) and was used in Marin et al. (2012b) as well as in the previous section to model X-ray polarization spectra emerging from MCG-6-30-15. Consequently, here we only summarize the input parameters used to compute the relativistic reflection spectra (the local polarization degree of the disk reprocessing being estimated according to the transfer equations of Chandrasekhar 1960).

In agreement with the NGC 1365 parametrization of Risaliti et al. (2013), a SMBH mass of $M = 2.0 \times 10^6$ $M_\odot$ associated with a dimensionless spin parameter $a = 1$ is assumed (an extreme Kerr BH). The X-ray source is localised on the rotation axis, at 2.5 gravitational radii above the black hole. The ray tracing between the lamp-post, the disk and the distant observer is conducted with the KY code (Dovčiak et al. 2004), see Fig. 9.4 (left-hand panel).

The relativistic reflection model used to simulate the polarization response of NGC 1365 is basic, yet instructive. As discussed in Sect. 9.2.1.1, the model neither includes radially structured surface ionization, nor intrinsically polarized, non-axisymmetric irradiation. Coronal emission that scatters off an ionized disk would increase the net polarization (Schnittman & Krolik 2010a). Our modeling thus again produces a lower limit on the polarization degree.

9.2.2.2 The complex absorption model

The case of NGC 1365 is explored by Miller & Turner (2013), who assume that the hard excess arises from a high column density gas, situated around the active nucleus and partially covering the X-ray source. In this scenario, a clumpy distribution of 1000 spherical clouds, with equal radius and constant density, is situated between an inner radius r_1 and an outer radius r_2 from the central source. The model has a larger covering factor along the equatorial plane, as suggested by the unified scheme of AGN (Antonucci 1993; Urry & Padovani 1995).

We computed the resulting polarization of a cloud distribution such as the ones presented in Karas et al. (2000) and Miller & Turner (2013). The model set-up is summarized in Fig. 9.4 (right-hand panel). The central, X-ray source is defined as a geometrically thin, emitting slab that

may represent the so-called hot inner flow. The emitting region is insensible to scattering and does not reach down to the ISCO in order to avoid a possible confusion with relativistic disk reflection. Inside a spherical shell constrained between $r_1 = 10$ and $r_2 = 20$ (in units of spheres radius) from the model's origin, a random distribution of scale-independent, Compton-thick absorbing spheres was generated. The covering factor of the cloud distribution varies systematically from the poles towards the equator and is ~ 0.55 for $i = 0°$, and > 0.75 for $i > 60°$.

The density of the absorbing, cold medium in a single cloud is equal to 1.5 $\times 10^{24}$ cm^{-2}, a value chosen to maximize the observed excess of X-ray emission above 10 keV (*the hard excess*), in comparison with extrapolated spectra from lower energies. This parametrisation is in perfect agreement with the modeling of Miller & Turner (2013) and much more sophisticated than the approach undertaken in Sect. 9.2.1.2, where partial covering was implemented in an *ad hoc* way. Note that STOKES includes multiple scattering in the Compton regime, a crucial ingredient according to the authors of the absorption scenario.

9.2.2.3 Resulting polarization signatures

The resulting polarization signatures, as a function of photon energy, are plotted in Fig. 9.5. P and $\Delta\Psi$ designate the same quantities as previously.

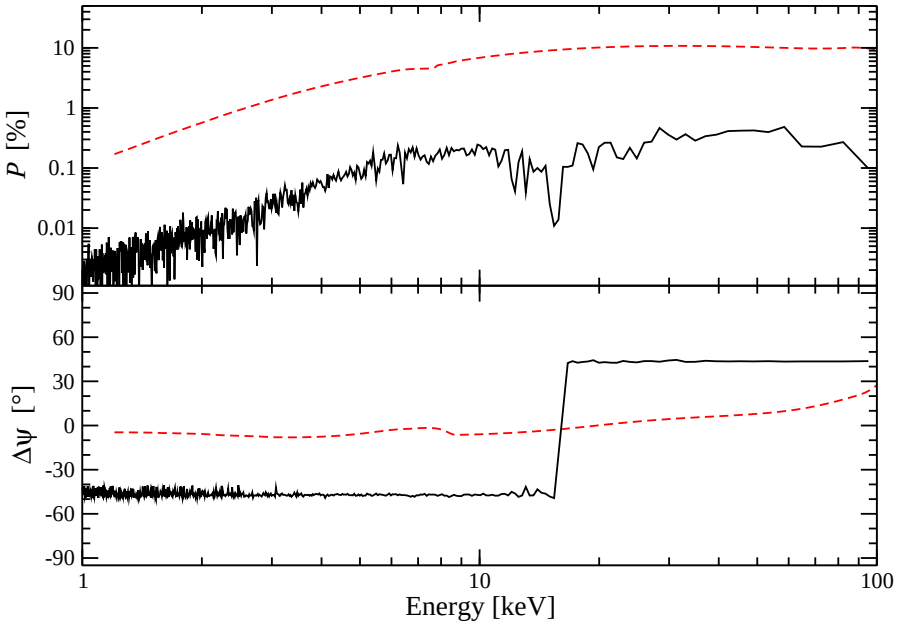

Figure 9.5: Percentage of polarization P and variation of the polarization angle $\Delta\psi$ with respect to its mean as a function of the energy. A viewing angle $i = 60°$, with respect to the symmetry axis of NGC 1365, is considered (Risaliti et al. 2013; Miller & Turner 2013). *Legend*: a fragmented absorption region (solid line) and a relativistic reflection model with an extreme Kerr SMBH with $a = 1$ (red dashed line).

Considering an inclination of $i = 60°$ for NGC 1365 (Risaliti et al. 2013), the reflection model is found to always produce a higher polarization degree than the absorption-dominated model (Fig. 9.5, top). The difference in P is globally constant with energy, with the relativistic model

being approximatively 15 times stronger in polarization than in the absorption case. For both scenarios, P decreases in the soft energy band, below the iron fluorescence line energy, but this trend is related to different mechanisms: in the relativistic case, it is a consequence of the mutual action of the matter's rapid motion, strong gravity effects close to the SMBH, and the energy-dependent albedo of the disk. In the absorption case, the energy-dependence of P is caused by dilution of the transmitted flux by primary emission from the source, set to favor the production of soft X-ray photons. In the relativistic reflection model, strong gravity effects tend to bent down the light back to the disk, and the dilution phenomenon is less significant. The minimum polarization degree produced by disk reflection is ≥ 0.1 % below 10 kev, and up to 10 % in the Compton hump regime. Meanwhile, the absorption scenario never reaches $P = 1$ %, even at high energies.

The most interesting results come from the variation of the polarization position angle (Fig. 9.5, bottom). The relativistic reflection scenario exhibits an energy-dependent $\Delta\Psi$ that varies significantly across the Fe Kα line. The behavior is related to the energy-dependent albedo and scattering phase function of the disk material. However, while the variation of Ψ remains smooth in the relativistic case, the absorption model shows an instantaneous $\Delta\Psi$ transition from the soft (below 15 keV) to the hard X-ray bands, associated with a local diminution of P. In the 1 – 15 keV band, radiation is not energetic enough to scatter through the highly covered equatorial plane and becomes absorbed. The few photons escaping from the model scatter perpendicularly on polar clouds, resulting in a polarization position angle $\Psi = 0°$ (Marin & Goosmann 2011; Marin et al. 2012c). Above 15 keV, the Compton scattering phase function becomes less isotropic and, due to the energy-dependence of the electron scattering cross-section, photons are able to reprocess along the equatorial plane without suffering heavy absorption. The net polarization position angle Ψ is equal to 90°. The competition between the Compton scattering cross section and the scattering phase function, leading to parallel or perpendicular polarization angle, results in an orthogonal switch specific to the prescription. The energy of the Ψ rotation is a complex function of opacity and covering fraction, and will be different for other parametrization

The results plotted in Fig. 9.3 and Fig. 9.5 show that, in principle, X-ray polarization can distinguish between the relativistic reflection and the absorption explanation for the broad iron line in MCG-6-30-15 and NGC 1365. However, there is one last step to achieve: measuring the polarization levels using an X-ray polarimeter.

9.3 Overview of the X-ray polarimeter possibilities

X-ray polarization measurements are photon hungry, as the I, Q and U-parameters of the Stokes vector must be recored with sufficient statistics. In case of an X-ray polarimeter with an ideal response to polarization, to detect a 1 % X-ray polarization signal against the statistical fluctuations in the instrumental response to the polarized signal, if we accept a 10σ standard deviation, $4{\times}10^6$ photons would be needed. Bright AGN only radiate at a rate of a few tens of counts per second per square meter in the X-ray band, so X-ray polarimetry is also time-consuming. Unfortunately, most of AGN situated in the local Universe are fainter than 10 cts/sec/m^2 (and the brightest $z >$ 1 quasars only radiate at a rate of 1 ct/s/m^2), so exposition times will increase. Past instruments based on graphite-crystal Bragg diffraction at 45° (Novick et al. 1972; Weisskopf et al. 1972) or Thomson/Compton scattering (Angel & Weisskopf 1970; Wolff et al. 1970; Novick & Wolff 1971) were not sensitive enough to overcome these limits..

We now present recent advances in X-ray polarimetry by looking at the latest generation of X-ray polarimeters based on the photoelectric effects. We will take as an example the Gas

Pixel Detector (GPD), the first instrument of this kind sensitive in the soft X-ray energy range. A non-exhaustive review of past X-ray missions that would have used the GPD as an on-board polarimeter follows and we then test our predictions for MCG-6-30-15 and NGC 1365 according to the polarization sensitivity of those miss

9.3.1 Technology: how to measure X-ray polarization?

One of the most elaborate, technologically-ready X-ray polarimeter is the Gas Pixel Detector (GPD, see Fig. 9.6). Developed in collaboration between the INFN of Pisa and INAF-IAPS groups in Rome (Costa et al. 2001; Bellazzini et al. 2003, 2006b,a; Bellazzini & Muleri 2010), the GPD is particularly sensitive to the X-ray polarization in the 2 – 10 keV energy range. The sensitivity follows the cross-section of the photoelectric effect, which is the key process of the detection mechanism. When a photon is captured by the GPD, it interacts with a low Z gas and creates a photoelectron[1] which is emitted with more probability into the direction of the photon electric field (i.e. the polarization vector), with a probability of being emitted in a particular azimuthal direction which is modulated with a cosine square modulation. The photoelectron ionizes the gas along its direction of motion, creating secondary photoelectrons, that are drifted and multiplied thanks to an appropriate electric field generated by a Gas Electron Multiplier. The amplified charges are eventually collected by a pixellated plane. The image of the photoelectron path is analyzed with a reconstruction algorithm that derives the absorption point and initial direction of emission of the photoelectron. From that starting point, the degree and angle of polarization of the incident radiation can be evaluated from the distribution of the photoelectrons azimuthal distribution throughout several reconstruction steps (see Bellazzini et al. 2006a for a complete review).

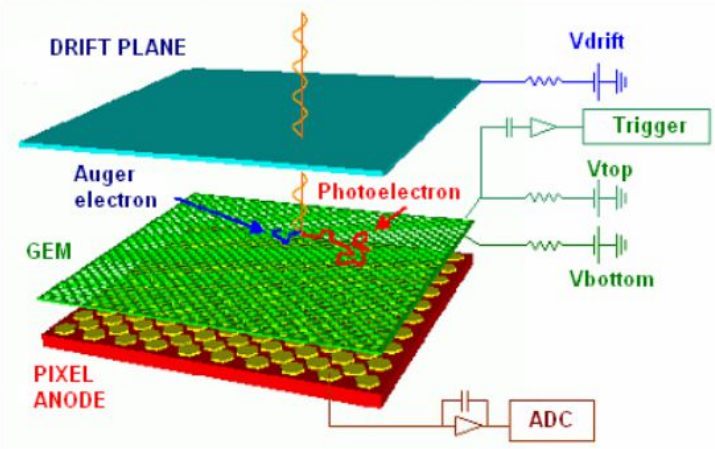

Figure 9.6: Overview of the GPD instrumental conception. GEM stands for Gas Electron Multiplier. The picture is taken from Costa et al. (2001)

The instrumental limit on the Minimum Detectable Polarization (MDP) of a polarimeter is

[1] Note that an Auger electron can be emitted in a random direction with respect to the photoelectron. It usually has very low energy and then it is absorbed close to the absorption point. Recording the Auger electron may help to distinguish the initial part of the photoelectron path.

evaluated as the polarization signal measured only because of statistical fluctuations. The underlying systematic effects are measured when observing a reference X-ray source with no polarization. The net MDP depends on the amplitude of the instrumental response to polarization and on the collected counts, and then on the collecting area of the telescope on which the polarimeter is mounted.

The GPD is not restricted to the 2 – 10 keV band. While the photoelectric cross-section is inversely proportional to (photon energy)$^{-3.5}$ far from absorption edges, the GPD is ready to explore X-ray polarimetry over a broader energy range when filled with a different gas mixture[2] . Detection of polarization signatures from the Compton hump, above 10 keV, is very helpful to constrain our models and strengthen their predictive power, in a similar way than for spectroscopy and timing analyzes

9.3.2 Past X-ray mission proposals (including a polarimeter)

The first measurement of extra-terrestrial, soft X-ray polarization goes back to the 1970's, when Novick et al. (1972) observed the whole Crab nebula (also known as M1, NGC 1952, Taurus A or SN 1054), including the pulsar. They detected a 15.4 % ± 5.2 % linear polarization associated with a 156° ± 10° photon position angle. The measurement by Novick et al. (1972) was in agreement with a possible synchrotron origin of the X-ray polarization, as the synchrotron mechanism is expected to produce high levels of polarization degree (see Sect. B.1). The detection was made possible using an Aerobee 350 unguided, suborbital, sounding rocket[3] equipped with the Thomson/Compton and Bragg polarimeters mentioned in Sect. 9.3. A few years later, Weisskopf et al. (1978b) took advantage of the Graphite Crystal X-ray polarimeter (2.6 – 5.2 keV, field of view 3°) on-board of the 8th Orbiting Solar Observatory (OSO-8), launched on 1975, to repeat the measurement of the Crab Nebula. Thanks to larger statistics, they were able to remove the pulsar contribution and put upper limits on Cygnus X-1 (Cyg X-1), Hercules X-1 (Her X-1) and Centaurus X-3 (Cen X-3) polarization levels (Weisskopf et al. 1978a).

Since then, the enthusiasm for X-ray polarization measurement decreased, partly because of the lack of new flying polarimeter.

The gas pixel technology is now mature enough to be put on-board of a satellite mission. Over the last decade, few proposals were made to install the GPD on either large observatories or polarimetry-dedicated missions. To introduce our next subsection, I would like to briefly mention three, so far unsuccessful missions that were proposed to carry X-ray polarimeters..

• **IXO**. The International X-ray Observatory *IXO* was a large X-ray observatory proposed by the combined efforts from the National Aeronautics and Space Administration (NASA), the European Space Agency (ESA) and the Japanese Aerospace Exploration Agency (JAXA). This L-class mission was developed for the 2010 Astrophysics Decadal Survey, "New Worlds, New Horizons" (Council 2010) and included, among a few other instruments, an X-ray polarimeter called XPOL (Bellazzini & Muleri 2010; Barcons et al. 2011; Petre et al. 2012). Working in the 2 – 10 keV band, the GPD-based XPOL was set to match the *IXO* mirror point spread function, and would have been able to detect very weak amounts of polarization even for faint source.

[2] Ne-DME or Ar-DME mixtures at high pressure to perform imaging polarimetry up to about 35 keV (Muleri et al. 2006; Soffitta et al. 2010; Fabiani et al. 2012).

[3] An Aerobee 350 rocket, fueled by gas and a nitric acid/aniline sustainer, had a payload of 227 kg. Its total mass was 3 839 kg for a core diameter of 0.56 m and a total length of 15.90 m. The flight altitude the rocket could reach was about 450 km, in the middle of the thermosphere.

• **NHXM**. When ESA released a call for medium-sized missions in July 2010, the New Hard X-ray Mission *NHXM* was proposed to simultaneously bring together high-sensitivity, hard-X-ray imaging, broadband spectroscopy and polarimetry (Tagliaferri & the NHXM Consortium 2012). One of the four telescopes on board of *NHXM* would have been coupled with two GPD instruments: a low energy polarimeter (LEP) and a medium energy polarimeter (MEP) to cover the 2 – 35 keV band.

• **XIPE**. *XIPE*, the X-ray Imaging Polarimetry Explorer (Soffitta et al. 2013), was proposed in June 2012 to an ESA call for small missions. The *XIPE* payload would have comprised an *Efficient X-ray Photoelectric Polarimeter (EXP)* dedicated to the observation of astrophysical sources in the 2–10 keV energy range. It was loaded with two Gas Pixel Detectors placed in the focal plane of two JET-X optics (Citterio et al. 1996), dedicated to distant targets. Two additional GPD would have faced the Sun to detect polarization from solar flares.

9.3.3 Observational prospects for MCG-6-30-15 and NGC 1365

The modeling results shown in Fig. 9.3 and Fig. 9.5 prove that X-ray polarimetry can help us to unravel the mystery of the apparent broadening of the iron Kα line in MCG-6-30-15 and NGC 1365 using two independent indicators: the relativistic scenario is expected to produce a polarization percentage at least ten times higher than for the absorption case, with a maximum P to be detected in the Compton hump regime. Additionally, the variation of the polarization angle is found to be distinctly different for the two scenarios: smooth and continuous variations of Ψ in the 5–9 keV band are expected from the reflection case, while the absorption by circumnuclear matter may produce either zero variation (MCG-6-30-15) or an abrupt, orthogonal rotation of Ψ around 15 keV between the soft and the hard X-ray bands (NGC 1365).

It is now interesting to test if the proposed X-ray missions presented in Sec. 9.3.2 would have been able to help discriminating between the two broadening mechanisms.

To do so, we compute the MDP at 99 % confidence level for *XIPE*, *NHXM* and *IXO* during a 1 Ms observation and taking into account that the background flux is negligible with respect to the source flux. The 2 – 10 keV fluxes are estimated at 2.70 ± 0.15 mCrab for MCG-6-30-15 (Krivonos et al. 2007) and ~ 1.0 mCrab for NGC 1365 (Brenneman et al. 2013). We find that the reflection scenario is within the polarization detectability of *XIPE* (maroon line), so any detection would strongly support the relativistic model. Further indications could be deduced from the variation of the polarization position angle if the observed polarization signal is significant enough. The blue line, representing the MDP of *NHXM*, indicates that the polarization signal originating from the relativistic reflection case can be detected almost across the whole 2–35 kev band. It covers in particular the iron line domain, where the $\Delta\Psi$ signature of strong gravity would be detected. In the case that the absorption scenario would produce enough polarization to be observed by *NHXM*, the broadband coverage of the LEP and MEP may successfully discriminate between the two scenarios by the detection, or the absence of the Ψ switch between the soft and the hard X-ray regimes. Finally, we show that *IXO* would have been the only mission to potentially detect the low polarization originating from the absorption models. The distinction between the two competitive cases would have come from the detection of either a smooth variation of Ψ (relativistic signature) or no variation at all (transmission through absorbing gas).

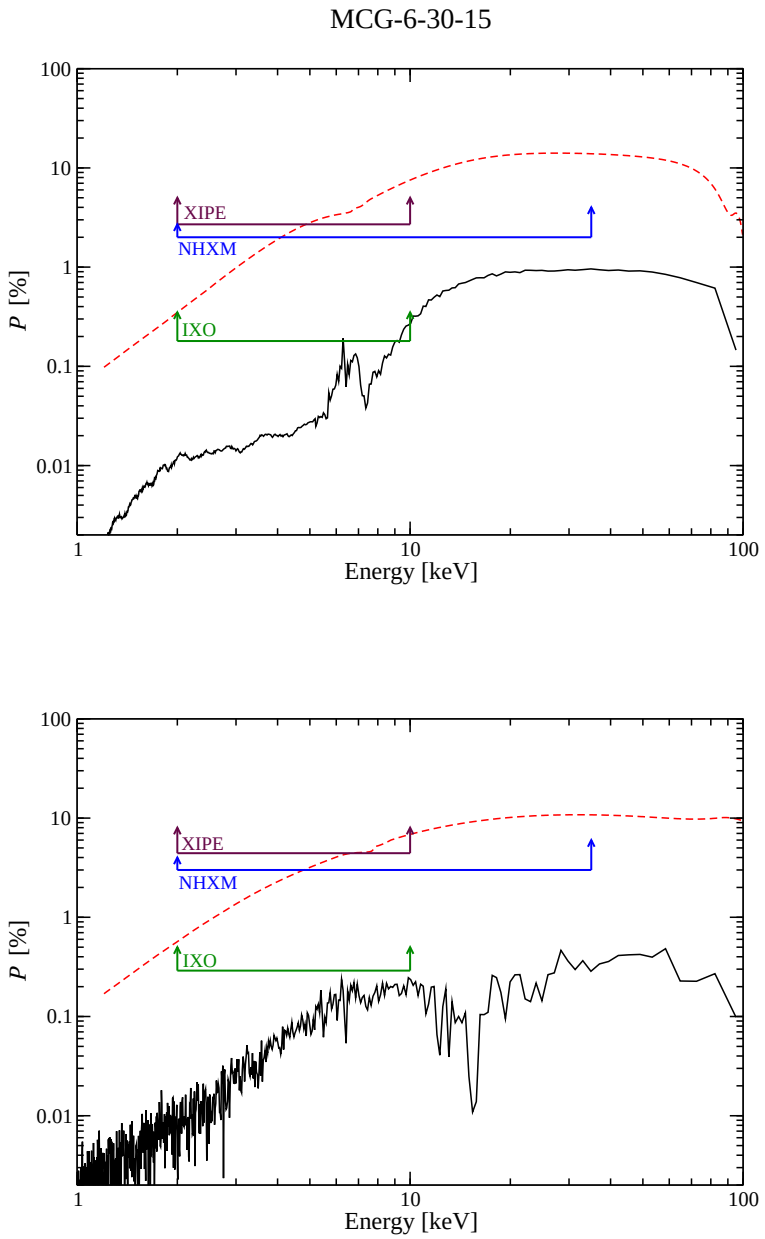

Figure 9.7: Minimum detectable polarization of the two scenarios for a 1 Ms observation of MCG-6-30-15 (top) and NGC 1365 (bottom). The observer's line-of-sight lies at 30° and 60°, respectively. The MDP for *XIPE* is represented by the maroon line, for *NHXM* in blue and for *IXO* in green. *Legend*: a fragmented absorption region (solid line) and a relativistic reflection model with an extreme Kerr SMBH with $a = 1$ (red dashed line).

9.4 Summary and discussion

In this chapter, we demonstrated that the interplay between optical/UV and X-ray bands can be helpful to constrain the AGN morphology, and we predicted that the polarization dichotomy

between type-1 and type-2 AGN should be conserved in the X-ray domain. To support the presence of a future X-ray polarimeter, we undertook and investigation of the spectropolarimetric signatures of two famous objects with an apparent broad iron line: MCG-6-30-15 and NGC 1365. By modeling the X-ray polarization spectra emerging from the two competing scenarios that are proposed to explain the broad Fe Kα line in those Seyfert galaxies, we demonstrate how X-ray polarimetry may independently discriminate between them. The shape of the polarization percentage and angle as a function of photon energy are found to be distinctly different between the reflection and the absorption cases. Relativistic reflection produces significantly stronger polarization in the 1–100 keV energy band than absorption. The spectrum of the polarization angle adds additional constraints: in the absorption case it shows either a constant shape (MCG-6-30-15) or an orthogonal switch (NGC 1365), whereas the relativistic reflection scenario typically leads to a smooth rotation of the polarization angle with photon energy. By comparing the predicted polarization of MCG-6-30-15 and NGC 1365 to the detectability levels of three different, proposed X-ray missions which included a polarimeter, we demonstrate that even a small mission (*XIPE*) can help to distinguish between the two scenarios. With a medium (*NHXM*) or a large (*IXO*) X-ray observatory equipped with a broadband polarimeter, the correct interpretation for the broad iron line would be unambiguous.

9.4.1 Refining the absorption and relativistic modeling

The exact geometry of the absorber situated along the observer's line-of-sight is unconstrained. To further support the results presented in this chapter, we must explore a range of different absorption scenarios and physical properties of the outflow. As stated by Miller & Turner (2013), the distribution of gas clouds around the central region of NGC 1365 must not be taken as an actual model. It may vary, both in its covering factor or column density. Lowering the covering factor results in a decrement of the net polarization as dilution from the unscattered input spectrum is enhanced. A different density parametrisation also affects the polarization degree. Optically thinner reprocessing clouds reduce the probabilities of scattering, thus decreasing P, while increasing the gas density slightly increases the polarized flux until the circumnuclear matter becomes optically too thick for the radiation to escape. Since absorption-dominated models are based upon continuum transmission through gas, the overall polarization degree is expected to be weaker than for (perpendicular) scattering off an accretion disk.

We have also started to investigate the polarization expected from a wind geometry such as the one suggested by Elvis (2000), see Chap 8. Similar wind geometries were investigated by Sim et al. (2008, 2010) and Schurch et al. (2009) from hydrodynamic simulations. For a distant observer looking at the far-end of the wind, the system is seen in absorption. Preliminary tests show that such wind models produce polarization that is slightly different from the one obtained for the conical outflows described in Sect. 9.2.1.2 but the results remain within the margins of our conclusions. Note that a partially ionized absorber may produce a stronger reprocessing component than a neutral wind. However, since forward-scattering predominates, the net polarization is again expected to be low but it may depend on the viewing angle, the geometry of the medium or its ionization structure.

It is also necessary to look into more realisations of the relativistic reflection scenario. In Sect. 9.2.1.1, we argue why changes in the irradiation geometry, the ionization of the accretion disk or the polarization of the primary radiation with respect to the current model should lead to stronger polarization. We still need to verify this assumption by adopting the radial ionization profile used in Svoboda et al. (2012), local reprocessing computations for ionized media and intrinsically polarized X-ray emission.

9.4.2 Polarization measurement across the iron line

The polarization position angle across the iron line turns out to be a particularly strong indicator for the correct scenario – if it can be constrained with a sufficiently powerful X-ray polarimetry mission and/or long enough observations. The bottom panel of Fig. 9.7 shows that in the case of relativistic reflection $\Delta\Psi$ follows a characteristic "S-shape" between 2 and 9 keV, whereas in the absorption scenario the distribution of $\Delta\Psi$ is either constant or only bipolar. The detection of a few degrees swing could be within the reach of a large mission, for which the MDP is significantly lower than the expected degree of polarization. The fact that in the absorption case only "parallel" or "perpendicular" polarization are allowed is related to the axis-symmetry of the cloud distribution (in the case of NGC 1365). The switch exists due to a change in the scattering albedo between the soft and the hard X-ray spectrum. Goosmann & Matt (2011) showed that a more gradual rotation of $\Delta\Psi$ can be obtained in a non-relativistic scenario once the distribution of scattering clouds is no longer symmetric. However, in this case the rotation can only evolve monotonically with photon energy between two limiting values determined by the net soft and hard X-ray polarization state. Such a scenario could not reproduce the S-shape variation of $\Delta\Psi$ seen in the relativistic model.

The results presented in this chapter have been published in Marin & Goosmann (2011), Marin et al. (2012b), Soffitta et al. (2013), Marin et al. (2013) and Marin & Tamborra (2013).

Chapter 10

Conclusions and perspectives

This manuscript investigates a wide range of AGN morphologies using spectropolarimetric modeling as a diagnostic tool. From the optical to the X-ray domain, we mostly focused on the continuum polarization emerging from a large set of reprocessing regions, while exploring the broadening mechanisms of the Fe Kα line in the last sections of this thesis. Monte Carlo simulations and complex radiative transfer are the pounding heart of our analyses, polarization being the blood of the manuscript.

10.1 Brief overview of the results

Understanding the complex radiative coupling between the inner regions of AGN remains a major challenge, as several effects of emission, absorption and reprocessing tend to complicate the observational picture. To disentangle this complexity, we ran series of AGN polarization models consisting of two, three and four components. Comparing our grid of modeling results to observational data, we presented new constraints on the size, opacity and morphology of real AGN (Chap 4). Applying our simulation to a concrete case, we confirmed the asymmetrical morphology of NGC 1068 and refined the observational constraints, implying a complex three-dimensional geometry leaning out of the plane-of-the-sky (Chap 5). As past observations of NGC 1068 were given for linear and circular polarization, we also demonstrated that multiple Mie scattering inside a torus funnel is not efficient enough scattering mechanism to explain the presence of circular polarization with a polarization degree of 0.1 %. Either the input spectrum has to be intrinsically linearly polarized (with the U-parameter of the Stokes vector > 0) or dichroic extinction must be favored; the latter option being the more realistic (Chap 6). Discussed all along the manuscript, we started to investigate the impact of fragmentation onto polarization modeling. It was shown that clumpy media tend to reduce the net polarization percentage but also alter the polarization position angle at edge-on inclinations. In this picture, the circumnuclear matter obscuring the equatorial plane is found to produce parallel polarization, an unexpected behavior that positively impacts the analysis of the observed AGN polarization dichotomy. The need for an equatorial scattering disk becomes less substantial. Finally, fragmented models give polarization percentages closer to the observations than continuous media (Chap 7). However, clumpy absorption is not the only way to produce obscuration along the quasar's equator and disk-born winds were also investigated. We explored the presence of WHIM outflows and concluded that the empirically-derived, wind structures challenge the usual AGN models. By tuning the wind's bending angle, the opening angle of the flow and the dust opacity along the equator, we successfully matched the observations (Chap 8). Finally, we proved that with current observational technology, X-ray polarization of bright type-1 AGN could help us to discriminate between the two competing scenarios that are proposed to explain the broad Fe Kα line in Seyfert 1 galaxies (Chap 9).

10.2 Towards more sophisticated models

While new constraints and numerous observational predictions have been found in this manuscript, the continuum polarization of uniform AGN models only represents one piece of the puzzle. In order to properly investigate the mechanisms ruling the complex radiative coupling in the core of quasars, several other physical aspects have to be taken into account.

Preliminary tests using distributions of constant-density spheres, with opacity and filling factors as external parameters, were presented in this report. The computation of a substantial grid of models is necessary to explore the impact of the size, density and composition of the clumps on the emerging spectral intensity and polarization as a function of the viewing direction. The coherent radiative coupling emerging from complex models is intended to be investigated in terms of linear polarization and compared to AGN observations from the literature (NGC 1068, the Circinus galaxy and Mrk 3 being the prime candidates). However, the computation of large model grids and extensive modeling studies of individual objects require a fast computational method that will soon be investigated using GPU coding (see Sect. 3.3.5).

Velocity fields have no impact on continuum polarization, but when taking into account emission and absorption processes, line shift and broadening are expected to appear in the polarization spectra. This could be used as a probe of the ionization stage, direction of motion and morphology of the reprocessing media. In this regard, the structure for quasars investigated in Chap. 8 would be a perfect, test field. Using our set of parameters, it would be interesting to reproduce the polarization degree of broad absorption lines seen through the outflowing WHIM. The theoretical presence of clouds of denser, colder media into the WHIM and responsible for the broad emission lines might be verified as well. We could then check the validity of our new parameter set against observational tests for the number distribution of BAL, NAL, and non-NAL quasars.

Absorption leading to heating and thermal re-emission of lower energy photons is also foretold to happen in the infrared band. So far, the dust models of STOKES include extinction effects but no thermal re-emission after absorption of the UV/optical continuum. More sophisticated dust types and dust emission in thermal or non-thermal equilibrium will be included in the code. Adding thermal (re)emission processes emerging from complex dust distributions in STOKES would enable very robust and consistent polarization/thermal emission models to be developed for many AGN from the UV to the IR bands. We will thereby put additional constraints on the dust composition and on the covering and filling factors in the clumpy reprocessing regions. Via the same method, it also becomes possible to study the wider vicinity of an AGN. The impact of stellar clusters or star burst regions on the spectrum and polarization could be evaluated and help to improve spectroscopic methods distinguishing between AGN and stellar emission in the optical/UV. This allows to verify past and future spectropolarimetry observations, in which the subtraction of the stellar component turns out to be ambivalent.

Complementary to spectral and polarization analyzes, it is noteworthy to point out that STOKES also computes the flight time of each registered photon and stores it separately in timing-dedicated files. Spectral variability can be used to probe the energy generation and inner structure of AGN. In the high energy domain, X-ray variability is of a peculiar interest to understand if AGN are scaled up versions of Galactic Black Hole (GBH) systems. Coupled to emission in other bands (particularly in the optical), X-ray emission can help us to understand how variability arises and what is the structure of the reprocessing media. We are going to explore the timing capacities in the context of polarization reverberation mapping (Gaskell et al. 2012) and time lags in X-ray reprocessing (Miyamoto & Kitamoto 1989).

To enlarge our vision of AGN, multi-wavelength observational campaigns and simulations taking into account cloud motions and emission/absorption lines are the next steps to be taken.

10.3 Scaling down to X-ray binaries

The results presented in this manuscript are applied to AGN but the method and the code are suitable for the exploration of a wide range of astrophysical sources. X-ray binaries (XRB) are the prime candidates as they are, at least, ten times brighter than AGN.

In XRB, the thermal emission produced by a black hole with ~ 10 $M_{\odot}$ peaks in the soft X-ray band (i.e. a few keV). To produce the hard X-ray spectrum observed in both cases, an optically thin, hot corona of thermally distributed electrons is believed to Comptonize (i.e. via the inverse Compton effect) soft photons to higher energies (Haardt & Maraschi 1991, 1993). The higher energetic component of the X-ray radiation that shines back onto the disk is reflected while the less energetic part ($<<$ 10 keV) is absorbed and partly reprocessed in emission lines. Exploring the accretion disk's physics in X-ray binaries could then help us to understand the mechanism responsible for the line skewing in AGN. The *ASCA/SIS* observation of the Seyfert 1 galaxy MCG-6-30-15 early confirmed the presence of a broad, distorted iron line. With the launch of *XMM-Newton* and later *Suzaku*, the detection of skewed Fe Kα lines then extended to stellar-mass black holes in binary systems (Miller et al. 2004) and neutron star XRB (Bhattacharyya & Strohmayer 2007), although Done & Diaz Trigo (2010) and Ng et al. (2010) challenged this view pointing out potential problems due to instrumental effects and/or uncertainties in the spectroscopic analysis.

The distorted Fe Kα emission line at 6.4 keV is thus a feature shared by stellar and supermassive black hole powered objects despite their difference in mass. It seems reasonable to assume that the red-wing extension is due to the same broadening mechanisms: Doppler and general relativity effects. However, taking into account the interaction between radiation and the hot coronal plasma above the accretion disk, or cold, distant obscuring material along the observer's line-of-sight, some thought about a different explanation in which the apparent red-wing is actually ascribed to the continuum emission and the line is not really broad. Relativistic scenarios usually point into the direction of rapidly spinning black holes, while complex absorption in in AGN systematically lowers the estimated black hole spin as the line is much less related to ISCO radius. In the case of low-mass XRB (LMXRB), Comptonization by the corona can cause overestimations of the equivalent width of the line and thus also lower the black hole spin estimation.

Similarly to the investigations presented in Chap. 9, we could explore the polarization signatures of XRB in order to draw predictions for future X-ray missions and discriminate between different scenarios. This is particularly interesting as XRB are luminous objects, and thus more easily detectable. Accreting stellar mass black holes are a key motivation for astrophysical X-ray polarimetry because the measured X-ray polarization can put important constraints on the angular momentum of the black hole and reveal specific properties of the accreted matter (Dovčiak et al. 2004; Schnittman & Krolik 2010b, 2013). New constraints on the thermal disk state, the morphology and optical thickness of the hot corona, as well as on the relativistic effects in both stellar-mass and supermassive black holes are in reach for several X-ray bright objects (e.g. Cyg X-1, GX 339-4, LMC X-1, LMC X-3, GRS 1915+105, 4U 1957+11).

Appendix A

Acronyms

- 3C: Third Cambridge Catalog
- AAT: Anglo-Australian Telescope
- AD: Accretion disk
- ADAF: Advection-Dominated Accretion Flow
- AGN: Active Galactic Nuclei
- BAL: Broad Absorption Line
- BEL: Broad Emission Line
- BER: Broad Emission Region
- BL Lac: BL Lacertae object
- BLR: Broad Line Region
- BLRG: Broad Line Radio Galaxy (similar to Seyfert 1 but radio loud)
- Cfa: (Harvard Smithsonian) Center for Astrophysics
- CPU: Central Processing Unit
- CXC: Chandra X-Ray Center
- ENLR: Extended Narrow Line Region (mixing with the host galaxy dust)
- ESA: European Space Agency
- ESO: European Southern Observatory
- EXP: Efficient X-ray Photoelectric Polarimeter
- FR (I or II): Fanaroff - Riley radio galaxy of type I or II
- FWHM: Full width at half maximum
- GBH: Galactic Black Hole
- GEM: Gas Electron Multiplier
- GPD: Gas Pixel Detector
- GPU: Graphic Processing Unit
- GRB: Gamma Ray Burst
- GSM: General Scattering Model (Young 2000)
- HETG: High Energy Transmission Grating (on-board of Chandra)
- HST: Hubble Space Telescope
- IGM: Intergalactic medium
- INAF-IAPS: Istituto Nazionale di Astrofisica / Istituto di Astrofisica e Planetologia Spaziali
- INFN: Istituto Nazionale di Fisica Nucleare
- IR: Infrared
- ISCO: Innermost Stable Circular Orbit
- ISM: Interstellar Medium
- IXO: International X-ray Observatory

- JAXA: The Japanese Aerospace Exploration Agency
- LBG: Lyman Break Galaxy
- LINER: Low Ionization Nuclear Emission line Region
- LMXRB: Low-Mass X-Ray Binary
- LOFAR: Low Frequency Array
- LTE: Local Thermodynamical Equilibrium
- MCG: Morphological Catalog of Galaxies (a Russian galaxy survey)
- MDAF: Magnetically-Dominated Accretion Flow
- MHD: Magneto-hydrodynamic
- MIDI: MID infrared Interferometric instrument (mounted on the VLT)
- MRI: Magneto Rotational Instability
- NAL: Narrow Absorption Line
- NASA: National Aeronautics and Space Administration
- NGC: New General Catalog (an amateur galaxy survey)
- NHBLR: Non-hidden BLR
- NHXM: The New Hard X-ray Mission
- NLR: Narrow Line Region
- NLRG: Narrow Line Radio Galaxy; similar to Seyfert 2 but radio loud
- NLS1: Narrow Line Seyfert 1 AGN
- NRAO: National Radio Astronomy Observatory
- NSF: National Science Foundation (United States of America)
- OSO-8: The 8th Orbiting Solar Observatory
- OVV: Optically Violently Variable
- PAH: Polycyclic Aromatic Hydrocarbon
- QSO: Quasi Stellar Object
- Quasar: Quasi stellar
- RNG: Random Number Generator
- RHESSI: Ramaty High Energy Solar Spectroscopic Imager
- S/N: Signal-to-noise ratio
- SED: Spectral Energy Distribution
- SKA: Square Kilometer Array
- SMBH: Super Massive Black Hole
- SN: Supernova
- SNR: Supernova Remnant
- STIS: Space Telescope Imaging Spectrograph (on-board of the HST)
- STScI: The Space Telescope Science Institute
- UFO: Ultra Fast Outflow
- ULX: Ultra Luminous X-ray sources
- UV: Ultra-Violet
- VLA: Very Large Array (United States of America)
- VLT: Very Large Telescope (Chili)
- VLTI: Very Large Telescope Interferometer (Chili)
- WA: Warm Absorber
- WHIM: Warm, Highly Ionized Matter
- XIPE: X-ray Imaging Polarimetry Explorer
- XPOL: X-ray polarimeter (on-board of IXO)
- XRB: X-Ray Binary

Appendix B

Polarization induced by magnetic fields

The following polarization mechanisms are not included in the main manuscript as they only concern magnetized sources that were not taken into account in this thesis. The intensity and localization of magnetic fields in AGN remain unknown, especially on sub-parsec scales. Thus, they will only be briefly described in order to complete the wide picture of the physical processes influencing polarization signals from AGN.

B.1 Synchrotron radiation

The synchrotron effect creates electromagnetic emission resulting from the relativistic motion of a charged particle in a magnetic field. The cyclotron pulsation qB/m, characterizing non-relativistic speeds, is then modified:

$$\omega_S = \frac{qB}{\gamma m_e} \tag{B.1}$$

with $\gamma = 1/\sqrt{1 - v^2/c^2}$ being the Lorentz factor, B the magnetic field, c the speed of light, q the electron charge and m_e the electron mass. In the relativistic case, the synchrotron emission is beamed along a solid angle $\theta \approx m_e c^2/E$, with E the total energy of the electron.

The calculation of the polarization of synchrotron radiation can be achieved looking at its perpendicular and parallel component:

$$P_\perp(\omega) = \frac{\sqrt{3} q^3 B \sin(\alpha)}{4\pi m c^2} \left[F(\frac{\omega}{\omega_c}) + G(\frac{\omega}{\omega_c}) \right] \tag{B.2}$$

$$P_\parallel(\omega) = \frac{\sqrt{3} q^3 B \sin(\alpha)}{4\pi m c^2} \left[F(\frac{\omega}{\omega_c}) - G(\frac{\omega}{\omega_c}) \right] \tag{B.3}$$

where

$$F(x) = \frac{\omega}{\omega_c} \int_{\frac{\omega}{\omega_c}}^{\infty} d\epsilon K_{5/3}(\epsilon) \tag{B.4}$$

$$G(x) = \frac{\omega}{\omega_c} K_{2/3}(\frac{\omega}{\omega_c}) \tag{B.5}$$

$$\omega_c = \frac{3}{2} \gamma^3 \omega_S \sin(\alpha) \tag{B.6}$$

with α the *pitch angle* and $K_{2/3}$, $K_{5/3}$ two modified Bessel functions of the second kind.

Synchrotron radiation is intrinsically highly polarized, with linear polarization degrees as high as 75 % and an emission polarized parallelly to the projected plane-of-the-sky (perpendicular to the line-of-sight), the "tell-tale" signature of synchrotron emission (Zweibel & Heiles 1997; Crutcher et al. 2003). Synchrotron radiation can be found in many astrophysical sources such as supernovae remnants (SNR, Claussen et al. 1997), radio-galaxies (Saikia & Salter 1988) and quasars (Angel & Stockman 1980).

B.2 Faraday rotation

When passing through a magnetized plasma, an electromagnetic wave will see its polarization plane rotated by an effect called Faraday rotation. The rotation angle β can be expressed in terms of:

$$\beta = \alpha\lambda \tag{B.7}$$

with λ being the photon wavelength and:

$$\alpha = \frac{q^3}{2\pi m_e^2 c^4} \int_0^d n_e B \, \mathrm{d}s \tag{B.8}$$

the Faraday rotation measure, where the electron density n_e multiplied by the projected magnetic field is integrated along the observer's line-of-sight d.

Faraday rotation is a widely used tool in astronomy for the measurement of magnetic fields, which can be estimated from rotation measurements at a given electron number density (Longair 1992). In particular, Faraday rotation measurements of polarized radio signals from extragalactic sources occulted by the solar corona can be used to estimate both the electron density distribution and direction, as well as the strength of the magnetic field in the coronal plasma (Mancuso & Spangler 2000). In the case of AGN, magnetic field studies of the parsec-scale jets can be achieved using the impact of Faraday rotation on the transverse polarization and total intensity (Gabuzda & Chernetskii 2003).

B.3 Zeeman effect

When an atom is surrounded by a magnetic field, each of its emitted lines will be split in a variable amount of equidistant lines, separated by an interval proportional to the magnetic field strength: this is the Zeeman effect (Zeeman 1897c,b,a). In order to correctly explore the Zeeman effect, it is relevant to introduce the spin concept and to take into account the hyperfine structure of the energy levels of the atom; a quantum treatment is thus indispensable.

The Zeeman degeneracy of a multiplet M with a total kinetic momentum $\vec{J}$ ($\vec{J} = \vec{L} + \vec{S}$) consists of (2$J$+1) equidistant sub-energetic levels such as -J $<$ M $<$ J. The difference in energy in comparison with the usual, non-magnetized energy level is given by:

$$\Delta E(M) = g_J M \hbar \omega_L \tag{B.9}$$

where g_J is the multiplet Landé factor:

$$g_J = \frac{3}{2} + \frac{S(S+1) - L(L+1)}{2J(J+1)} \tag{B.10}$$

and ω_L is the Larmor pulsation:

$$\omega_L = \frac{qB}{2m_e} \tag{B.11}$$

It is possible to show from the previous equations that the emitted radiation resulting from the transitions between two multiplet terms, according to the selection criteria derived from quantum mechanics, is polarized (Condon & Shortley 1963; Elitzur 1996). The nature of the polarization depends on the ΔM transition as well as on the orientation of the magnetic field relative to the observer line-of-sight. When $\Delta M = 0$, the emitted photon is linearly polarized but also diluted in the emission line, since it was not frequency-shifted. If $\Delta M = \pm 1$, a frequency change is associated with the radiation, giving rise to Zeeman equidistant features. The emitted radiation is linearly polarized for a line-of-sight perpendicular to B and circularly polarized along the magnetic field direction.

The Zeeman effect is the most frequently used process in astrophysics to characterize magnetized objects (Troland & Heiles 1982), from stars (Brown et al. 1991) to extragalactic sources (Robishaw 2008).

B.4 Hanle effect

In non-magnetic regimes, some spectral lines might be linearly polarized by an anisotropic irradiation exciting the emitting atoms and molecules and causing resonnant scattering (see Sect. 3.2.7). But, in the case of a magnetized environment, a depolarization effect appears, coupled to a rotation of the polarization plane; a mechanism known as the Hanle effect[1] (Hanle 1924, 1926). Any relevant study of the Hanle effect must undergo a quantum approach, mandatory to describe the non-equilibrium between the sub-levels population of the Zeeman energy levels, responsible for the polarization of the radiation (Alnis et al. 2003).

The Hanle effect is very subtle and not yet largely know to the community of polarization-enthusiast astronomers. It is rather different from the Zeeman effect, as its polarization is not intrinsic to emission but induced by the magnetic environment. The Hanle effect associated with the Sun and its atmosphere was studied by Leroy et al. (1977), Sahal-Brechot et al. (1977) and Bommier & Sahal-Brechot (1982) but remains poorly used for the analyzes of extra-solar bodies.

[1] Again, Wilhelm Hanle was not the first to discover the lately known *Hanle effect*. The magnetic-field-dependence of the polarization of light resonantly scattered from a sample of atoms was previously investigated by Wood (1922) and Wood & Ellett (1923, 1924). Hanle's real credit comes for his classical explanation of the effect.

Appendix C

Personal publication

Refereed :

- Probing the origin of the iron Kα line around stellar and supermassive black holes using X-ray polarimetry, Marin, F.; and Tamborra, F.; accepted for publication in ASR

- Off-axis irradiation and the polarization of broad emission lines in active galactic nuclei, Goosmann, R. W.; Gaskell, C. M.; and Marin, F.; submitted to ASR

- A structure for quasars under the scope of polarization - I. The UV/optical polarization dichotomy of type-1 and type-2 AGN, Marin, F.; and Goosmann, R. W.; 2013, MNRAS, 436, 2522

- Modelling the X-ray polarimetric signatures of complex geometry: the case study of the "changing look" active galactic nucleus NGC 1365, Marin, F.; Porquet, D.; Goosmann, R. W.; Dovciak, M.; Muleri, F.; Grosso, N.; and Karas, V.; 2013, MNRAS, 436, 1615

- XIPE: the X-ray Imaging Polarimetry Explorer, Soffitta, P.; 40+ collaborators including Marin, F.; 2013, Experimental Astronomy, 32

- Modeling optical and UV polarization of AGNs II : Polarization imaging and complex reprocessing, Marin, F.; Goosmann, R. W.; Gaskell, C. M.; Porquet, D.; and Dovciak, M.; 2012, A&A, 548, A121

- X-ray polarimetry as a new tool to discriminate reflection from absorption scenarios – Predictions for MCG-6-30-15, Marin, F.; Goosmann, R. W.; Dovciak, M.; Muleri, F.; Porquet, D.; Grosso, N.; Karas, V.; and Matt, G.; 2012, MNRAS, 426, L101

Proceedings :

• Dust in the wind II: Polarization imaging from disk-born outflows, Marin, F.; and Goosmann, R. W.; SF2A-2013: Proceedings of the Annual meeting of the French Society of Astronomy and Astrophysics, Eds.: L. Cambresy, F. Martins, E. Nuss, & A. Palacios, pp.475-478

• Dust in the wind I: Spectropolarimetric signatures from disk-born outflows, Marin, F.; and Goosmann, R. W.; SF2A-2013: Proceedings of the Annual meeting of the French Society of Astronomy and Astrophysics, Eds.: L. Cambresy, F. Martins, E. Nuss, & A. Palacios, pp.479-482

• UV and optical polarization modeling of thermal active galactic nuclei : impact of the narrow line region, Marin, F.; and Goosmann, R. W.; SF2A-2012: Proceedings of the Annual meeting of the French Society of Astronomy and Astrophysics, Eds.: S. Boissier, P. de Laverny, N. Nardetto, R. Samadi, D. Valls-Gabaud and H. Wozniak, pp.587-590

• Modeling the optical/UV polarization while flying around the tilted outflows of NGC 1068, Marin, F.; Goosmann, R.W.; and Dovciak, M.; Journal of Physics: Conference Series, Volume 372, Issue 1, pp. 012065 (2012)

• Modeling the polarization of radio-quiet AGN: from the optical to the X-ray band, Marin, F.; and Goosmann, R. W.; SF2A-2011: Proceedings of the Annual meeting of the French Society of Astronomy and Astrophysics Eds.: G. Alecian, K. Belkacem, R. Samadi and D. Valls-Gabaud, pp.597-600

Appendix D

(accepted) Observing Time proposals

This appendix presents the two observing time proposals that were accepted by the European Southern Observatory (ESO) in order to test the hypothesis that the remarkably strong velocity dependence of broad emission line variability seen in many AGN is due to strong off-axis flaring in the accretion disk. It is thought to cause the oberved, extremely asymmetric Balmer lines with the broad peak redshifted or blueshifted by thousands of $km \cdot s^{-1}$ (Gaskell 2010, 2011).

Because of the difficulty in explaining these extreme objects, exotic models have been proposed such as close supermassive black hole binaries or a gravitational recoil of a black hole after a merger (Popović et al. 2011). An new, alternative explanation is that the variability is caused by temporary off-axis irradiation. It is important to test the off-axis flare model for a number of reasons. If the model is correct, black hole masses can be determined reliably from the BLR, but in the case of off-axis illumination, the azimuthal phase of the continuum source must be taken into account to properly evaluate the SMBH mass. On the other hand, if the model is not correct, there is much more uncertainty and other explanations of the anomalous observations are needed. This affects, for example, our estimates of the fraction of close supermassive black hole binaries. If the off-axis flaring model is correct, this represents a major paradigm change for energy generation in AGN.

The observations have been taken and are actually tested with a new version of STOKES. It represents a new project that started at the end of the thesis, thus not developed through the main chapters.

Part of the results obtained by these observations have been published in Goosmann et al. (2013).

EUROPEAN SOUTHERN OBSERVATORY

Organisation Européenne pour des Recherches Astronomiques dans l'Hémisphère Austral
Europäische Organisation für astronomische Forschung in der südlichen Hemisphäre

OBSERVING PROGRAMMES OFFICE • Karl-Schwarzschild-Straße 2 • D-85748 Garching bei München • e-mail: opo@eso.org • Tel.: +49-89-32 00 64 73

APPLICATION FOR OBSERVING TIME PERIOD: **89A**

Important Notice:

By submitting this proposal, the PI takes full responsibility for the content of the proposal, in particular with regard to the names of CoIs and the agreement to act according to the ESO policy and regulations, should observing time be granted

1. Title Category: **B–7**

Spectropolarimetry of extreme AGN line profiles: binary black holes, recoiling black holes, or off-axis variability?

2. Abstract / Total Time Requested

Total Amount of Time:

AGNs showing extremely asymmetric Balmer lines with the broad peak redshifted or blueshifted by thousands of km/s provide what is perhaps the most severe challenge to our standard paradigm of an AGN being a single black hole surrounded by an axisymmetric accretion disc, broad-line region, and torus. Because of the difficulty in explaining these extreme objects, exotic models have been proposed such as close supermassive black hole binaries or a gravitational recoil of a black hole after a merger. An new alternative explanation is to have the variability of AGNs be off axis. This model makes very specific predictions about the velocity dependence of the polarization of the broad Balmer lines in AGNs showing extreme displaced peaks. We are proposing to carry out spectropolarimetry of a sample of bright AGNs with the most extreme Balmer line profiles to test these predictions and distinguish between the different explanations offered for these objects.

3.

Run	Period	Instrument	Time	Month	Moon	Seeing	Sky	Mode	Type
A	89	FORS2	7.3h	may	g	0.8	CLR	s	

4. Number of nights/hours Telescope(s) Amount of time

a) already awarded to this project:

b) still required to complete this project:

5. Special remarks:

6. Principal Investigator: mgaskell

6a. Co-investigators:

R.R.J.	Antonucci	1943
R.W.	Goosmann	1582
F.	Marin	1582
V.	Motta	1842

7. Is this proposal linked to a PhD thesis preparation? State role of PhD student in this project

8. Description of the proposed programme

A – Scientific Rationale: Because the energy radiated from black-hole accretion over the history of the universe exceeds that from stars, and because the binding energy of a supermassive black hole (SMBH) exceeds that of its host galaxy by orders of magnitude, AGNs have had a profound effect on the evolution of galaxies and the universe. AGNs provide the most widely-used method of measuring black hole masses across cosmic time. In studying all these things it is important that we have a correct model of AGNs. Our current standard model for AGNs is that each AGN contains a SMBH surrounded by a flatted, axially-symmetric distribution of accreting dust and gas. The continuum emission is dominated by a thermal continuum arising from an accretion flow (see Gaskell 2008) and line emission is dominated by emission from the broad-line region (BLR). The broad-line region (see Gaskell 2009 for a review) is a rotating, turbulent disc that is both optically and physically thick. When this distribution of gas is seen face-on we see "logarithmic" centrally-peaked line profiles; when it is seen somewhat inclined to the line of sight we see the characteristic double-humped "disk-like" profile (see Gaskell 2010).

A significant fraction of AGNs show broad-line profiles that cannot be explained by this axisymmetric BLR model. They show strong asymmetric displaced BLR peaks. Two examples are shown in the top half of the figure on the next page. Gaskell (2003) suggested that these AGNs could be explained with *two* SMBHs, each with its own associated BLR, and thus resembling a spectroscopic binary. Unfortunately, line profile variability showed that the displaced emission-line peaks were emission from a disc, and separate BLRs each with its own associated SMBH (Gaskell & Snedden 1999). In recent years, however, there has been much interest in detecting close SMBH binaries from the line emission and the Gaskell (1983) binary BLR suggesting has received renewed attention with the suggestion that some of the more extreme Balmer line asymmetries are due to binaries (e.g., Boroson & Lauer 2009). Another very interesting possibility is that some displaced broad-line peak objects are associated with black holes that are recoiling after merging (Komossa, Zhou, & Lu 2008).

The binary black hole model has considerable difficult explaining the observations (see Gaskell 2010a). Gaskell (2008) pointed out that continuum variability has to be *off-axis*. Gaskell (2010b) showed that this could readily explain profiles like those shown at the top of the Figure below and also solve a wide range of AGN mysteries. Polarization provides important insights into the structure of AGNs (Antonucci 2002). It was, in fact, polarization that led to the confirmation to our current standard unified model of AGNs (Antonucci 1993). Spectropolarimetry provides the strongest tests of the off-axis variability model (Gaskell 2010b) since departures from axisymmetry produce strong linear polarization. The model predicts that the polarization will be a minimum at the velocity of the offset peak and a maximum on the other side of the line (see bottom left figure on next page). Since the off-axis flare will probably not be along the line of nodes, the position angle of polarization will rotate across the line.

There is already limited evidence that the velocity dependence of polarization across the Balmer lines is similar to the Gaskell (2010b) model - see bottom right figure. In this proposal we are seeking to extend this, and in particular see if the polarization behaviour seen in the bottom left figure is indeed seen in displaced-BLR-peaks AGNs. It should be noted that this is a very strong and definite prediction. If the model is correct, this behaviour must be seen.

To investigate this we have chosen the seven brightest and most extreme displaced BLR peak AGNs readily accessible in the S. hemisphere (south of +15 degrees). In order to achieve the necessary signal-to-noise ratio in a single OB we have restricted ourselves to AGNs brighter than V = 17.5. We must stress that it is important for several reasons that we observe a sample of objects. Crudely the prediction of the off-axis model is that the minimum in polarization is on the same side are the offset peak and the polarization peak is on the opposite side. If it is just random (as might be expected in the binary black hole scenario), then we would get a positive result 50% of the time. Clearly to approach a 3σ result we need to observe some half dozen or more AGNs. A second reason for observing more than one object is that the polarization in a given object might not be high enough.[**POST SUBMISSION COMMENT: I wish I hadn't said that! It makes it sound like there is a chance of failure. In fact, no line polarization is a very interesting result since the model predicts that the line WILL be polarized. What I should have said is that ANY RESULTS IS INTERESTING.**] Another reason is that the position angle crossing over tells us information, but this only happens if the flaring region is not on the line of nodes.

B – Immediate Objective:

We will obtain spectropolarimetry of the Hβ to Hα regions of seven bright AGNs showing extremely asymmetric displaced broad Balmer line peaks.

From these we will extract total flux spectra, the wavelength dependencies of the position angles and percentages of polarization, and the related error estimates. The end products will be similar to the WHT spectra of Mrk 6 shown in the bottom right of the figure below. From the total flux spectra we will determine the radial velocities of the strong displaced peaks. From the position angle spectra we will measure the cross-over point where the position angle is changing most rapidly. From the percentage polarization spectrum we will determine at what radial velocity the polarization is a minimum and where it is a maximum. The model of Gaskell (2010) predicts that both the cross-over velocity for the position angle, and the velocity of minimum polarization should

Description of the proposed programme (continued)

coincide with the radial velocity of the displaced peak. We will be qualitatively testing these predictions for the seven AGNs using the data and Monte Carlo models developed by Co.I.'s Goosmann & Marin using the code *STOKES* (Goosmann & Gaskell 2007).

We expect the highest signal-to-noise ratio for Hα, but we will also look for similar effects in Hβ and even the He I and He II lines. Although our focus is on the spectropolarimetric behaviour of the Balmer lines, we will also be looking at the wavelength variation of the continuum polarization, the orientation of the **E** vector relative to the axis of radio emission (where measurable), and the relationship between the line and continuum polarization.

Attachments (Figures)

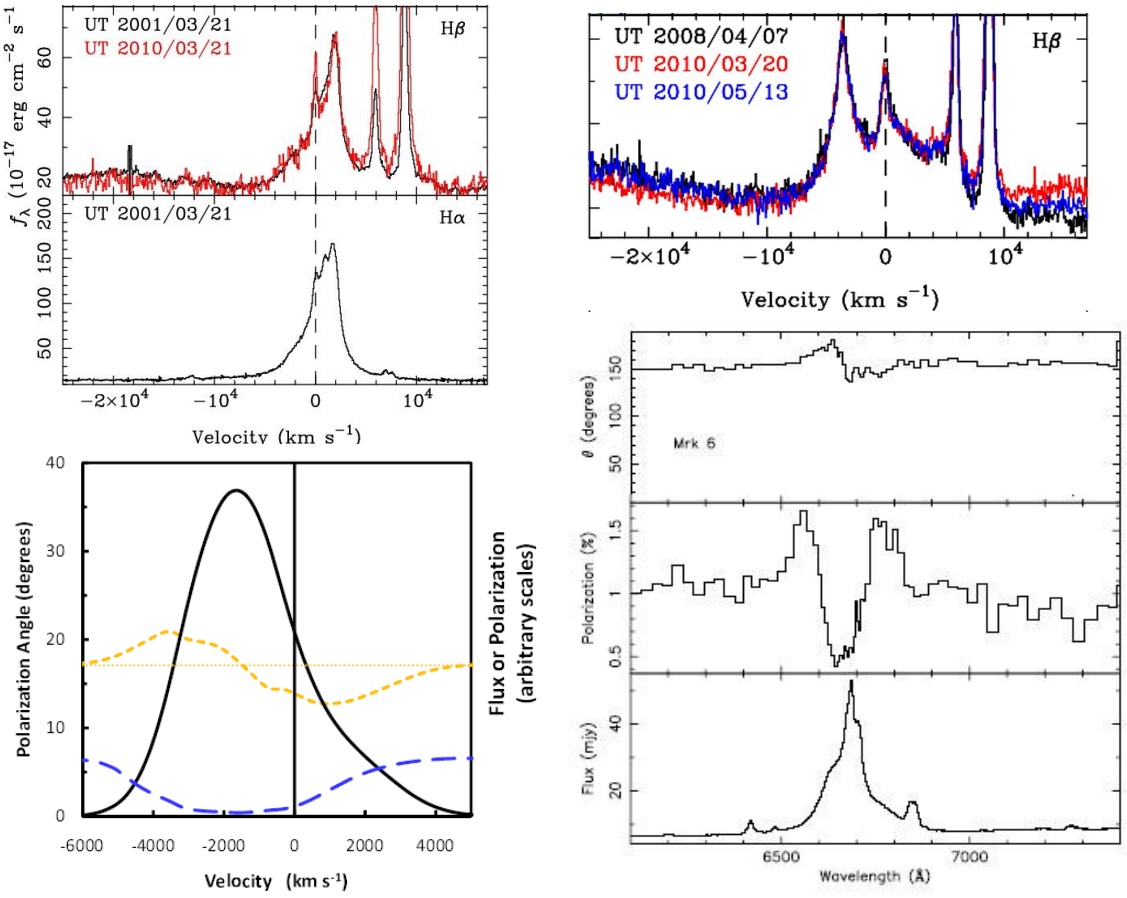

FIGURES.

Top row: SDSS and second-epoch spectra of SDSS J094603+013923 [left] and SDSS J153636+044127 [right] (From Boroson et al. 2011).

Bottom row: [Left] Illustrative predicted total flux (solid line), velocity dependence of percentage polarization (dashed line), and position angle (dotted line) for the off-axis variability model (from Gaskell 2010). [Right] A 1.3 hr observation of Mrk 6 (V = 15) with the William Herschel 4.2-m telescope (Smith et al. 2002). Note the qualitative agreement with the predictions on the left.

9. Justification of requested observing time and observing conditions

Lunar Phase Justification: We require grey time (less than 7 days from the New Moon) because ETC calculator shows we can reach S/N$\simeq$ 100 for our sample at reasonable exposure time.

Time Justification: (including seeing overhead)

The average magnitude of our AGN sample is $V \sim 17$ mag. We used FORS2 time calculator (version 3.2.7) with sky conditions 7 days from the New Moon, 1.6 airmass, and 0.8arcsec seeing, GRIS_300V, slit 1.0 arcsec to obtain the exposure time required to get S/N$\simeq$ 100. From the experience of other observers in FORS2/PMOS with similar targets, 1hr exposure time suffice to acquire the desired quality of the data.

Using slow reading and maximum exposure time of 15min in two exposures per OB, we require 4 exposures, thus $15min \times 4 = 1.0hr$ per candidate.

The overhead are estimated as 720s for telescope pointing, acquisition and slit setup; $42s \times 2 = 84s$ for readout in PMOS spectroscopy; thus, a total of roughly 13min overhead. Considering 2 observing blocks to acquire 4 exposures, we obtain 26min overhead per target. We estimate 7.3h will yield spectra of sufficient quality for our seven AGN sample.

Each object must be observed at the parallactic angle to avoid flux losses, especially in the bluest part of the spectra. Because we need 1.2 hrs on-target to achieve the desired S/N we will request a waiver for a longer OB in Phase II (1.0 hr + 13 min = 1.2 hr). This will decrease the amount of overhead in 13min. per target, i.e. 1.3 hrs. In the case that a longer OB is not approved, we will use the time estimated using an OB of 1hr duration.

9a. Telescope Justification:

The VLT/FORS2/PMOS is needed in order to obtain the desired spectropolarimetric data with high signal-to-noise. No other 8-m class telescope in Chile has the polarimetric capabilities we need for our sample.

9b. Observing Mode Justification (visitor or service):

We are requesting service mode because our targets are spread over the entire semester. On the other hand, we are requesting simple spectropolarimetry with long-slit spectra with the low-resolution grism that can be achieved in moderate seeing and in grey time.

9c. Calibration Request:

Standard Calibration

10. Report on the use of ESO facilities during the last 2 years

86.A-0412(A) & 86.A-0412(B) (P.I. V. Motta): pre-imaging and FORS2/MXU spectroscopy of 10 lens galaxy groups. Due to FIMS technical problems, the observations done in 2010 were not useful (wrong size of the slits in the masks). All lens groups are scheduled to be observed observed during the second semester of 2011.

10a. ESO Archive - Are the data requested by this proposal in the ESO Archive (http://archive.eso.org)? If so, explain the need for new data.

FORS2/PMOS archive (*http : //archive.eso.org/eso/eso_archive_main.html*) shows no other observation of our candidates.

10b. GTO/Public Survey Duplications:

11. Applicant's publications related to the subject of this application during the last 2 years

Denney, K. D., Peterson, B. M., Gaskell, C. M. et al. 2009, ApJ, 704, L80 *Diverse Kinematic Signatures from Reverberation Mapping of the Broad-Line Region in AGNs*

Gaskell C. M. 2009, New Astron. Rev., 53, 140: *What broad emission lines tell us about how active galactic nuclei work*

Nazarova, L. S., Bochkarev, N. G., Gaskell, C. M. 2010, IAU Symp. 267, 126 *The Structure of the BLR in 3C 390.3*

Gaskell C. M. 2010, Nature, 463, E1 *Close supermassive binary black holes*

Gaskell, C. M. 2010, ApJ Submitted [arXiv:1008.1057] Off-Axis Energy Generation in Active Galactic Nuclei: Explaining Broad-Line Profiles, Spectropolarimetric Observations, and Velocity-Resolved Reverberation Mapping

12. List of targets proposed in this programme

Run	Target/Field	α(J2000)	δ(J2000)	ToT	Mag.	Diam.	Additional info	Reference star
A	SDSSJ001244 -102226	00 12 44.02	-10 22 26.2	1.0	17.07		z=0.2287	
A	SDSSJ015530 -085704	01 55 30.01	-08 57 04.0	1.0	16.84		z=0.1648	
A	SDSSJ094603 +013923	09 46 03.94	+01 39 23.7	1.0	17.5		z=0.2198	
A	SDSSJ111916 +110107	11 19 16.13	+11 01 07.1	1.0	17.36		z=0.3936	
A	SDSSJ153636 +044127	15 36 36.22	+04 41 27.0	1.0	17.07		z=0.3889	
A	PKS 0235+023	02 35	+02 30	1.0	17.1		z=0.209; J1950	
A	3C 227	09 47	+07 25	1.0	16.7		z=0.085828; J1950	

Target Notes: A note about the targets and/or strategy of selecting the targets during the run. Note that coordinates of the first five targets are J2000 while the last two are J1950.

13. Scheduling requirements

14. Instrument configuration

Period	Instrument	Run ID	Parameter	Value or list
89	FORS2	A	PMOS	GRIS300V, GRIS150I, GG435, OG590

EUROPEAN SOUTHERN OBSERVATORY

Organisation Européenne pour des Recherches Astronomiques dans l'Hémisphère Austral
Europäische Organisation für astronomische Forschung in der südlichen Hemisphäre

OBSERVING PROGRAMMES OFFICE • Karl-Schwarzschild-Straße 2 • D-85748 Garching bei München • e-mail: opo@eso.org • Tel.: +49-89-32 00 64 73

APPLICATION FOR OBSERVING TIME PERIOD: **90A**

Important Notice:

By submitting this proposal, the PI takes full responsibility for the content of the proposal, in particular with regard to the names of CoIs and the agreement to act according to the ESO policy and regulations, should observing time be granted

1. Title Category: **B–7**

Using Spectropolarimetric Variability to Probe the Energy Generation and Inner Structure of an AGN

2. Abstract / Total Time Requested

Total Amount of Time:

We plan to carry out a six-month spectropolarimetric campaign to monitor the bright AGN Ark 120 to test the hypothesis that the remarkably strong velocity dependence of broad emission line variability seen in many AGNs is due to strong off-axis flaring in the accretion disc. The flaring model predicts characteristic velocity dependencies of the degree and the position angle of polarization. These dependencies have been seen in Ark 120 and other AGNs, but other models have been proposed which can also explain the observations. A key prediction of the off-axis flaring model is that the polarization velocity dependencies will vary strongly. We are proposing to look for these well-defined polarization variability signatures in an AGN which exhibits frequent line profile changes. Verification of the off-axis flare model would be an important advance in understanding the energy production in AGNs and would solve many broad-line region puzzles.

3.

Run	Period	Instrument	Time	Month	Moon	Seeing	Sky	Mode	Type
A	90	FORS2	1h	oct	n	1.0	THN	s	
B	90	FORS2	1h	oct	n	1.0	THN	s	
C	90	FORS2	1h	nov	n	1.0	THN	s	
D	90	FORS2	1h	dec	n	1.0	THN	s	
E	90	FORS2	1h	dec	n	1.0	THN	s	
F	90	FORS2	1h	jan	n	1.0	THN	s	
G	90	FORS2	1h	feb	n	1.0	THN	s	
H	90	FORS2	1h	mar	n	1.0	THN	s	
I	90	FORS2	1h	mar	n	1.0	THN	s	
J	90	FORS2	1h	any	n	1.0	THN	s	

4. Number of nights/hours Telescope(s) Amount of time

a) already awarded to this project:

b) still required to complete this project:

5. Special remarks:

This is a monitoring campaign. The distribution of observations per month arises from our desire to obtain observations at approximately 22 day intervals (∼ the Nyquist frequency for the BLR light-crossing time) starting at the beginning of the semester.

6. Principal Investigator: MGASKELL

6a. Co-investigators:

R.R.J.	Antonucci	1943
E.M.	Benitez	1775
R.W.	Goosmann	1582
D.	Hiriart	1775

Following CoIs moved to the end of the document ...

7. Is this proposal linked to a PhD thesis preparation? State role of PhD student in this project

8. Description of the proposed programme

A – Scientific Rationale: The growth of supermassive black holes and the relationship between black holes and galaxy evolution has become one of the most important and most active areas of research in astronomy in recent years. Thermal active galactic nuclei (AGNs) are supermassive black holes growing through accretion at a relatively high rate (see Antonucci 2011 for a review of thermal versus non-thermal AGNs). Since thermal AGNs can readily be detected to very early times they are our best way of studying black hole growth over cosmic time. However, we must first understand how AGNs work. To know this we need (a) to understand the energy-generation mechanism and (b) to understand the structure and kinematics of the regions around the black hole. The broad-line region (BLR) offers our best probe of the innermost regions of an AGN. Our standard picture of a thermal AGN is that the energy is produced through the conversion of gravitational potential energy into heat and radiation by means of an accretion disc (Lynden-Bell 1969). A variety of lines of evidence strongly point to the existence of a dusty torus outside the accretion disc (see, for example, the review of Antonucci 1993), and to the BLR being the inwards extension of the torus inside the dust-sublimation radius (see review by Gaskell 2009). Observations show that the BLR and accretion disc occupy the same range of radii (see Gaskell 2008).

This axisymmetric torus + BLR + accretion disc paradigm largely explains the orientation dependence of AGN properties (see Antonucci 1993), and details such as BLR line profiles and velocity-resolved reverberation mapping results (see Gaskell 2009). However, as emphasized by Gaskell (2010, 2011), there are a number of major puzzles which do not have ready explanations in this paradigm. These include: AGNs whose BLR peaks show relative redshifts or blueshifts of thousands of kilometers per second, rapidly changing kinematic signatures (varying between inflow and outflow signatures in the same object on unphysically short timescales), variability of line profiles over remarkably narrow velocity ranges, the independence small regions of line profiles to continuum variability, and the strong velocity dependence of the polarization of the BLR. These puzzles point to worrying, major, and perhaps fundamental, gaps in the axisymmetric paradigm and our understanding of AGNs. Extreme cases have led to the invocation of scenarios such as binary supermassive black holes or recoiling black holes (see review by Popovic 2011). Gaskell (2010, 2011) has proposed instead that all of the above mentioned problems can readily be solved if the continuum variability is non-axisymmetric. In this picture there are strong off-axis flaring active regions on the disc. These regions are analogous to active regions on the sun. Because of the inverse-square law, the parts of the BLR closest to flares respond very strongly. This explains the variability of narrow velocity ranges of line profiles.

It is important to test the off-axis flaring model for a number of reasons. If the model is correct, our picture of the inner structure of AGNs is secure. This would give us confidence, for example, that black hole masses can be determined reliably from the BLR. On the other hand, if the model is *not* correct, there is much more uncertainty and other explanations of the anomalous observations are needed. This affects, for example, our estimates of the fraction of close supermassive black hole binaries. If the off-axis flaring model is correct, this represents a major paradigm change for energy generation in AGNs. The putative flares must be magnetic reconnection events (as on the sun) so, rather than the steady thermalization of gravitational potential energy in the standard accretion disc model of Lynden-Bell (1969), Pringle & Rees (1972), Shakura & Sunyaev (1973), etc., a large fraction of the gravitational potential energy released must be stored in magnetic fields instead rather than being thermalized immediately.

Some radiation in AGNs is always scattered. Departures from symmetry about the line of sight will produce linear polarization of this radiation, so there will be polarization signatures of off-axis flares. The predicted polarization signature of a single off-axis flaring region is given in Gaskell (2010) and shown in Figure A below. This is a very strong and definite prediction. If the model is correct, this behaviour must be seen. A second, and equally strong prediction, is that as the BLR profiles change with the turning off and on of different active regions, the polarization must change in a manner consistent with this.

We believe that these two predictions provide the most powerful tests of the off-axis flare model. We have been awarded VLT FORS time in 89A (observations pending) for spectropolarimetry of a sample of AGNs with extreme line profiles (BLR peaks displaced by thousands of km/s). The 89A observations are to test the first prediction (i.e., Figure A, below) for the most extreme objects. In this proposal we are asking for time to test the second prediction, variability of the velocity-dependent polarization. To test this we have selected the bright nearby type-1 AGN, Ark 120. Ark 120 is an excellent target for this for multiple reasons: (a) it is one of the brightest AGNs in the sky (V mag. of 13.5), (b) the sizes of the emitting regions are well know from many reverberation mapping studies, (c) it shows the sort of complex BLR profiles the off-axis flaring theory proposes explains, (d) it is already known to show variable line and continuum polarization, and (e) it is a "reliable performer" for changes in line profiles and flux. Figure B shows how the V magnitude varies during a typical observing season, figure C shows that there are significant line profile changes during an observing season, the RMS spectrum in figure D shows that Ark 120 is an example of an AGN where the line variability is strongest in quite narrow velocity ranges, and the left and right panels of figure E show that the velocity dependence of the polarization can change radically over a one-year period.

B – Immediate Objective: We want to obtain spectropolarimetry of the AGN Ark 120 covering the

Description of the proposed programme (continued)

wavelength range λ4430 to λ7380 at four positions of retarder every 22 or so for six months. (see below for the reasons for choosing 22 days for the sample.) The observed region covers most of the main optical emission lines in Ark 120. From these sets of spectra we will extract the total flux, percentage of polarization, and the angle of polarization as a function of wavelength. The quality of the spectra will be significantly higher than the spectrum in the right-hand panel of figure E. We will then subtract out the light of the host galaxy and correct for interstellar polarization and instrumental zero points. Co-I's F. Marin and R. Goosmann are working on modelling velocity-dependent polarization using the state-of-the-art Monte Carlo polarization code STOKES, written by R. Goosmann (see Goosmann & Gaskell 2007). We hope to be able to de-tangle the variability of the separate flares. Each individual flare should produce a polarization signture as in Figure A with the polarization dropping to near zero at the precice velocity of the flare.
Co-I's E. Benitez and D. Hiriat have been using POLIMA, the imagining polarimeter on the 84 cm telescope on San Pedro Martir (Hiriat el al. 2005), to follow the broad-band polarization changes. Our observations show that the continuum polarization has varied this year already by amounts comparable to past variability. The POLIMA monitoring will allow us to catch any rapid polarization variability that might be missed by out 22-day or so sampling, and it will provide an independent cross check of the continuum polarization derived from the VLT spectropolarimetry. Based on our POLIMA observations, and past polarization variability (including that in Fig. E), we consider it unlikely that the polarization of Ark 120 will not vary.

Attachments (Figures)

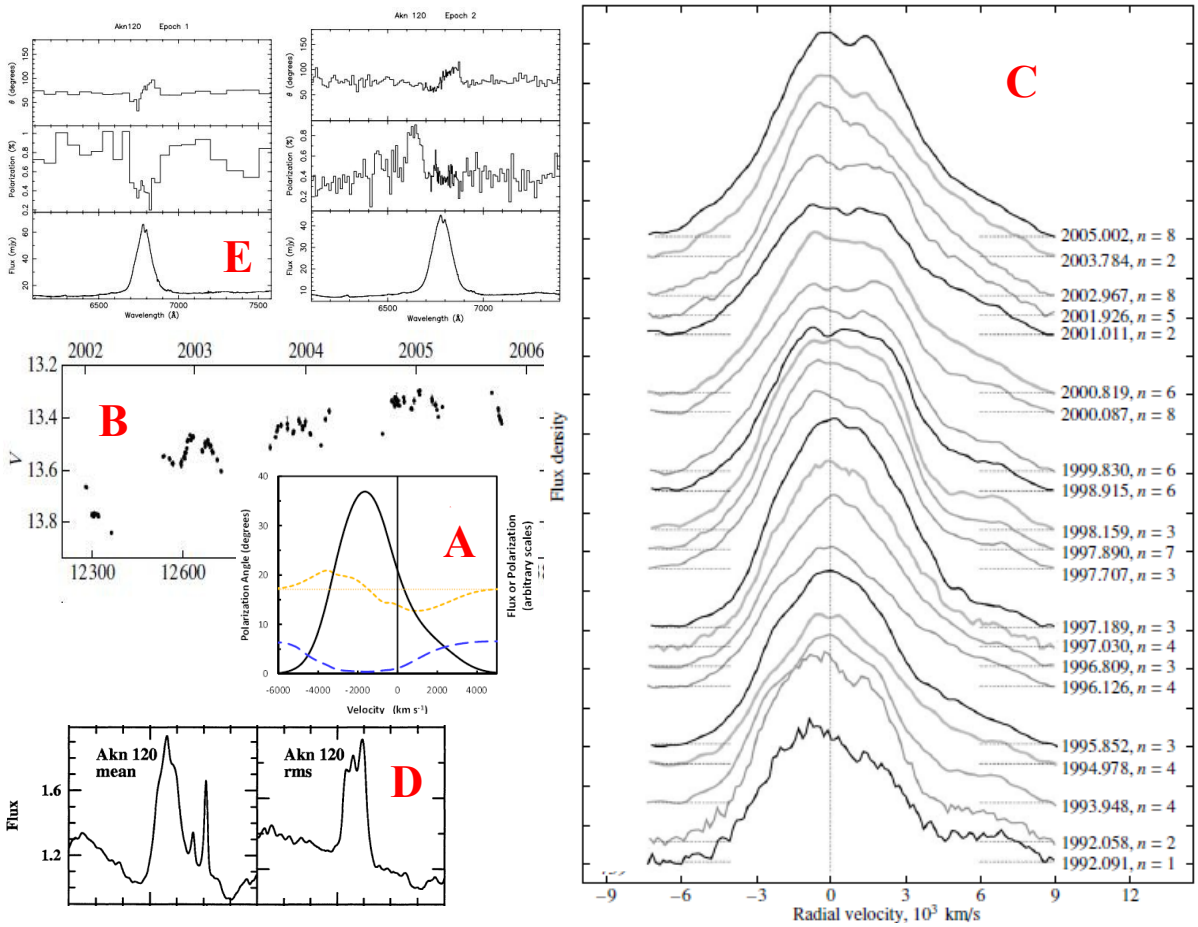

9. Justification of requested observing time and observing conditions

Lunar Phase Justification: The Exposure Time Calculator shows that, because Ark 120 is a very bright AGN, the signal-to-noise ratio is little affected by even a full moon.

Time Justification: (including seeing overhead) The polarization of Hα in Ark 120 has been observed to vary between 0.18% and 0.8% and the continuum polarization has been observed to vary between 0.35% and more than 1%. To see the expected variations in the wavelength dependence of the polarization across the Balmer lines (see figures) we therefore need to measure the polarization to $\sim \pm 0.02\%$ per resolution element. Both the FORS exposure time calculator and archival FORS spectropolarimetric observations with a similar setup show that a total exposure time (the sum of the times for the four retarder settings) of the order of 45 minutes is needed at each epoch. We are therefore requesting one-hour blocks at each epoch. Inspection of line profile variability data (see figure above) and the movie of the line profile variability made by the Ohio State group (URL in Peterson 2006) verifies that, as is expected on theoretical grounds, profile changes take place on a BLR light crossing timescale or longer. The light-crossing timescale of the region emitting the Balmer lines has been determined to vary between about 35 - 60 days (Peterson & Gaskell 1991; Peterson et al. 2004; Doroshenko, Sergeev, & Pronik 2008). To optimize our scientific return we want to monitor at approximately the Nyquist frequency. We are therefore planning to observe approximately every 22 days. To maximize the probability of catching the expected variability we want start the monitoring right at the start of the semester and end right at the end. This gives us 9 epochs during the semester. To improve the calibration and remove small systematic effects we are also requesting one hour of time to observe polarization standards (stars of zero or known polarization and possibly a probe star near Ark 120) with the same instrumental setup we use for Ark 120. The dates of observation of the polarizations standards are not critical.

9a. Telescope Justification:

Spectropolarimetry is very photon intensive and therefore needs large telescopes. The VLT is the only ESO telescope equipped with a suitable spectropolarimeter. Service mode observing is also essential for a monitoring project like this.

9b. Observing Mode Justification (visitor or service):

We are requesting observations in service mode because we only need observations of one hour separated by three weeks.

9c. Calibration Request:

Special Calibration - Adopt a special calibration

10. Report on the use of ESO facilities during the last 2 years

• 089.A-0486(A) (P.I. V. Motta): data is being taken. • 089.B-0959(B) (P.I. M. Gaskell): data is being taken.

10a. ESO Archive - Are the data requested by this proposal in the ESO Archive (http://archive.eso.org)? If so, explain the need for new data.

Ark 120 was observed spectropolarimetrically with FORS2 and the 300V grism for 40 minutes in 2000. Although this polarization spectrum has the same signal-to-noise ratio that we are seeking, it has only half the resolution. This makes it hard to study the polarization profile and to remove narrow-line contributions to line profiles. Ark was also observed in 2002 with the 600R grating for 1 hour. This gives an Hα profile of the same quality that we are seeking, but does not get Hβ. Both this and the 2000 observations are also, of course, isolated observations while we are looking for variability of the polarization on the light-crossing time. Nonetheless, because these old archival observations extend our baseline, we plan to compare the velocity dependence of the polarization in these two observations with our new monitoring data.

10b. GTO/Public Survey Duplications:

11. Applicant's publications related to the subject of this application during the last 2 years

Antonucci, R.R.J. 2012, A&ApTr, in press: Thermal and Nonthermal Radio Galaxies

Bentez, E., ... Hiriart, et al., 2011, Rev. Mex. Ast. Conf. Ser., 40, 44: Long-Term Optical Photopolarimetric Monitoring of Blazars at San Pedro Mrtir

Denney, K.D., Peterson, B.M., ... Gaskell, C.M. et al., 2010, ApJ, 721, 715: Reverberation Mapping Measurements of Black Hole Masses in Six Local Seyfert Galaxies

Karas, V., Dovciak, M., Muleri, F., Goosmann, R., Matt, G., 2011, Bull. Am. Ast. Soc, 12, #19.06, Polarization in the Lamp-post Model of Black-hole Accretion Discs - II

Gaskell, C.M. 2010, Nature, 463, E1: Close supermassive binary black holes

Gaskell, C.M. 2010, Baltic Ast., 20, 392: Off-Axis Variability of AGNs: a New Paradigm for Broad Lines and Continuum Emitting Regions

Gaskell, C.M. 2010, ApJ., 20, 392: Off-Axis Variability of AGNs: a New Paradigm for Broad Lines and Continuum Emitting Regions

Gaskell, C.M., Goosmann, R.W., Merkulova, N.I., Shakhovskoy, N.M., Shoji, M., 2012, ApJ, 749, 1: Discovery of Polarization Reverberation in NGC 4151

Kishimoto, M., Hnig, S.F., Antonucci, R.R.J., et al.A&A, 527, 121: The innermost dusty structure in active galactic nuclei as probed by the Keck interferometer

Marin, F., Goosmann, R.W., 2011, SF2A-2011, 597: Modeling the polarization of radio-quiet AGN: from the optical to the X-ray band

Mediavilla, E., ... Motta, V., et al., ApJ, 730, 16: The Structure of the Accretion Disk in the Lensed Quasar SBS 0909+532

Zhang, K., Dong, X.-B., Wang, T.-G., Gaskell, C.M., ApJ, 737, 71: The Blueshifting and Baldwin Effects for the [O III] λ5007 Emission Line in Type 1 Active Galactic Nuclei

12. List of targets proposed in this programme

Run	Target/Field	α(J2000)	δ(J2000)	ToT	Mag.	Diam.	Additional info	Reference star
A	Ark 120	05 16 11	-00 08 59	1	13.5			
B	Ark 120	05 16 11	-00 08 59	1	13.5			
C	Ark 120	05 16 11	-00 08 59	1	13.5			
D	Ark 120	05 16 11	-00 08 59	1	13.5			
E	Ark 120	05 16 11	-00 08 59	1	13.5			
F	Ark 120	05 16 11	-00 08 59	1	13.5			
G	Ark 120	05 16 11	-00 08 59	1	13.5			
H	Ark 120	05 16 11	-00 08 59	1	13.5			
I	Ark 120	05 16 11	-00 08 59	1	13.5			
J	Polarization stan-dards	00 00 00	00 00 00	1	10			

Target Notes: Polarization standards for determining instrumental polarization etc. to be specified at Phase 2

13. Scheduling requirements

This proposal involves time-critical observations, or observations to be performed at specific time intervals.

14. Instrument configuration

Period	Instrument	Run ID	Parameter	Value or list
90	FORS2	A	PMOS	GRIS600V, GG435
90	FORS2	B	PMOS	GRIS600V, GG435
90	FORS2	C	PMOS	GRIS600V, GG435
90	FORS2	D	PMOS	GRIS600V, GG435
90	FORS2	E	PMOS	GRIS600V, GG435
90	FORS2	F	PMOS	GRIS600V, GG435
90	FORS2	G	PMOS	GRIS600V, GG435
90	FORS2	H	PMOS	GRIS600V, GG435
90	FORS2	I	PMOS	GRIS600V, GG435
90	FORS2	J	PMOS	GRIS600V, GG435

6b. Co-investigators:

...continued from box 6a.

F.	Marin	1582
V.	Motta	1842

Bibliography

Abramowicz, M. A., Chen, X., & Taam, R. E. 1995, Astrophys. J., 452, 379

Abramowicz, M. A. & Fragile, P. C. 2011, ArXiv e-prints: 1104.5499

Alfvén, H. & Herlofson, N. 1950, Phys. Rev., 78, 616

Alnis, J., Blushs, K., Auzinsh, M., et al. 2003, Journal of Physics B Atomic Molecular Physics, 36, 1161

Angel, J. R. P. 1969, Astrophys. J., 158, 219

Angel, J. R. P. & Martin, P. G. 1973, Astrophys. J.l, 180, L39

Angel, J. R. P. & Stockman, H. S. 1980, Annu. Rev. Astron. Astrophys., 18, 321

Angel, J. R. P., Stockman, H. S., Woolf, N. J., Beaver, E. A., & Martin, P. G. 1976, Astrophys. J. Lett., 206, L5

Angel, J. R. P. & Weisskopf, M. C. 1970, Astron. J, 75, 231

Antonucci, R. 1993, Annu. Rev. Astron. Astrophys., 31, 473

Antonucci, R. 2012, Astron. & Astrophys. Trans. in press. ArXiv e-prints: 1101.0837

Antonucci, R., Hurt, T., & Miller, J. 1994, Astrophys. J., 430, 210

Antonucci, R. R. J. 1982, Nature, 299, 605

Antonucci, R. R. J. 1983, Nature, 303, 158

Antonucci, R. R. J. 1984, Astrophys. J., 281, 112

Antonucci, R. R. J. & Miller, J. S. 1985, Astrophys. J., 297, 621

Arav, N., Barlow, T. A., Laor, A., & Blandford, R. D. 1997, Mon. Not. R. Astron. Soc., 288, 1015

Arav, N., Barlow, T. A., Laor, A., Sargent, W. L. W., & Blandford, R. D. 1998, Mon. Not. R. Astron. Soc., 297, 990

Arav, N., Kaastra, J., Kriss, G. A., et al. 2005, Astrophys. J., 620, 665

Arny, T. T. 1966, Astrophys. J., 145, 572

Axon, D. J., Capetti, A., Macchetto, F., Sparks, W. B., & Boksenberg, A. 1996, Vistas in Astronomy, 40, 29

Axon, D. J., Marconi, A., Capetti, A., et al. 1998, Astrophys. J.l, 496, L75

Bailey, J., Axon, D. J., Hough, J. H., et al. 1988, Mon. Not. R. Astron. Soc., 234, 899

Baker, J. C. & Hunstead, R. W. 1995, Astrophys. J. Lett., 452, L95

Baker, J. C. & Hunstead, R. W. 1996a, Astrophys. J. Lett., 461, L59

Baker, J. C. & Hunstead, R. W. 1996b, Astrophys. J. Lett., 468, L131

Balbus, S. A. & Hawley, J. F. 1991, Astrophys. J., 376, 214

Balbus, S. A. & Hawley, J. F. 1998, Reviews of Modern Physics, 70, 1

Ballantyne, D. R., Weingartner, J. C., & Murray, N. 2003, Astron. Astrophys., 409, 503

Barcons, X., Barret, D., Bautz, M., et al. 2011, ArXiv e-prints: 1102.2845

Bartko, H., Martins, F., Fritz, T. K., et al. 2009, Astrophys. J., 697, 1741

Barvainis, R. 1987, Astrophys. J., 320, 537

Begelman, M. C. & McKee, C. F. 1983, Astrophys. J., 271, 89

Bellazzini, R., Angelini, F., Baldini, L., et al. 2006a, Nuclear Instruments and Methods in Physics Research A, 560, 425

Bellazzini, R., Angelini, F., Baldini, L., et al. 2003, in Society of Photo-Optical Instrumentation Engineers (SPIE) Conference Series, Vol. 4843, Society of Photo-Optical Instrumentation Engineers (SPIE) Conference Series, ed. S. Fineschi, 383–393

Bellazzini, R., Baldini, L., Brez, A., et al. 2006b, in Society of Photo-Optical Instrumentation Engineers (SPIE) Conference Series, Vol. 6266, Society of Photo-Optical Instrumentation Engineers (SPIE) Conference Series

Bellazzini, R. & Muleri, F. 2010, Nuclear Instruments and Methods in Physics Research A, 623, 766

Bennett, A. S. 1962, Mem. R. Astron. Soc., 68, 163

Benson, A. J., Bower, R. G., Frenk, C. S., et al. 2003, Astrophys. J., 599, 38

Berriman, G., Schmidt, G. D., West, S. C., & Stockman, H. S. 1990, Astrophys. J. Suppl. Ser., 74, 869

Bertout, C., Collin-Souffrin, S., & Lasota, J. P., eds. 1991, Structure and emission properties of accretion disks, ed. C. Bertout, S. Collin-Souffrin, & J. P. Lasota

Best, P. N. 2007, New Astron. Rev., 51, 168

Best, P. N., Kaiser, C. R., Heckman, T. M., & Kauffmann, G. 2006, Mon. Not. R. Astron. Soc., 368, L67

Bhattacharyya, S. & Strohmayer, T. E. 2007, Astrophys. J. Lett., 664, L103

Bianchi, S., Corral, A., Panessa, F., et al. 2008, Mon. Not. R. Astron. Soc., 385, 195

Bland-Hawthorn, J., Gallimore, J. F., Tacconi, L. J., et al. 1997, Astrophys. Space Sci., 248, 9

Blandford, R. D. & Königl, A. 1979, Astrophys. J., 232, 34

Blandford, R. D. & McKee, C. F. 1982, Astrophys. J., 255, 419

Blandford, R. D. & Payne, D. G. 1982, Mon. Not. R. Astron. Soc., 199, 883

Blandford, R. D. & Rees, M. J. 1978, Phys. Scr., 17, 265

Blustin, A. J., Page, M. J., Fuerst, S. V., Branduardi-Raymont, G., & Ashton, C. E. 2005, Astron. Astrophys., 431, 111

Bock, J. J., Neugebauer, G., Matthews, K., et al. 2000, Astron. J., 120, 2904

Bohlin, R. C., Savage, B. D., & Drake, J. F. 1978, Astrophys. J., 224, 132

Bohren, C. F. & Huffman, D. R. 1983, Absorption and scattering of light by small particles, ed. New York: Wiley

Bolton, J. G., Stanley, G. J., & Slee, O. B. 1949, Nature, 164, 101

Bommier, V. & Sahal-Brechot, S. 1982, Sol. Phys., 78, 157

Bon, E., Gavrilović, N., La Mura, G., & Č. Popović, L. 2009, New Astron. Rev., 53, 121

Bond, G. R. & Siewert, C. E. 1967, Astrophys. J., 150, 357

Boroson, T. A. & Green, R. F. 1992, Astrophys. J. Suppl. Ser., 80, 109

Bottorff, M., Korista, K. T., Shlosman, I., & Blandford, R. D. 1997, Astrophys. J., 479, 200

Bottorff, M. C., Korista, K. T., & Shlosman, I. 2000, Astrophys. J., 537, 134

Brenneman, L. W. & Reynolds, C. S. 2006, Astrophys. J., 652, 1028

Brenneman, L. W., Risaliti, G., Elvis, M., & Nardini, E. 2013, Mon. Not. R. Astron. Soc., 429, 2662

Bridle, A. H., Hough, D. H., Lonsdale, C. J., Burns, J. O., & Laing, R. A. 1994, Astron. J., 108, 766

Brown, J. C. & McLean, I. S. 1977, Astron. Astrophys., 57, 141

Brown, S. F., Donati, J.-F., Rees, D. E., & Semel, M. 1991, Astron. Astrophys., 250, 463

Bundy, K., Georgakakis, A., Nandra, K., et al. 2008, Astrophys. J., 681, 931

Burbidge, G. R. 1959, in IAU Symposium, Vol. 9, URSI Symp. 1: Paris Symposium on Radio Astronomy, ed. R. N. Bracewell, 541

Burbidge, G. R., Burbidge, E. M., & Sandage, A. R. 1963, Reviews of Modern Physics, 35, 947

Cao, X. 2010, Astrophys. J., 724, 855

Capetti, A., Axon, D. J., Macchetto, F., Sparks, W. B., & Boksenberg, A. 1995, Astrophys. J., 446, 155

Capetti, A., Axon, D. J., Macchetto, F. D., Marconi, A., & Winge, C. 1999, Mem. Soc. Astron. Italiana, 70, 41

Capetti, A., Macchetto, F. D., & Lattanzi, M. G. 1997, Astrophys. Space Sci., 248, 245

Carlson, R. W. & Fenner, W. R. 1972, Astrophys. J., 178, 551

Chambers, K. C., Miley, G. K., & van Breugel, W. 1987, Nature, 329, 604

Chandrasekhar, S. 1960, Radiative transfer, ed. S. Chandrasekhar

Chardin, J., Aubert, D., & Ocvirk, P. 2012, Astron. Astrophys., 548, A9

Chartas, G., Brandt, W. N., Gallagher, S. C., & Garmire, G. P. 2002, Astrophys. J., 579, 169

Chartas, G., Brandt, W. N., Gallagher, S. C., & Proga, D. 2007, Astron. J., 133, 1849

Chelouche, D. & Netzer, H. 2005, Astrophys. J., 625, 95

Chiaberge, M., Capetti, A., & Celotti, A. 1999, Astron. Astrophys., 349, 77

Chrysostomou, A., Clark, S. G., Hough, J. H., et al. 1996, Mon. Not. R. Astron. Soc., 278, 449

Chrysostomou, A., Gledhill, T. M., Ménard, F., et al. 2000, Mon. Not. R. Astron. Soc., 312, 103

Chrysostomou, A., Menard, F., Gledhill, T. M., et al. 1997, Mon. Not. R. Astron. Soc., 285, 750

Cicone, C., Feruglio, C., Maiolino, R., et al. 2012, Astron. Astrophys., 543, A99

Citterio, O., Campano, S., Conconi, P., et al. 1996, in Society of Photo-Optical Instrumentation Engineers (SPIE) Conference Series, Vol. 2805, Society of Photo-Optical Instrumentation Engineers (SPIE) Conference Series, ed. R. B. Hoover & A. B. Walker, 56–65

Claussen, M. J., Frail, D. A., Goss, W. M., & Gaume, R. A. 1997, Astrophys. J., 489, 143

Code, A. D., Meade, M. R., Anderson, C. M., et al. 1993, Astrophys. J.l, 403, L63

Cohen, M. H., Ogle, P. M., Tran, H. D., et al. 1995, Astrophys. J. Lett., 448, L77

Cole, S., Lacey, C. G., Baugh, C. M., & Frenk, C. S. 2000, Mon. Not. R. Astron. Soc., 319, 168

Collier, S., Crenshaw, D. M., Peterson, B. M., et al. 2001, Astrophys. J., 561, 146

Condon, E. U. & Shortley, G. H. 1963, The theory of atomic spectra

Costa, E., Soffitta, P., Bellazzini, R., et al. 2001, Nature, 411, 662

Costantini, E. 2010, Space Sci. Rev., 157, 265

Council, N. R. 2010, New Worlds, New Horizons in Astronomy and Astrophysics (The National Academies Press)

Cracco, V., Ciroi, S., di Mille, F., et al. 2011, Mon. Not. R. Astron. Soc., 418, 2630

Crenshaw, D. M. & Kraemer, S. B. 2000, Astrophys. J. Lett., 532, L101

Crenshaw, D. M. & Kraemer, S. B. 2005, Astrophys. J., 625, 680

Crenshaw, D. M., Kraemer, S. B., & George, I. M. 2003, Annu. Rev. Astron. Astrophys., 41, 117

Croft, S., van Breugel, W., de Vries, W., et al. 2006, Astrophys. J., 647, 1040

Croton, D. J., Springel, V., White, S. D. M., et al. 2006, Mon. Not. R. Astron. Soc., 365, 11

Crutcher, R., Heiles, C., & Troland, T. 2003, in Lecture Notes in Physics, Berlin Springer Verlag, Vol. 614, Turbulence and Magnetic Fields in Astrophysics, ed. E. Falgarone & T. Passot, 155–181

Curtis, H. C. 1921, Bull. Nat. Res. Coun., 2, 171

Czerny, B. & Hryniewicz, K. 2012, Journal of Physics Conference Series, 372, 012013

Daltabuit, E., Canto, J., & Quisbert, J. 1976, Rev. Mexicana Astron. Astrofis., 2, 23

Daniel, J.-Y. 1980, Astron. Astrophys., 87, 204

Das, V., Crenshaw, D. M., Hutchings, J. B., et al. 2005, Astron. J., 130, 945

Das, V., Crenshaw, D. M., & Kraemer, S. B. 2007, Astrophys. J., 656, 699

Das, V., Crenshaw, D. M., Kraemer, S. B., & Deo, R. P. 2006, Astron. J., 132, 620

Dauser, T., Wilms, J., Reynolds, C. S., & Brenneman, L. W. 2010, Mon. Not. R. Astron. Soc., 409, 1534

Davidson, K. & Netzer, H. 1979, Reviews of Modern Physics, 51, 715

Davies, H., Bethe, H. A., & Maximon, L. C. 1954, Physical Review, 93, 788

Davies, R. I., Thomas, J., Genzel, R., et al. 2006, Astrophys. J., 646, 754

de La Calle Pérez, I., Longinotti, A. L., Guainazzi, M., et al. 2010, Astron. Astrophys., 524, A50

Dean, A. J., Clark, D. J., Stephen, J. B., et al. 2008, Science, 321, 1183

Debye, P. 1909, Annalen der Physik, 335, 57

della Ceca, R., Lamorani, G., Maccacaro, T., et al. 1994, Astrophys. J., 430, 533

Di Matteo, T. 1998, Mon. Not. R. Astron. Soc., 299, L15

Di Matteo, T., Celotti, A., & Fabian, A. C. 1999, Mon. Not. R. Astron. Soc., 304, 809

Done, C. & Diaz Trigo, M. 2010, Mon. Not. R. Astron. Soc., 407, 2287

Dovčiak, M., Karas, V., & Yaqoob, T. 2004, Astrophys. J. Suppl. Ser., 153, 205

Dovčiak, M., Muleri, F., Goosmann, R. W., Karas, V., & Matt, G. 2011, Astrophys. J., 731, 75

Draine, B. T. & Lee, H. M. 1984, Astrophys. J., 285, 89

Draine, B. T. & Weingartner, J. C. 1997, Astrophys. J., 480, 633

Dullemond, C. P. & van Bemmel, I. M. 2005, Astron. Astrophys., 436, 47

Dumont, A.-M., Abrassart, A., & Collin, S. 2000, Astron. Astrophys., 357, 823

Dumont, A.-M., Collin-Souffrin, S., & Nazarova, L. 1998, Astron. Astrophys., 331, 11

Eales, S., Rawlings, S., Law-Green, D., Cotter, G., & Lacy, M. 1997, Mon. Not. R. Astron. Soc., 291, 593

Edelson, R. A., Malkan, M. A., & Rieke, G. H. 1987, Astrophys. J., 321, 233

Edge, D. O., Shakeshaft, J. R., McAdam, W. B., Baldwin, J. E., & Archer, S. 1959, Mem. R. Astron. Soc., 68, 37

Elitzur, M. 1996, Astrophys. J., 457, 415

Elitzur, M. 2005, ArXiv e-prints: astro-ph/0512025

Elitzur, M. 2007, in Astronomical Society of the Pacific Conference Series, Vol. 373, The Central Engine of Active Galactic Nuclei, ed. L. C. Ho & J.-W. Wang, 415

Elitzur, M. & Ho, L. C. 2009, Astrophys. J. Lett., 701, L91

Elitzur, M. & Shlosman, I. 2006, Astrophys. J. Lett., 648, L101

Elvis, M. 2000, Astrophys. J., 545, 63

Elvis, M. 2002a, in Astronomical Society of the Pacific Conference Series, Vol. 255, Mass Outflow in Active Galactic Nuclei: New Perspectives, ed. D. M. Crenshaw, S. B. Kraemer, & I. M. George, 303

Elvis, M. 2002b, in Astronomical Society of the Pacific Conference Series, Vol. 258, Issues in Unification of Active Galactic Nuclei, ed. R. Maiolino, A. Marconi, & N. Nagar, 51

Elvis, M. 2004, in Astronomical Society of the Pacific Conference Series, Vol. 311, AGN Physics with the Sloan Digital Sky Survey, ed. G. T. Richards & P. B. Hall, 109

Elvis, M. 2012, in Astronomical Society of the Pacific Conference Series, Vol. 460, AGN Winds in Charleston, ed. G. Chartas, F. Hamann, & K. M. Leighly, 186

Emmering, R. T., Blandford, R. D., & Shlosman, I. 1992, Astrophys. J., 385, 460

Eracleous, M. 2006, in Astronomical Society of the Pacific Conference Series, Vol. 360, Astronomical Society of the Pacific Conference Series, ed. C. M. Gaskell, I. M. McHardy, B. M. Peterson, & S. G. Sergeev, 217

Evans, A. 1994, The dusty universe, ed. Evans, A.

Evans, D. S., Wills, D., & Wills, B. J., eds. 1972, IAU Symposium, Vol. 44, External galaxies and quasi-stellar objects, proceedings from IAU Symposium no. 44 held in Uppsala, Sweden, 10-14 August 1970.

Everett, J. E. 2005, Astrophys. J., 631, 689

Everett, J. E. 2007, Astrophys. Space Sci., 311, 269

Everett, J. E. & Murray, N. 2007, Astrophys. J., 656, 93

Fabian, A. C. 2012, Annu. Rev. Astron. Astrophys., 50, 455

Fabian, A. C., Barcons, X., Almaini, O., & Iwasawa, K. 1998, Mon. Not. R. Astron. Soc., 297, L11

Fabian, A. C., Rees, M. J., Stella, L., & White, N. E. 1989, Mon. Not. R. Astron. Soc., 238, 729

Fabian, A. C., Vaughan, S., Nandra, K., et al. 2002, Mon. Not. R. Astron. Soc., 335, L1

Fabiani, S., Bellazzini, R., Berrilli, F., et al. 2012, in Society of Photo-Optical Instrumentation Engineers (SPIE) Conference Series, Vol. 8443, Society of Photo-Optical Instrumentation Engineers (SPIE) Conference Series

Fath, E. A. 1909a, Popular Astronomy, 17, 504

Fath, E. A. 1909b, Lick Observatory Bulletin, 5, 71

Feltre, A., Hatziminaoglou, E., Fritz, J., & Franceschini, A. 2012, Mon. Not. R. Astron. Soc., 426, 120

Ferland, G. J., Williams, R. E., Lambert, D. L., et al. 1984, Astrophys. J., 281, 194

Fernandes, C. A. C., Jarvis, M. J., & Rawlings, S. 2009, in Astronomical Society of the Pacific Conference Series, Vol. 408, The Starburst-AGN Connection, ed. W. Wang, Z. Yang, Z. Luo, & Z. Chen, 154

Field, G. B. & Rogers, R. D. 1993, Astrophys. J., 403, 94

Fischer, O., Henning, T., & Yorke, H. W. 1994, Astron. Astrophys., 284, 187

Fischer, O., Henning, T., & Yorke, H. W. 1996, Astron. Astrophys., 308, 863

Fontanot, F., Cristiani, S., & Vanzella, E. 2012, Mon. Not. R. Astron. Soc., 425, 1413

Francis, P. J., Hewett, P. C., Foltz, C. B., et al. 1991, Astrophys. J., 373, 465

Frank, J., King, A., & Raine, D. J. 2002, Accretion Power in Astrophysics: Third Edition

Fresnel, A.-J. 1821, Annales de Chimie et de Physique, 17, 101

Fry, E. S. & Kattawar, G. W. 1981, App. Opt., 20, 2811

Gabuzda, D. C. & Chernetskii, V. A. 2003, Mon. Not. R. Astron. Soc., 339, 669

Galeev, A. A., Rosner, R., & Vaiana, G. S. 1979, Astrophys. J., 229, 318

Gallagher, S. C. & Everett, J. E. 2007, in Astronomical Society of the Pacific Conference Series, Vol. 373, The Central Engine of Active Galactic Nuclei, ed. L. C. Ho & J.-W. Wang, 305

Gallagher, S. C., Schmidt, G. D., Smith, P. S., et al. 2005, Astrophys. J., 633, 71

Gallimore, J. F., Baum, S. A., O'Dea, C. P., Brinks, E., & Pedlar, A. 1994, Astrophys. J.l, 422, L13

Gaskell, C. M. 1988, Astrophys. J., 325, 114

Gaskell, C. M. 2008, in Revista Mexicana de Astronomia y Astrofisica Conference Series, Vol. 32, 1–11

Gaskell, C. M. 2009, New Astron. Rev., 53, 140

Gaskell, C. M. 2010, ArXiv e-prints : 1008.1057

Gaskell, C. M. 2011, Baltic Astronomy, 20, 392

Gaskell, C. M. & Goosmann, R. W. 2013, Astrophys. J., 769, 30

Gaskell, C. M., Goosmann, R. W., Antonucci, R. R. J., & Whysong, D. H. 2004, Astrophys. J., 616, 147

Gaskell, C. M., Goosmann, R. W., Merkulova, N. I., Shakhovskoy, N. M., & Shoji, M. 2012, Astrophys. J., 749, 148

Gaskell, C. M., Klimek, E. S., & Nazarova, L. S. 2007, ArXiv e-prints : 0711.1025

Gaskell, C. M. & Sparke, L. S. 1986, Astrophys. J., 305, 175

Gehrels, T. 1972, Astrophys. J.l, 173, L23

Gehrels, T. & Teska, T. M. 1960, Publ. Astron. Soc. Pac., 72, 115

Georgantopoulos, I. & Zezas, A. 2003, Astrophys. J., 594, 704

George, I. M. & Fabian, A. C. 1991, Mon. Not. R. Astron. Soc., 249, 352

Gil, J. J. & Bernabeu, E. 1985, Optica Acta, 32, 259

Gil, J. J. & Bernabeu, E. 1986, Optica Acta, 33, 185

Ginzburg, V. L. 1951, Dokl. Akad. Nauk SSSR, 76, 377

Ginzburg, V. L. & Ozernoi, L. M. 1977, Astrophys. Space Sci., 50, 23

Gliozzi, M., Panessa, F., La Franca, F., et al. 2010, Astrophys. J., 725, 2071

Gliozzi, M., Sambruna, R. M., & Foschini, L. 2007, Astrophys. J., 662, 878

Goad, M. R., O'Brien, P. T., & Gondhalekar, P. M. 1993, Mon. Not. R. Astron. Soc., 263, 149

Goodrich, R. W. & Miller, J. S. 1988, Astrophys. J., 331, 332

Goodrich, R. W. & Miller, J. S. 1994, Astrophys. J., 434, 82

Goodrich, R. W. & Miller, J. S. 1995, Astrophys. J. Lett., 448, L73

Goosmann, R. W. & Gaskell, C. M. 2007, Astron. Astrophys., 465, 129

Goosmann, R. W., Gaskell, C. M., & Marin, F. 2013, ArXiv e-prints: 1311.224

Goosmann, R. W., Gaskell, C. M., & Shoji, M. 2007a, in IAU Symposium, Vol. 238, IAU Symposium, ed. V. Karas & G. Matt, 375–376

Goosmann, R. W., Gaskell, C. M., & Shoji, M. 2007b, in Astronomical Society of the Pacific Conference Series, Vol. 373, The Central Engine of Active Galactic Nuclei, ed. L. C. Ho & J.-W. Wang, 485

Goosmann, R. W. & Matt, G. 2011a, in SF2A-2011: Proceedings of the Annual meeting of the French Society of Astronomy and Astrophysics, ed. G. Alecian, K. Belkacem, R. Samadi, & D. Valls-Gabaud, 583–586

Goosmann, R. W. & Matt, G. 2011b, Mon. Not. R. Astron. Soc., 415, 3119

Gordon, K. D., Misselt, K. A., Witt, A. N., & Clayton, G. C. 2001, Astrophys. J., 551, 269

Greenstein, J. L. 1963, Nature, 197, 1041

Greenstein, J. L. & Schmidt, M. 1964, Astrophys. J., 140, 1

Guedel, M., Guinan, E. F., & Skinner, S. L. 1997, Astrophys. J., 483, 947

Gupta, R., Mukai, T., Vaidya, D. B., Sen, A. K., & Okada, Y. 2005, Astron. Astrophys., 441, 555

Haardt, F. 1997, Mem. Soc. Astron. Italiana, 68, 73

Haardt, F. & Maraschi, L. 1991, Astrophys. J. Lett., 380, L51

Haardt, F. & Maraschi, L. 1993, Astrophys. J., 413, 507

Haardt, F., Maraschi, L., & Ghisellini, G. 1994, Astrophys. J. Lett., 432, L95

Hahn, Y. & Rule, D. W. 1977, Journal of Physics B Atomic Molecular Physics, 10, 2689

Haiman, Z. & Loeb, A. 1998, Astrophys. J., 503, 505

Hamann, F. 2000, Quasistellar Objects: Intrinsic AGN Absorption Lines, ed. P. Murdin

Hanle, W. 1924, Z. Physik, 30, 93

Hanle, W. 1926, Z. Physik, 35, 346

Häring, N. & Rix, H.-W. 2004, Astrophys. J. Lett., 604, L89

Hawkins, M. R. S. 2004, Astron. Astrophys., 424, 519

Hawley, J. F. & Balbus, S. A. 1991, Astrophys. J., 376, 223

Hazard, C., Mackey, M. B., & Shimmins, A. J. 1963, Nature, 197, 1037

Heymann, F. & Siebenmorgen, R. 2012, Astrophys. J., 751, 27

Hines, D. C. 1994, PhD thesis, Texas University

Hirose, S., Krolik, J. H., De Villiers, J.-P., & Hawley, J. F. 2004, Astrophys. J., 606, 1083

Hjelm, M. & Lindblad, P. O. 1996, Astron. Astrophys., 305, 727

Ho, L. & Kormendy, J. 2000, Supermassive Black Holes in Active Galactic Nuclei, ed. P. Murdin

Hoenig, S. F., Kishimoto, M., Antonucci, R., et al. 2012, ArXiv e-prints: 1206.4307

Hönig, S. F., Beckert, T., Ohnaka, K., & Weigelt, G. 2007, in Astronomical Society of the Pacific Conference Series, Vol. 373, The Central Engine of Active Galactic Nuclei, ed. L. C. Ho & J.-W. Wang, 487

Hönig, S. F. & Kishimoto, M. 2010, Astron. Astrophys., 523, A27

Hopkins, P. F., Hernquist, L., Cox, T. J., et al. 2006, Astrophys. J. Suppl. Ser., 163, 1

Hoyle, F. & Fowler, W. A. 1963, Mon. Not. R. Astron. Soc., 125, 169

Hunter, C. 1962, Astrophys. J., 136, 594

Inoue, H. & Matsumoto, C. 2003, Publ. Astron. Soc. Jpn., 55, 625

Jaffe, W., Meisenheimer, K., Röttgering, H. J. A., et al. 2004, Nature, 429, 47

Jannuzi, B. T., Smith, P. S., & Elston, R. 1993, Astrophys. J.s, 85, 265

Jansky, K. G. 1932, Proc. IRE, 20, 1920

Jansky, K. G. 1933, Proc. IRE, 21, 1387

Jansky, K. G. 1935, Proc. IRE, 23, 1158

Jeans, J. H. 1902, Royal Society of London Philosophical Transactions Series A, 199, 1

Jorstad, S. G., Marscher, A. P., Lister, M. L., et al. 2005, Astron. J., 130, 1418

Jorstad, S. G., Marscher, A. P., Mattox, J. R., et al. 2001, Astrophys. J. Suppl. Ser., 134, 181

Kaastra, J. S. & Mewe, R. 1993, Astron. Astrophys. Suppl. Ser., 97, 443

Kalos, M. H. & Whitlock, P. A. 2008, Monte Carlo Methods: Second Revised and Enlarged Edition (Wiley-VCH Verlag)

Karas, V., Czerny, B., Abrassart, A., & Abramowicz, M. A. 2000, Mon. Not. R. Astron. Soc., 318, 547

Kartje, J. F. 1995, Astrophys. J., 452, 565

Kartje, J. F. & Königl, A. 1996, Vistas in Astronomy, 40, 133

Kartje, J. F., Königl, A., & Elitzur, M. 1999, Astrophys. J., 513, 180

Karzas, W. J. & Latter, R. 1961, Astrophys. J. Suppl. Ser., 6, 167

Kaspi, S. & Behar, E. 2006, Astrophys. J., 636, 674

Kawaguchi, T., Mineshige, S., Machida, M., Matsumoto, R., & Shibata, K. 2000, Publ. Astron. Soc. Jpn., 52, L1

Kay, L. E. 1994, Astrophys. J., 430, 196

Kazanas, D., Fukumura, K., Behar, E., Contopoulos, I., & Shrader, C. 2012, ArXiv: 1206.5022

Keel, W. C. 1980, Astron. J., 85, 198

Keel, W. C., Chojnowski, S. D., Bennert, V. N., et al. 2012, Mon. Not. R. Astron. Soc., 420, 878

Kellermann, K. I., Lister, M. L., Homan, D. C., et al. 2004, Astrophys. J., 609, 539

Kellermann, K. I., Sramek, R., Schmidt, M., Shaffer, D. B., & Green, R. 1989, Astron. J., 98, 1195

Kiepenheuer, K. O. 1950, Phys. Rev., 79, 738

Kishimoto, M. 1999, Astrophys. J., 518, 676

Klein, O. & Nishina, Y. 1929, Z. Phys., 52, 11

Knigge, C., Scaringi, S., Goad, M. R., & Cottis, C. E. 2008, Mon. Not. R. Astron. Soc., 386, 1426

Koch, H. W. & Motz, J. W. 1959, Reviews of Modern Physics, 31, 920

Komesaroff, M. M., Roberts, J. A., Milne, D. K., Rayner, P. T., & Cooke, D. J. 1984, Mon. Not. R. Astron. Soc., 208, 409

Komossa, S. 1999, ISAS Report, p. 149-160, T. Takahashi, H. Inoue (eds), 149

Konigl, A. 1981, Astrophys. J., 243, 700

Königl, A. 2007, in Revista Mexicana de Astronomia y Astrofisica, vol. 27, Vol. 27, Revista Mexicana de Astronomia y Astrofisica, vol. 27, 91–101

Konigl, A. & Kartje, J. F. 1994, Astrophys. J., 434, 446

Kormendy, J. & Gebhardt, K. 2001, in American Institute of Physics Conference Series, Vol. 586, 20th Texas Symposium on relativistic astrophysics, ed. J. C. Wheeler & H. Martel, 363–381

Kriss, G. A. 2004, in IAU Symposium, Vol. 222, The Interplay Among Black Holes, Stars and ISM in Galactic Nuclei, ed. T. Storchi-Bergmann, L. C. Ho, & H. R. Schmitt, 223–228

Kristian, J. 1973, Astrophys. J. Lett., 179, L61

Krivonos, R., Revnivtsev, M., Lutovinov, A., et al. 2007, Astron. Astrophys., 475, 775

Krolik, J. H. & Begelman, M. C. 1988, Astrophys. J., 329, 702

Krolik, J. H., McKee, C. F., & Tarter, C. B. 1981, Astrophys. J., 249, 422

Kwan, J. & Krolik, J. H. 1981, Astrophys. J., 250, 478

La Franca, F., Gregorini, L., Cristiani, S., de Ruiter, H., & Owen, F. 1994, Astron. J., 108, 1548

Laming, J. M. 1990, Astrophys. J., 362, 219

Landstreet, J. D. & Angel, J. R. P. 1972, Astrophys. J.l, 174, L127

Laor, A. 1991, Astrophys. J., 376, 90

Lawrence, A. 1991, Mon. Not. R. Astron. Soc., 252, 586

Lee, C. M. & Pratt, R. H. 1975, Phys. Rev. A, 12, 1825

Lee, H. W. 1994, Mon. Not. R. Astron. Soc., 268, 49

Lee, H.-W. & Blandford, R. D. 1997, Mon. Not. R. Astron. Soc., 288, 19

Lee, H.-W., Blandford, R. D., & Western, L. 1994, Mon. Not. R. Astron. Soc., 267, 303

Legg, M. P. C. & Westfold, K. C. 1968, Astrophys. J., 154, 499

Lei, F., Dean, A. J., & Hills, G. L. 1997, Space Sci. Rev., 82, 309

Lenoble, J. 1985, Radiative transfer in scattering and absorbing atmospheres: Standard computational procedures

Leroy, J. L., Ratier, G., & Bommier, V. 1977, Astron. Astrophys., 54, 811

Li, A. 2008, In "The Central Engine of Active Galactic Nuclei", ASP Conference Series, Vol. 373, Xi'an, China, 16-21 October, 2007, eds. L. C. Ho and J.-M. Wang, ArXiv e-prints: 0808.4117

Liu, B. F., Mineshige, S., & Ohsuga, K. 2003, Astrophys. J., 587, 571

Liu, B. F., Mineshige, S., & Shibata, K. 2002, Astrophys. J. Lett., 572, L173

Lobanov, A., Hardee, P., & Eilek, J. 2003, New Astron. Rev., 47, 629

Lobanov, A. P. & Zensus, J. A. 2001, Science, 294, 128

Lodato, G. 2007, Nuovo Cimento Rivista Serie, 30, 293

Longair, M. S. 1992, High energy astrophysics. Vol.1: Particles, photons and their detection

Lonsdale, C. J., Dyck, H. M., Capps, R. W., & Wolstencroft, R. D. 1980, Astrophys. J. Lett., 238, L31

Lynden-Bell, D. 1969a, Nature, 223, 690

Lynden-Bell, D. 1969b, Nature, 223, 690

Lynden-Bell, D. 1978, Phys. Scr., 17, 185

Macchetto, F., Capetti, A., Sparks, W. B., Axon, D. J., & Boksenberg, A. 1994, Astrophys. J.l, 435, L15

Malkan, M. A. 1984, Astrophys. J., 287, 555

Mancuso, S. & Spangler, S. R. 2000, Astrophys. J., 539, 480

Manzini, A. & di Serego Alighieri, S. 1996, Astron. Astrophys., 311, 79

Maoz, D., Nagar, N. M., Falcke, H., & Wilson, A. S. 2005, Astrophys. J., 625, 699

Marin, F., Goosmann, R., & Dovčiak, M. 2012a, Journal of Physics Conference Series, 372, 012065

Marin, F. & Goosmann, R. W. 2011, in SF2A-2011: Proceedings of the Annual meeting of the French Society of Astronomy and Astrophysics, ed. G. Alecian, K. Belkacem, R. Samadi, & D. Valls-Gabaud, 597–600

Marin, F. & Goosmann, R. W. 2012, in SF2A-2012: Proceedings of the Annual meeting of the French Society of Astronomy and Astrophysics, ed. S. Boissier, P. de Laverny, N. Nardetto, R. Samadi, D. Valls-Gabaud, & H. Wozniak, 587–590

Marin, F. & Goosmann, R. W. 2013a, Mon. Not. R. Astron. Soc., 436, 2522

Marin, F. & Goosmann, R. W. 2013b, in SF2A-2013: Proceedings of the Annual meeting of the French Society of Astronomy and Astrophysics, ed. L. Cambresy, F. Martins, E. Nuss, & A. Palacios, 475–478

Marin, F. & Goosmann, R. W. 2013c, in SF2A-2013: Proceedings of the Annual meeting of the French Society of Astronomy and Astrophysics, ed. L. Cambresy, F. Martins, E. Nuss, & A. Palacios, 479–482

Marin, F., Goosmann, R. W., Dovčiak, M., et al. 2012b, Mon. Not. R. Astron. Soc., 426, L101

Marin, F., Goosmann, R. W., Gaskell, C. M., Porquet, D., & Dovčiak, M. 2012c, Astron. Astrophys., 548, A121

Marin, F., Porquet, D., Goosmann, R. W., et al. 2013, Mon. Not. R. Astron. Soc., 436, 1615

Marin, F. & Tamborra, F. 2013, ArXiv e-prints: 1309.1684

Marsaglia, G. 1985, IEEE Trans. Computers, 34, 756

Marscher, A. P. 2005, Mem. Soc. Astron. Italiana, 76, 168

Marscher, A. P., Jorstad, S. G., D'Arcangelo, F. D., et al. 2008, Nature, 452, 966

Martin, P. G. 1974, Astrophys. J., 187, 461

Martin, P. G. 1988, Astrophys. J. Suppl. Ser., 66, 125

Martin, R. G. 2008, Mon. Not. R. Astron. Soc., 387, 830

Mathews, W. G. & Capriotti, E. R. 1985, in Astrophysics of Active Galaxies and Quasi-Stellar Objects, ed. J. S. Miller, 185–233

Mathewson, D. S. & Ford, V. L. 1970a, Astron. J., 75, 778

Mathewson, D. S. & Ford, V. L. 1970b, Astrophys. J. Lett., 160, L43

Mathis, J. S., Rumpl, W., & Nordsieck, K. H. 1977, Astrophys. J., 217, 425

Mathur, S., Elvis, M., & Wilkes, B. 1995, Astrophys. J., 452, 230

Mathur, S., Wilkes, B., Elvis, M., & Fiore, F. 1994, Astrophys. J., 434, 493

Matsumoto, M. & Nishimura, T. 1998, ACM Trans. Model. Comput. Simul., 8, 3

Matthews, T. A. & Sandage, A. R. 1963, Astrophys. J., 138, 30

McCarthy, P. J., van Breugel, W., Spinrad, H., & Djorgovski, S. 1987, Astrophys. J. Lett., 321, L29

McGlynn, S., Clark, D. J., Dean, A. J., et al. 2007, Astron. Astrophys., 466, 895

McKinney, J. C. 2006, Mon. Not. R. Astron. Soc., 368, 1561

McMaster, W. H. 1961, Reviews of Modern Physics, 33, 8

Meier, D. L. 2005, Astrophys. Space Sci., 300, 55

Merritt, D. & Ferrarese, L. 2001, Mon. Not. R. Astron. Soc., 320, L30

Merzbacher, E. 1961, Quantum mechanics, ed. Wiley, New York

Metropolis, N. & Ulam, S. 1949, Journal of the American Statistical Association, 44, 335

Mie, G. 1908, Annalen der Physik, 330, 377

Miller, J. M., Raymond, J., Fabian, A. C., et al. 2004, Astrophys. J., 601, 450

Miller, J. S. & Antonucci, R. R. J. 1983, Astrophys. J. Lett., 271, L7

Miller, J. S. & Goodrich, R. W. 1990, Astrophys. J., 355, 456

Miller, J. S., Goodrich, R. W., & Mathews, W. G. 1991, Astrophys. J., 378, 47

Miller, K. A. & Stone, J. M. 2000, Astrophys. J., 534, 398

Miller, L. & Turner, T. J. 2013, ArXiv e-prints : 1303.4309

Miller, L., Turner, T. J., & Reeves, J. N. 2008, Astron. Astrophys., 483, 437

Miller, L., Turner, T. J., & Reeves, J. N. 2009, Mon. Not. R. Astron. Soc., 399, L69

Miniutti, G. & Fabian, A. C. 2004, Mon. Not. R. Astron. Soc., 349, 1435

Miniutti, G., Fabian, A. C., Anabuki, N., et al. 2007, Publ. Astron. Soc. Jpn., 59, 315

Miniutti, G., Fabian, A. C., Goyder, R., & Lasenby, A. N. 2003, Mon. Not. R. Astron. Soc., 344, L22

Misawa, T., Charlton, J. C., Eracleous, M., et al. 2007, Astrophys. J. Suppl. Ser., 171, 1

Mishchenko, M. I. 1991, Astrophys. J., 367, 561

Mishchenko, M. I., Travis, L. D., & Macke, A. 2000, T-Matrix Method and Its Applications, ed. M. I. Mishchenko, J. W. Hovenier, & L. D. Travis, 147

Misselt, K. A., Gordon, K. D., Clayton, G. C., & Wolff, M. J. 2001, Astrophys. J., 551, 277

Miyamoto, S. & Kitamoto, S. 1989, Nature, 342, 773

Modest, M. F. 1993, Radiative heat transfer. Mc Graw-Hill Series in Mechanical Engineering, New York

Moore, R. L. & Stockman, H. S. 1981, Astrophys. J., 243, 60

Moore, R. L. & Stockman, H. S. 1984, Astrophys. J., 279, 465

Mor, R., Netzer, H., & Elitzur, M. 2009, Astrophys. J., 705, 298

Morganti, R., Holt, J., Saripalli, L., Oosterloo, T. A., & Tadhunter, C. N. 2007, Astron. Astrophys., 476, 735

Morganti, R., Oosterloo, T., Holt, J., Tadhunter, C., & van der Hulst, J. M. 2003, The Messenger, 113, 67

Morganti, R., Oosterloo, T., & Tsvetanov, Z. 1998, Astron. J, 115, 915

Mueller, H. 1948, J. Opt. Soc. Am., 38, 551

Muleri, F., Bellazzini, R., Costa, E., et al. 2006, in Society of Photo-Optical Instrumentation Engineers (SPIE) Conference Series, Vol. 6266, Society of Photo-Optical Instrumentation Engineers (SPIE) Conference Series

Murray, N. & Chiang, J. 1995, Astrophys. J. Lett., 454, L105

Murray, N., Chiang, J., Grossman, S. A., & Voit, G. M. 1995, Astrophys. J., 451, 498

Nagirner, D. I. & Poutanen, J. 1993a, Astron. Astrophys., 275, 325

Nagirner, D. I. & Poutanen, Y. J. 1993b, Astron. Lett., 19, 262

Nahar, S. N. 2000, in Atomic Data Needs for X-ray Astronomy, ed. M. A. Bautista, T. R. Kallman, & A. K. Pradhan, 77

Nakada, M. P., Neupert, W. M., & Thomas, R. J. 1974, Sol. Phys., 37, 429

Nandra, K., George, I. M., Mushotzky, R. F., Turner, T. J., & Yaqoob, T. 1997, Astrophys. J., 477, 602

Nandra, K., O'Neill, P. M., George, I. M., & Reeves, J. N. 2007, Mon. Not. R. Astron. Soc., 382, 194

Narayan, R. & Yi, I. 1994, Astrophys. J. Lett., 428, L13

Nayakshin, S. 2005, Mon. Not. R. Astron. Soc., 359, 545

Nenkova, M., Sirocky, M. M., Nikutta, R., Ž. Ivezić, & Elitzur, M. 2008a, Astrophys. J., 685, 160

Nenkova, M., Sirocky, M. M., Nikutta, R., Ž. Ivezić, & Elitzur, M. 2010, Astrophys. J., 723, 1827

Nenkova, M., Sirocky, M. M., Ž. Ivezić, & Elitzur, M. 2008b, Astrophys. J., 685, 147

Nenkova, M., Ž. Ivezić, & Elitzur, M. 2002, Astrophys. J. Lett., 570, L9

Netzer, H. 1990, in Active Galactic Nuclei, ed. R. D. Blandford, H. Netzer, L. Woltjer, T. J.-L. Courvoisier, & M. Mayor, 57–160

Netzer, H. & Laor, A. 1993, Astrophys. J. Lett., 404, L51

Netzer, H. & Peterson, B. M. 1997, in Astrophysics and Space Science Library, Vol. 218, Astronomical Time Series, ed. D. Maoz, A. Sternberg, & E. M. Leibowitz, 85

Ng, C., Díaz Trigo, M., Cadolle Bel, M., & Migliari, S. 2010, Astron. Astrophys., 522, A96

Nicastro, F., Krongold, Y., & Elvis, M. 2008, Mem. Soc. Astron. Italiana, 79, 1178

Nicastro, F., Martocchia, A., & Matt, G. 2003, Astrophys. J. Lett., 589, L13

Nikulin, N. S., Kuvshinov, V. M., & Severny, A. B. 1971, Astrophys. J.l, 170, L53

Novick, R., Weisskopf, M. C., Berthelsdorf, R., Linke, R., & Wolff, R. S. 1972, Astrophys. J. Lett., 174, L1

Novick, R. & Wolff, R. S. 1971, in IAU Symposium, Vol. 41, New techniques in Space Astronomy, ed. F. Labuhn & R. Lust, 159

O'Brien, P. T., Dietrich, M., Leighly, K., et al. 1998, Astrophys. J., 509, 163

O'Brien, P. T., Reeves, J. N., Simpson, C., & Ward, M. J. 2005, Mon. Not. R. Astron. Soc., 360, L25

O'Connell, D. J. K., ed. 1971, Study week on nuclei of galaxies

Ogle, P. M. 1998, PhD thesis, California Institute of Technology

Ogle, P. M., Brookings, T., Canizares, C. R., Lee, J. C., & Marshall, H. L. 2003, Astron. Astrophys., 402, 849

Ogle, P. M., Cohen, M. H., Miller, J. S., et al. 1999, Astrophys. J. Suppl. Ser., 125, 1

Oke, J. B. 1963, Nature, 197, 1040

Oknyanskij, V. L. & Horne, K. 2001, in Astronomical Society of the Pacific Conference Series, Vol. 224, Probing the Physics of Active Galactic Nuclei, ed. B. M. Peterson, R. W. Pogge, & R. S. Polidan, 149

Oort, J. H. & Walraven, T. 1956, Bull. Astron. Inst. Neth., 12, 285

Osterbrock, D. E. 1978, Proceedings of the National Academy of Science, 75, 540

Osterbrock, D. E. 1989, Astrophysics of gaseous nebulae and active galactic nuclei

Osterbrock, D. E. 1991, Reports on Progress in Physics, 54, 579

Osterbrock, D. E. & Mathews, W. G. 1986, Annu. Rev. Astron. Astrophys., 24, 171

Ostriker, E. C., McKee, C. F., & Klein, R. I. 1991, Astrophys. J., 377, 593

O'Sullivan, S. P. & Gabuzda, D. C. 2008, in The role of VLBI in the Golden Age for Radio Astronomy

Pacholczyk, A. G. & Weymann, R. J. 1968, Astron. J, 73, 870

Packham, C., Escuti, M., Boreman, G., et al. 2008, in Society of Photo-Optical Instrumentation Engineers (SPIE) Conference Series, Vol. 7014, Society of Photo-Optical Instrumentation Engineers (SPIE) Conference Series

Packham, C., Radomski, J. T., Roche, P. F., et al. 2005, Astrophys. J. Lett., 618, L17

Packham, C., Young, S., Hough, J. H., Axon, D. J., & Bailey, J. A. 1997, Mon. Not. R. Astron. Soc., 288, 375

Padovani, P. 1993, Mon. Not. R. Astron. Soc., 263, 461

Page, K. L., O'Brien, P. T., Reeves, J. N., & Turner, M. J. L. 2004, Mon. Not. R. Astron. Soc., 347, 316

Page, K. L., Reeves, J. N., O'Brien, P. T., & Turner, M. J. L. 2005, Mon. Not. R. Astron. Soc., 364, 195

Panessa, F. & Bassani, L. 2002, Astron. Astrophys., 394, 435

Panessa, F., Carrera, F. J., Bianchi, S., et al. 2009, Mon. Not. R. Astron. Soc., 398, 1951

Patrick, A. R., Reeves, J. N., Lobban, A. P., Porquet, D., & Markowitz, A. G. 2011, Mon. Not. R. Astron. Soc., 416, 2725

Pentericci, L., Fontana, A., Vanzella, E., et al. 2011, Astrophys. J., 743, 132

Pequignot, D., Petitjean, P., & Boisson, C. 1991, Astron. Astrophys., 251, 680

Perrin, F. 1942, J. Chem. Phys., 10, 415

Perrin, F. & Abragam, A. 1951, J. Phys. Rad., 2, 69

Peterson, B. M. 1993, Publ. Astron. Soc. Pac., 105, 247

Peterson, B. M. 1997, An introduction to Active Galactic Nuclei, ed. Cambridge University Press

Peterson, B. M. 1998, Advances in Space Research, 21, 57

Peterson, B. M. 2006, in Lecture Notes in Physics, Berlin Springer Verlag, Vol. 693, Physics of Active Galactic Nuclei at all Scales, ed. D. Alloin, 77

Peterson, B. M. & Wandel, A. 2000, Astrophys. J. Lett., 540, L13

Petitjean, P., Boisson, C., & Pequignot, D. 1990, Astron. Astrophys., 240, 433

Petre, R., Bregman, J., Bautz, M., et al. 2012, in Society of Photo-Optical Instrumentation Engineers (SPIE) Conference Series, Vol. 8443, Society of Photo-Optical Instrumentation Engineers (SPIE) Conference Series

Piconcelli, E., Jimenez-Bailón, E., Guainazzi, M., et al. 2005, Astron. Astrophys., 432, 15

Pier, E. A. & Krolik, J. H. 1992, Astrophys. J. Lett., 399, L23

Pier, E. A. & Krolik, J. H. 1993, Astrophys. J., 418, 673

Pogge, R. W. 1988a, Astrophys. J., 328, 519

Pogge, R. W. 1988b, Astrophys. J., 332, 702

Popović, L. C. 2006, Serbian Astronomical Journal, 173, 1

Popović, L. C., Shapovalova, A. I., Chavushyan, V. H., et al. 2008, Publ. Astron. Soc. Jpn., 60, 1

Popović, L. C., Shapovalova, A. I., Ilić, D., et al. 2011, Astron. Astrophys., 528, A130

Porquet, D. & Dubau, J. 2000, Astron. Astrophys. Suppl. Ser., 143, 495

Porquet, D., Dubau, J., & Grosso, N. 2010, Space Sci. Rev., 157, 103

Pounds, K. A., Nandra, K., Stewart, G. C., George, I. M., & Fabian, A. C. 1990, Nature, 344, 132

Pounds, K. A. & Page, K. L. 2006, Mon. Not. R. Astron. Soc., 372, 1275

Pounds, K. A., Reeves, J. N., King, A. R., et al. 2003, Mon. Not. R. Astron. Soc., 345, 705

Poutanen, J. & Vilhu, O. 1993, Astron. Astrophys., 275, 337

Pozdnyakov, L. A., Sobol, I. M., & Syunyaev, R. A. 1983, Astrophys. Space Phys. Rev., 2, 189

Press, W. H., Teukolsky, S. A., Vetterling, W. T., & Flannery, B. P. 1992, Numerical recipes in C. The art of scientific computing

Pringle, J. E. 1981, Annu. Rev. Astron. Astrophys., 19, 137

Pringle, J. E. & Rees, M. J. 1972, Astron. Astrophys., 21, 1

Proga, D. 2005, Astrophys. J. Lett., 630, L9

Proga, D. 2007, in Astronomical Society of the Pacific Conference Series, Vol. 373, The Central Engine of Active Galactic Nuclei, ed. L. C. Ho & J.-W. Wang, 267

Proga, D. & Kallman, T. R. 2004, Astrophys. J., 616, 688

Raban, D., Jaffe, W., Röttgering, H., Meisenheimer, K., & Tristram, K. R. W. 2009, Mon. Not. R. Astron. Soc., 394, 1325

Radomski, J. T., Packham, C., Levenson, N. A., et al. 2008, Astrophys. J., 681, 141

Raman, C. V. 1928, Ind. J. Phys., 2, 387

Raman, C. V. & Krishnan, K. S. 1928a, Nature, 122, 278

Raman, C. V. & Krishnan, K. S. 1928b, Nature, 121, 711

Rawlings, S. & Jarvis, M. J. 2004, Mon. Not. R. Astron. Soc., 355, L9

Reber, G. 1940, Astrophys. J., 91, 621

Rees, M. J. 1967, Mon. Not. R. Astron. Soc., 137, 429

Rees, M. J., Begelman, M. C., Blandford, R. D., & Phinney, E. S. 1982, Nature, 295, 17

Reeves, J. N., Fabian, A. C., Kataoka, J., et al. 2006, Astronomische Nachrichten, 327, 1079

Reeves, J. N., O'Brien, P. T., Braito, V., et al. 2009, Astrophys. J., 701, 493

Reeves, J. N. & Turner, M. J. L. 2000, Mon. Not. R. Astron. Soc., 316, 234

Reichard, T. A., Richards, G. T., Hall, P. B., et al. 2003, Astron. J., 126, 2594

Reynolds, C. S., Fabian, A. C., Brenneman, L. W., et al. 2009, Mon. Not. R. Astron. Soc., 397, L21

Reynolds, C. S. & Nowak, M. A. 2003, Phys. Rep., 377, 389

Rieger, F. M. & Mannheim, K. 2005, Chinese Journal of Astronomy and Astrophysics Supplement, 5, 311

Risaliti, G., Braito, V., Laparola, V., et al. 2009, Astrophys. J. Lett., 705, L1

Risaliti, G., Elvis, M., & Nicastro, F. 2002, Astrophys. J., 571, 234

Risaliti, G., Harrison, F. A., Madsen, K. K., et al. 2013, Nature, 494, 449

Roberge, W. G. 1996, in Astronomical Society of the Pacific Conference Series, Vol. 97, Polarimetry of the Interstellar Medium, ed. W. G. Roberge & D. C. B. Whittet, 401

Robishaw, T. 2008, PhD thesis, University of California, Berkeley

Rokaki, E., Collin-Souffrin, S., & Magnan, C. 1993, Astron. Astrophys., 272, 8

Rowan-Robinson, M. 1977, Astrophys. J., 213, 635

Rowan-Robinson, M. & Crawford, J. 1989, Mon. Not. R. Astron. Soc., 238, 523

Rudy, R. J. & Schmidt, G. D. 1988, Astrophys. J., 331, 325

Ruiz, J. R., Crenshaw, D. M., Kraemer, S. B., et al. 2005, Astron. J., 129, 73

Sahal-Brechot, S., Bommier, V., & Leroy, J. L. 1977, Astron. Astrophys., 59, 223

Saikia, D. J. & Salter, C. J. 1988, Annu. Rev. Astron. Astrophys., 26, 93

Salem, S. I., Panossian, S. L., & Krause, R. A. 1974, Atomic Data and Nuclear Data Tables, 14, 91

Salpeter, E. E. 1964, Astrophys. J., 140, 796

Sandage, A. & Miller, W. C. 1966, Astrophys. J., 144, 1238

Sanders, D. B. & Mirabel, I. F. 1996, Annu. Rev. Astron. Astrophys., 34, 749

Scargle, J. D., Caroff, L. J., & Noerdlinger, P. D. 1970, Astrophys. J. Lett., 161, L115

Schartmann, M., Meisenheimer, K., Camenzind, M., et al. 2008, Astron. Astrophys., 482, 67

Schmid, H. M., Appenzeller, I., & Burch, U. 2003, Astron. Astrophys., 404, 505

Schmidt, M. 1963, Nature, 197, 1040

Schmitt, H. R., Antonucci, R. R. J., Ulvestad, J. S., et al. 2001, Astrophys. J., 555, 663

Schnatz, T. W. & Siewert, C. E. 1971, Mon. Not. R. Astron. Soc., 152, 491

Schnittman, J. & Krolik, J. 2010a, in Bulletin of the American Astronomical Society, Vol. 42, AAS/High Energy Astrophysics Division #11, 725

Schnittman, J. D. & Krolik, J. H. 2010b, Astrophys. J., 712, 908

Schnittman, J. D. & Krolik, J. H. 2013, ArXiv e-prints: 1302.3214

Schurch, N. J., Done, C., & Proga, D. 2009, Astrophys. J., 694, 1

Scofield, J. H. 1989, Phys. Rev. A, 40, 3054

Serkowski, K. 1973, Astrophys. J.l, 179, L101

Seyfert, C. K. 1943, Astrophys. J., 97, 28

Shabala, S. S., Kaviraj, S., & Silk, J. 2011, Mon. Not. R. Astron. Soc., 413, 2815

Shafter, A. & Jura, M. 1980, Astron. J., 85, 1513

Shakura, N. I. & Sunyaev, R. A. 1973, Astron. Astrophys., 24, 337

Shapley, H. 1921, Bull. Nat. Res. Coun., 2, 194

Shemmer, O., Brandt, W. N., Netzer, H., Maiolino, R., & Kaspi, S. 2006, Astrophys. J. Lett., 646, L29

Shen, T. M., Chen, C. Y., & Wang, Y. S. 2007, J. Quant. Spectrosc. Radiat. Trans., 107, 323

Shibata, K. & Uchida, Y. 1985, Publ. Astron. Soc. Jpn., 37, 31

Shields, G. A. 1977, Astrophys. Lett., 18, 119

Shields, G. A. 1978, Nature, 272, 706

Shields, G. A. 1999, Publ. Astron. Soc. Pac., 111, 661

Silk, J. & Rees, M. J. 1998, Astron. Astrophys., 331, L1

Sim, S. A., Long, K. S., Miller, L., & Turner, T. J. 2008, Mon. Not. R. Astron. Soc., 388, 611

Sim, S. A., Proga, D., Miller, L., Long, K. S., & Turner, T. J. 2010, Mon. Not. R. Astron. Soc., 408, 1396

Sitko, M. L., Sitko, A. K., Siemiginowska, A., & Szczerba, R. 1993, Astrophys. J., 409, 139

Skrutskie, M. F., Schneider, S. E., Stiening, R., et al. 1997, in Astrophysics and Space Science Library, Vol. 210, The Impact of Large Scale Near-IR Sky Surveys, ed. F. Garzon, N. Epchtein, A. Omont, B. Burton, & P. Persi, 25

Slipher, V. M. 1917, Lowell Obs. Bull., 3, 59

Smith, D. M., Lin, R. P., Turin, P., et al. 2002a, Solar Phys., 210, 33

Smith, H. J. & Hoffleit, D. 1963, Nature, 198, 650

Smith, J. E., Robinson, A., Alexander, D. M., et al. 2004, Mon. Not. R. Astron. Soc., 350, 140

Smith, J. E., Robinson, A., Young, S., Axon, D. J., & Corbett, E. A. 2005, Mon. Not. R. Astron. Soc., 359, 846

Smith, J. E., Young, S., Robinson, A., et al. 2002b, Mon. Not. R. Astron. Soc., 335, 773

Smith, P. S. 1996, in Astronomical Society of the Pacific Conference Series, Vol. 110, Blazar Continuum Variability, ed. H. R. Miller, J. R. Webb, & J. C. Noble, 135

Smolčić, V. 2009, Astrophys. J. Lett., 699, L43

Sobolev, V. V. 1963, A treatise on radiative transfer.

Soffitta, P., Barcons, X., Bellazzini, R., et al. 2013, Exp. Astron.

Soffitta, P., Costa, E., Muleri, F., et al. 2010, in Society of Photo-Optical Instrumentation Engineers (SPIE) Conference Series, Vol. 7732, Society of Photo-Optical Instrumentation Engineers (SPIE) Conference Series

Soleillet, P. 1929, Ann. Phys., 12, 23

Steenbrugge, K. C., Kaastra, J. S., Crenshaw, D. M., et al. 2005, Astron. Astrophys., 434, 569

Stockman, H. S., Moore, R. L., & Angel, J. R. P. 1984, Astrophys. J., 279, 485

Stockton, A., Fu, H., & Canalizo, G. 2006, New Astron. Rev., 50, 694

Stokes, G. G. 1852, Trans Cambridge Phil. Soc., 9, 339

Stratton, J. A. & Chu, L. J. 1941a, Journal of Applied Physics, 12, 230

Stratton, J. A. & Chu, L. J. 1941b, Journal of Applied Physics, 12, 236

Sturm, E., Hasinger, G., Lehmann, I., et al. 2006, Astrophys. J., 642, 81

Suganuma, M., Yoshii, Y., Kobayashi, Y., et al. 2006, Astrophys. J., 639, 46

Sunyaev, R. A. & Titarchuk, L. G. 1980, Astron. Astrophys., 86, 121

Sunyaev, R. A. & Titarchuk, L. G. 1985, Astron. Astrophys., 143, 374

Surzhykov, A., Fritzsche, S., & Stöhlker, T. 2001, Physics Letters A, 289, 213

Svoboda, J., Dovčiak, M., Goosmann, R. W., et al. 2012, Astron. Astrophys., 545, A106

Tadhunter, C. & Tsvetanov, Z. 1989, Nature, 341, 422

Tagliaferri, G. & the NHXM Consortium. 2012, Mem. Soc. Astron. Italiana, 83, 360

Tanaka, Y., Nandra, K., Fabian, A. C., et al. 1995, Nature, 375, 659

Tielens, A. G. G. M. 2005, The Physics and Chemistry of the Interstellar Medium

Tindo, I. P., Ivanov, V. D., Mandel'Stam, S. L., & Shuryghin, A. I. 1972, Sol. Phys., 24, 429

Tombesi, F., Cappi, M., Reeves, J. N., & Braito, V. 2012a, Mon. Not. R. Astron. Soc., 422, L1

Tombesi, F., Cappi, M., Reeves, J. N., et al. 2012b, ArXiv e-prints : 1212.4851

Tombesi, F., Cappi, M., Reeves, J. N., et al. 2011, Astrophys. J., 742, 44

Tombesi, F., Cappi, M., Reeves, J. N., et al. 2010, Astron. Astrophys., 521, A57

Tran, H. D., Lyke, J. E., & Mader, J. A. 2011, Astrophys. J. Lett., 726, L21

Trimble, V. 1992, in American Institute of Physics Conference Series, Vol. 254, American Institute of Physics Conference Series, ed. S. S. Holt, S. G. Neff, & C. M. Urry, 647–656

Tristram, K. R. W., Meisenheimer, K., Jaffe, W., et al. 2007, Astron. Astrophys., 474, 837

Troland, T. H. & Heiles, C. 1982, Astrophys. J., 252, 179

Turner, T. J., Miller, L., Kraemer, S. B., Reeves, J. N., & Pounds, K. A. 2009, Astrophys. J., 698, 99

Ulrich, M.-H., Maraschi, L., & Urry, C. M. 1997, Annu. Rev. Astron. Astrophys., 35, 445

Unger, S. W., Pedlar, A., Axon, D. J., et al. 1987, Mon. Not. R. Astron. Soc., 228, 671

Urry, C. M. & Padovani, P. 1995, Publ. Astron. Soc. Pac., 107, 803

van den Bosch, R. C. E., Gebhardt, K., Gültekin, K., et al. 2012, Nature, 491, 729

Veilleux, S., Shopbell, P. L., & Miller, S. T. 2001, Astron. J, 121, 198

Veron-Cetty, M.-P. & Veron, P. 1987, A Catalogue of quasars and active nuclei

Viskanta, R. & Menguc, M. P. 1987, Progress in Energy and Combustion Science, 13, 97

Vollmer, B., Beckert, T., & Duschl, W. J. 2004, Astron. Astrophys., 413, 949

von Montigny, C., Bertsch, D. L., Chiang, J., et al. 1995, Astrophys. J., 440, 525

Wada, K. & Norman, C. A. 2002, Astrophys. J. Lett., 566, L21

Walter, R. & Courvoisier, T. J.-L. 1992, Astron. Astrophys., 266, 57

Wang, H.-Y., Wang, T.-G., & Wang, J.-X. 2005, Astrophys. J., 634, 149

Wang, H.-Y., Wang, T.-G., & Wang, J.-X. 2007, Astrophys. J. Suppl. Ser., 168, 195

Wang, J., Fabbiano, G., Risaliti, G., et al. 2010, Astrophys. J. Lett., 719, L208

Wang, J.-M. & Zhang, E.-P. 2007, Astrophys. J., 660, 1072

Watanabe, M., Nagata, T., Sato, S., Nakaya, H., & Hough, J. H. 2003, Astrophys. J., 591, 714

Waterman, P. C. 1965, Proc. IEEE, 53, 805

Weaver, K. A., Nousek, J., Yaqoob, T., Hayashida, K., & Murakami, S. 1995, Astrophys. J., 451, 147

Weedman, D. W. 1977, Annu. Rev. Astron. Astrophys., 15, 69

Weiler, K. W. & de Pater, I. 1980, Astron. Astrophys., 91, 41

Weiler, K. W. & de Pater, I. 1983, Astrophys. J.s, 52, 293

Weiler, K. W. & Raimond, E. 1977, Astron. Astrophys., 54, 965

Weingartner, J. C. & Draine, B. T. 2001, Astrophys. J., 553, 581

Weisskopf, M. C., Berthelsdorf, R., Epstein, G., et al. 1972, Review of Scientific Instruments, 43, 967

Weisskopf, M. C., Kestenbaum, H. L., Long, K. S., Novick, R., & Silver, E. H. 1978a, Astrophys. J. Lett., 221, L13

Weisskopf, M. C., Silver, E. H., Kestenbaum, H. L., Long, K. S., & Novick, R. 1978b, Astrophys. J. Lett., 220, L117

Weymann, R. J., Morris, S. L., Foltz, C. B., & Hewett, P. C. 1991, Astrophys. J., 373, 23

Whipple, F. L. & Greenstein, J. L. 1937, Proc. Nat. Acad. Sci., 23, 177

Whitney, B. A. 2011, Bull. Astron. Soc. Ind., 39, 101

Whitney, B. A. & Wolff, M. J. 2002, Astrophys. J., 574, 205

Whittle, M. 2000, Seyfert Galaxies, ed. P. Murdin

Whysong, D. & Antonucci, R. 2004, Astrophys. J., 602, 116

Williams, R. E. 1982, Astrophys. J., 261, 170

Wilms, J., Reynolds, C. S., Begelman, M. C., et al. 2001, Mon. Not. R. Astron. Soc., 328, L27

Wilson, A. S. 1996, Vistas in Astronomy, 40, 63

Wilson, A. S. & Ulvestad, J. S. 1982, Astrophys. J., 263, 576

Winter, L. M., Mushotzky, R. F., & Reynolds, C. S. 2006, Astrophys. J., 649, 730

Wittkowski, M., Hauschildt, P. H., Arroyo-Torres, B., & Marcaide, J. M. 2012, Astron. Astrophys., 540, L12

Wittkowski, M., Kervella, P., Arsenault, R., et al. 2004, Astron. Astrophys., 418, L39

Wolf, S. 2003, Astrophys. J., 582, 859

Wolf, S. & Henning, T. 1999, Astron. Astrophys., 341, 675

Wolff, R. S., Angel, J. R. P., Novick, R., & vanden Bout, P. 1970, Astrophys. J. Lett., 160, L21

Wood, K. 1997, Astrophys. J.l, 477, L25

Wood, K. & Jones, T. J. 1997, Astron. J, 114, 1405

Wood, R. W. 1922, Royal Soc. London Proc. Series A, 102, 1

Wood, R. W. & Ellett, A. 1923, Royal Soc. London Proc. Series A, 103, 396

Wood, R. W. & Ellett, A. 1924, Phys. Rev., 24, 243

Wu, X.-B. & Han, J. L. 2001, Astrophys. J. Lett., 561, L59

Wu, Z.-Q., Li, Y.-M., Duan, B., Zhang, H., & Yan, J. 2009, Chinese Physics Letters, 26, 123202

Yaqoob, T. & Padmanabhan, U. 2004, Astrophys. J., 604, 63

Young, S. 2000, Mon. Not. R. Astron. Soc., 312, 567

Young, S., Hough, J. H., Axon, D. J., Bailey, J. A., & Ward, M. J. 1995, Mon. Not. R. Astron. Soc., 272, 513

Young, T. 1801, Philosophical Transactions of the Royal Society of London, 91, 23

Zeeman, P. 1897a, Phil. Mag., 44, 55

Zeeman, P. 1897b, Phil. Mag., 43, 226

Zeeman, P. 1897c, Nature, 55, 347

Zel'dovich, Y. B. & Novikov, I. D. 1964, Sov. Phys. Dokl., 158, 811

Zhang, E.-P. & Wang, J.-M. 2006, Astrophys. J., 653, 137

Zubko, V. G. & Laor, A. 2000, Astrophys. J. Suppl. Ser., 128, 245

Zweibel, E. G. & Heiles, C. 1997, Nature, 385, 131